

## University of Southampton Research Repository ePrints Soton

Copyright © and Moral Rights for this thesis are retained by the author and/or other copyright owners. A copy can be downloaded for personal non-commercial research or study, without prior permission or charge. This thesis cannot be reproduced or quoted extensively from without first obtaining permission in writing from the copyright holder/s. The content must not be changed in any way or sold commercially in any format or medium without the formal permission of the copyright holders.

When referring to this work, full bibliographic details including the author, title, awarding institution and date of the thesis must be given e.g.

AUTHOR (year of submission) "Full thesis title", University of Southampton, name of the University School or Department, PhD Thesis, pagination

**UNIVERSITY OF SOUTHAMPTON**  
**ENERGY TECHNOLOGY RESEARCH GROUP**

Faculty of Engineering and the Environment

**EXPERIMENTAL AND NUMERICAL  
RESEARCH ON PHARMACEUTICAL  
AEROSOLS**

by

**Dehao Ju**

Thesis for the degree of Doctor of Philosophy

May 2012



# Abstract

With the background of health issues regarding the consumption of tobacco, the widespread availability of safer nicotine products and a harm reduction policy is encouraged. A cigarette alternative is designed to deliver a dose of medicinal nicotine within a timeframe comparable to that of a cigarette, and gives much of what smokers expect from a cigarette without the risks of smoking tobacco.

The general purpose of this Ph.D. project is to study the process of flashing atomization and dispersion, with a view to supporting the development of a cigarette replacement device. In order to test the effectiveness of the nicotine formulations, the analysis is carried out sizing the droplets of the aerosols at the position where human oropharynx locates, to support the further research on the deposition of droplets in the human respiratory tract.

A mechanical lung has been assembled and programmed to trigger the ‘cigarette-like’ devices with different inhalation profiles, and a dual laser system has been designed to measure the global actuation flow characteristics (e.g. spray velocity and opacity). In order to efficiently acquire sufficient droplet information (e.g. diameter and aspect ratio) from images of in and out of focus droplets, a multi-threshold algorithm is developed and successfully implemented in the automatic particle/droplet image analysis (PDIA) system. It increases the depth of field (DoF) of small particles with diameters smaller than 50 $\mu$ m, and it performs more efficiently than the dual threshold methods which are widely used in the commercial software.

A numerical multi-component two-phase actuation flow model has been developed, in order to test different formulations within various flow domains of the cigarette replacement devices. The simulated results of the numerical model have been validated with the experimental measurements and the results of previous researchers. In order to acquire an aerosol with relatively low and steady mass flow rate of nicotine, it is recommended that the mass fraction of propellant (HFA 134a) should be kept around 75%~90% to avoid the sharp temperature drop causing the sensation of freezing. The actuator nozzle diameter should be 0.2mm~0.3mm to produce a flow with relatively low mass flow rate. Furthermore the numerical model is capable of predicting the residual mass median diameter (MMD) of the spray, by using evaporation model of multi-component liquid droplets, to quantify the sprays.

Two different formulations with 95% and 98% mass fraction of HFA 134a, and two prototype cigarette alternatives with different expansion chamber volumes, have been analyzed by the numerical model and compared with the dual laser measurements. In addition, it considers the spray character by high speed imaging, with the special interest in the flashing phenomena and droplet sizes. It concludes that a larger expansion chamber volume enhances the propellant evaporation, recirculation, bubble generation and growth inside the chamber, and it made a significant improvement to produce finer sprays. Although the formulation with 98% of HFA 134a can generate smaller droplets, the formulation with 95% of HFA 134a produces more steady puffs with relatively low mass flow rate.





# List of contents

<b>ABSTRACT .....</b>	<b>I</b>
<b>LIST OF CONTENTS .....</b>	<b>III</b>
<b>LIST OF FIGURES .....</b>	<b>VII</b>
<b>LIST OF TABLES .....</b>	<b>XVII</b>
<b>AUTHOR’S DECLARATION.....</b>	<b>XIX</b>
<b>ACKNOWLEDGEMENTS.....</b>	<b>XXI</b>
<b>ABBREVIATIONS .....</b>	<b>XXIII</b>
<b>NOMENCLATURE.....</b>	<b>XXV</b>
<b>CHAPTER 1 .....</b>	<b>1</b>
<b>INTRODUCTION.....</b>	<b>1</b>
1.1 BACKGROUND .....	2
1.1.1 Introduction .....	2
1.1.2 Basic design concept of Oxette® at an early stage.....	3
1.2 MOTIVATION AND OBJECTIVES.....	7
1.3 THESIS OUTLINE .....	9
<b>CHAPTER 2 .....</b>	<b>11</b>
<b>LITERATURE REVIEW .....</b>	<b>11</b>
2.1 INTRODUCTION.....	12
2.2 TECHNICAL REVIEW ON ATOMIZATION METHODOLOGY .....	12
2.2.1 Introduction .....	12
2.2.2 Basic types of Atomizers and their performances.....	13
2.2.3 Atomizer with internal impingement.....	19
2.2.4 Discussion and Recommendation. ....	21
2.3 REVIEW ON FLASHING/BOILING ATOMIZATION .....	22
2.3.1 Introduction .....	22
2.3.2 Effect of expansion chamber geometry. ....	23
2.3.3 Review on pressurized metered dose inhaler (pMDI).....	26
2.4 REVIEW ON LUNG FUNCTION AND RELEVANT PARTICLE DEPOSITION.....	29
2.4.1 Introduction .....	29
2.4.2 Human lung volume and smoking profiles.....	29
2.4.3 Influence of particle size upon the deposition in the human lung.....	32
2.5 CHAPTER SUMMARY .....	35
<b>CHAPTER 3 .....</b>	<b>37</b>
<b>EXPERIMENTAL SYSTEMS, MEASUREMENT TECHNIQUES AND INSTRUMENTATION...37</b>	
3.1 INTRODUCTION.....	38
3.2 MECHANICAL LUNG DEVICE .....	38
3.2.1 Introduction .....	38
3.2.2 Design specification.....	38
3.2.3 Design calculations .....	40
3.2.4 Design concept .....	41
3.2.5 Rig assembly and Labview control system.....	44
3.2.6 Pressure sensor circuit connection and calibration .....	46
3.2.7 Piston motion programming and error testing .....	48

3.2.8 Additional documents.....	51
3.2.9 Final Notes.....	51
3.3. DUAL LASER BEAM METHOD .....	52
3.3.1 Introduction.....	52
3.3.2 Velocity calculation.....	54
3.4 A RIG TO MEASURE THE MASS DEPOSITION IN THE LUNG.....	55
3.4.1 Introduction.....	55
3.4.2 Design Concept.....	56
3.4.3 Design reference.....	57
3.4.4 Design calculation.....	57
3.5 CHAPTER SUMMARY .....	60
<b>CHAPTER 4.....</b>	<b>61</b>
<b>PARTICLE/DROPLET IMAGE ANALYSIS .....</b>	<b>61</b>
4.1 INTRODUCTION .....	62
4.2 PRINCIPLE OF THE DPIA PROGRAM.....	64
4.2.1 General experimental principle.....	64
4.2.2 Particle/droplet identification .....	66
4.2.3 Calibration procedure.....	71
4.2.4 Weighting factor for correction of the particle/droplet size distribution.....	72
4.3 PDIA EXPERIMENT INSTRUMENT CONSIDERATIONS .....	72
4.3.1 Brief introduction to CCD camera.....	72
4.3.2 Conceptual experimental design .....	73
4.4 CALIBRATION WITH DIODE LASER .....	75
4.4.1 Pixel sensitivity test at focal plane .....	76
4.4.2 Determination of acceptable depth of field with the dual threshold method.....	76
4.4.3 Determination of real particle/droplet characters from the calibration process by dual threshold methods .....	80
4.4.4 Determination of acceptable depth of field with the multi-threshold method.....	84
4.4.5 Determination of real particle/droplet characters from the calibration process by multi-threshold methods .....	87
4.4.6 Comparisons of curve matching methods.....	87
4.4.7 Analysis on the aspect ratio and sphericity of the calibration circles.....	89
4.4.8 Overlapping particles.....	92
4.5 GLASS SPHERE MEASUREMENTS.....	94
4.5.1 Measurement.....	94
4.5.2 Glass sphere results analysis.....	94
4.6 CHAPTER SUMMARY .....	99
<b>CHAPTER 5.....</b>	<b>101</b>
<b>NUMERICAL MODELING FOR A MULTI-COMPONENT TWO PHASE ACTUATION FLOW .....</b>	<b>101</b>
5.1 INTRODUCTION .....	102
5.2 DESCRIPTION OF THE MULTI-COMPONENT ACTUATION FLOW.....	104
5.3 MATHEMATICAL THEORY.....	106
5.3.1 Calculation of conditions for the flow in the metering chamber .....	107
5.3.2 Calculation of conditions for the flow in the expansion chamber .....	109
5.4 IMPLEMENTATION OF MULTI-COMPONENT ACTUATION FLOW MODEL .....	112
5.4.1 Introduction.....	112
5.4.2 Results .....	113
5.4.3 Summary.....	119
5.5 PREDICTIONS OF THE ACTUATION FLOW CHARACTERS WITH DIFFERENT FORMULATIONS AND GEOMETRIES .....	120
5.5.1 Introduction.....	120
5.5.2 Results .....	121

5.5.3 Summary .....	125
5.6 CHAPTER SUMMARY .....	126
<b>CHAPTER 6 .....</b>	<b>127</b>
<b>LOCAL AND GLOBAL SPRAY ANALYSIS OF OXETTE®.....</b>	<b>127</b>
6.1 INTRODUCTION .....	128
6.2 METHOD .....	129
6.2.1 Mathematical modeling .....	131
6.2.2 Experimental measurement method.....	133
6.3 RESULTS .....	134
6.3.1 Measurements of actuation flow characteristics by the dual laser method .....	134
6.3.2 Prediction of flow characteristics by the numerical multi-component actuation flow model...	139
6.3.3 Prediction of residual droplet sizes of the aerosol at x=100mm from the actuator nozzle.....	146
6.3.4 Internal and external spray characters.....	149
6.3.5 Drop sizing at an axial distance of x=100mm from the actuator nozzle .....	161
6.4 CHAPTER SUMMARY .....	167
<b>CHAPTER 7 .....</b>	<b>169</b>
<b>CONCLUSIONS AND FURTHER WORK .....</b>	<b>169</b>
7.1 CONCLUSION .....	170
7.1.1 Experimental findings.....	170
7.1.2 Computational findings .....	170
7.2 FURTHER RESEARCH.....	171
7.2.1 Experimental work.....	171
7.2.2 Computational work .....	172
7.3 RECOMMENDATIONS TO KIND CONSUMER LTD. ....	172
<b>APPENDICES .....</b>	<b>175</b>
APPENDIX I: FLOW CHARTS OF THE NUMERICAL MULTI-COMPONENT TWO-PHASE ACTUATION FLOW MODEL .....	175
APPENDIX II: THERMOPHYSICAL PROPERTIES OF DIFFERENT COMPONENTS.....	178
AII.1 HFA 134a ( $C_2H_2F_4$ ).....	178
AII.2 Ethanol ( $C_2H_6O$ ).....	178
AII.3 1, 2-Propylene Glycol ( $C_3H_8O_2$ ).....	179
AII.4 Nicotine ( $C_{10}H_{14}N_2$ ) .....	180
AII.5 Air.....	180
AII.6 Oxygen ( $O_2$ ) .....	181
AII.7 Nicotine Acid ( $C_5H_4NCO_2H$ ) .....	181
AII.8 Oleic Acid ( $C_8H_{17}CH:CH(CH_2)_7CO_2H$ ).....	181
AII.9 Menthol ( $C_{10}H_{19}OH$ ).....	181
APPENDIX III: FLUID CHARACTERS .....	182
AIII.1 Fluid flow through a nozzle or orifice.....	182
AIII.2 The functions and definitions of gas mixture properties .....	185
AIII.3 The functions and definitions of liquid mixture properties.....	186
AIII.4 Properties of the liquid and gas mixture at saturated condition in a closed container.....	187
AIII.5 Representative diameters of a spray.....	190
APPENDIX IV FORMULATION COMPONENTS OF THE CIGARETTE REPLACEMENT DEVICE (OXETTE®).....	192
AIV.1 Formula 1, 2, 3.....	192
AIV.2 Formula 4.....	193
AIV.3 Formulations tested with dual laser beam method.....	194
AIV.4 Formulations tested with high speed imaging method .....	194
APPENDIX V: PROGRAMMING FUNCTIONS.....	194
AV.1 Multi-component droplet evaporation model.....	194
AV.2 Approximation of the first derivative by Lagrange interpolating polynomial .....	198
APPENDIX VI PARTS LISTS OF THE EXPERIMENTAL RIGS .....	200

<i>AVI.1 Parts list of the mechanical lung.....</i>	<i>200</i>
<i>AVI.2 Parts list of the mass deposition rig.....</i>	<i>201</i>
<b>REFERENCES.....</b>	<b>203</b>

# List of figures

Figure 1.1 Single storage cigarette system and the dimension of the axis cross section. ...	4
Figure 1.2 Two part storage cigarette system and the dimension of the axis cross section.	5
Figure 2.1 Schematic diagram of a plain-orifice atomizer (Lefevre, 1989).....	13
Figure 2.2 SMD variations with different injection pressures for a plain-orifice atomizer at NTP (Elkot., 1982; test liquid: HFA 134a; test gas: air, thermoproperties in AII.1 and AII.5).....	14
Figure 2.3 Schematic diagram of a pressure-swirl atomizer (Lefevre, 1989).....	15
Figure 2.4 SMD variations with different injection pressures for a pressure-swirl atomizer (Wang et al., 1987; test liquid: HFA 134a;; test gas: air, thermoproperties in AII.1 and AII.5; spray cone angle: 20°; nozzle diameter: 0.2mm). ....	16
Figure 2.5 Lorenzetto-Lefebvre plain-jet airblast atomizer (Lorenzetto et al, 1977). ....	16
Figure 2.6 SMD variations with different injection pressures of air, air/liquid ratios and relative velocities between air and liquid for a plain-jet airblast atomizer (Lorenzetto et al., 1977; test liquid: HFA 134a; test gas: air, thermoproperties in AII.1 and AII.5; nozzle diameter: 0.2mm). ....	17
Figure 2.7 Schematic diagram of an effervescent atomizer (Sovani et al., 2001). ....	18
Figure 2.8 SMD variations with different injection pressures for an effervescent atomizer (Buckner et al., 1993; test liquid: HFA 134a; test gas: air, thermoproperties in AII.1 and AII.5; ALR=5; model coefficient $\epsilon$ : 0.25). ....	19
Figure 2.9 Schematic diagram of an internal impinging atomizer (Wang et al., 2005)....	20
Figure 2.10 Dependence of SMD on atomization pressure (Wang et al., 2005; test liquid: melt metal; $P_a$ : air inlet pressure; $P_L$ : liquid inlet pressure). ....	21
Figure 2.11 Combination of effervescent and pressure-swirl atomizer (recommended design for Oxette®).....	22
Figure 2.12 The effect of the orifice diameter ratio on the flow pattern in the expansion chamber (Sher et al., 2008). ....	24
Figure 2.13 Flow schematics for flashing/boiling flow in the expansion chamber (Rashkovan et al., 2006).....	26
Figure 2.14 pressurized Metered-Dose inhaler geometry (Finlay, 2001). ....	27

Figure 2.15 MMD varies with pressure & quality of fluid (Clark, 1991). .....	28
Figure 2.16 Visualizations of internal flow regime inside the expansion chamber of a typical pMDI (Versteeg et al., 2006). .....	28
Figure 2.17 Different parameters in lung volume (Palsson et al., 2003). .....	29
Figure 2.18 Nomogram relating indices of lung function to stature and age for healthy adult males and females of European descent (Cotes et al., 2006). .....	31
Figure 2.19 Cigarette smoke inhalation patterns in deep and low inhalation fractions (Tobin et al., 1982). .....	32
Figure 2.20 Various sections of the respiratory tract (National Cancer Institute). .....	33
Figure 3.1 Mechanical Lung rig assembly: Top: Inspection chamber, quick release handles, pressure sensor port & free-port, exhaust port (with non-return valve), piston with low-friction polymer o-ring and Cylinder; Lower left: Inspection chamber, pressure sensor mount and testing devices location; lower right: Electro-cylinder and fan filter. ..	42
Figure 3.2 A sketch of mechanical lung rig control system. ....	43
Figure 3.3 Mechanical Lung rig Rig assembly and connection to PC. ....	44
Figure 3.4 Labview Control Panel for the Mechanical Lung rig. ....	45
Figure 3.5 Labview block diagram for Mechanical Lung rig control. ....	45
Figure 3.6 Pressure Sensor Circuit Connection of Mechanical Lung rig (VS: voltage supply; Pressure sensor: 4: output '+'; 5: supply '+'; 6: supply '-'; 10: output '-'). .....	46
Figure 3.7 Pressure Sensor Circuit Connection and Calibration devices for Mechanical Lung rig (manometer in the left). .....	47
Figure 3.8 The variations of calibrated absolute pressures with amplified output voltages from pressure sensor (43A-002G). ....	48
Figure 3.9 The velocity profile of piston displacement in the mechanical lung. ....	49
Figure 3.10 CAD drawing of the mechanical lung rig assembly. ....	50
Figure 3.11 Volume and pressure variations in the mechanical lung under shallow inhalation and deep inhalation (the pressure was measured by pressure sensor installed in the mechanical lung). .....	51
Figure 3.12 Dual laser beam method experiment layout. ....	53
Figure 3.13 Realistic signals acquired by dual laser beam method, and it is impossible to simply read off a time delay (V: detected voltage, $V_0$ : mean voltage detected). .....	54

Figure 3.14 Mass fraction deposition rig simulating drop deposition phenomena in different human lung sections (parts list in Appendix VI.2).....	56
Figure 3.15 Combination of the mass deposition rig and the mechanical lung rig.....	57
Figure 3.16 The inner dimensions of the container in the mass deposition rig. ....	58
Figure 3.17 Influence of drop size upon the deposition with various gap heights of the container.....	59
Figure 3.18 Variations of 10 $\mu$ m drop deposition proportion with different gap heights of the mass deposition rig.....	60
Figure 4.1 Composite image of Patterson Globes and Circles calibration graticule showing objects of increasing diameter (rows) and at increasing defocus distances (columns) for the determination of an acceptable DoF.....	64
Figure 4.2 Image of glass spheres dispersed in water.....	65
Figure 4.3 Schematic representation of a particle shadow image and intensity profiles across X-X for an in-focused particle. ....	67
Figure 4.4 Images of defocused particles analyzed with dual threshold method: (a) a typical defocused particle and (b) an excessively defocused particle.....	68
Figure 4.5 Analysis of the defocused particles shown in the Figure 4.4 with multi-threshold method.....	70
Figure 4.6 Images after each processing step (a): original image; (b): image after ROI selection; (c) image after thresholding; (d): image after removing border objects.....	71
Figure 4.7 Image of a particle captured by a CCD camera (composed of pixels). ....	72
Figure 4.8 PDIA system experiment layout for real spray analysis.....	73
Figure 4.9 PDIA calibration layout with diode laser system in the lab. ....	74
Figure 4.10 Schematic diagram of the PDIA calibration rig. ....	75
Figure 4.11 The variations of the ratio of the calculated pixel area and the actual pixel area at focal plane based on the 145 $\mu$ m, 110 $\mu$ m, 74 $\mu$ m, 37 $\mu$ m and 18 $\mu$ m calibration circles at focal plane.....	76
Figure 4.12 Total area variations against the in-focused area at different defocused distances for 145 $\mu$ m, 110 $\mu$ m, 74 $\mu$ m, 37 $\mu$ m and 18 $\mu$ m calibration circles by dual threshold methods (left: Yule et al., 1978; right: Kashdan et al., 2003).....	77



Figure 4.13 Ratio of halo area and total area variations at different defocused distances for 145 $\mu$ m, 110 $\mu$ m, 74 $\mu$ m, 37 $\mu$ m and 18 $\mu$ m calibration circles by dual threshold methods (left: Yule et al., 1978; right: Kashdan et al., 2003). .....	78
Figure 4.14 Ratio of lower area and total area variation at different defocused distances for 145 $\mu$ m, 110 $\mu$ m, 74 $\mu$ m, 37 $\mu$ m and 18 $\mu$ m calibration circles by dual threshold methods (left: Yule et al., 1978; right: Kashdan et al., 2003). .....	79
Figure 4.15 Acceptable DoF approximation from 145 $\mu$ m, 110 $\mu$ m, 74 $\mu$ m, 37 $\mu$ m and 18 $\mu$ m calibration circles by dual threshold methods. ....	80
Figure 4.16 Total area variation with the ratio of halo area and total area for 145 $\mu$ m, 110 $\mu$ m, 74 $\mu$ m, 37 $\mu$ m and 18 $\mu$ m calibration circles by dual threshold methods (left: Yule et al., 1978; right: Kashdan et al., 2003). ....	81
Figure 4.17 Defocus distance variations with the ratio of halo area and total area for 145 $\mu$ m, 110 $\mu$ m, 74 $\mu$ m, 37 $\mu$ m and 18 $\mu$ m calibration circles by Kashdan et al. (2003) threshold method.....	82
Figure 4.18 Defocus distance variations with the ratio of halo area and total area for 145 $\mu$ m, 110 $\mu$ m, 74 $\mu$ m, 37 $\mu$ m and 18 $\mu$ m calibration circles by Yule et al. (1978) threshold method. ....	82
Figure 4.19 Total area variation with the ratio of halo area and total area for 145 $\mu$ m, 74 $\mu$ m, 37 $\mu$ m and 18 $\mu$ m calibration circles by dual threshold methods at two different illumination intensities (left: Yule et al., 1978; right: Kashdan et al., 2003). ....	83
Figure 4.20 Area variations against each intensity threshold for 225 $\mu$ m, 110 $\mu$ m, 37 $\mu$ m and 18 $\mu$ m calibration circles at different defocused position. ....	85
Figure 4.21 Area variations against each intensity threshold for the 110 $\mu$ m calibration circle at different defocused position.....	86
Figure 4.22 Acceptable DoF approximation from 270 $\mu$ m, 225 $\mu$ m, 180 $\mu$ m, 145 $\mu$ m, 110 $\mu$ m, 74 $\mu$ m, 37 $\mu$ m and 18 $\mu$ m calibration circles by multi-threshold methods. ....	86
Figure 4.23 Compare two curves by the discrete DTW (top) and compare the same curves by continuous DTW (bottom). (a) shows two curves with a little difference. (b) and (c) illustrate the comparison results with two different samplings of the curves. (d: the warping distance of the comparison). ....	88

Figure 4.24 Error generated by each curve matching method for the particle diameter of 4.5 $\mu$ m and 88 $\mu$ m at different defocused position.....	89
Figure 4.25 Aspect ratio (left) and sphericity (right) variations at different defocused distances for 145 $\mu$ m and 18 $\mu$ m calibration circles by the dual threshold method of Yule (1978) and the multi-threshold method.....	90
Figure 4.26 Process of the overlapping circular particles by step: (a): original image; (b): image after the 22nd threshold; (c): image after the 56th threshold; (d): image after the 97th threshold). ....	92
Figure 4.27 (a) shows the particle 1 and 2 with small overlapping fraction; (b) shows the particle 3 and 4 with large overlapping fraction; (c) and (d) show the separated particles from (a) and (b). ....	93
Figure 4.28 Comparison of number-based distributions of 70~110 $\mu$ m (left) and 100~200 $\mu$ m (right) glass spheres by PDA (Danby, 2010), dual threshold method (Yule et al., 1978) and multi-threshold method. ....	96
Figure 4.29 Comparison of volume-based distributions of 70~110 $\mu$ m (left) and 100~200 $\mu$ m (right) glass spheres by PDA (Danby, 2010), dual threshold method (Yule et al., 1978) and multi-threshold method. ....	96
Figure 4.30 Comparison of the number-based (left) and volume based (right) distributions of the 1 $\mu$ m~50 $\mu$ m glass spheres produced by the multi-threshold method with the data generated by laser diffraction and microscopy (Stevens, 2006). ....	97
Figure 4.31 (a): images of the moving glass spheres and the quiescent glass spheres at different defocused distancess ( $D_F/D=4.13$ for sphere 1 and 3; $D_F/D=0.75$ for sphere 2 and 4). (b) and (c): the aspect ratios the sphericities of the moving glass spheres 1 to 4 of Figure 4.30a at each threshold. ....	98
Figure 4.32 Comparisons of the aspect ratios (left) and sphericities (right) acquired by the dual threshold method of Yule (1978) and the multi-threshold method for the 70 $\mu$ m~110 $\mu$ m and 100 $\mu$ m~200 $\mu$ m glass spheres.....	99
Figure 5.1 Pressurised metered-dose inhaler. ....	104
Figure 5.2 Simplified flow model for a typical pMDI. ....	105
Figure 5.3 Comparison of present model results and the data of Dunbar (1996) (single component actuation flow).....	115

Figure 5.4 Temporal variation of properties within the expansion chamber and actuation flow for the formulations with different mass fraction of propellant HFA 134a. ....	117
Figure 5.5 Peak exit velocities and spray durations measured by the dual laser method for the formulations with different mass fraction of HFA 134a at x=25mm, compared to the numerical predictions.....	118
Figure 5.6 Relative light obscuration for the formulations with different mass fraction of HFA 134a at x=100mm (pMDI).....	119
Figure 5.7 Temporal variation of the pressure and the temperature in the expansion chamber for four formulations with different mass fractions of HFA 134a (with a requirement of 0.012g oxygen and 0.1mg nicotine for one inhalation, the nozzle diameter is 0.3mm and ½ cigarette volume is used for oxygen storage).....	122
Figure 5.8 Variations of the nicotine mass flow rates for four formulations with different mass fractions of HFA 134a (with a requirement of 0.012g oxygen and 0.1mg nicotine for one inhalation, the nozzle diameter is 0.3mm and ½ cigarette volume is used for oxygen storage).....	123
Figure 5.9 Temporal variations of the pressure and the temperature in the expansion chamber with different actuation nozzle diameters (test formulation: Formula 4 (Appendix AIV.4.1); no oxygen in the metering chamber).....	124
Figure 5.10 Variations of the nicotine mass flow rates with different actuation nozzle diameters (test formulation: Formula 4 (Appendix AIV.4.1); no oxygen in the metering chamber). ....	124
Figure 5.11 Variations of the nicotine mass flow rates with different oxygen storage volumes (test formulation: Formula 4 (Appendix AIV.4.1); with a requirement of 0.012g oxygen and 0.1mg nicotine for one inhalation). ....	125
Figure 6.1 Schematic diagram of Oxette® geometry of interest. ....	130
Figure 6.2 Pressure variations in the lung under shallow inhalation and deep inhalation measured by the pressure sensor installed in the mechanical lung.....	131
Figure 6.3 Graphic description of droplet evaporation model along a turbulent jet.....	132
Figure 6.4 Relative light obscuration for the spray generated by Oxette® 1 with KDCRA103 (95% HFA 134a) and KDCRA122 (98% HFA 134a) under the 1 <sup>st</sup> deep inhalation (left: at x=25mm; right: at x=100mm).....	136

Figure 6.5 Relative light obscuration for the spray generated by Oxette® 2 with KDCRA103 (95% HFA 134a) and KDCRA122 (98% HFA 134a) under the 1 <sup>st</sup> deep inhalation (left: at x=25mm; right: at x=100mm). .....	137
Figure 6.6 Relative light obscuration for the spray generated by Oxette® 2 with KDCRA103 (left column: 95% HFA 134a) and KDCRA122 (right column: 98% HFA 134a) under the 1 <sup>st</sup> , the 2 <sup>nd</sup> and the 3 <sup>rd</sup> shallow inhalation (top row: at x=25mm; bottom row: at x=100mm). .....	138
Figure 6.7 Predicted temporal variations of the actuation flow properties at the exit of the actuator nozzle for two formulations (KDCRA103 with 95% HFA 134a and KDCRA122 with 98% HFA 134a) under sequential times of the deep inhalation. (Left column: Oxette® 1; Right column: Oxette® 2). .....	141
Figure 6.8 Predicted temporal variations of the actuation flow properties at the exit of the actuator nozzle for KDCRA103 (95% HFA 134a) under sequential times of the shallow inhalation (left column: Oxette® 1; right column: Oxette® 2). .....	143
Figure 6.9 Predicted temporal variations of predicted initial MMD at the exit of the actuator nozzle for KDCRA103 (95% HFA 134a) and KDCRA122 (98% HFA 134a) under the 1 <sup>st</sup> deep inhalation; and only for KDCRA103 under sequential times of the shallow inhalation (left column: Oxette® 1; right column: Oxette® 2). .....	146
Figure 6.10 The predicted ratios of the residual diameter at x=100mm from the actuator nozzle and initial diameter at the exit of the actuator nozzle under the 1 <sup>st</sup> shallow inhalation for KDCRA103 (95% HFA 134a) and KDCRA122 (98% HFA 134a). .....	148
Figure 6.11 Predicted temporal variations of predicted residual MMD of the spray generated by Oxette® 2 at x=100mm from the actuator nozzle for KDCRA103 (95% HFA 134a) and KDCRA122 (98% HFA 134a) under the 1 <sup>st</sup> deep inhalation (left); and only for KDCRA103 under sequential times of the shallow inhalation (right). .....	149
Figure 6.12 Visualization during 0.001s ~ 0.013s after the start of the 1 <sup>st</sup> shallow inhalation: (a) with Oxette® 1 for KDCRA103 (95% HFA 134a); (b) with Oxette® 1 for KDCRA122 (98% HFA 134a); (c) with Oxette® 2 for KDCRA103 (95% HFA 134a); and (d) with Oxette® 2 for KDCRA122 (98% HFA 134a). .....	150
Figure 6.13 Visualization of internal flow regime inside expansion chamber of Oxette® 1: (a) presents the cross section of the expansion chamber and the actuator nozzle without	

any flows; (b) ~ (f) sequential images of the internal flow in the expansion chamber recorded at 500Hz.....	151
Figure 6.14 A sample of jet generated under 1 <sup>st</sup> shallow inhalation with Oxette® 2 for KDCRA103 (95% HFA 134a) (a) unprocessed image and (b) thresholded image.....	153
Figure 6.15 Left: The corresponding jet tip penetration and Right: jet penetration rate along the jet during the first 0.001s~0.012s under 1st shallow inhalation profile for KDCRA103 (95% HFA 134a) and KDCRA122 (98% HFA 134a). ....	154
Figure 6.16 Spray visualization from 0.1s to 1.1s under the 1 <sup>st</sup> shallow inhalation with Oxette® 2 for KDCRA103 (left: 95% HFA 134a) and KDCRA122 (right: 98% HFA 134a). ....	156
Figure 6.17 Spray visualization at the expansion region from 0.151s to 0.158s under 1 <sup>st</sup> shallow inhalation with Oxette® 2 for KDCRA122 (98% HFA 134a).....	159
Figure 6.18 Mean streamlines of the flow in a constriction examined by Domnick et al. (1995).....	159
Figure 6.19 Close visualizations on the pulsations near the exit of the actuator nozzle under 1 <sup>st</sup> shallow inhalation with Oxette® 2 for KDCRA103 (95% HFA 134a), sequentially recorded at 5kHz.....	161
Figure 6.20 Number and volume based size distributions of the droplets for the spray generated by KDCRA103 (95% HFA 134a) and KDCRA122 (98% HFA 134a) under the 1 <sup>st</sup> shallow inhalation. ....	162
Figure 6.21 Large drop in (b) formed by the ligament from (a) due to the turbulent mixing. ....	162
Figure 6.22 The background intensity variations of the droplet images for the spray generated by Oxette® 2 with KDCRA103 (left: 95% HFA 134a) and KDCRA122 (right: 98% HFA 134a) under 1 <sup>st</sup> , 2 <sup>nd</sup> and 3 <sup>rd</sup> shallow inhalation at x=100mm from the actuator nozzle.....	166
Figure A.1 Flow chart of the numerical multi-component two-phase actuation flow model. ....	175
Figure A.2 Flow chart of the mass and the energy balance in the metering chamber of the numerical multi-component two-phase actuation flow model. ....	176

Figure A.3 Flow chart of the mass and the energy balance in the expansion chamber of the numerical multi-component two-phase actuation flow model.....	177
Figure A.4 A schematic diagram of the compressible flow through a convergence nozzle. .....	184
Figure A.5 A schematic diagram of the two phase compressible flow through a convergence nozzle. ....	184
Figure A.6 A schematic diagram of the mixture of multi-component liquid and gases in a closed container.....	189
Figure A.7 Assembly drawing for the mass deposition rig with the numbered items listed in Table A.9.....	201
Figure A.8 Assembly photo of the mass deposition rig. ....	201



# List of tables

Table 2.1 Particle deposition proportions in different lung section with various particle sizes. ....	34
Table 3.1 Variables of programming for the piston motion in the mechanical lung rig (Parker, 2003).....	48
Table 3.2 Different lung region volumes (Stahlhofen et al., 1989). ....	57
Table 4.1 PDIA system instruments. ....	74
Table 5.1 Dimensions of a typical pMDI (Dunbar, 1996). ....	105
Table 5.2 The formulations and the geometries implemented in the numerical predictions by the multi-component two-phase flow model. ....	120
Table 6.1 Axial spray velocity generated by KDCRA103 (95% HFA 134a) and KDCRA122 (98% HFA 134a) with Oxette® 2 under different inhalation profiles at x=25mm and x=100mm. ....	139
Table 6.2 Predicted mass fraction of the formulations actuated during each sequentially deep or shallow inhalation for KDCRA103 (95% HFA 134a) and KDCRA122 (98% HFA 134a) with Oxette® 1 and Oxette® 2. ....	144
Table 6.3 Half spray cone angles and spreading rates under 1 <sup>st</sup> shallow inhalation with Oxette® 2 for KDCRA103 (95% HFA 134a) and KDCRA122 (98% HFA 134a) from 0.1s to 1.4s. ....	158
Table 6.4 Mean diameters (µm) at different time scales under the 1 <sup>st</sup> shallow inhalation with Oxette® 2 for KDCRA103 (95% HFA 134a) and KDCRA122 (98% HFA 134a). ....	163
Table 6.5 Mean diameters (µm) at each test under 1 <sup>st</sup> shallow inhalation with Oxette® 2 for KDCRA103 (95% HFA 134a) and KDCRA122 (98% HFA 134a).....	165
Table A.1 Mean diameters and their applications (Lefevre, 1989).....	191
Table A.2 Mass distributions of Formulas 1, 2, 3. ....	192
Table A.3 HFA 134a requirement for different formulations (Formula 1, 2 and 3) in 20ml canister. ....	193
Table A.4 HFA 134a requirement for different formulations (Formula 1, 2 and 3) in 30ml canister. ....	193
Table A.5 Mass distribution of Formula 4 .....	193



Table A.6 Mass distribution of different formulations analyzed by the dual laser beam method. ....	194
Table A.7 Mass distribution of different formulations analyzed by the high speed imaging method. ....	194
Table A.8 Parts list of the mechanical lung rig (section 3.2, Chapter 3).....	200
Table A.9 Parts list of the mass deposition rig (section 3.4, Chapter 3).....	202

# Author's declaration

I, Dehao Ju, declare that the thesis entitled EXPERIMENTAL AND NUMERICAL RESEARCH ON PHARMACEUTICAL AEROSOLS and the work presented in the thesis are both my own, and have been generated by me as the result of my own original research. I confirm that:

§ this work was done wholly or mainly while in candidature for a research degree at this University;

§ where any part of this thesis has previously been submitted for a degree or any other qualification at this University or any other institution, this has been clearly stated;

§ where I have consulted the published work of others, this is always clearly attributed;

§ where I have quoted from the work of others, the source is always given. With the exception of such quotations, this thesis is entirely my own work;

§ I have acknowledged all main sources of help;

§ where the thesis is based on work done by myself jointly with others, I have made clear exactly what was done by others and what I have contributed myself;

§ parts of this work have been published as:

- Ju, D., Shrimpton, J., Hearn, A., 2010. The effect of reduction of propellant mass fraction on the injection profile of metered dose inhalers. *International Journal of Pharmaceutics* 391(1-2), 221–229.
- Ju, D., Shrimpton, J., Hearn, A., 2012. A multi-thresholding algorithm for sizing out of focus particles. *Particle & Particle Systems Characterization*. (Accepted for publication April 2012).
- Ju, D., Shrimpton, J., Moira, B., Hearn, A., 2012. Effect of expansion chamber geometry on atomization and spray dispersion characters of a flashing mixture containing inerts. Part I. Numerical predictions and dual laser measurements. *International Journal of Pharmaceutics*. (Accepted for publication April 2012).
- Ju, D., Shrimpton, J., Moira, B., Hearn, A., 2012. Effect of expansion chamber geometry on atomization and spray dispersion characters of a flashing mixture containing inerts. Part II. High speed imaging measurements. *International Journal of Pharmaceutics*. (Accepted for publication April 2012).



# Acknowledgements

There are many people that deserve my deepest gratitude. It goes first and foremost to my supervisor, Dr. John Shrimpton, for having given me this opportunity and most of all for having been constantly supportive, available and patient with me. I will always be grateful for his constant encouragement and guidance. Without his consistent and illuminating instruction, this thesis could not have reached its present form. I must thank Professor Kai H. Luo and Dr. Graham Roberts providing me valuable comments and examining me halfway of my Ph.D. project. In addition, studying and doing research at University of Southampton gave me the chance to meet many talented researchers: the discussions we have had provided me a lot of interesting ideas that I hope I will have the chance to develop in the next future. Of course, the help from Alex Hearn and Moira Bowdrey, and the finance support from Kind Consumer Ltd. ([www.kindconsumer.com](http://www.kindconsumer.com)) are important.

I am very grateful to my friends and colleagues here who have supported me in various ways. I would particularly like to thank Simon. R. Klitz, without his manufacturing skills, the experimental work would not be set up efficiently and accurately; I would like to thank Matt Danby for helping me with setting up the mechanical lung rig; I would like to thank Agisilaos Kourmatzis, Mihaela Stevar and Jiao Shou (Michael) being helpful and amusing during our time together in the lab; I would like to thank Sina Haeri and Robert-Jan Koopmans Simon Lewis for helping me with numerical simulation problems.

Finally, my thanks would go to my beloved parents, Zixuan Ju and Fenji Zhao, for their loving considerations and great confidence in me all through these years. My friends also deserve my sincere gratitude for surviving me from the tedious work and they are: Biling Chen, Man Zhang, Ashley Lin, Violet Lin, Xiaochen Si, Aiqing Zheng, Iris Wu, Kangping Zhang, Yu Zhao, Jianyue Zhu, Ruofan Zhang, Jiannan Yang, Jingjing Wang, Ling-ying hung, Shiyo Lin, Huifang Xiao, Junwei Za, Xinfu Luo, Chenxi Hao, Jin Sun, Xin Meng, Zaidi Tu, Gongcheng Chen, Bo Wang, Chuan Wang, Yilin Huo, Yifang Gao, Min Quan.



# Abbreviations

ADC	Analogue to digital converter
ALR	Air/liquid mass flow rate ratio
CCD	Charged coupled device
CFD	Computational fluid dynamics
CPU	Central processing unit
DAC	Digital to analogue converter
DAQ	Data acquisition
DC	Direct current
DEM	Discrete element method
DoF	Depth of field
DTW	Dynamic Time Warping
EC	Expansion Chamber
FBD	Free body diagram
FoV	Field of view
LDA	Laser Doppler Anemometry
MC	Metering Chamber
MDI	Metered dose inhaler
MMD	Mass median diameter
NTP	Normal temperature (20°C) and Pressure (1atm/101325Pa)
PC	Personal computer
PDA	Phase Doppler Anemometry
PDIA	particle/droplet image analysis
PDF	Probability density function
pMDI	Pressurized-metered dose inhaler
ROI	Region of interest
SATP	Standard ambient temperature and pressure
SMD	Sauter mean diameter
STD	standard deviation
STM	standard deviation method
STP	Standard temperature and pressure
VI	Virtual instrument



# Nomenclature

Symbol	Definition	Unit
A	cross-section area (or image pixels)	m <sup>2</sup> (or pixels)
A <sub>H</sub>	halo area	pixels
A <sub>infocus</sub>	total area at focal plane	pixels
A <sub>T</sub>	particle interior area	pixels
A <sub>18</sub>	total area of the 18μm calibration circle at focal plane	pixels
c <sub>p/v</sub>	specific heat capacity at constant pressure/volume	J/(kgK)
C <sub>d</sub>	discharge coefficient	-
d <sub>o</sub>	orifice diameter	m
D	Particle/droploet diameter	m
D <sub>F</sub>	defocused distance	m
D <sub>145</sub>	diameter of the 145μm calibration circle	m
f	vapour mass fraction (vapour/gas mixture ratio)	-
h	specific enthalpy	J/kg
h <sub>fg</sub>	latent energy of evaporation	J/kg
F	force	N
H	enthalpy (or the height of the image field of view)	J (or m)
I	light/colour intensity	grayscale
K <sub>E</sub>	a constant to calculate camera exposure time	
L	length	m
m	mass	kg
$\dot{m}$	mass flow rate	kg/s
M	molecular weight	kg/mol
Ma	Mach number	-
n <sub>i</sub>	weighting factor for the particles with a diameter of D <sub>i</sub>	
p	pressure	Pa
Δp	injection pressure differential across nozzle	Pa
P	perimeter	pixel
q	quality of fluid (gas/mixture mass fraction)	-
R	resistance	Ω
S	sphericity	
t	time or (film thickness)	s or (m)
T	temperature	K
u	axial velocity	m/s
W	the width of the image field of view	m

## Greek

Symbol	Definition	Unit
$\gamma$	heat capacity ratio	-
$\rho$	density	kg/m <sup>3</sup>



$\phi$	volume fraction	-
$\mu$	Dynamic viscosity	kg/(m•s)
$\nu$	Kinematic viscosity	m <sup>2</sup> /s
$\sigma$	Surface tension	N/m; kg/s <sup>2</sup>
$\theta$	spray cone angle	°

### Subscript

Symbol	Definition
L	lower threshold
H	higher threshold
P	propellant
T	total
a	air
atm	atmosphere
b	background
c	critical
ds	downstream
ec	expansion chamber
exp	camera exposure
g	gas (excluding vapour)
l (or L)	Liquid (or lower)
m	mixture
max	maximum
mc	metering chamber
min	minimum
out	outlet flow
p	particle
peak	peak
r	relatively
t	nozzle throat
us	upstream

### Superscript

Symbol	Definition
n	new time level
o	old time level
T	total
*	critical value
-	mixture or average

### Universal Constants

Symbol	Definition	Value	Unit
R	universal gas constant	8.314	J/(mol•K)

# Chapter 1

## Introduction

---

This chapter provides some background of health issues regarding to the consumption of tobacco and encourages the widespread availability of safer nicotine products and harm reduction policy. This chapter also introduces the main objectives and outline of the whole Ph.D. thesis, with the concern on developing an alternative of smoking tobacco. Due to the design restrictions, an early design concept of the cigarette replacement device, using only pressurized oxygen as a propellant, was abandoned. A volatile propellant (HFA 134a) was recommended as an alternative.

---

## 1.1 Background

### 1.1.1 Introduction

The World Health Organization (WHO) estimated in 2004 that there were 5.4 million smoking related deaths each year worldwide, more than that caused by Tuberculosis, Malaria and HIV put together. The WHO estimates based on current trends that tobacco use will cause more than 8.3 million deaths annually by 2030 at which point they will represent almost 10% of all deaths globally (World Health Organization, 2008). On average across the globe, adult male and female smokers lost an average of 13.2 and 14.5 years of life respectively, due to smoking (Centers for Disease Control and Prevention, 2002). Department of Health estimated that in excess of 100,000 people die each year due to smoking in the UK (UK Department of Health, 2006). Over the last 50 years, six million Britons have died from tobacco-related diseases, three million of whom died in middle age (15-69) losing on average 20 years of life (Peto, 1994).

It is believed that the innovation into practical alternatives for the tobacco user is the key in saving lives. If an effective, affordable and safe replacement for the tobacco cigarette can be adopted widely by smokers who cannot or will not quit, it would deliver far-reaching public health benefits by saving thousands of life years lost prematurely in every generation.

There is an emerging consensus supported by a wealth of science, that pure medicinal nicotine carries relatively little health risk (Medicines Healthcare products Regulatory Agency, 2010). It is the combustion of the tobacco and the tar in tobacco that causes harm, containing over 4,000 chemicals including at least 69 cancer-causing substances (International Agency for Research on Cancer, 2002). Nicotine is chemically very similar to caffeine and has a very similar metabolic effect on the body. However, nicotine is addictive and those craving nicotine can find it extremely difficult to cease or cut down. 75% of current smokers have tried to give up smoking at some point. However research indicates that despite nearly half of all smokers not expecting to be smoking in a year's time, only 2-3% of these actually stop permanently each year (West, 2006).

The fine particulates within tobacco smoke deliver the much smaller molecules of nicotine to the brain in approximately six seconds after inhalation. A craver of nicotine has therefore traditionally been faced with no real alternative to a tobacco cigarette in

terms of speed of craving satisfaction. Low concentrations of nicotine mimics the effects of neurotransmitters in the brain that influence emotion and cognition and can generate feelings of pleasure.

Kind Consumer Ltd. has developed a technology platform for optimal inhalation delivery. The technology is a non-electronic, breath-operated nicotine delivery system that delivers a reproducible dose of nicotine formulation targeted for lung delivery as an aerosol released from the device via a breath-actuated valve. The technology contains no tobacco and does not involve combustion or heat of any nature in its operation. The 'cigarette' device is named as Oxette® by Kind Consumer Ltd. A user actuates the valve to regulate their nicotine intake in a manner similar to that of smoking. Each device will give a comparable number of puffs as a conventional tobacco cigarette.

### **1.1.2 Basic design concept of Oxette® at an early stage**

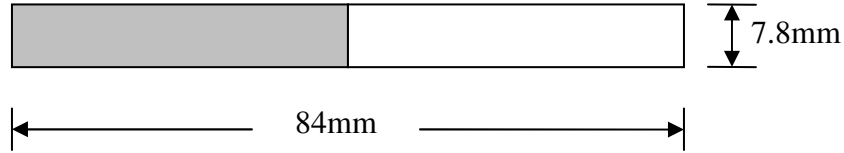
Granger (2005) reported that oxygen can be used as a therapy to reduce both the desire for nicotine and withdrawal symptoms (e.g. depression, difficulty sleeping or anger). However, there are some technical and safety issues associated with the use of Oxygen in small hand held devices. At an early stage, the design concept of Oxette® is to use oxygen as the propellant of the nicotine formulations to match the specifications below (Shrimpton, 2008).

From the literature supplied by Kind Consumer Ltd., the following features are required for the design:

- Total inhaled flow rate is around 2 liters/second on average.
- Duration of inhalation is around 2 seconds.
- The cigarette' should provide 20 inhalations between refills.
- The 'Pack' should provide 20 'Cigarette' refills.
- Each inhalation should provide 0.012g oxygen and 0.1mg nicotine.
- The dimension of the axis cross section of a typical 'cigarette' is 80mm×7.8mm as shown in Figure 1.1.

From the report of Shrimpton (2008), a single storage cigarette system and a two-part storage cigarette system are introduced below, respectively, along with the capacity calculations and thermodynamic analysis under an ambient condition of normal temperature (25°C) and pressure (1atm/101325Pa) (NTP) following the ideal gas law.

### *Single storage cigarette system*



*Figure 1.1 Single storage cigarette system and the dimension of the axis cross section.*

A schematic diagram of the axis cross section of Oxette® is shown in Figure 1.1, assuming maximum available space for oxygen storage in the Oxette® is half the size of a standard cigarette which is  $2.007 \times 10^{-6} \text{ m}^3$ . At NTP, assuming 20 inhalations are required per cigarette and 0.012g oxygen is provided per inhalation, the pressure of  $\text{O}_2$  storage in the cigarette is  $9.262 \times 10^6 \text{ Pa}$  (92.62bar) which is excessive; nevertheless, assuming one inhalation is required per cigarette, the pressure of  $\text{O}_2$  storage in the cigarette is  $4.634 \times 10^5 \text{ Pa}$  (4.6bar).

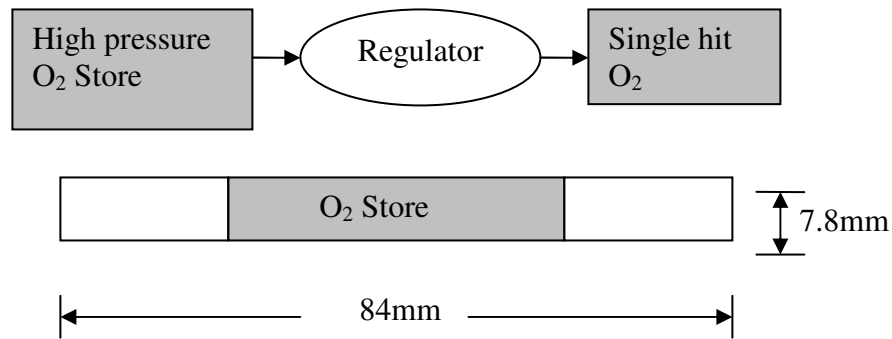
In addition, 20 refills are required per pack with 20 inhalations between refills. Assuming maximum available space for in pack oxygen storage is half the size of a standard cigarette packet, i.e. the dimension for the pack with 20 cigarettes in 7-6-7 arrangement is 87.5mm×56mm×23.5mm, where half pack volume is  $5.758 \times 10^{-5} \text{ m}^3$ . At an ambient condition of NTP, the pressure of  $\text{O}_2$  storage in pack is  $6.459 \times 10^6 \text{ Pa}$  (64.59bar).

In order to make an early comment as to whether adiabatic cooling of the depressurizing oxygen gas is an issue, there is a need to work out the mass fraction of oxygen to inhaled air. The volume of  $\text{O}_2$  based on the requirement of 0.012g  $\text{O}_2$  per inhalation in mass is  $8.517 \times 10^{-6} \text{ m}^3$ . As an inhalation is approximately 2 liters/s for about 2 seconds and it is  $4 \times 10^{-3} \text{ m}^3$  in total, the inhaled air required is 3.991 liters in volume and 5.09g in mass. Mass fraction of  $\text{O}_2$  in the air is calculated as 0.0024, which suggests that temperature of inhaled mixture will be near ambient.

With the aim to define the contracting sub-sonic section of a de-laval nozzle such that the throat of the nozzle is sonic and mass flow is controlled by the physics of the system rather than mechanical restricting valves, an actuation flow through the nozzle is studied for  $\text{O}_2$ . From the previous calculations at the ambient condition of NTP, the initial pressure and temperature of the  $\text{O}_2$  storage are  $9.262 \times 10^6 \text{ Pa}$  and 298.15K for the 20 inhalation cigarette. Mass flow rate of  $\text{O}_2$  required is  $6 \times 10^{-6} \text{ kg/s}$  for 0.012g per inhalation

of 2s duration. Hence, by equation AIII.1.13, the nozzle throat area for sonic conditions  $A^*$  is calculated as  $1.4896 \times 10^{-9} \text{m}^2$  which corresponds to a diameter of  $4.355 \times 10^{-5} \text{m}$  (44 $\mu\text{m}$ ). From isentropic relations, with a Mach number of one at the throat, the temperature of  $\text{O}_2$  ( $T_t$ ) and the pressure ( $P_t$ ) at the throat are determined as  $T_t = 248.5 \text{K}$  (-24.69°C) (equation AIII.1.7) and  $P_t = 4.893 \times 10^6 \text{Pa}$  (equation AIII.1.6). And, assuming the ambient conditions are NTP, the exit temperature of  $\text{O}_2$ ,  $T_e$ , is 81.76K (-191°C) (equation AIII.1.4); The exit Mach number,  $\text{Ma}_e$ , is 3.193, indicating an exit velocity of approximately 550m/s (equation AIII.1.7 & AIII.1.11); The exit area,  $A_e$ , is  $7.579 \times 10^{-9} \text{m}^2$ , which corresponds to a diameter of  $9.824 \times 10^{-5} \text{m}$  (98 $\mu\text{m}$ ) (equation AIII.1.14). Based on the mass fractions of  $\text{O}_2$  and inhaled air (at the ambient condition of NTP) required for an overall inhalation rate of 2 liters per second, the mixture temperature is calculated as 297.69K (24.54°C).

#### *Two part storage cigarette system*



*Figure 1.2 Two part storage cigarette system and the dimension of the axis cross section.*

A single storage cigarette system has been introduced above. The aim here is to look at the possibility of utilizing a two part storage system within the cigarette (Figure 1.2), with a main high-pressure store feeding a low-pressure, single inhalation store. If the driver pressure is reduced, the throat diameter of the nozzle will increase, and therefore would improve the ease of tooling for the device.

By assuming the entire storage available is utilized for a single inhalation store the upper limit on the geometry of the delivery nozzle can be found. Assuming that the maximum storage space within the cigarette is half the volume of a cigarette  $2.007 \times 10^{-6} \text{m}^3$ , if this was a single inhalation store (i.e. one inhalation from a single refill), at the ambient condition of NTP, the pressure of  $\text{O}_2$  storage in cigarette is  $4.634 \times 10^5 \text{Pa}$  (4.6bar).

Similar to the calculations for the single storage cigarette system, this results that the nozzle throat area  $A^*$  is  $2.9776 \times 10^{-8} \text{ m}^2$  and a diameter of  $1.9471 \times 10^{-4} \text{ m}$  (195  $\mu\text{m}$ ), and at the throat the temperature of  $\text{O}_2$  ( $T_t$ ) is 248.5K (-24.69°C) and the pressure ( $P_t$ ) is  $2.4478 \times 10^5 \text{ Pa}$ . Assuming the ambient conditions are NTP, the exit temperature of  $\text{O}_2$  ( $T_e$ ) is 192.4K (-80.8°C) and the exit Mach number  $\text{Ma}_e$  is 1.2072, and it indicates an exit velocity of approximately 319m/s; The exit area  $A_e$  is  $3.0746 \times 10^{-8} \text{ m}^2$  which is a diameter of  $1.9786 \times 10^{-4} \text{ m}$  (198  $\mu\text{m}$ ). Based on the mass fractions of  $\text{O}_2$  and inhaled air (at NTP) required for an overall inhalation rate of 2 liters per second, the mixture temperature is calculated as 297.92K (24.77°C).

### ***Summary***

The major points to be made from the analysis of single storage and two-part storage cigarette systems are:

- The mass/pressure of oxygen in the pack is not a design pinch point in terms of capacity. Typically the oxygen pressure in the pack needs to be up to 70bar, easily within the specification of other off the shelf oxygen canisters.
- The cigarette oxygen mass is a design pinch point for the design specification of 20 inhalations before a refill. Around 5bar pressure is lost every inhalation for the volume assumed, requiring a pressure drop of 100bar over 20 inhalations for the volume of the cigarette. This impacts the pack pressure (the pack pressure must exceed the cigarette pressure in order to refill it).
- Since there is also a requirement that the first and the last (20<sup>th</sup>) inhalation should have reasonably constant characteristics, this forces up the baseline pressure of the entire system considerably. It is suggested that the requirement of 20 inhalations per cigarette between refills of oxygen from the pack may need to be reduced considerably to perhaps 2 or 3.
- Mass fraction of  $\text{O}_2$  is small in terms of total mass per inhalation. This suggests that temperature of inhaled mixture will be near ambient.
- A thermodynamic analysis of the oxygen decompression centred on using a de Laval nozzle to control the oxygen mass flow rate. For large cigarette pressures (up to 100bar) extremely small throat diameters are required. The scales are possible, but probably not feasible within the context of a disposable device.

- A modified cigarette device was also considered, with a high and a low pressure chambers. The low pressure chamber regulates the mass of oxygen per inhalation and the reduced pressure within this chamber permits a more feasible throat diameter.

***Recommendations/Actions from the above analysis are:***

- A decision must be made as how many inhalations are desired from the cigarette. If 20 inhalations were a design requirement then the oxygen pressure is likely to be significant. A high oxygen pressure also increases the control/metering/safety challenges. One alternative is to reduce the number of inhalations per refill. The other is to make the cigarette integral to the pack, and to market the pack as a refillable oxygen store, into which various liquid based ‘flavours’ may be added.
- The suggested metering method, a De Laval nozzle should be assessed against off the shelf devices provided by companies such as Air Products and BOC. This approach has the advantage of no moving parts, however tooling may be expensive, and the throat may be prone to blockage.
- Instead of pressurized oxygen, flashing propellant (e.g. HFA 134a) is recommended to drive the flow (Cripps et al., 2000), with similar design principle of a pressurized metered dose inhaler (pMDI) (Newman, 2005).

Overall, the primary recommendation is that the dual requirements of a removable ‘cigarette’ containing oxygen for 20 inhalations present significant engineering difficulties within the context of a disposable unit. In this Ph.D. thesis, using the pressurized oxygen as a propellant is abandoned, and mainly the flow with a flashing propellant and nicotine is analyzed.

## **1.2 Motivation and objectives**

The general purpose of the Ph.D. research work is to study the process of flashing atomization and dispersion, with a view to supporting the development of a breath-activated device to deliver a dose of medical nicotine, via an aerosol that mimics the action of smoking. And it gives much of what smokers expect from a cigarette without the risks of smoking within a timeframe comparable to that of cigarette. In order to test the effectiveness of the nicotine formulations, the analysis is carried on sizing the droplet of the aerosols at the position where human oropharynx locates, to support the further



research on the deposition of droplets in the human respiratory tract. The combination of the experimental study and the numerical analysis is implemented thought the whole project.

Within this aim there are *three specific objectives* that will constitute the major part of the research activity.

- Fundamental investigation of the flashing atomization.

Instead of chlorofluorocarbons (CFCs), flashing hydrofluoroalkanes (HFA) propellants have been widely used in the pharmaceutical industry for the delivery of fine particles human respiratory tract (Cripps et al., 2000). Typical formulations of the pressurized metered dose inhalers (pMDIs) are closely tied to the inhaler delivery system to engineer the correct amount of cavitation upstream of the orifice exit to produce atomization, without excessively cooling the system to the point of freezing. Preliminary findings suggest that the nicotine formulations have different volatility characteristics, and hence there is a requirement to investigate at a fundamental level the two phase flow within the pMDI internal flow passages. The output from this research work is expected to guide the development of the atomizer technology and to provide information as to how to obtain maximum atomization efficiency from the available energy.

- Research on the droplet size distributions of the inhaled aerosol.

A key requirement of the Oxette® design is that the nicotine is inhaled deeply into the lung, and therefore the need is to ensure the nicotine is in the form of very small droplets (around 2~5 $\mu$ m in diameter). Research on the droplet size distribution of the spray forms the basis for estimating the quantity of inhaled aerosol which reached the various parts of the respiratory tract. It provides the reference to optimize the inhaler and is therefore one of the essential factors in the characterization of the effectiveness of different formulas targeted to different lung sections. A simple rig has been designed in section 3.4, Chapter 3, to test how droplets deposit in different respiratory sections. In order to acquire sufficient information on the small droplets with the diameter of 2~5 $\mu$ m from images, a new droplet sizing methodology has been developed and will be presented in Chapter 4.

- Measurement and evaluation of spray plume characteristics

Another key requirement of the Oxette® design is that the spray plume generated by the atomizing device (Oxette®) should have the visual appearance of cigarette smoke.

There is therefore a need to quantify the smoke opacity, its momentum and to suggest ways to improve the operation of the spray. This will be achieved with a mix of experimental and computational research work, and a key objective here is to quantify the relative quality of the spray start and spray end, since poor operation in these regimes will lead to clogging and eventual failure of the device. A mechanical rig simulating a human smoking has been designed to trigger the breath activated Oxette® in section 3.2, Chapter 3. It allows optical systems to measure the actuation spray characters, where two main corresponding spray analysis techniques--dual laser method and high speed imaging are implemented.

### **1.3 Thesis outline**

This thesis contains a total of seven chapters:

Chapter 2 reviews the literature regarding the basic atomization methodologies, with special concerns on how the chamber dimensions and nozzle diameters affect the performance of the flashing atomization and pharmaceutical atomization. The basic reference data from the literature on the human lung volume and smoking inhalation profiles helps the design of a mechanical lung rig to mimic human smoking behavior. Further information on how particle sizes influence the deposition in different human respiratory sections is also reviewed in section 2.3 in order to assemble a lung mass fraction deposition rig.

Chapter 3 describes the design specification, basic calculations, usage and control of the mechanical lung rig (section 3.2) and lung mass fraction deposition rig (section 3.4). The former rig is to imitate different human smoking inhalations (deep or shallow) and triggers the ‘cigarette’ devices (Oxette®) along with optical measurements of the inhaled aerosols. The later rig is to test the inhalable mass fraction of formulations depositing in various lung sections. Furthermore, a simple and cheap dual laser method is introduced in section 3.3 to analyze the spray characters such as the flow velocity and the plume opacity.

Chapter 4 presents a methodology that enables efficient acquisition of sufficient droplet information (e.g. diameter and aspect ratio) from images of in and out of focus droplets. This newly developed multi-threshold algorithm is successfully implemented in

the automatic particle/droplet image analysis (PDIA) system and has been tested by three set of glass spheres with diameter of  $1\mu\text{m}\sim 50\mu\text{m}$ ,  $70\mu\text{m}\sim 110\mu\text{m}$  and  $100\mu\text{m}\sim 200\mu\text{m}$ .

Chapter 5 describes the multi-component two-phase actuation flow characteristics within a pressurized-metered dose inhaler (pMDI) domain and develops a numerical model to simulate the flow. This model is capable of simulating the actuation flow with different nicotine formulations and various pMDI geometries to provide outlet velocity, temperature, actuation duration and prediction of droplet sizes. The numerical predictions of the performance of Oxette® devices are compared with the results of the dual laser measurements and previous researchers.

Chapter 6 predicts the residual mass median diameter (MMD) of the spray issuing from Oxette® by using evaporation model of multi-component liquid droplets with the help of the numerical actuation flow model developed in Chapter 5 to quantify the sprays. Two different formulations with 95% and 98% mass fraction of HFA 134a, and two prototype cigarette alternatives with different expansion chamber volumes, have been analyzed by the numerical model and compared with the dual laser measurements. Furthermore this chapter considers the spray character issued from the above devices with the above formulations by the high speed imaging measurement, with the special interest in the flashing phenomena and droplet sizes. Compared with the different designs and formulations, the change in performance explored in the research presented will facilitate development of a cigarette alternative.

Chapter 7 summarizes the work completed and concludes the thesis. The scope for future work is discussed, and some recommendations based on the work are proposed.

## Chapter 2

### Literature Review

---

The previous chapter illustrates the background and motivation of this Ph.D. project. The overall aim is to design and test a cigarette replacement device (Oxette®). This chapter reviews the literature about the conventional atomization methods, the effects of expansion chamber geometry on the atomization and the influence of different particle sizes on the deposition of aerosol along different regions of the human lung. A combination of effervescent and pressure-swirl atomizer is recommended, which can produce a fine aerosol with relatively slow outlet velocity. However it is abandoned due to the restrictions of design requirements. Alternatively, a flashing/boiling atomization technique with a propellant of HFA 134a is recommended and is mainly studied in this Ph.D. project. It is suggested that the orifice diameter ratio of the expansion chamber can be set between 0.65 and 0.8 to produce better sprays. In order to deliver the nicotine formulations efficiently to the deep lung sections, the diameters of the fine droplets should be kept around 2~5 $\mu$ m. Otherwise, they will be exhaled or deposit in the upper respiratory sections due to the impaction.

---

## 2.1 Introduction

With the aim to make the cigarette replacement devices (Oxettes®) give much of what smokers expect from a tobacco, three major points must be reviewed. First, it is required to find an atomization methodology to produce fine aerosols from nicotine formulations, which makes the plume look like a tobacco smoke. Second, an investigation of how the geometry of the expansion chamber affects the atomization is carried out to optimize the performance of the Oxettes®. Last, the effect of particle sizes on the deposition of nicotine formulations in different regions of human respiratory tract is reviewed, to find optimal particle sizes which allow an efficient consumption of the formulations.

## 2.2 Technical Review on Atomization Methodology

### 2.2.1 Introduction

In order to find suitable atomization methodology for Oxette®, the performances of different atomizers from the literatures are required to be reviewed. With the aim to make the aerosol generated from the Oxette® look like a traditional tobacco smoke, the mean diameter of the droplets is suggested to be around 2~5µm. At this stage, existing atomization methods will be tested to find whether they can meet the design requirements of Oxette®. Here are the initial conditions and assumptions for the tests:

- (1) The ambient condition is under normal temperature (20°C) and pressure (1atm/101325Pa) (NTP).
- (2) As discussed in section 1.1 (Chapter 1), for a handy and disposable device, the injection pressure is recommended not to exceed 1MPa. The injection pressure of Oxette® is generated from the mixture of oxygen and HFA 134a vapour, if the oxygen is a requirement for a puff. If only pure HFA 134a is used as a propellant, the injection pressure is the saturated vapour pressure of HFA 134a at ambient temperature.
- (3) Kind Consumer Ltd. provides that the actuation nozzle size of Oxette® is 0.2mm.
- (4) As the cigarette device is breath-actuated, and in order to reduce the amount of formulation impacting on the tongue and palate, the maximum spray cone angle is suggested to be 20° which is the same as that of an aerosol issued from a pMDI (Dunbar, 1996). It should be noted that the spray cone angle in this chapter is defined as the angle formed by two straight lines drawn from the discharge orifice to cut the spray contours.

(5) The test liquid is pure HFA 134a which is the main component of the nicotine formulation (see Appendix IV), and the test gas is air. Their thermoproperties can be found in Appendix II.

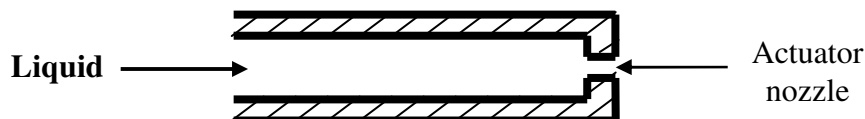
(6) It is assumed that only primary droplet breakup due to aerodynamic loading (Finlay, 2001) is taken into account. Post-nozzle droplet evaporation or other phase-changing effect is not considered.

(7) From the private communication with Hearn (2010), the chamber of the Oxette® holds roughly 0.6ml each fill. A smoker normally inhales 1L~3L air during the smoking (Tobin et al., 1982). Assuming 20%~80% of the formulation would be inhaled, an average air/liquid mass flow ratio (ALR) during the inhalation is 2~8.

### 2.2.2 Basic types of Atomizers and their performances

The atomization quality is described by several representative droplet diameters of the spray, as detailed in Appendix III.5. No single parameter can completely define a drop size distribution (Lefevre, 1989). However, as recommended by Mugele et al. (1951), we use Sauter Mean Diameter (SMD) in this section for comparisons of different atomization methodologies.

#### *Plain-orifice atomizer*



*Figure 2.1 Schematic diagram of a plain-orifice atomizer (Lefevre, 1989).*

The plain-orifice is the most common type of atomizer and the most simply made. The best known example of it is the fuel injector. In a plain-orifice atomizer (Figure 2.1), the liquid is accelerated through a nozzle, forms a liquid jet, and then forms droplets (Lefevre, 1989).

Elkoth (1982) analyzed several fuels and fuel mixtures with different viscosities, surface tensions and densities. He found the changes of the fuels affect the SMD of the spray injected from a plain-orifice atomizer. Based on his numerical and experimental investigations, he derived following relationship for the mean drop size:

$$SMD = 3.08 v_l^{0.385} (\sigma_l \rho_l)^{0.737} \rho_a^{0.06} \Delta p_l^{-0.54} \quad (2.1)$$

Where  $v_l$ ,  $\sigma_l$  and  $\rho_l$  are the kinematic viscosity, surface tension and density of the liquid,  $\rho_a$  is the ambient air density, and  $\Delta p_l$  is the injection pressure of the liquid.

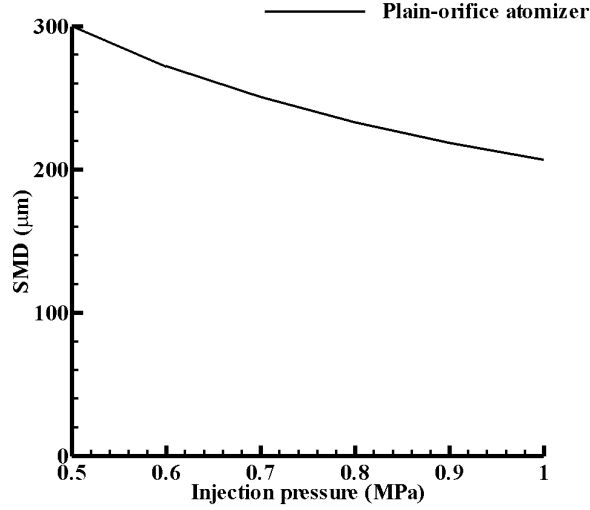


Figure 2.2 SMD variations with different injection pressures for a plain-orifice atomizer at NTP (Elkot, 1982; test liquid: HFA 134a; test gas: air, thermoproperties in AII.1 and AII.5).

Liquid phase of HFA 134a was tested under different injection pressures, and the variations of predicted SMD of the spray generated from a typical plain-orifice atomizer are shown in Figure 2.2. SMD is larger than 200μm, even when the injection pressure reaches the maximum of design specification (1MPa, as mentioned in Chapter 1). It does not meet the requirement of fine droplets with mean diameter around 5μm.

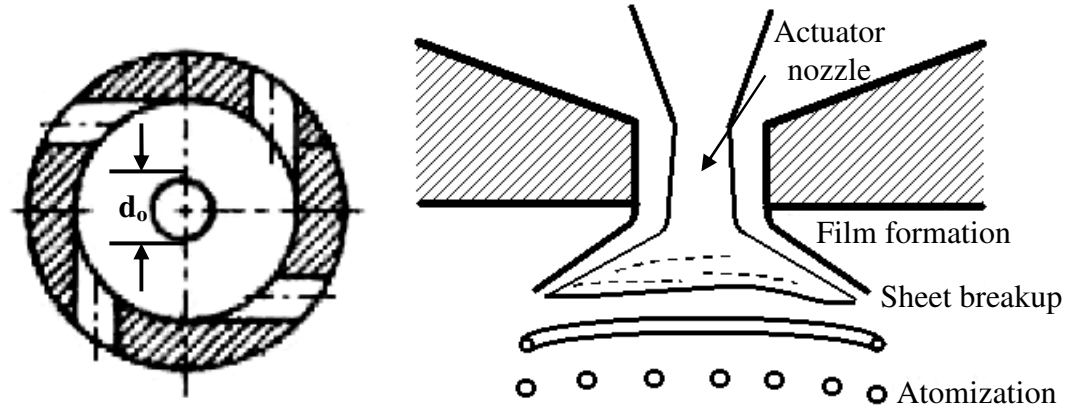
*Pressure-swirl atomizer*

Figure 2.3 Schematic diagram of a pressure-swirl atomizer (Lefevre, 1989).

In a pressure-swirl atomizer, as shown in Figure 2.3, a circular outlet orifice is preceded by a swirl chamber into which liquid flows through a number of tangential holes, slots or ports. The swirling liquid creates a core of gas that extends from the discharge orifice to the rear of the swirl chamber. The liquid emerges from the orifice as an annular sheet, which spreads radially outward to form a hollow conical spray. Hydrodynamic instabilities and shear forces lead to the break-up of the sheet and the formation of ligaments that subsequently disintegrate into droplets (Lefevre, 1989). The advantages of the pressure-swirl atomizer include simplicity of construction, reliability, good atomization, and low injection pressure requirement.

Wang et al. (1987) studied the factors governing the atomization process in pressure-swirl atomizer nozzles. The measurements of SMD are conducted on the nozzles of different sizes and spray cone angles. Various liquids with different viscosities and surface tensions were tested to generate the following equation:

$$SMD = 4.52 \left( \frac{\sigma \mu_l^2}{\rho_a \Delta p_l^2} \right)^{0.25} \left( t \cos \frac{\theta}{2} \right)^{0.25} + 0.39 \left( \frac{\sigma \rho_l}{\rho_a \Delta p_l} \right)^{0.25} \left( t \cos \frac{\theta}{2} \right)^{0.75} \quad (2.2)$$

where  $\theta$  is the spray angle, and the film thickness,  $t$ , is defined by Suyari and Lefevre (1986)

$$t = 2.7 \left( \frac{d_o \dot{m}_l \mu_l}{\rho_l \Delta p_l} \right)^{0.25} \quad (2.3)$$



where  $d_o$  is the diameter of the actuator nozzle and  $\dot{m}_l$  is the mass flow rate of the liquid.

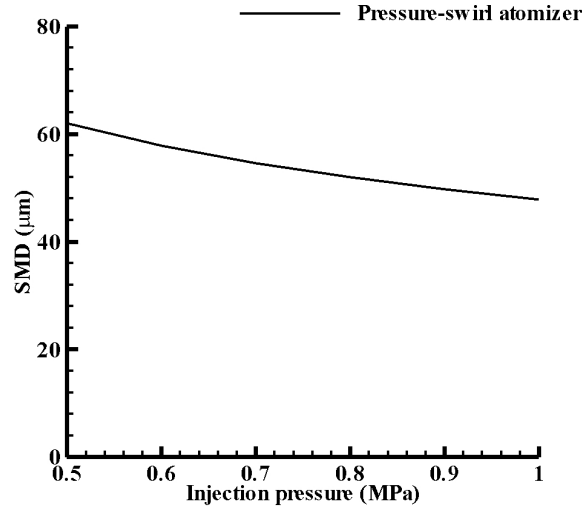


Figure 2.4 SMD variations with different injection pressures for a pressure-swirl atomizer (Wang *et al.*, 1987; test liquid: HFA 134a;; test gas: air; thermoproperties in AII.1 and AII.5; spray cone angle: 20°; nozzle diameter: 0.2mm).

Due to the changes of injection pressure, the predicted SMD of discharged HFA 134a from a pressure-swirl atomizer are shown in Figure 2.4. Compared to the plain-orifice atomizer (Figure 2.2), the pressure-swirl atomizer requires less injection pressure to produce better sprays. When the injection pressure reaches 1MPa, the SMD is around 48μm, which is only a quarter of that generated by the plain-orifice atomizer.

#### ***Plain-jet airblast atomizer***

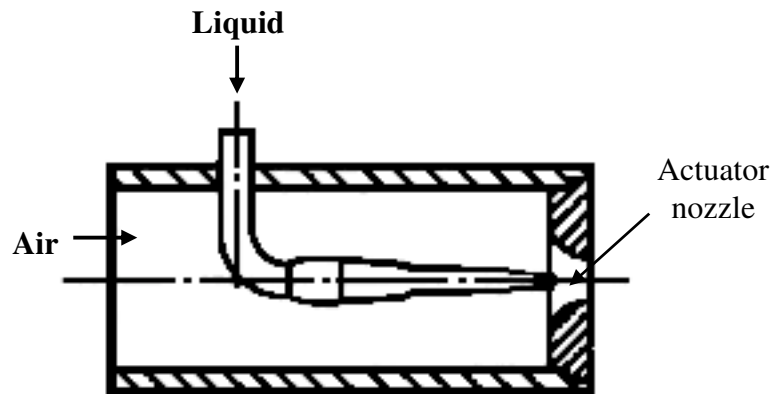


Figure 2.5 Lorenzetto-Lefebvre plain-jet airblast atomizer (Lorenzetto *et al.*, 1977).

Lorenzetto et al. (1977) analyzed a plain-jet airblast atomizer, as shown in Figure 2.5. In this type of nozzle, the liquid is exposed to a stream of air flowing at high velocity, and then liquid drops are blasted out through the nozzle.

From the analysis of the experimental data obtained on the performance of the plain-jet airblast atomizer that were tested over a wide range of liquid properties and actuation conditions, Lorenzetto et al. (1977) derived the following relationship:

$$SMD = 0.95 \frac{(\sigma_l \dot{m}_l)^{0.33}}{u_r \rho_l^{0.37} \rho_a^{0.30}} \left(1 + \frac{1}{ALR}\right)^{1.70} + 0.13 \mu_l \left(\frac{\mu_l d_o}{\sigma \rho_l}\right)^{0.5} \left(1 + \frac{1}{ALR}\right)^{1.70} \quad (2.4)$$

where ALR is the air/liquid mass flow rate ratio and  $u_r$  is the relative velocity between air and liquid.

Figure 2.6 shows SMD variations with changing the injections pressures of the air and relative velocities between HFA 134a (liquid) and air. It indicates that the increase of ALR will optimize the atomization, and high relative velocity enhances the aerodynamic effect on the flow to produce better spray. However, for a handy and disposable device, it is difficult to provide such high relative velocity.

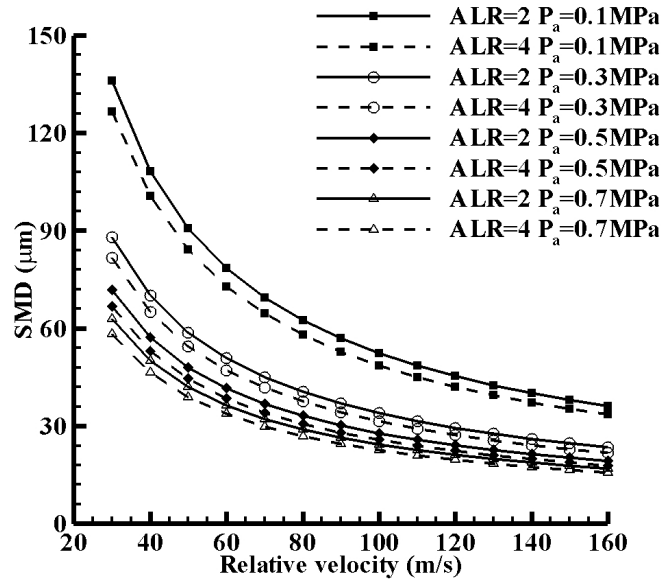


Figure 2.6 SMD variations with different injection pressures of air, air/liquid ratios and relative velocities between air and liquid for a plain-jet airblast atomizer (Lorenzetto et al., 1977; test liquid: HFA 134a; test gas: air, thermoproperties in AII.1 and AII.5; nozzle diameter: 0.2mm).

### Effervescent atomizer

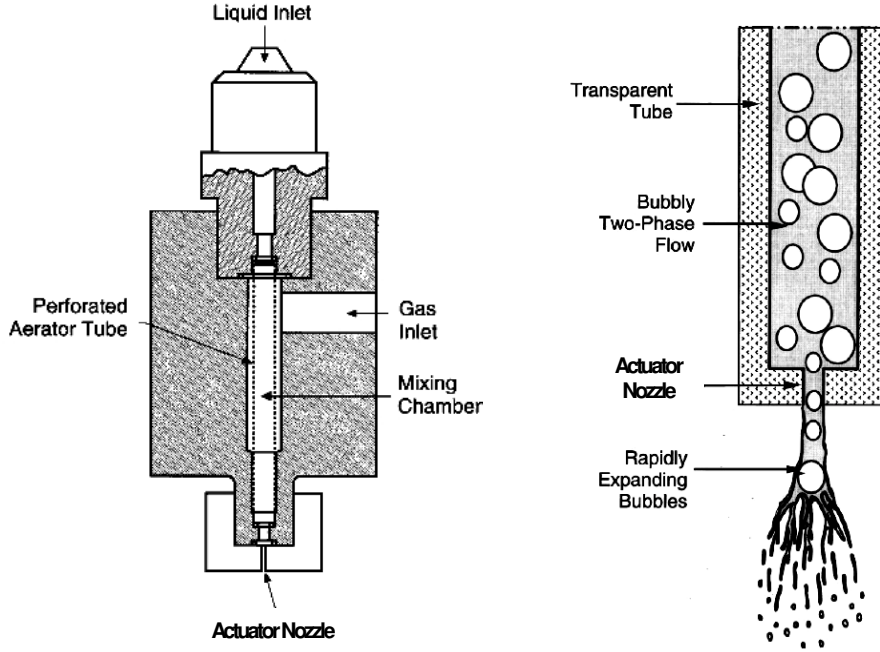


Figure 2.7 Schematic diagram of an effervescent atomizer (Sovani et al., 2001).

Effervescent atomization is essentially different from other methods of twin-fluid atomization and leads to significant improvements in performances in terms of smaller drop sizes and lower injection pressures. As shown in Figure 2.7, the atomizing gas is injected into the liquid at very low velocity to form a bubbly two-phase mixture upstream of the discharge orifice. Owing to its relatively low density, the gas occupies a significant proportion of the total cross-sectional flow area. This improves atomization by reducing the characteristic liquid dimensions within the discharge orifice. The atomization process is further enhanced by the rapid expansion of bubbles at the nozzle exit that shatters the issuing liquid stream into ligaments and drops (Sovani et al., 2001).

Equation 2.5 for SMD is obtained from the study of Buckner et al. (1993), which is based on their tests of different liquids, air/liquid mass flow rate ratios and injection pressures.

$$SMD = \frac{12\sigma_l}{\rho_l[u_l^2 + \varepsilon \cdot ALR \cdot u_a^2 - (u_l + \varepsilon \cdot ALR \cdot u_a)^2 / (1 + \varepsilon \cdot ALR)]} \quad (2.5)$$

where  $u_l^2$  is proportional to the injection pressure, and  $\varepsilon$  is a model coefficient which is 25% (Buckner et al., 1993).

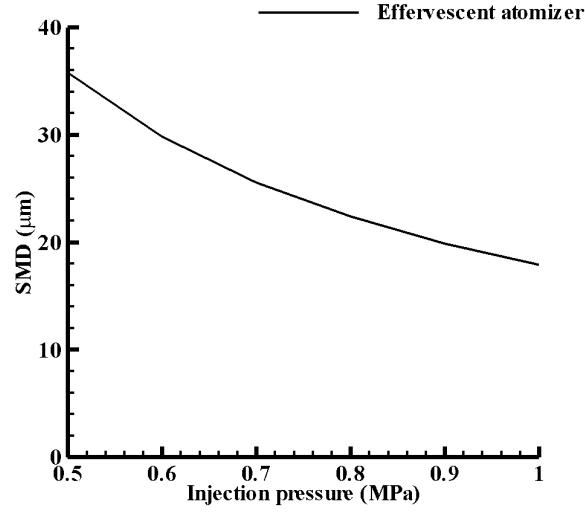


Figure 2.8 SMD variations with different injection pressures for an effervescent atomizer (Buckner et al., 1993; test liquid: HFA 134a; test gas: air, thermoproperties in AII.1 and AII.5; ALR=5; model coefficient  $\varepsilon$ : 0.25).

Assuming ALR=5 (averaged value based on the conditions in section 2.2.1), when the injection pressure reaches 1MPa, as shown in Figure 2.8, SMD of the spray generated from a typical effervescent atomizer is around 18 $\mu$ m, which provides a finer spray than the previous ones.

### 2.2.3 Atomizer with internal impingement

Wang et al. (2005) introduced a newly designed atomizer with an internal impinging mechanism, which provides a good spray performance at low injection pressure. A schematic sketch of the atomizer is shown in Figure 2.9, where  $d_i=1.3\text{mm}$ ,  $d_a=6.35\text{mm}$ ,  $d_o=0.3\text{mm}$  and  $\alpha=57.5^\circ$  (Wang et al., 2005).

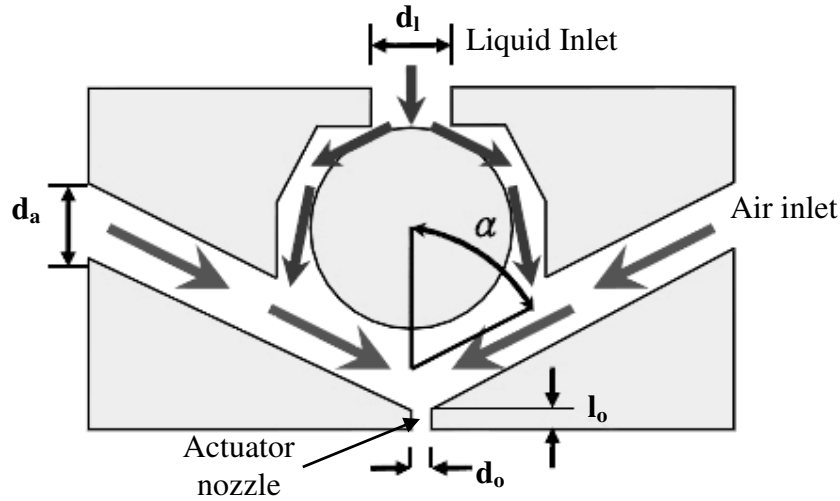


Figure 2.9 Schematic diagram of an internal impinging atomizer (Wang et al., 2005).

Wang et al. (2005) tested the atomizer with melt metal and air under different injection pressures, and the SMD variations of the sprays are shown in Figure 2.10. When the liquid injection pressure is 2.5bar, the SMD reaches  $4\mu\text{m}$  with the air injection pressure of 3.5bar. Compared to the previous atomization methodology, the impinging atomizer provides a much finer atomization at relatively lower injection pressure. However, in order to produce the fine spray with SMD smaller than  $10\mu\text{m}$ , it requires the air injection pressure to be higher than 3bar (Figure 2.10). It is a challenge in mechanical design to store and keep the pressurized air above a certain pressure level in a handy and disposable device.

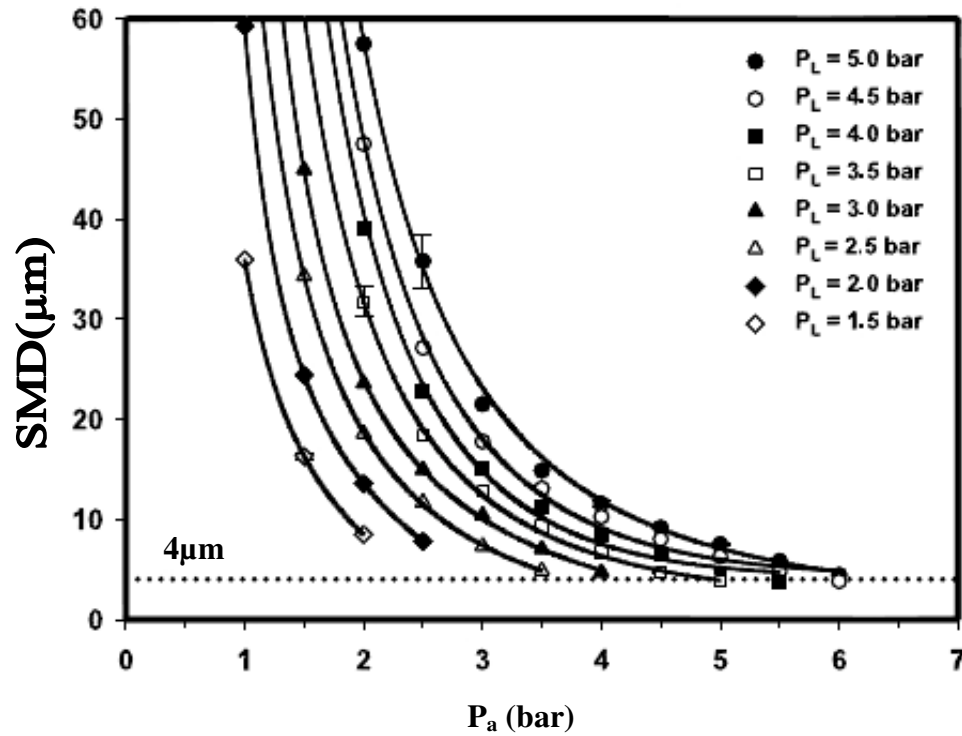


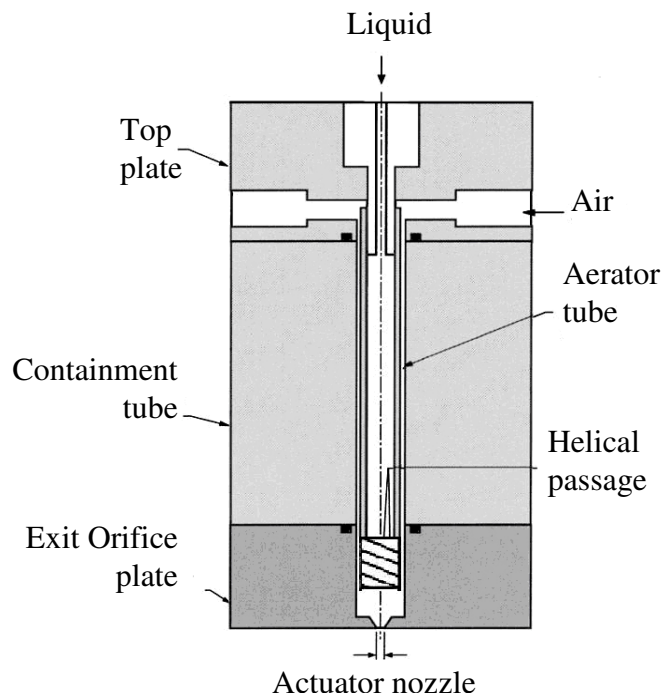
Figure 2.10 Dependence of SMD on atomization pressure (Wang et al., 2005; test liquid: melt metal;  $P_a$ : air inlet pressure;  $P_L$ : liquid inlet pressure).

#### 2.2.4 Discussion and Recommendation.

Four conventional atomizers, including plain-orifice, pressure-swirl, plan-jet airblast and effervescent atomizers have been reviewed. It did not identify an obvious single atomizer design that would satisfy the design constraints of the cigarette replacement device (Oxette®). Although the newly developed impinging atomizer by Wang et al. (2005) can produce fine sprays at low injection pressure, it is difficult to keep a pressurized air above a certain pressure for each inhalation without refill for a handy and disposable device.

From the cigarette geometry point of view and based on the reviewed literature, a combination of effervescent and pressure-swirl atomizer is recommended as shown in Figure 2.11. A small amount of air with low velocity is injected into the liquid stream and forms bubbles in the aerator tube. The bubbly two-phase mixture flows downward and is ejected through a helical passage that can reduce the discharging velocity to generate a spray.

From the formulation component point of view, a flashing propellant can be used as an alternative to the relatively complex mechanical design, and it will be discussed in next section.



*Figure 2.11 Combination of effervescent and pressure-swirl atomizer (recommended design for Oxette®).*

## 2.3 Review on flashing/boiling atomization

### 2.3.1 Introduction

The flashing atomization method has been studied for many years for improving the atomization of liquid jets. When a pressurized bubbly mixture is driven out through an orifice, the mixture pressure abruptly drops and the bubbles undergo a rapid expansion process, which under some circumstances results in a rapid disintegration of the liquid bulk into small droplets (atomization). In practical systems the liquid to be dispersed does not normally contain bubbles, and therefore nucleation is needed to ensure spray formation. An intense nucleation is usually achieved when the bulk liquid or a specific component of the mixture becomes superheated when the mixture pressure drops (flash boiling).

A typical atomizer of this type consists of two orifices, separated by an expansion chamber (see Figure 2.12). Nuclei formation occurs at the first orifice, the bubbles then grow inside the expansion chamber and the bubbly flow discharges (while the bubbles rapidly expand) to the atmosphere through the second orifice. The liquid that is introduced to the atomizer may be composed of a single component, gas dissolved liquid (effervescent), or multi-component mixture.

As compared to spray formation by mechanical means, spray formation by flash boiling is characterized by smaller mean diameter, higher homogeneity, wider cone angle and shorter penetration depth for the same operating pressure. Spray formation by flash boiling provides the opportunity to generate the desired spray at low injection pressures (Sher et al., 2008).

Some researchers employed the phase transition of superheated liquids to produce flashing atomization (e.g. Suzuki et al., 1978, Oza et al., 1983 and Park et al., 1994 cited in Zhang et al., 2005, p.2050) and others used the fuel containing dissolved gas to produce the flashing phenomenon for improving atomization. In the latter case, upon injection, the gas dissolved will come out of the blended fuel and form bubbles within the liquid fuel due to the rapid reduction of pressure. When growing and reaching a condition where the viscosity and surface tension can be overcome by the expansion force of the separated gas, the bubbles explode and form flashing atomization at the exit of the nozzle, resulting in an improvement in atomization. Solomon et al. (1985) studied the effect of air dissolved in fuel on spray characteristics. They suggested that, for liquid fuel with a low concentration of air, an expansion chamber was necessary in the injector passage in order to improve atomization. Huang et al. (1994) and Senda et al. (1999) investigated the phase transition of liquefied CO<sub>2</sub> dissolved in diesel fuel to initiate flash boiling and improve atomization of diesel fuel (cited in Zhang et al., 2005, p.2050). They concluded that, to improve liquid atomization, the concentration of dissolved CO<sub>2</sub> in liquid fuel should be above a certain value.

### **2.3.2 Effect of expansion chamber geometry.**

As early as 1902, Gebaure (as cited by Sanders, 1970) concluded that a spray is achieved only when the inlet orifice diameter is smaller than that of the discharge orifice. When the ratio of inlet orifice diameter and the discharge orifice diameter was larger than



unity, a jet is obtained. Rotheim and Fulton (1933, 1950 as cited in Bar-Kohany, 2004) found that the finest spray is obtained when the diameter of the inlet orifice is 0.38mm and the diameter of the discharge orifice is 0.53mm (ratio of 0.72). Katz-Zeigerson and Sher (1998) found that depending on the atomization conditions (for injection conditions in the range of 200~600kPa and 25~60°C), the optimal ratio is between 0.6 and 0.75. Figure 2.12 ( $d_i$ : inlet diameter;  $d_e$ : exit diameter) shows schematically the effect of the orifice diameter ratio on the flow pattern. With large orifice diameter ratios ( $d_i/d_e > 2$ ), no bubbles were observed. For ratios between 1.1 and 1.8, a stratified oscillating flow occurs, along with bubble coalescence. However, with orifice diameter ratios between 0.65 and 0.8, a homogeneous bubbly pattern disperses throughout the whole chamber volume (Sher et al., 2008).

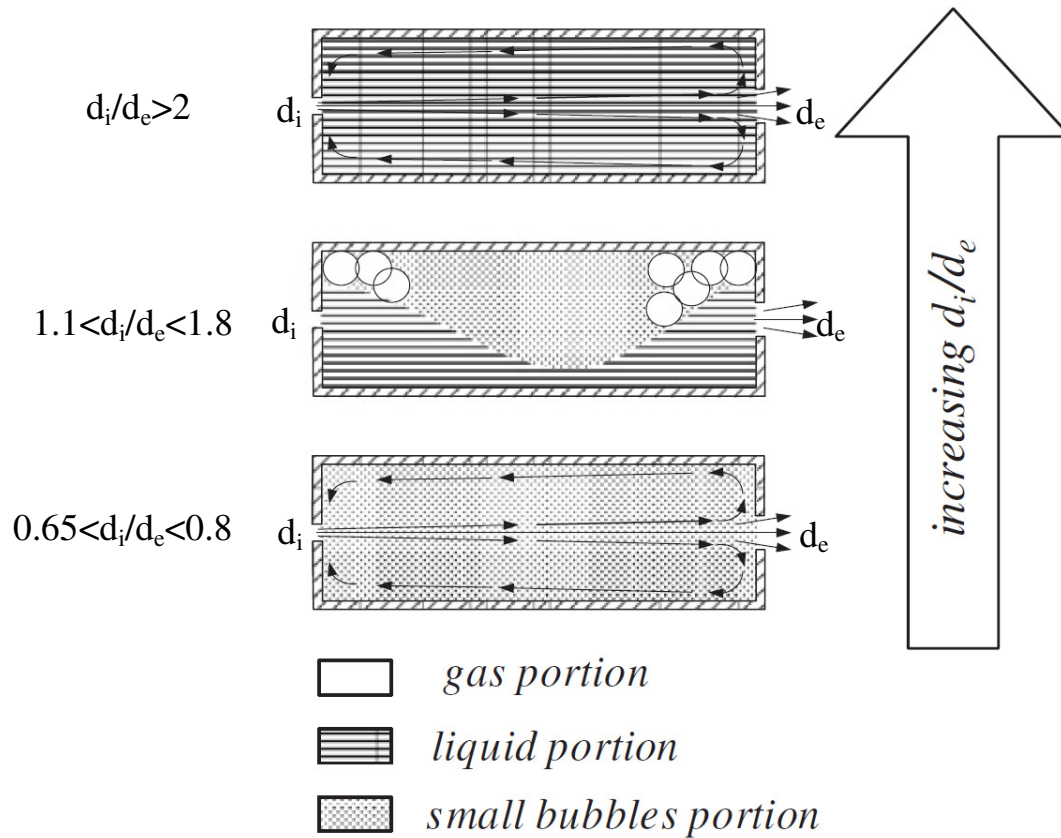


Figure 2.12 The effect of the orifice diameter ratio on the flow pattern in the expansion chamber (Sher et al., 2008).

From the research of Rashkovan et al. (2006), Figure 2.13 shows in qualitative terms the real flashing/boiling flow patterns in the expansion chamber. A liquid jet enters the expansion chamber through the left-hand orifice, and leaves the chamber through the

right-hand orifice. In this case, the orifice diameters ratio is 0.68, and the chamber diameter ( $D_{CH}$ ) is 10 mm. When a chamber length of 5mm is used (Figure 2.13), the liquid flows straight through the chamber and through the discharge orifice without impinging on the opposite chamber wall. It seems that for a longer chamber (10, 30 and 50 mm), a notable backflow occurs along the walls of the chamber, which indicates a toroidal vortex flow inside the chamber. The backflow along the chamber walls diminishes for long chambers and/or high orifice diameter ratios. At the center of the 10-mm-long chamber, non-homogeneous regions were observed. The large gas bubbles (Figure 2.13) develop in the vortex core and, after reaching an appreciable size, expel outward toward the chamber wall. This expelling process leads to periodic short non-uniformities in the spray. A further increase of the length of the chamber to 30mm (Figure 2.13) causes toroidal vortex stretching and decreases rotation speed and, consequently, the non-uniformities in the flow pattern disappear. A homogeneous bubbly pattern prevails throughout the whole volume of the chamber. For a chamber of 50mm (Figure 2.13) a similar flow pattern to that shown for the 30mm long chamber occurs. In this case however, a longer residence time for the bubbles is available; consequently, the bubbles are larger, the larger bubbles experience larger buoyancy and flow stratification develops: a bubbly pattern in the upper part of the chamber and a liquid pattern in the lower part.

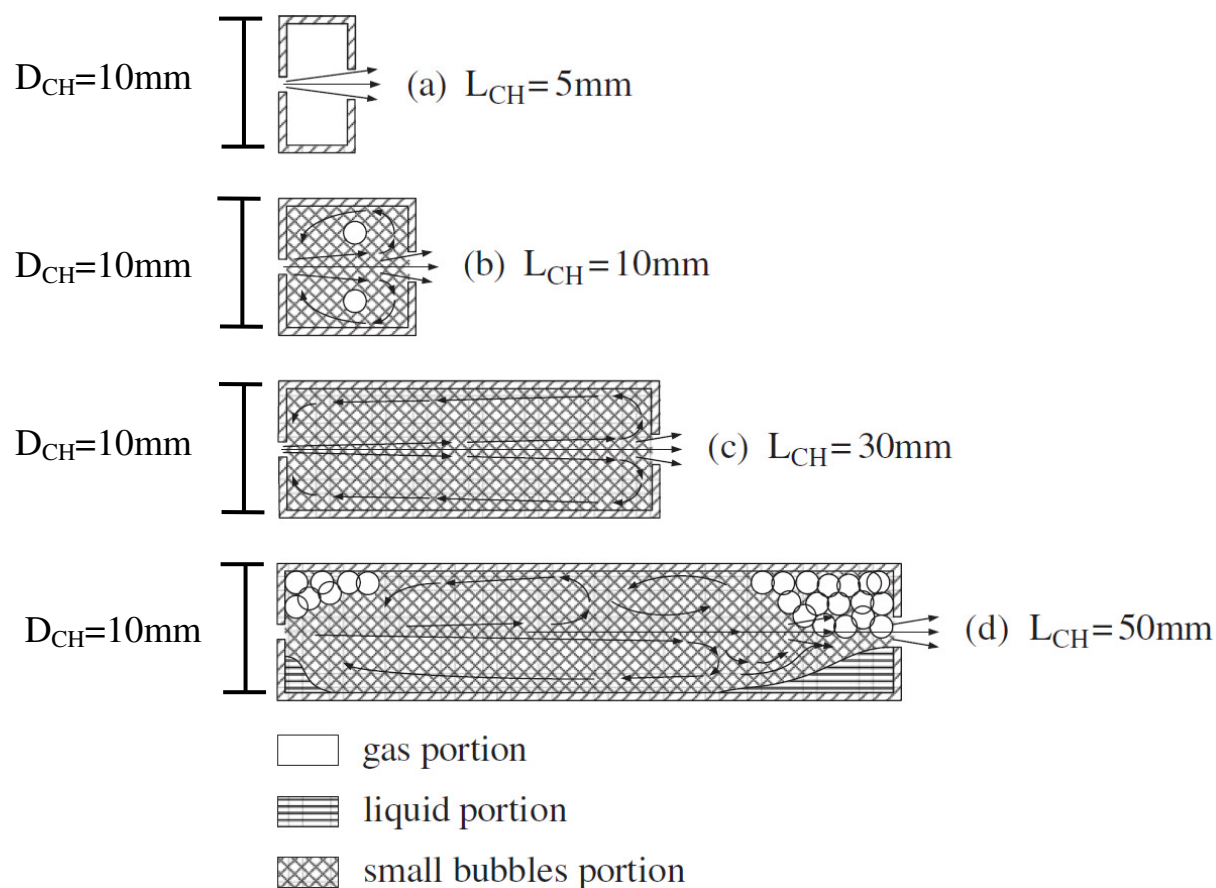


Figure 2.13 Flow schematics for flashing/boiling flow in the expansion chamber  
(Rashkovan et al., 2006).

### 2.3.3 Review on pressurized metered dose inhaler (pMDI)

A pressurized-metered dose inhaler (pMDI) is a widely used pharmaceutical device, and it is designed to deliver aerosolized medication deep into the lung (Finlay, 2001). Devices of this type have existed since the 1950s and have changed little in their conceptual design since that time. To obtain a single dose, a consumer first actuates the device by squeezing the canister into the canister casing, while simultaneously inhaling via the casing mouthpiece (Figure 2.14).

The basic design of pMDIs relies on aerosol propellant technology, in which a high vapour-pressure substance contained under pressure in a canister is released, sending liquid propellant at relatively high speed from the canister. Drug is mixed homogeneously in the propellant in the canister. By metering the release of a given volume of propellant, a metered dose of drug is delivered in the propellant volume. Breakup of the propellant

into liquid droplets that vaporize rapidly leaving the residual nonvolatile drug in the form of aerosol particles that are of suitable size for inhalation into the lung.

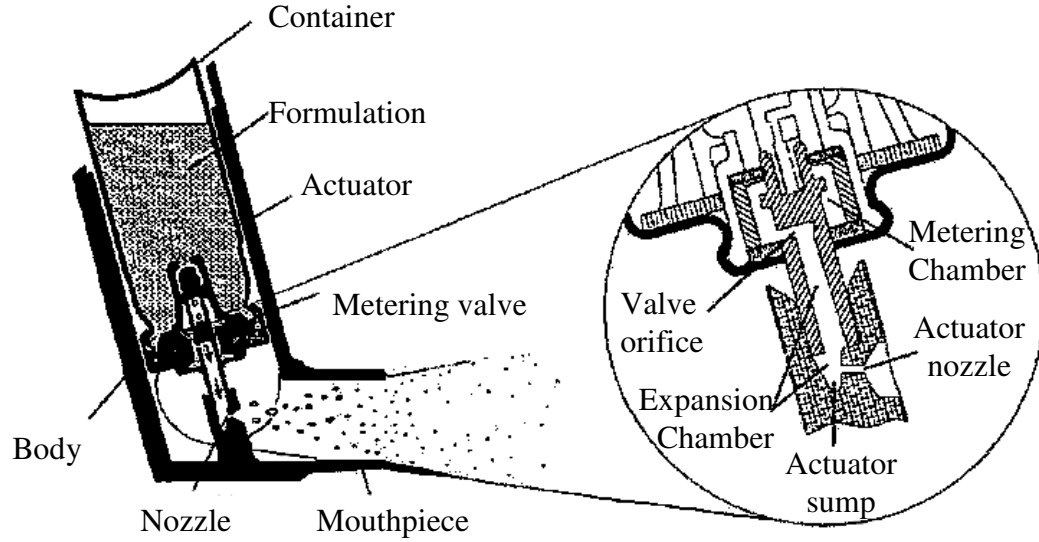


Figure 2.14 pressurized Metered-Dose inhaler geometry (Finlay, 2001).

A typical pMDI geometry is shown in Figure 2.14. Volatile HFA 134a is usually used as the propellant of the formulations in a pharmaceutical pMDI (Cripps et al., 2000). From the experiment by Clark (1991), the mass median diameter (MMD) of the spray generated from a typical pMDI can be calculated from the quality of the fluid (gas/total fluid mass ratio) ( $q_{ec}$ ) and pressure ( $p_{ec}$ ) in the expansion chamber by equation 2.6. As shown in Figure 2.15, fine spray with the MMD of  $5\mu\text{m}$ – $10\mu\text{m}$  can be obtained at  $p_{ec}=6\text{bar}$  and  $q_{ec}=0.4$ .

$$MMD = \frac{8.02}{q_{ec}^{0.56} \left( \frac{p_{ec} - p_{atm}}{p_{atm}} \right)^{0.46}} \quad (2.6)$$

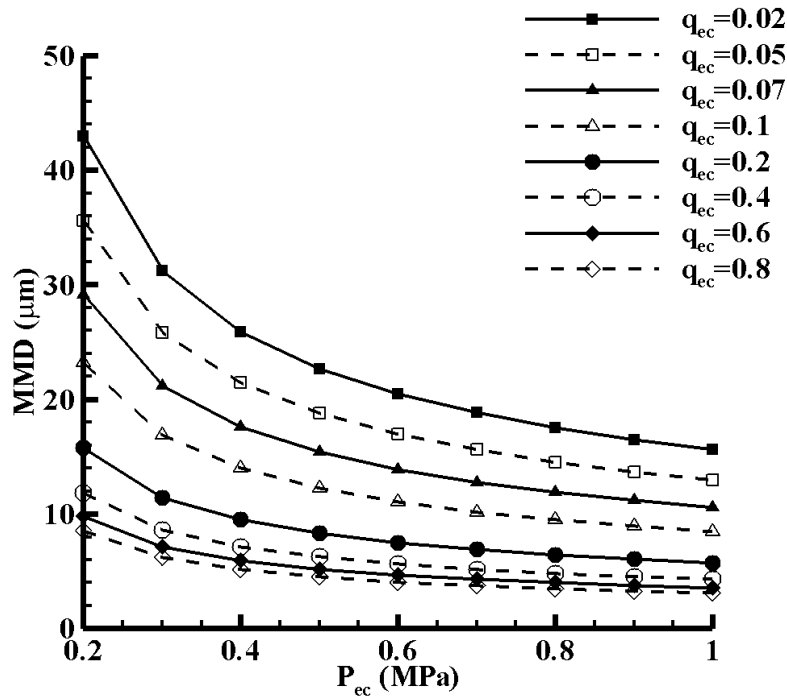


Figure 2.15 MMD varies with pressure & quality of fluid (Clark, 1991).

The internal flow regime inside expansion chamber was visualized by Versteeg (2006) as shown in Figure 2.16. The flashing propellant HFA 134a evaporates rapidly in the expansion chamber, which forms a flashing/boiling bubbly flow inside. Visualizations of the internal flows in the expansion chamber of the Oxette® will be presented in Chapter 6.

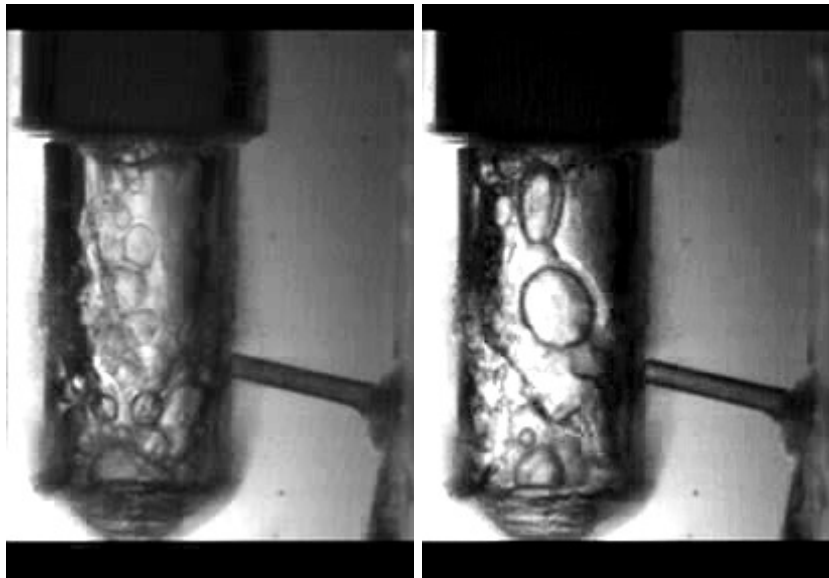


Figure 2.16 Visualizations of internal flow regime inside the expansion chamber of a typical pMDI (Versteeg et al., 2006).

## 2.4 Review on lung function and relevant particle deposition

### 2.4.1 Introduction

In order to test the mechanical operation and measure the performance characteristics of different breath actuated drug-delivery devices, two test rigs have been designed. One is to simulate the effect of human inhalation and the other is designed to acquire the information on the deposition of pressurized aerosols in the human respiratory tract. The information about the lung function, particle deposition fraction in different lung sections and smoking profiles will be obtained from previous work.

### 2.4.2 Human lung volume and smoking profiles

Lung volumes and lung capacities for a typical human being with different phases of the respiratory cycle are shown in Figure 2.17, which refer to the volume of air associated. Lung volumes are directly measured and lung capacities are inferred from lung volumes. The average total lung capacity of a 70kg, average-sized adult male is about 6 liters (Palsson et al., 2003), but only a small amount of this capacity is used during normal breathing. The breathing mechanism in humans is called "tidal breathing". Tidal breathing represents the volume of air that is inhaled and exhaled in normal and resting breathing.

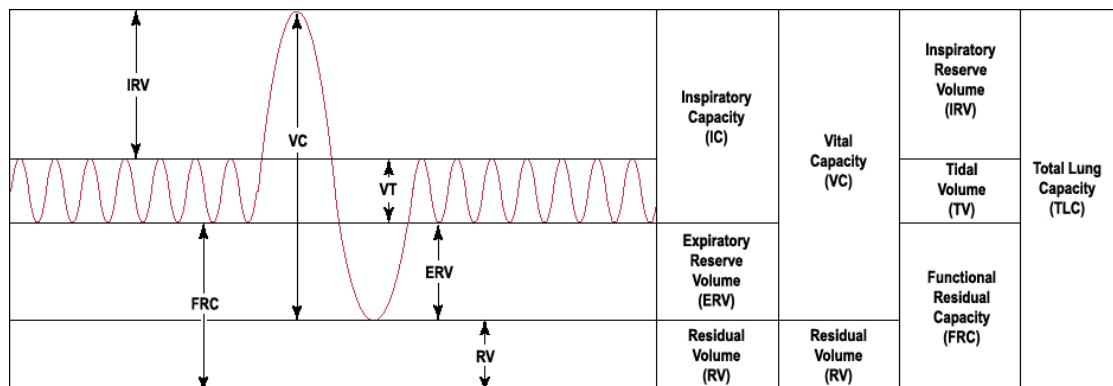


Figure 2.17 Different parameters in lung volume (Palsson et al., 2003).

The values presented below are based on the research of Palsson et al. (2003) for a 70 kg, average-sized adult male:

- Tidal volume (VT) is the amount of air breathed in or out during normal respiration.

$$VT = 0.5L \quad (2.7)$$

- Residual volume (RV) is the amount of air left in the lungs after a maximal exhalation.

$$RV = 1.2L \quad (2.8)$$

- Expiratory reserve volume (ERV) is the amount of additional air that can be pushed out after the end expiratory level of normal breathing.

$$ERV = 1.2L \quad (2.9)$$

- Vital capacity (VC) is the maximum volume of air that can be voluntarily moved in and out of the respiratory system.

$$VC = IRV + VT + ERV = 4.6 L \quad (2.10)$$

- Total lung capacity (TLC) is the volume of air contained in the lung at the end of maximal inspiration.

$$TLC = IRV + VT + ERV + RV = 6.0 L \quad (2.11)$$

- Inspiratory reserve volume (IRV) is the additional air that can be inhaled after a normal tidal breath in.

$$IRV = VC - (VT + ERV) = 3.0 L \quad (2.12)$$

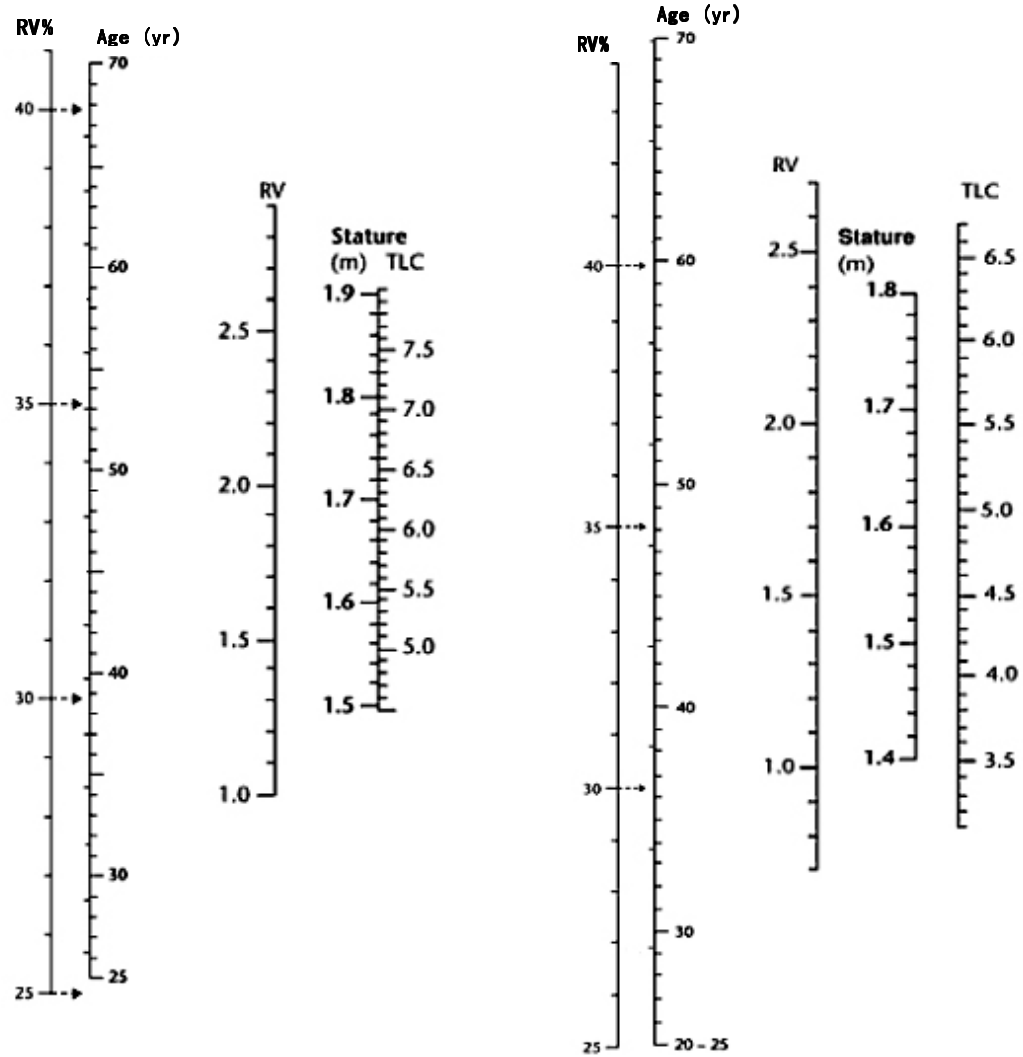
- Functional residual capacity (FRC) is the amount of air that stays in the lungs during normal breathing.

$$FRC = ERV + RV = 2.4 L \quad (2.13)$$

- Inspiratory capacity (IC) is the maximal volume that can be inspired following a normal expiration.

$$IC = TV + IRV = 3.5 L \quad (2.14)$$

Figure 2.18 shows how the lung volume parameters vary with the age and the height of healthy adult males and females of European descent (Cotes et al., 2006), where it indicates that RV% is related only to age and TLC only to stature. The above values of lung volumes are implemented in this thesis. Tobin et al. (1982) studied 19 smokers with respiratory inductive plethysmography and plotted the smoking profiles under deep and shallow inhalations which are shown in Figure 2.19. Under the deep inhalation profile, the maximum inhalation volume reaches up to 2.2L during 4 seconds, while under the shallow inhalation the minimum inhalation volume is down to 0.5L with the duration of 1.2 seconds. These two boundary conditions of smoking profiles are mainly simulated by the mechanical lung designed in section 3.2, Chapter 3.



*Adult males of European descent*

*Adult females of European descent*

Figure 2.18 Nomogram relating indices of lung function to stature and age for healthy adult males and females of European descent (Cotes et al., 2006).



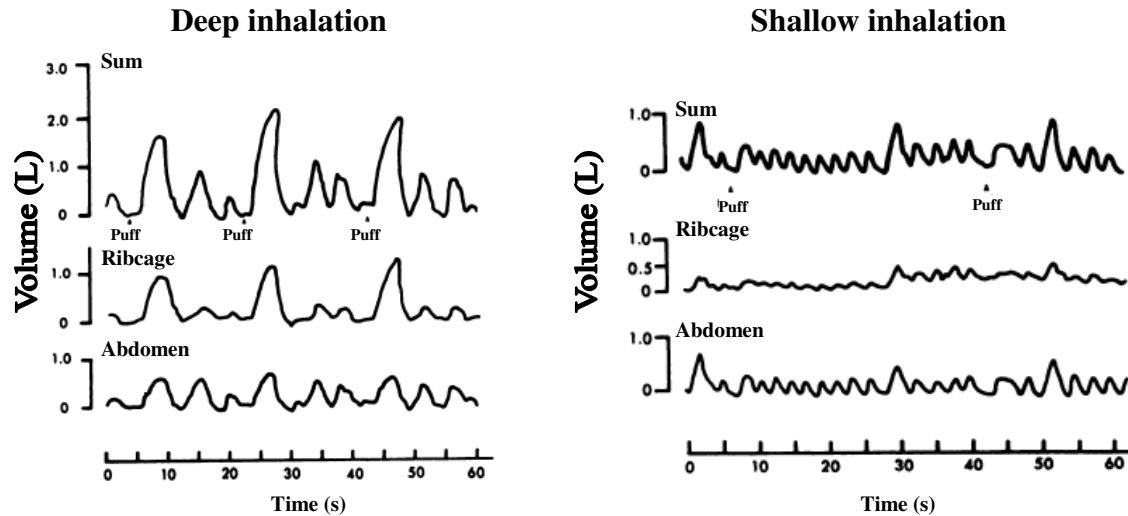


Figure 2.19 Cigarette smoke inhalation patterns in deep and low inhalation fractions (Tobin et al., 1982).

### 2.4.3 Influence of particle size upon the deposition in the human lung

Research in the regional deposition of inhaled particles forms the basis for estimating the quantity of inhaled aerosol which reached the various parts of the respiratory tract (Figure 20). It provides the reference to optimize the inhaler and is therefore one of the essential factors in the characterization of the effectiveness of different formulations. The information on the particle deposition in different human lung sections is reviewed here.

### Bronchi, Bronchial Tree, and Lungs

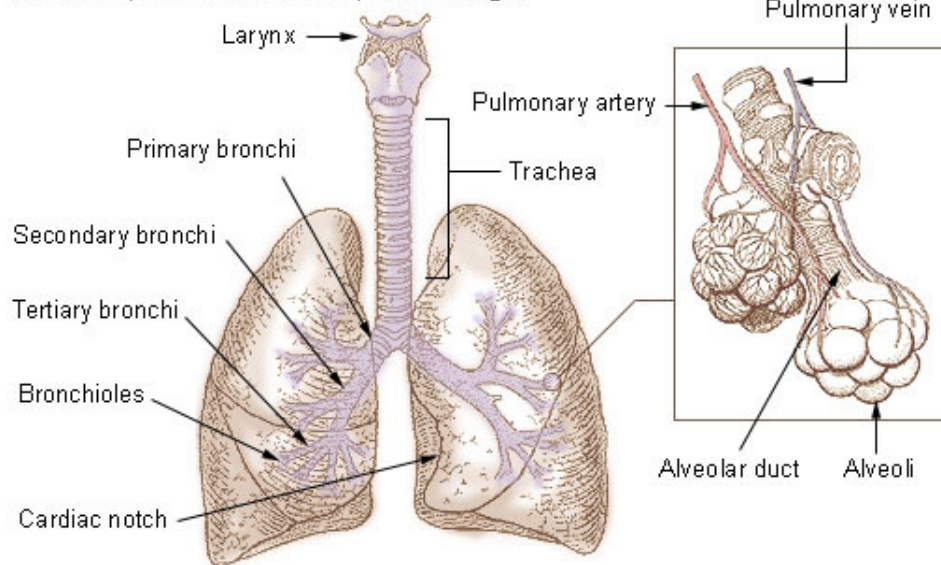


Figure 2.20 Various sections of the respiratory tract (National Cancer Institute).

In the 21<sup>st</sup> century, several researchers have studied particle deposition flow by computational fluid dynamics (CFD) and calibrated through their experimental simulations. Oldham et al. (2000) built a CFD model and a hollow silicone rubber rig to simulate the particle flow in the human tracheobronchial regions. Zhang et al. (2002) simulated an oscillatory inhalation flow as in a representative triple bifurcation airway model using a commercial finite-volume code with user-enhanced programs, which has been validated with experimental particle deposition data and deposition patterns for double bifurcations. Grgic et al. (2004) studied extrathoracic deposition by using an idealized average human mouth and throat replica through CFD and experimental work. Van Ertbruggen et al. (2008) performed CFD simulations in a 3D scaled-up model of an alveolated bend with rigid walls that incorporated essential geometrical characteristics of human alveolar structures and compared numerical predictions with experimental flow measurements made in the same model by particle image velocimetry (PIV). Jayaraju et al. (2008) simulated the flow in a human mouth–throat model under normal breathing conditions (30L/min) by RANS  $k-\omega$  (without near-wall corrections), DES and LES methods, similarly the PIV method was taken to validate the computational model. Ma et

al. (2009) has validated CFD predictions of flow field and particle trajectory with experiments within a scaled-up model of alveolate airways.

Accurate modeling of air flow and aerosol transport in the human lung is essential for quantitative predictions of pulmonary aerosol deposition. However, CFD simulations in the real lung geometries have been scarce.

Through experimental studies, several researchers have attempted to investigate the how particle sizes affect the deposition patterns in different human lung sections. Three of those are picked as the reference for our rig design (Table 2.1).

Particle size ( $\mu\text{m}$ )	Deposition (%)		Exhaled (%)
	Upper respiratory+mouth	Alveolar	
1	0	54	46
2	37	34~42	21~29
3	55	17~30	15~18
4	68	11~26	6~21
5	73	8~23	4~19
Ref: Brown et al., 1950			
6		8~30	
8		2~20	
9		15	
10		3~10	
Ref: Lippmann et al., 1969			
1	0	16	84
2	2	40	58
3	12	50	38
4	32	42	26
5	53	30	17
6	73	17	10
7	81	11	8
8	88	5	7
Ref: Newman S.P., 1985			

*Table 2.1 Particle deposition proportions in different lung section with various particle sizes.*

We are interested in the particle deposition fraction in the Alveolar part where the amount of the deposits affects the effectiveness of the nicotine formulations. Table 2.1 shows the effect of particle size on the deposition of different lung sections, which was investigated by the previous researchers. Brown et al. (1950) developed a test rig to determine the upper respiratory and alveolar deposition of the inhaled dust. Over 100 tests were operated by using the dust with median particle diameters ranging from  $1\mu\text{m}$  to  $5\mu\text{m}$ . Lippmann et al. (1969) made 93 studies on 34 volunteers, the test aerosols were

spherical monodisperse insoluble iron oxide particles containing radioactive tags and ranging in median diameter from 2.1 $\mu\text{m}$  to 12.5 $\mu\text{m}$ . They emphasized that, for each individual subject, the alveolar deposition fraction decreased with increasing the particle sizes. Similar to the work done by Lippmann et al. (1969), Newman S.P. (1985) obtained deposition patterns by using  $^{99\text{m}}\text{Tc}$ -labeled Teflon particles with diameter of 1 $\mu\text{m}$ ~8 $\mu\text{m}$  delivered from a metered dose inhaler (MDI). Different from the conclusions of Brown et al. (1950) and Lippmann et al. (1969), he found that, with increasing particle diameters, there is a peak deposition fraction in Alveolar which is up to 50% with the particle diameter of 3 $\mu\text{m}$ . However, if the particle diameter is smaller than 3 $\mu\text{m}$ , e.g. for the 1 $\mu\text{m}$  particles, most of the aerosol would be exhaled up to 84%. Therefore, an optimum particle size is around 2 $\mu\text{m}$  ~ 5 $\mu\text{m}$  for the deposition in the deep lung.

## 2.5 Chapter summary

From the literature review on the conventional atomization methodologies, an obvious single atomizer design that can satisfy the design specifications of a handy, disposable cigarette replacement device (Oxette®) was not identified. A combination of effervescent and pressure-swirl atomizer is recommended, which can produce a fine aerosol with relatively slow outlet velocity. However it is abandoned in this Ph.D. project, because it is complex and expensive to manufacture a disposable device than a pMDI which is widely used in the drug delivery industry.

Alternatively, a flashing/boiling atomization technique with a propellant of HFA 134a is recommended and is mainly studied in this project. The review on expansion chamber dimensions suggests that the orifice diameter ratio can be set between 0.65 and 0.8 (Figure 2.12), which gives a chance to generate small bubbles from the jets entering the expansion chamber. The larger the expansion chamber volume, the more residual time for the propellant evaporation, recirculation and bubble generation and growth, which produces better sprays.

In order to deliver the nicotine formulations efficiently to the deep lung sections, the fine droplet size should be kept around 2~5 $\mu\text{m}$ . Otherwise, they will be exhaled or deposit in the upper respiratory sections due to the impaction.



## **Chapter 3**

# **Experimental systems, Measurement Techniques and Instrumentation**

---

The previous chapter reviews the literature about the conventional atomization methods, the effects of expansion chamber geometry on the atomization and the influence of the particle size on the deposition of aerosol along different regions of the human lung. A flashing/boiling atomization technique with a propellant of HFA 134a is chosen to be studied in this Ph.D. project. This chapter is devoted to the description of the experimental apparatus, measurement techniques and associated instrumentation used within the project, with the aim to trigger the cigarette replacement devices (Oxettes®) under different smoking profiles and measure the characteristics of the generated aerosols.

---

## **3.1 Introduction**

With the aim to test the applicability of the breath activated cigarette replacement devices (Oxettes®), and measure the characteristics of the produced aerosols, three experimental devices are introduced here. The first section (section 3.2) describes a mechanical rig designed to simulate the human smoking behaviour to trigger the Oxettes®. The second section (section 3.3) introduces a dual laser beam method to analyze spray characteristics, such as the plume velocity and relative opacity. The third section (section 3.4) presents a simple rig designed to measure the aerosol deposition fractions in different human respiratory sections.

## **3.2 Mechanical Lung Device**

### **3.2.1 Introduction**

In order to test the mechanical operation and measure the performance characteristics of different breath actuated drug-delivery devices, not only for this Ph.D. project, a test rig to simulate the effect of human inhalation has been designed. Since there is a broad spectrum of human respiratory behaviour, due to factors such as aging, health and medical conditions such as asthma, an important requirement for the test apparatus is that it is flexible enough to accurately reproduce a range of human inhalation responses. With this requirement, the test device has been designed on the basis of reproducibility and controllability. This has been achieved by basing the rig around a computer controlled electro-mechanical setup, commonly used in high-precision automation applications. The rig design primarily consists of a mechanically driven piston-cylinder arrangement simulating diaphragm motion to model the changes in human lung volume during the inhalation. This is coupled to a transparent inspection chamber to facilitate visual inspection and optical measurements of the aerosolized product to be taken.

### **3.2.2 Design specification**

A study of the literature (section 2.4, Chapter 2) reveals that largest possible volume which may be inhaled (referred to as vital capacity, VC) is typically just over 4L in adults and this is subject to considerable variation between individuals. However, this does not necessarily reflect the typical volume inhaled during a single dose use of a pulmonary drug delivery device. For example, for cigarette testing, the International Standards

Organization (ISO) defines a single puff volume as 35mL (International Organisation for Standardization, 2005) and experimental data has shown that cigarette smokers can typically inhale between 40 and 90mL (Kolonen et al., 1992). For devices such as passive dry powder inhalers, the United States Pharmacopeia (USP) guidelines for measuring emitted dosage define an inhaled volume as 4L (cited in Chavan et al. 2002). To accommodate this wide variation and to provide some margin of flexibility, a maximum volume for inhalation of 6L for the test rig has been chosen.

Again, depending on the device and the user, there is considerable intersubject variation in the inhalation rate. Typically, adult males inhale at a flow rate of 18L/min for tidal breathing using aerosol delivery devices and this flow rate reduces for younger users (Finlay, 2001). The ISO standard for cigarette implied flow rate is much lower, since puff duration is defined to be 2s (International Organisation for Standardization, 2005) yielding a mean flow rate of around 1L/min. In reality, experimental data shows that the flow rate variation is between 0.9 and 2.1L/min (Kolonen et al., 1992). Typical passive pharmaceutical devices are tested with flow rates of 60L/min which corresponds to upper range of the peak inspiration rate from spirometry data (Carilli et al., 1974). In reality, inhalation flow rates are time dependant, and only peak at about half of the inhaled volume (Carilli et al., 1974). Although expiration flow rates are not a requirement to simulate currently (although the peak expiration flow rate is greater than that during inspiration) to accommodate future rig requirements, the peak flow rate has been specified to produce flow rates up to 100L/min.

The USP guidelines for pharmaceutical devices specifies a constant pressure drop of 4kPa (cited in Chavan et al. 2002) for the device, and experimental data on commercially available dry power inhalers finds the pressure drop to be between 1.3kPa to 1.4kPa depending on the device (Lee et al., 1996). Unlike pharmaceutical devices with generally a fixed geometry, it has been found that the pressure drop across a burning cigarette decreases from 3.3kPa to 1.3kPa as the length reduces during use (Danby, 2008). In order to facilitate this range of pressures and provide future flexibility, the rig has been specified to produce pressure drops of up to 10kPa.

In order to adequately test user devices for their mechanical reliability and performance, it is essential that the test rig should be able to produce both repeatable and



adjustable characteristics to accommodate the broad spectrum of possible user behaviour. Hence, the actuation device driving the piston has been chosen to be an electro-cylinder (Figure 3.1, lower right). It can be controlled very easily to produce a smooth rapid linear motion and can produce large axial forces. The high precision of these devices also means the reproducibility of simulated inhalation events is achievable. Typically, the linear actuator can be programmed easily by a PC interface and this flexibility will allow simulation of a range of inhalation profiles to match experimental findings.

### 3.2.3 Design calculations

The cylinder bore diameter,  $d_{bore}$  has been chosen to be 210mm to enable a small bench-top footprint and to provide a reasonable stroke length for the actuator. The displaceable volume of air,  $V_{displaced}$  in the cylinder is simply:

$$V_{displaced} = \frac{\pi \cdot d_{bore}^2}{4} L_{stroke} \quad (3.1)$$

This defines the displacement of the piston,  $L_{stroke}$  to be 170mm, where  $V_{displaced}$  is recommended previously as 6L. To accommodate limit switches and stroke stopping range, the electro-cylinder has been based on total stroke length of 350mm. Although this may appear excessive, the additional cost overhead for this larger stroke length is not significant and additional future requirements are more likely to be met.

Based on the specified pressure drop,  $p_{drop}$  the maximum force on the surface of the piston,  $F_{piston}$  can be found.

$$F_{piston} = p_{drop} \cdot \frac{\pi \cdot d_{bore}^2}{4} \quad (3.2)$$

Hence  $F_{piston}$  is 0.35kN based on a pressure drop of 10kPa. It should be recognised that the peak force generated by the electro-cylinder will need to exceed this due to the additional force required to overcome the resistance of the piston seal and to accelerate the piston itself.

Based on the peak volume flow rate,  $\dot{V}_{displaced}$  we can determine the maximum required piston displacement rate,  $\dot{x}_{piston}$ .

$$\dot{V}_{displaced} = \frac{\pi \cdot d_{bore}^2}{4} \dot{x}_{piston} \quad (3.3)$$

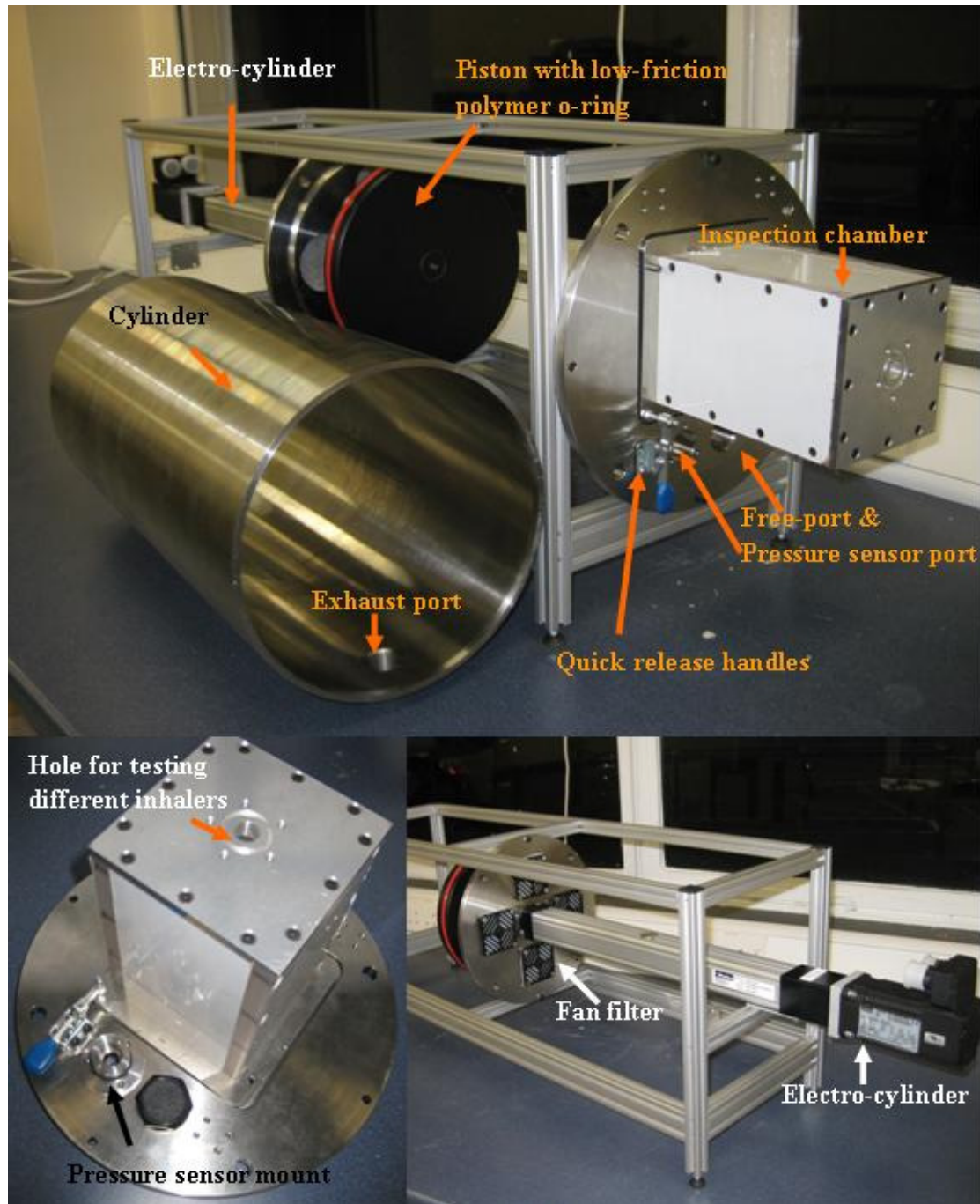
Based on a peak flow rate of 1.7L/s, this requires a maximum piston displacement rate of 50mm/s.

### 3.2.4 Design concept

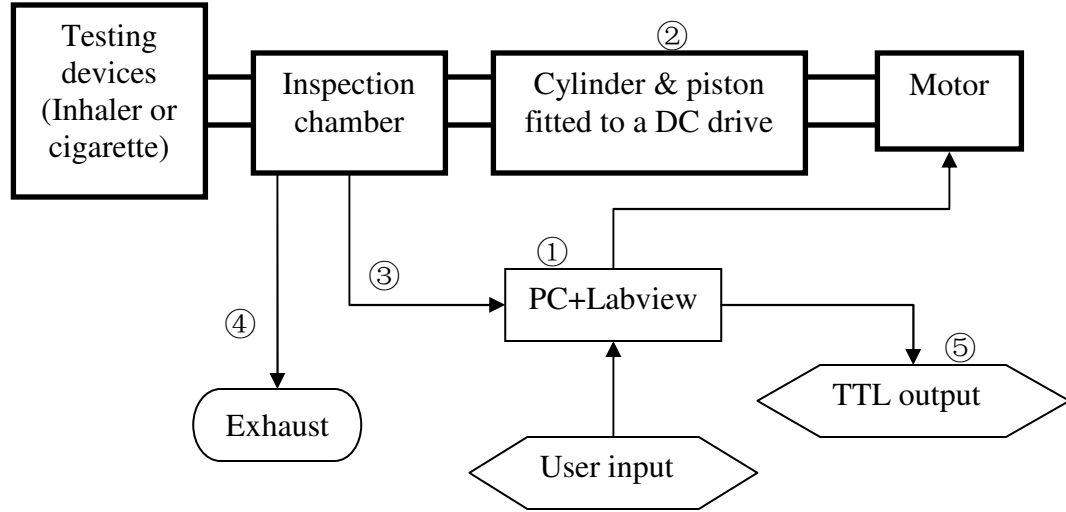
In order to enable optical measurements of the in vitro inhaled products, a transparent chamber has been designed with Laser Doppler Anemometry (LDA), Phase Doppler Anemometry (PDA) and high-speed video recording access. Because it is likely this will require occasional cleaning, a design with a quick release mechanism with relocation pins has been chosen (Figure 3.1, top).

A pressure sensor is housed in a proprietary sealed plug to allow access for recalibration (if necessary) but also replacement in case of sensor failure. The inspection chamber can be fitted with different device holders to facilitate a variety of inhalation products to be tested easily (Figure 3.1, lower left).

To accommodate the possibility of increased humidity effects and condensation, the exhaust outlet has been positioned on the lower cylinder half, where vapour can escape without possible damage to the cylinder surface. (Figure 3.1, top)



*Figure 3.1 Mechanical Lung rig assembly: Top: Inspection chamber, quick release handles, pressure sensor port & free-port, exhaust port (with non-return valve), piston with low-friction polymer o-ring and Cylinder; Lower left: Inspection chamber, pressure sensor mount and testing devices location; lower right: Electro-cylinder and fan filter.*



*Figure 3.2 A sketch of mechanical lung rig control system.*

In order to control the mechanical rig to simulate from single to hundreds of inhalations, a control system is required and a sketch is shown in Figure 3.2. A PC ① running LabView and supporting LabView interfaced hardware drives the rig. User inputs to the PC include the number of inhalations and different inhalation profiles defining the velocity of the piston ②. A pressure transducer ③ records the pressure-time profile inside the mechanical lung caused by the piston motion. In this way inhalation rate as a function of time, inhalation time and the total volume of air inhaled can be precisely controlled. During an inhalation, the exhaust valve ④ remains closed. For multiple inhalations it is opened while the piston is returning to its initial position. Ranges of transistor-transistor logic (TTL) outputs ⑤ are implemented to trigger various measurement systems at various time delays after the start of inhalation.

### 3.2.5 Rig assembly and Labview control system



*Figure 3.3 Mechanical Lung rig Rig assembly and connection to PC.*

The motion of the piston is controlled by the servo drive (Figure 3.3), which is connected to a PC via a serial port. The controlling software is LabView 8.2 and the screenshot of its control panel is shown in Figure 3.4, where the user can choose several inhalation profiles of different people.

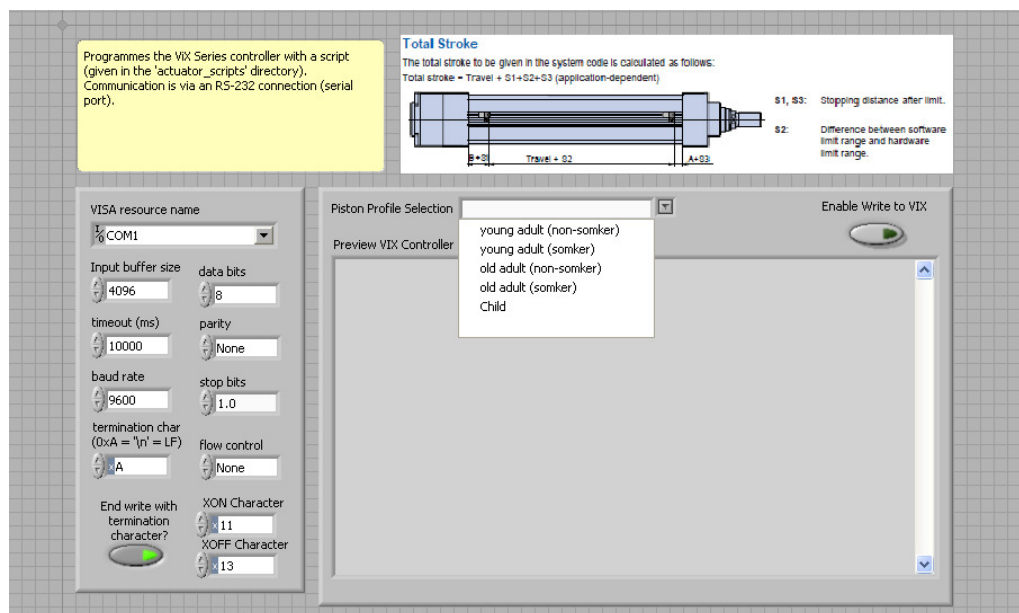


Figure 3.4 Labview Control Panel for the Mechanical Lung rig.

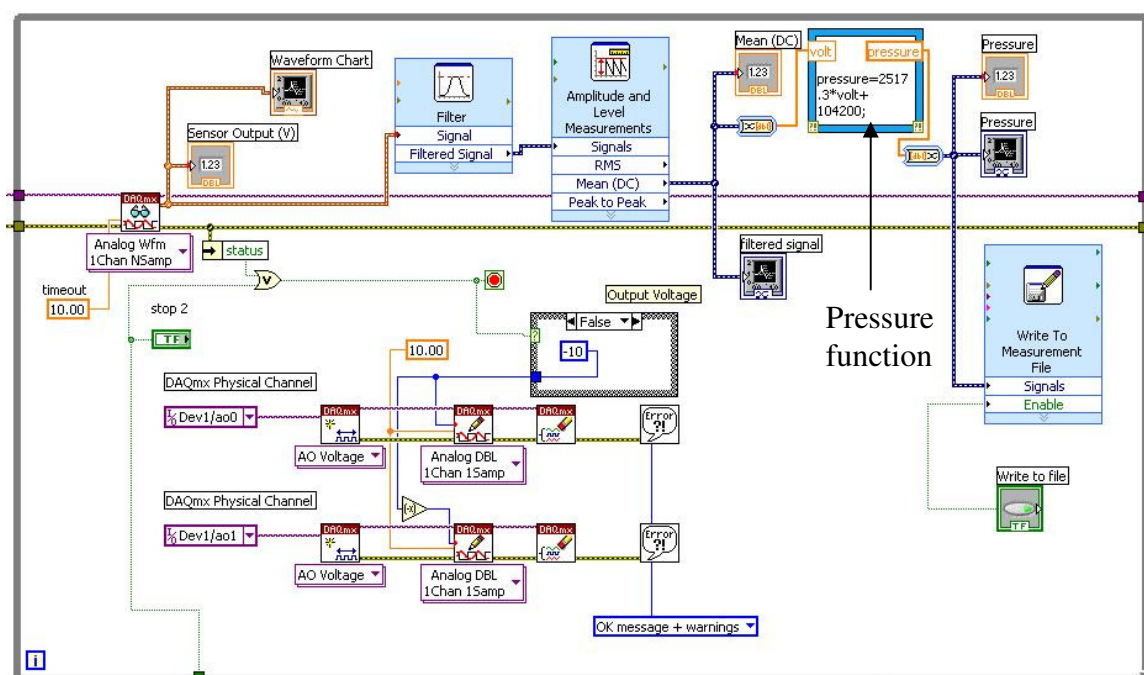
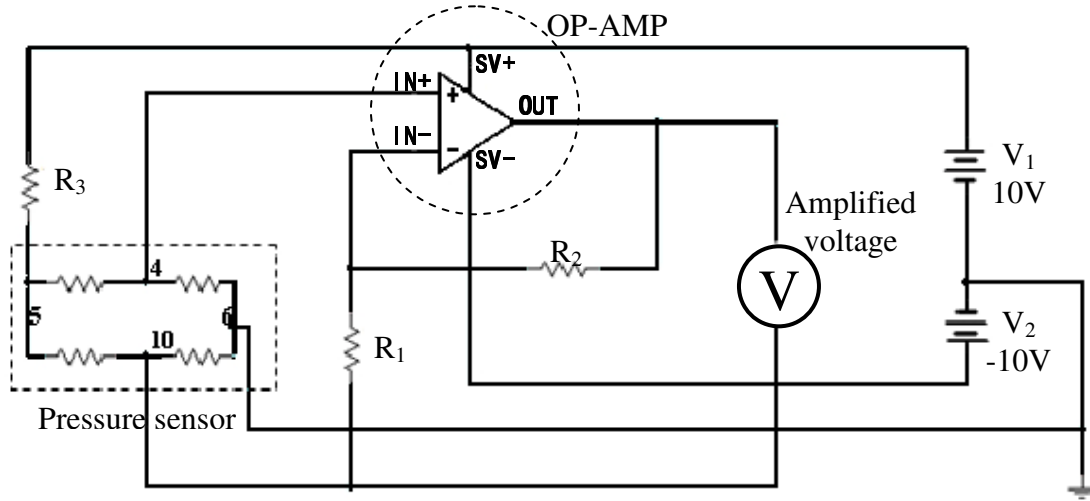


Figure 3.5 Labview block diagram for Mechanical Lung rig control.

Figure 3.5 shows the Labview 8.2 block diagram for controlling the rig motion and recording the output from the pressure sensor. The original voltage signal is measured with a frequency of 100kHz, and then a low frequency (25Hz) band pass filter is applied to reduce the noise. The pressure function is acquired by the calibration of the pressure sensor in section 3.2.6.

### 3.2.6 Pressure sensor circuit connection and calibration



*Figure 3.6 Pressure Sensor Circuit Connection of Mechanical Lung rig (VS: voltage supply; Pressure sensor: 4: output '+'; 5: supply '+'; 6: supply '-'; 10: output '-').*

A pressure sensor is implemented to record the pressure variations in the mechanical lung under different inhalation profiles. Since it is difficult for the Data Acquisition Card (DAC: PCI-6024E) to detect the small output voltage of the pressure sensor (around 10 mV), an operational amplifier (OP-AMP: NE5534AP) is used to increase the output range. As shown in Figure 3.6, the power supply of the OP-AMP is 20V ( $\pm 10$ V which is supplied by the analog output from the DAC) and that of pressure sensor is +10V; the resistor  $R_1 = 603\Omega$  and  $R_2 = 393k\Omega$ . In order to provide the proper current for the pressure sensor, an extra resistor ( $R_3 = 2.5k\Omega$ ) is connected in series with it. Finally, DAC records the amplified voltage which is then converted by the pressure function (equation 3.4) into the corresponding absolute pressure.





*Figure 3.7 Pressure Sensor Circuit Connection and Calibration devices for Mechanical Lung rig (manometer in the left).*

A manometer and a gauge are used for calibrating the pressure sensor as shown in Figure 3.7. There is a linear relationship between the absolute pressure and the amplified output voltage from the pressure sensor as expressed by equation 3.4 and shown in Figure 3.8. It should be noted that if the pressure sensor is replaced by a new one, it requires another calibration.

The absolute pressure has the relation with the amplified output voltage as:

$$pressure = 1.042 \times 10^5 + 2.5173 \times 10^3 \cdot Voltage \quad (3.4)$$



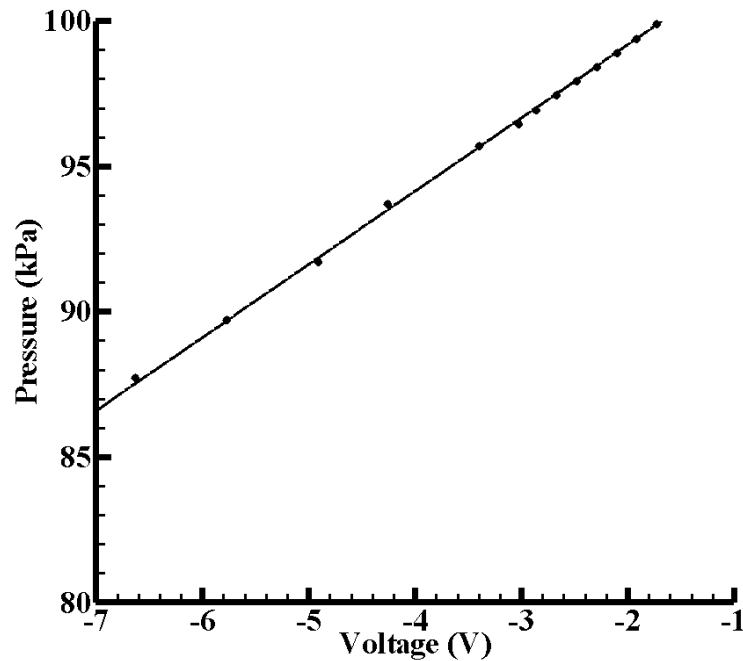


Figure 3.8 The variations of calibrated absolute pressures with amplified output voltages from pressure sensor (43A-002G).

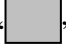

### 3.2.7 Piston motion programming and error testing

#### *Piston movement programming*

In order to make the mechanical lung simulate the smoking inhalation profiles as shown in Figure 2.19, a dynamic control of the piston motion is required to be programmed. The piston is connected to a gear box and a motor which are controlled by a servo drive with inputting numerical codes. The default variables of the codes provided by Parker (2003) are listed in Table 3.1. The revolutions can be referred to the revolutions of the motor, and by default one revolution is divided into 4,000 steps by Parker (2003). After a series of experimental calibrations, one revolution makes an axial displacement of 4.88mm.

Symbol	Meaning	Unit
v	motor velocity	rev/s
t	time	s
AA	motor acceleration	rev/s <sup>2</sup>
AD	motor deceleration	rev/s <sup>2</sup>
step	unique variable defined by Parker (2003)	steps

Table 3.1 Variables of programming for the piston motion in the mechanical lung rig (Parker, 2003).

As shown in Figure 3.9, the profile of a dynamic motion is divided into discrete time domains. The velocity is set to be constant ( $v_1, v_2, v_3$ ) with the same default motor acceleration (AA) and deceleration (AD) of  $100\text{rev/s}^2$  in each time domain ( $t_1, t_2, t_3$ ). The area covered by “” under the thick line “” is the number of revolutions of the motor, which can be calculated by equation 3.5.

$$\text{revolutions} = \frac{V_1^2}{2AA} + V_1\left(T_1 - \frac{V_1}{AA}\right) + \frac{(V_1 - V_2)^2}{2AD} + V_2T_2 + \frac{(V_2 - V_3)^2}{2AD} + V_3T_3 + \frac{V_3^2}{2AD} \quad (3.5)$$

For an extension, a general equation can be written as:

$$\text{revolutions} = \sum_i^n V_i T_i + \sum_i^{n-1} \frac{(V_i - V_{i+1})^2}{2AD} - \frac{V_1^2}{2AA} + \frac{V_n^2}{2AD} \quad (3.6)$$

where  $i$  is the index of the time domain and  $n$  is the number of total time domains.

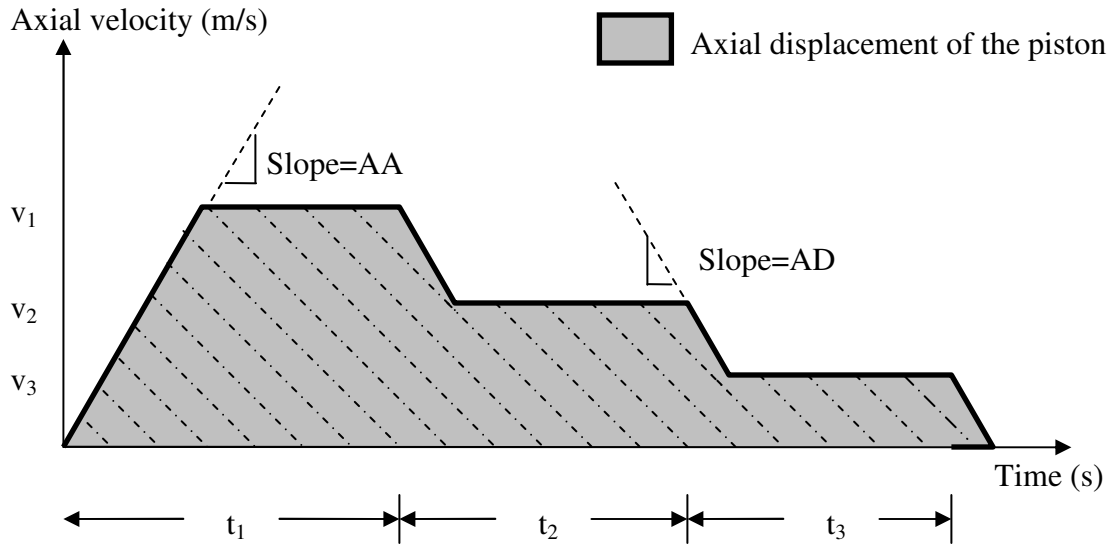


Figure 3.9 The velocity profile of piston displacement in the mechanical lung.

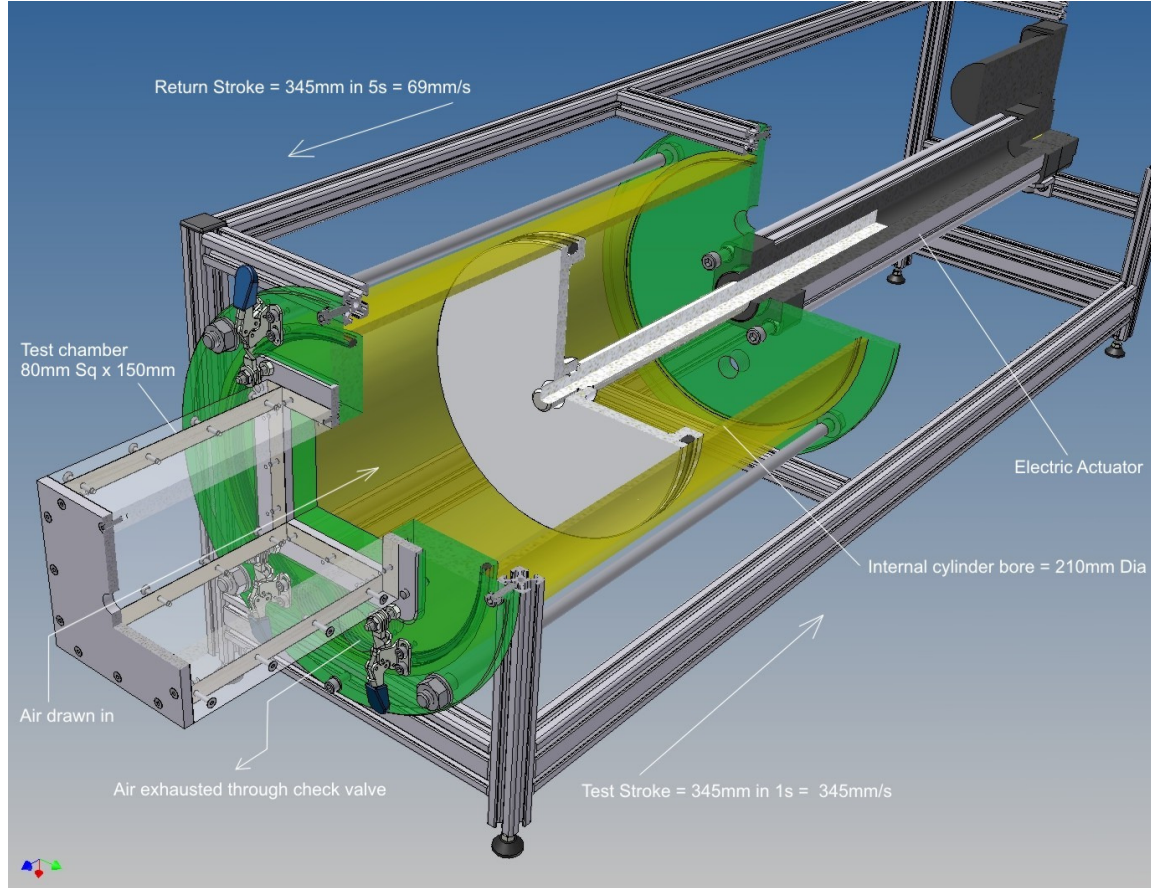
As mentioned previously, there is a relation between motor revolutions and piston transverse movement:

$$\text{piston axial displacement} = 4.88\text{mm} \times \text{motor revolutions} \quad (3.7)$$

There is always an error after each motion profile which is 150~300 steps of the motor (0.0375~0.075 revolution). It can be compensated by making the piston move another 0.0375~0.075 revolution after each profile (a mean of 0.06 revolution is used in this project).

### *The calculation of the piston original position*

As mentioned in Chapter 2 (Figure 2.17), there is a residual volume (RV) in the human lung. In the mechanical lung as shown in Figure 3.10, RV is composed of the volumes of the test chamber (for observation) and the cylinder in front of the piston.



*Figure 3.10 CAD drawing of the mechanical lung rig assembly.*

The volume of the test chamber is:

$$V_{chamber} = 80^2 \times 150 \text{ mm}^3 = 9.6 \times 10^5 \text{ mm}^3 \approx 0.001 \text{ m}^3 \quad (3.8)$$

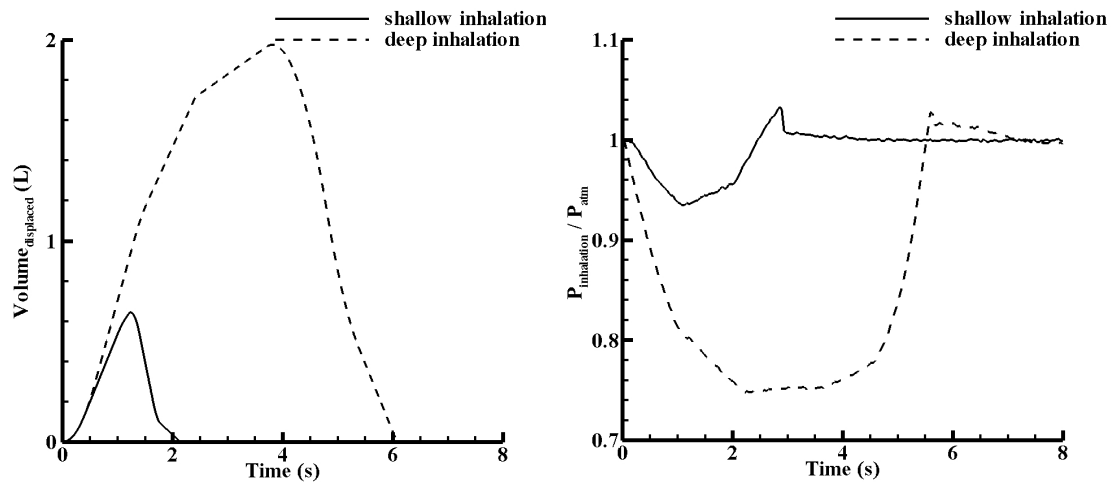
The area of the piston is:

$$A_{piston} = \pi \left( \frac{210}{2} \right)^2 \text{ mm}^2 = 34618.5 \text{ mm}^2 = 3.46185 \times 10^{-2} \text{ m}^2 \quad (3.9)$$

In this project, the value of RV (equation 2.8, Chapter 2) is used to calculate the piston position. The distance between the front edge of the cylinder and the piston is **0.111m** to keep a RV of 1.2L.

### ***Pressure variation inside mechanical lung***

The displaced volume variations in the mechanical lung under shallow inhalation and deep inhalation of smoking patterns (Tobin et al., 1982) are illustrated in Figure 3.11. It provides reasonable results compared to the lung volume variations of the smokers as shown in Figure 2.19. The corresponding pressure variations were measured by the pressure sensor installed in the mechanical lung ( $p_{\text{inhalation}}$ : inhalation pressure,  $p_{\text{atm}}$ : atmosphere pressure). The duration of the shallow inhalation is 1.2s and that of the deep inhalation is 3.8s. After that the pressure starts to increase till a pressure above the ambient pressure during the exhalation.



*Figure 3.11 Volume and pressure variations in the mechanical lung under shallow inhalation and deep inhalation (the pressure was measured by pressure sensor installed in the mechanical lung).*

### **3.2.8 Additional documents**

Further detailed information on the motor, servo drive, programming commands etc. can be found from the documentations of Parker Hannifin Corp. (<http://www.parker.com/>).

### **3.2.9 Final Notes**

There are some requirements before and during the operation:

1. The rig needs to be “warmed up” before operations, which means to make the piston move slowly along the cylinder and return. It prevents the rig from sharp/high voltage input and also allows the pressure sensor get enough power

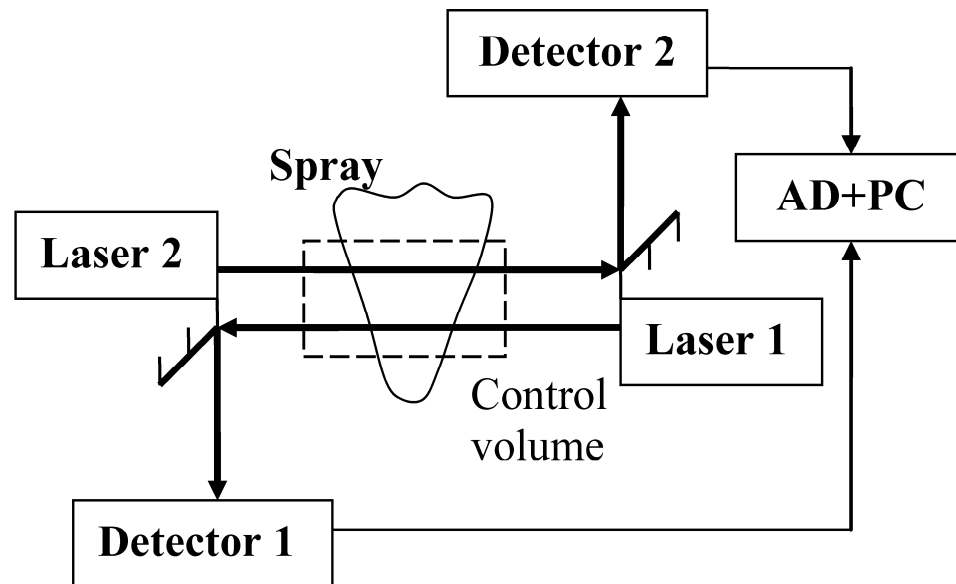
input (The reasonable output voltage measured from DAC is between 0.95V-1.4V).

2. Although the rig can repeat the same profile more than 1000 loops automatically, it is recommended to operate it under monitoring, due to the cumulative error in piston zero position. A solution to this problem is to add a zero piston position sensor and a feedback control loop.

### **3.3. Dual Laser Beam Method**

#### **3.3.1 Introduction**

In order to acquire the key information on the actuation flow simply and reliably, the dual laser beam method is applied to characterize the spray. There are several optical methods widely used which allow for accurate characterization of particle velocities and sizes such as Phase Doppler Anemometry (PDA) (Albrecht, 2003). The dual laser beam method is a variant of the Laser Doppler Anemometry (LDA) method to determine velocity, using two parallel laser beams instead of laser interference, and two detectors are employed. Both LDA and PDA are very accurate however the optical arrangements are more complicated. The dual laser beam method is a much simpler method which also allows for spray velocity and concentration measurement, which was developed by Dyakowski and Williams (1993).



*Figure 3.12 Dual laser beam method experiment layout.*

As shown in Figure 3.12, two laser beams (Helium-Neon Laser: MELLES GRIOT, 30mW max output, wavelength of 632.8nm) form two control volumes across which the spray plume passes. The light intensity change of the two laser beams due to beam obscuration by the spray is detected by two photodiodes and recorded by a PC based data acquisition card (DAC). When the spray passes through the first laser beam there will be a drop in voltage waveform from the correlative photodiode and similarly this will occur when it traverses the second beam. The distance between the two laser beams is known (3mm in this project), and the time delay can be measured by the delayed signal acquired as a result of the spray taking a finite time to traverse the two beams, therefore the spray velocity can be calculated. Here, this time delay is determined by a cross-correlation procedure (Dyakowski and Williams, 1993), which represents the amount of time it takes a spray element to travel through the two laser beams.

### 3.3.2 Velocity calculation

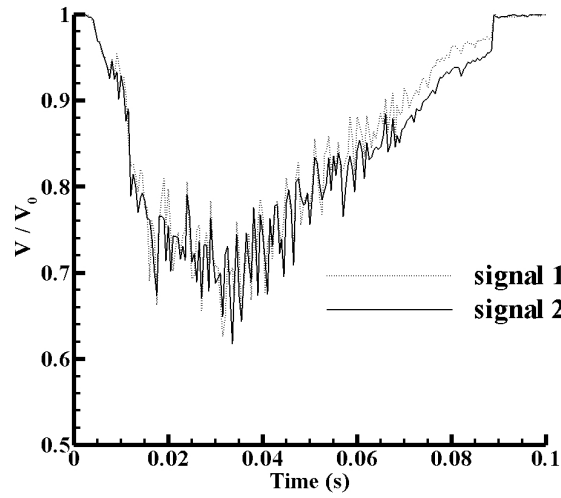


Figure 3.13 Realistic signals acquired by dual laser beam method, and it is impossible to simply read off a time delay ( $V$ : detected voltage,  $V_0$ : mean voltage detected).

Figure 3.13 shows an example of the signal that was acquired from the two photodiodes after the spray traversed the beams. It is not possible to simply read off a time delay; and therefore a statistical algorithm must be employed to determine the velocity. Assuming that the two laser beams are close enough (3mm in this work) so that effects of deceleration are negligible, a cross-correlation procedure determines the time delay between them (Dyakowski and Williams, 1993). This time delay represents the amount of time it takes for the whole spray plume travel through the two laser beams.

With the known distance between the two beams, the mean velocity of the spray (assuming that the control volume allows for minimal acceleration). The discrete form of the equation 3.10 (Dyakowski and Williams, 1993) represents the cross correlation ( $R_{xy}$ ) between two signals  $x(t)$  and  $y(t)$ , and it is employed in this measurement.

$$R_{xy}(k\Delta t) = \frac{1}{n-k} \sum_{i=1}^{n-k} (x(i\Delta t) - \bar{x})(y((i+k)\Delta t) - \bar{y}), \text{ where } -n < k < n \quad (3.10)$$

where  $k$  represents the 'x' array being shifted by ' $k$ ' (integer) positions to the 'y' array,  $\Delta t$  is the time step size,  $i$  is the index of the arrays,  $\bar{x}$  and  $\bar{y}$  are the mean value of array 'x' and 'y' respectively.

To acquire a more useful and normalized comparison, the cross-correlation coefficient  $\rho_{xy}$  is computed by equation 3.12 which gives values between -1 and 1, where  $\sigma_x$  and  $\sigma_y$  are the standard deviations of 'x' array and 'y' array respectively.  $\rho_{xy} = 1$  indicates perfect correlation,  $\rho_{xy} = 0$  indicates no correlation and  $\rho_{xy} = -1$  indicates perfect anti-correlation.

$$\tau_k = k\Delta t \quad (3.11)$$

$$\rho_{xy}(\tau_k) = \frac{R_{xy}(\tau_k)}{\sigma_x \sigma_y} \quad (3.12)$$

To summarize, the time delay  $\tau_k^*$  where  $\rho_{xy}$  is maximum, defines the time it took for the spray plume traversed the two laser beams thus the velocity can very easily be computed from equation 3.13.

$$u_{plume} = \frac{d_{beams}}{\tau_k^*} \quad (3.13)$$

where  $d_{beams}$  is the distance between the two beams.

Furthermore, assuming the spray is uniform and the droplets are spherical, the depth of the voltage drop is proportional to the surface area (of sum of the droplets) occluding the laser beam, and for a given spray mass it is an indication of the droplet sizes. Therefore a non-dimensional relative light obscuration term is introduced, which is defined by the ratio between the voltage drop when the spray traverses through the laser beams and the peak voltage when there is no spray passing. Although this cannot provide the absolute spray concentration or droplet size, it still can provide some relative measurement of spray opacity due to formulation variations. In addition the duration of the waveform gives an indication of the spread of droplet diameters present in a spray, since they will decelerate as a function of diameter.

### 3.4 A rig to measure the mass deposition in the lung

#### 3.4.1 Introduction

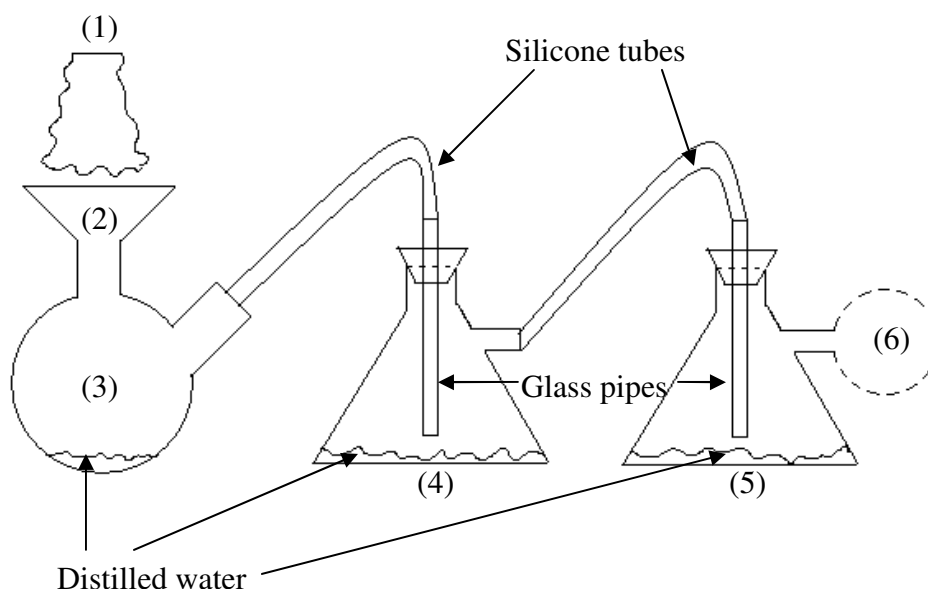
A rig is designed to get the information on the deposition of pressurized aerosols in the human respiratory tract. Research in the regional deposition of inhaled drops forms the



basis for estimating the quantity of inhaled aerosol which reaches the various parts of the respiratory tract. It provides the reference to optimize the inhaler and is therefore one of the essential factors in the characterization of the effectiveness of different formulations targeted to different lung sections.

### 3.4.2 Design Concept

With the reference to the particle deposition information reviewed in Table 2.1, a design of a pharmaceutically standard system is designed to record the inhalable mass fraction of the formulations depositing in various lung sections, as sketched in Figure 3.14.



*Figure 3.14 Mass fraction deposition rig simulating drop deposition phenomena in different human lung sections (parts list in Appendix VI.2).*

The system is typically constructed from standard laboratory glassware, connected with silicone tubes. (1) is the spray generated from the inhaler or other supply. Containers (2)+(3), (4) and (5) are designed to simulate mouth+throat, tracheo-bronchial and alveolar regions, respectively, where the distilled water is used to absorb the droplets. (6) is the flow rig which can be the mechanical lung built in section 3.2. The larger the droplet, the more likely it is to impact higher up the lung, and the less efficiently the drug will be absorbed into the bloodstream. Typically ten inhalations are pulled through the system,

and the integral amount of drug in each of the three containers will be measured by Kind Consumer Ltd., to give good estimate of the relative deposition rate in each lung section. This is a reliable, simple and quick method to determine the effectiveness a device over a wide parametric range prior to investigating the device performance with more detailed methods. A combination of the lung deposition rig and the mechanical lung is in operation in this project (Figure 3.15).

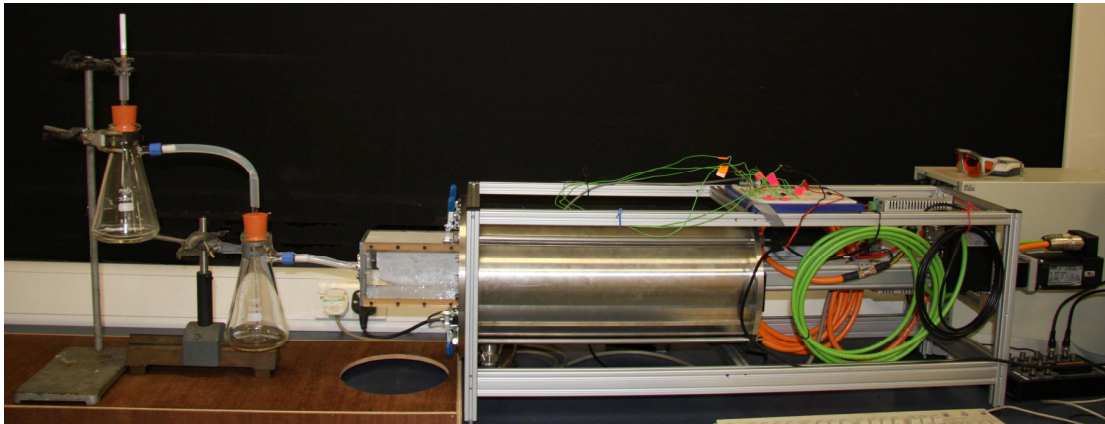


Figure 3.15 Combination of the mass deposition rig and the mechanical lung rig.

### 3.4.3 Design reference

Respiratory tract	Volume (ml)
Extrathoracic region (mouth+throat)	50
Tracheo-bronchial region	100~180
Alveoli region	2,000~4000

Table 3.2 Different lung region volumes (Stahlhofen et al., 1989).

The different lung region volumes are listed in Table 3.2 (Stahlhofen et al., 1989). Although the sizes of the three main parts are extremely different, it does not affect the performance of the mass deposition rig. The amount of the mass fraction deposition in each section can be changed by adjusting the height of the glass tubes inside the containers, which allows the rig to match the data from the literature listed in Table 2.1.

### 3.4.4 Design calculation

As shown in Figure 3.14, there is a gap between the glass tube and surface of the distilled water in the container (4) and container (5). The gap height can be adjusted due to different injected particle size and deposition information stated in Table 2.1. In order to find how the gap height affects the deposition, a computational fluid dynamics (CFD)

analysis is operated in the flow domain shown in Figure 3.16 which is the inner dimensions of container (4) and (5).

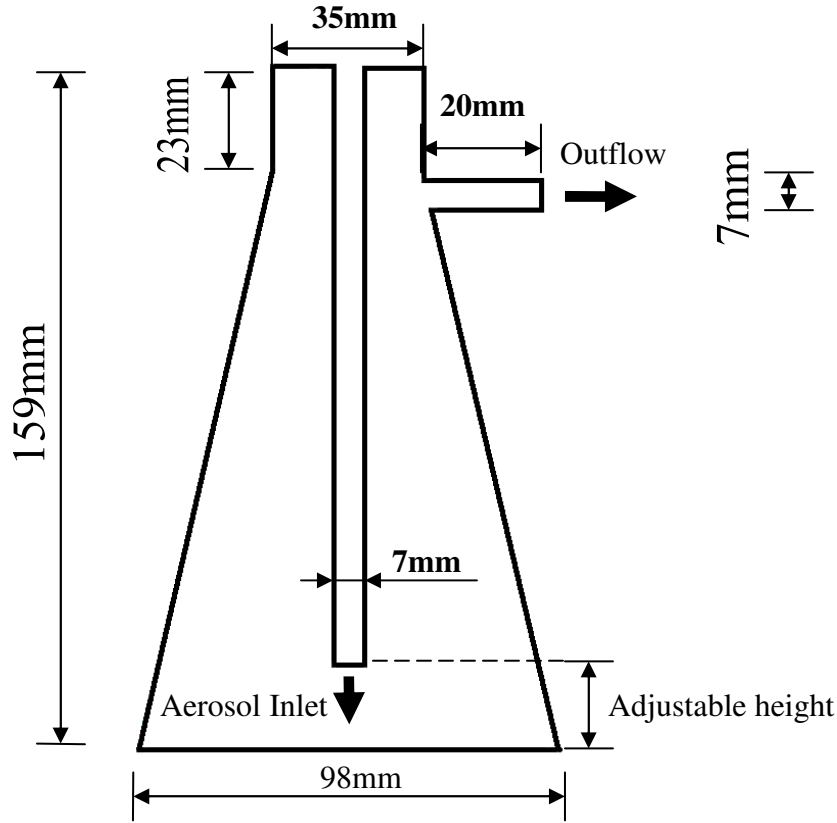


Figure 3.16 The inner dimensions of the container in the mass deposition rig.

The particle trajectories of the spherical drops with diameter of  $1\mu\text{m}$ – $20\mu\text{m}$  were computed with the CFD package (Gambit 2.4.6 & Fluent 6.3.26), at a mouth flow rate of 500 ml/s (mean smoking flow rate with deep inhalation profile as shown in Figure 2.19). According to the results there is a low Reynolds number flow ( $\text{Re}=1\sim 10$ ), a laminar flow model is used here. Particle trajectories are governed by an equation that balances the mass acceleration of the particle with the forces acting on it. For the spherical drops with  $1\mu\text{m}$ – $20\mu\text{m}$  diameter, Brownian diffusion is negligible (Darquenne et al., 1997; Darquenne et al., 1999) and the main forces acting on the drops are the drag force and the gravitational force. For a particle of density  $\rho_p$  and diameter  $d_p$ , assuming it is Stokes flow, the relevant governing equation is

$$\frac{d\vec{u}_p}{dt} = \frac{18\mu}{\rho_p d_p^2} (\vec{u}_g - \vec{u}_p) + \vec{g} \quad (3.14)$$

where  $\vec{u}_p$  is the particle velocity,  $\vec{u}_g$  is the velocity of the fluid (carrier gas) and  $\vec{g}$  is the gravitational force.

A group of drops with same diameter and uniformly distributed were injected into the container to find the mass deposition fractions. Figure 3.17 shows the effects of drop sizes and gap heights on the mass deposition fractions. Three conditions are investigated: 80%, 90% and 99% of the initial mass absorbed by the distilled water.

Assuming the mean diameter of the droplets produced from the Oxettes® is 10 $\mu\text{m}$ , Figure 3.18 shows how a group of drops with same diameter of 10 $\mu\text{m}$  deposit with different gap heights. From literature (Table 2.1), 90% of the droplets deposit in the upper respiratory, 5% deposit in the Alveolar and 5% are exhaled. Therefore, the gap height of the first container is set to be 2.5mm, where 90% of the drops can be absorbed. Second container should absorb half of the left 10% drops and release the rest 5% of the original drops, so the gap height of second container is set to be 12mm.

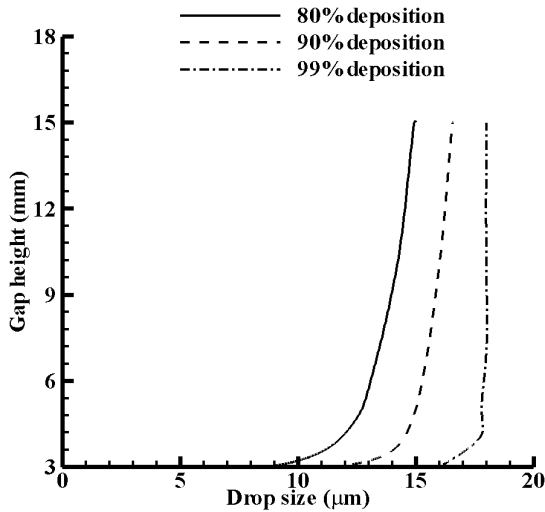
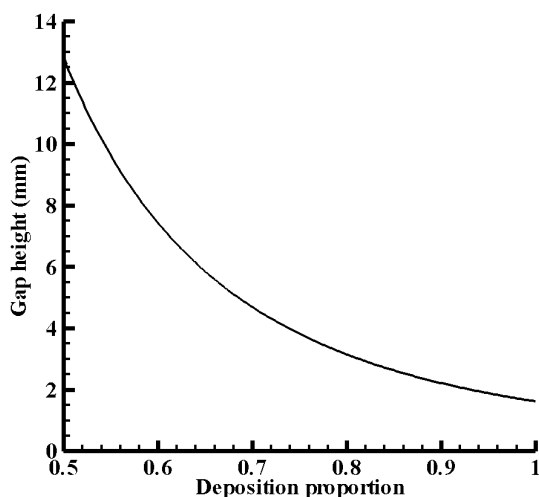


Figure 3.17 Influence of drop size upon the deposition with various gap heights of the container.



*Figure 3.18 Variations of 10 $\mu$ m drop deposition proportion with different gap heights of the mass deposition rig.*

### 3.5 Chapter summary

A mechanical lung rig has been assembled to simulate different human inhalation profiles. This is coupled to a transparent inspection chamber to facilitate visual inspection and optical measurements of the aerosolized products from Oxette®.

A simple and cheap spray analysis technique, dual laser beam method, has been introduced, which can easily obtain the information on the spray velocity and relative density.

A rig measure the mass of formulations deposition in the lung has also been built, with ability to test different size drops, which provides the information on the effectiveness of different formulations targeted to different lung sections. However, it is not implemented for the further work in this Ph.D. project due to the time limitation.

## Chapter 4

# Particle/Droplet Image Analysis

---

In the previous chapter, a mechanical lung has been assembled and programmed to trigger the ‘cigarette-like’ devices with different inhalation profiles, and a dual laser system has been designed to measure the global actuation flow characteristics (e.g. spray velocity and opacity). In this chapter, a methodology is presented that enables efficient acquisition of sufficient droplet information (e.g. diameter and aspect ratio) from images of in and out of focus droplets. The newly developed multi-threshold algorithm is successfully implemented in the automatic particle/droplet image analysis (PDIA) system. It increases the depth of field (DoF) of small particles ( $D < 50\mu\text{m}$ ), and the multi-threshold method performed more efficiently than the dual threshold methods (Yule et al., 1978 and Kashdan et al., 2003). When testing the  $70\mu\text{m} \sim 110\mu\text{m}$  and  $100\mu\text{m} \sim 200\mu\text{m}$  moving glass spheres, the dual threshold method can only detect 11%~29% of the particles found by the multi-threshold method. The multi-threshold method is also capable of generating the aspect ratios of particles more accurately than the dual threshold methods. Furthermore, with the analysis of the glass spheres with diameter of  $1\mu\text{m} \sim 50\mu\text{m}$ , the multi-threshold method is applicable in sizing the pharmaceutical aerosols with the mass median diameter of  $2\mu\text{m} \sim 5\mu\text{m}$ .

---

## 4.1 Introduction

Photography is the process of forming visible images directly or indirectly by the action of light or other forms of radiation on sensitive surfaces. Recently image processing techniques have been widely adopted in analyzing spray droplets and solid particles because it offers several important advantages over alternative particle sizing techniques such as Phase Doppler Anemometry (Albrecht et al., 2003). Among these advantages are the simplicity and relative inexpensiveness of photographic apparatus, flexibility, and the capability of detecting and analyzing non-spherical particles.

The aspect ratio of non-spherical particles plays an important role in the study of respiratory tract deposition of inhaled pharmaceutical aerosols. The interception of the tip of a particle with an airway wall should be taken into account in the study of the inhalation of elongated particles. Accordingly, Chan and Gonda (1989) have previously noted that high aspect ratio drug particles are easily delivered to the peripheral lung. However these particles exhibit aerodynamic properties that reduce their deposition in the upper airways as compared to mass equivalent spherical particles (Chan and Gonda, 1989; Johnson and Martonen, 1994; Crowder and Martonen, 2002;), interception is expected to increase their deposition in smaller peripheral airways (Chan and Gonda, 1989).

Image forming is a direct method of recording information on particles as opposed to the indirect methods utilizing diffraction, scattering, resonant scattering and interferometry (Chigier, 1991). Direct photography allows one plane at a time to be imaged with exposure time down to a micro-second with short duration flash lamps or a nanosecond with pulsed lasers. Further advantages of photography include: the relative insensitivity to optical properties of particles, measurement of particle velocities by using double or multiple exposures, and it provides the visual evidence that may invalidate the measurement by other techniques e.g. due to multiple scattering. However, accurately sizing of out of focus particles requires consideration.

A developed digital image analysis technique capable of sizing particles of arbitrary shape and size and with wide dynamic range accounting for out of focus effects is refined. The fundamental principles of the technique and a description of the calibration procedure in which the image processing routine was verified with calibration data of known particle sizes were described in Kashdan et al. (2003). The measurement

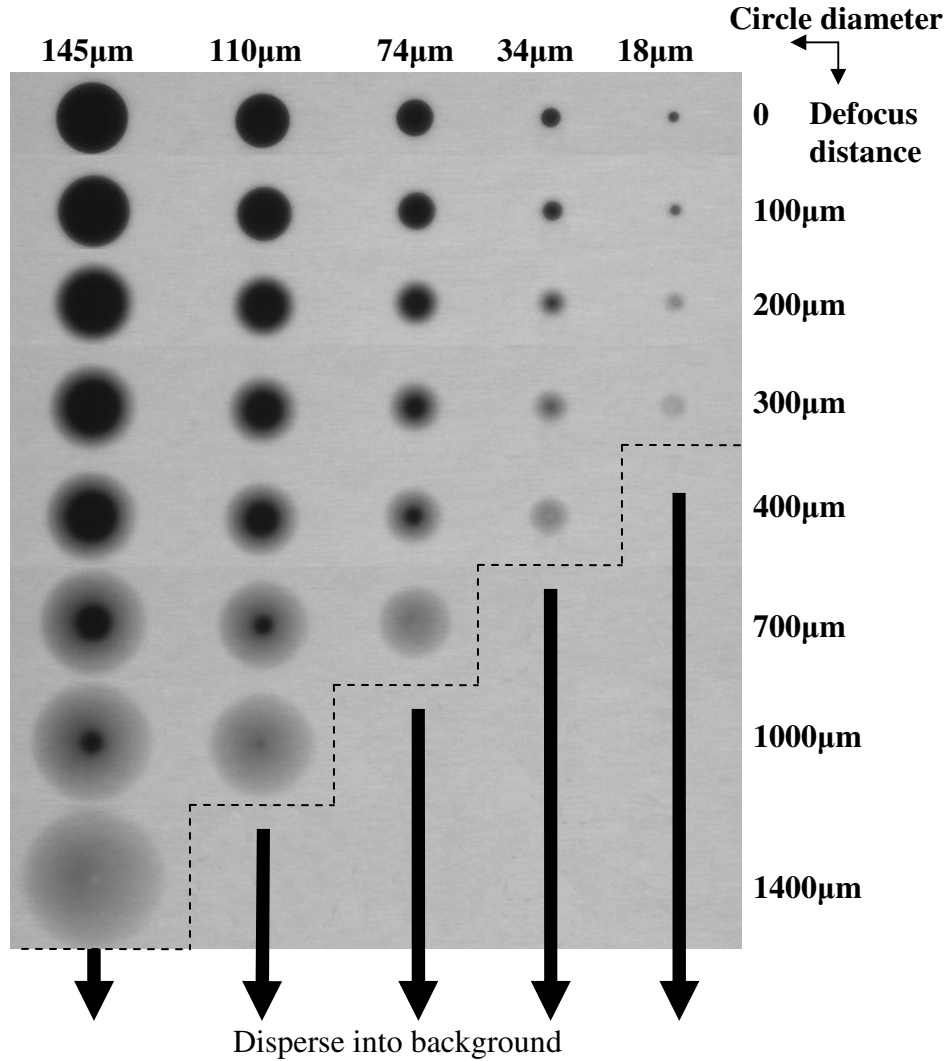
performance of the particle/droplet image analysis (PDIA) system has been assessed initially in terms of individual object diameters ( $D$ ). The aim of this experimental investigation is to assess the robustness and accuracy of the technique and to improve it by using localized and dynamic thresholding. The accuracy of the threshold method determines the precision of particle/droplet characters in PDIA, and here three threshold methodologies are evaluated. Two existing methods (named dual threshold methods) are based on the work from Yule et al. (1978) and Kashdan et al. (2003), which are commonly used in commercial particle/droplet analysis software. However, dual threshold methods cannot detect excessively defocused particles, which will be explained in section 4.2.2. Generally, smaller particles have a smaller viable depth of field than larger ones (Kashdan et al., 2003 and Yule et al., 1978). In order to detect more small particles ( $D < 50\mu\text{m}$ ) from a certain set of images, a larger measurable depth of field is preferred in the image process. The newly developed methodology, named the multi-threshold method, increases the acceptable depth of field of particles especially for the small ones compared to the dual threshold method. It enables more small particles to be detectable in PDIA.

Section 4.3 explains the layout of the measurement system. Section 4.4 makes a first step to describe the calibration procedure for PDIA with charged coupled device (CCD) camera and diode laser system by using calibration graticule (Patterson Globes and Circles), from which the usage of software, comparison of different threshold methodologies and depth of field (DoF) determination were studied. Here, the DoF is defined as the distance range along the optical axis within which the particle is considered to exist. In order to test the applicability of PDIA, the characteristics of a population of glass spheres of known size were analyzed using the diode laser system. Detailed discussion of the results generated by different threshold methods will be presented in section 4.5.



## 4.2 Principle of the DPIA program

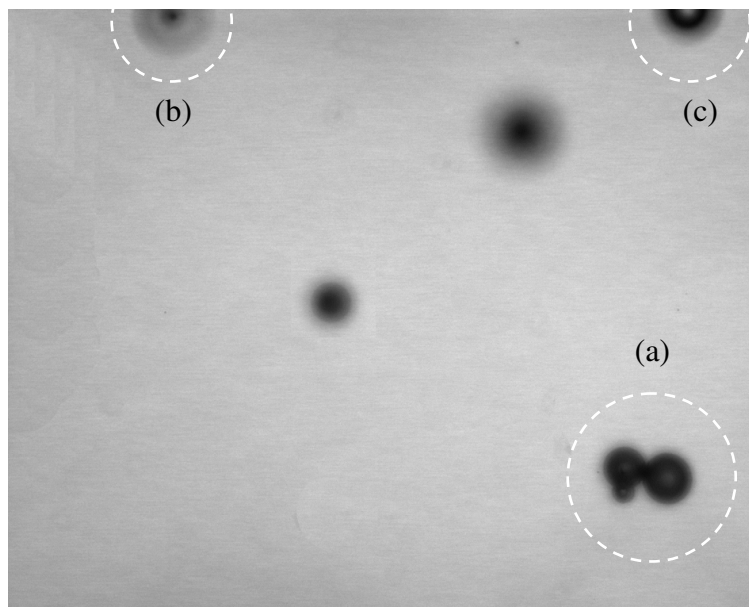
### 4.2.1 General experimental principle



*Figure 4.1 Composite image of Patterson Globes and Circles calibration graticule showing objects of increasing diameter (rows) and at increasing defocus distances (columns) for the determination of an acceptable DoF.*

Figure 4.1 shows a composite image matrix of the Patterson Globes and Circles obtained by the PDIA system with increasing diameter and at increasing defocus distances, in which the top row corresponds to the in-focus object diameters: 145μm, 110μm, 74μm, 37μm and 18μm. Subsequent rows correspond to the same objects at defocus distances of 100μm, 200μm, 300μm, 400μm, 700μm, 1000μm, and 1400μm. Obviously the out-of-focus particles look larger than they really are and become bigger

but fainter with the increase in the defocus distance until they disperse into the background. From Figure 4.1, it indicates that the basic problem to be solved concerning image processing algorithms is the light diffraction at the particle image boundary: the grayscale varies continuously and the appropriate value of the threshold grayscale should be determined. A detailed comparison of different threshold methods is discussed in section 4.2.2.



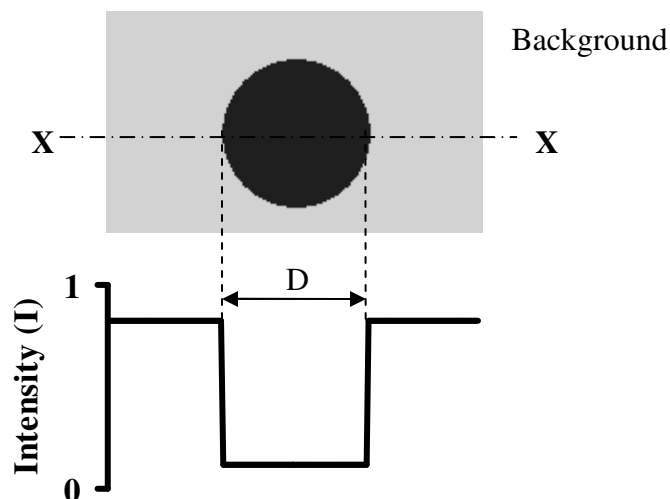
*Figure 4.2 Image of glass spheres dispersed in water.*

In measuring a group of particles dispersed in three dimensional space, the two dimensional image captured by the camera system probably contains the images of off-focused particles, overlapping particles and particles touching the image boundary, which can cause a measurement error. A photo of dispersed glass spheres acquired by PDIA system is shown in Figure 4.2, illustrating the overlapping particles in region (a), off-focused particles and particles touching the image boundary in region (b) and (c) respectively. For accurate measurement, the off-focus particles should be sized correctly. Overlapping particles can be processed assuming the particles are spherical, which will be explained in section 4.4.8. This image process algorithm rejects particles touching the edge of the image field-of-view since the amount of particle out of field-of-view cannot be estimated. Another important consideration is the acceptable depth of field (DoF) criterion which can be estimated from Figure 4.1, however, a quantitative determination

of DoF is given during the calibration procedure (section 4.4). When the same DoF criterion is imposed on polydispersed particles contained within a finite measuring volume, a number of smaller drops may be considered out of DoF and eliminated from the counting throughout the image processing. To restore the missing small particles remaining outside the DoF or to avoid losing larger particles touching the edges of images, the number of particles within the DoF region should be multiplied by weighting factors corresponding to each size group (Koh, et al. 2001). If a particle remains outside the depth of field around the focal point, the particle should not be counted.

#### **4.2.2 Particle/droplet identification**

The PDIA system is used to detect connected regions or groupings of pixels in an image and then make selected measurements of those regions which are commonly referred to as particles. A particle is a contiguous region of nonzero value pixels. In order to distinguish the droplets/particles from the illumination background within the image a threshold is applied. Particles can be extracted from a grayscale image by thresholding the image into background and foreground states. Zero valued pixels are in the background state, and all non-zero valued pixels are in the foreground. Particle analysis functions can easily produce statistical information—such as the presence of particles, their number, size, shape and location. A typical particle analysis process scans through an entire image, detects all the particles in the image, and outputs information on each particle with the parameters such as perimeter, area, aspect ratio and particle centre positions.



*Figure 4.3 Schematic representation of a particle shadow image and intensity profiles across X-X for an in-focused particle.*

Figure 4.3 shows a schematic representation of a theoretical in-focus droplet positioned at the centre of the plane of best focus and the corresponding idealized intensity profile across the object centre. It clearly illustrates that the contrast between the particle shadow and the background is very sharp and that the corresponding grey scale gradient is steep, thus the droplet diameter ( $D$ ) is relatively easy to measure.

If the droplet is located at some displacement from the focal plane of the objective lens, the resulting shadow image becomes defocused. As illustrated by Figure 4.4, defocused particles no longer have the sharp contrast as observed in Figure 4.3 and there exists a continuous graduation of intensity between the dark object centre and the light image background. The region between the background threshold and the inner dark region in Figure 4.4(a) is termed the particle 'halo' and typically has a constant intensity gradient. Dual threshold methods and multi-threshold method are implemented to analyze those defocused particles.

### Dual threshold methods

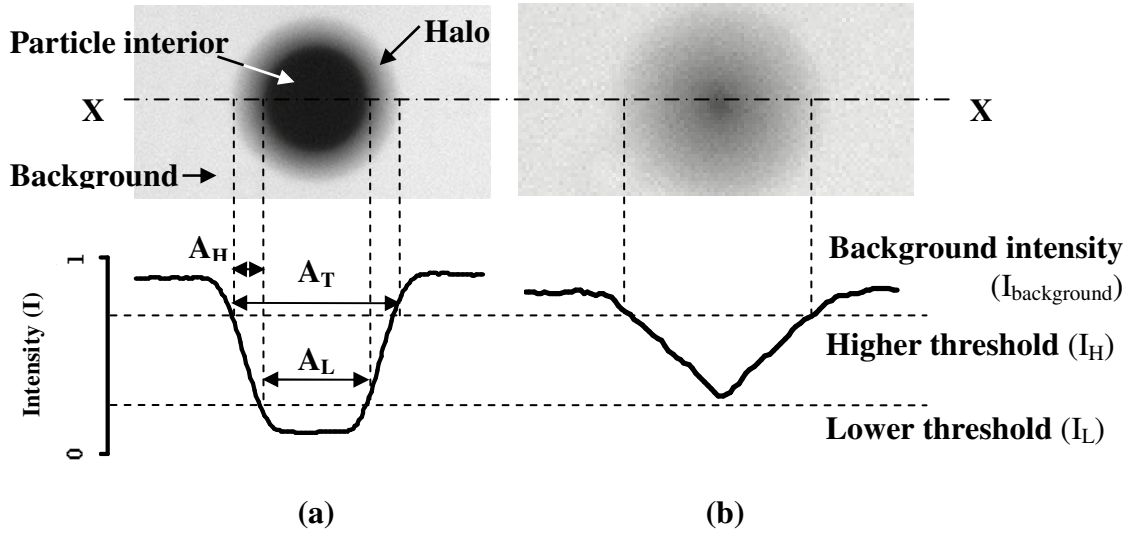


Figure 4.4 Images of defocused particles analyzed with dual threshold method: (a) a typical defocused particle and (b) an excessively defocused particle.

The total area of the particle ‘halo’ ( $A_H$ ) as shown in Figure 4.4(a), expressed here as the number of pixels in the ‘halo’ region. It increases with increasing defocused distances and is used to extract the true object diameter. The PDIA method uses this information as a means of determining the location of a particle or droplet relative to the plane of best focus, which is robust and commonly used in commercial particle/droplet analysis (Kashdan et al., 2003).

In order to define the accurate particle size, lower threshold ( $I_L$ ) and higher threshold ( $I_H$ ) are defined in dual threshold methods, as shown in Figure 4.4(a). The particle interior is extracted by the lower threshold ( $I_L$ ), which is the total pixel count with the intensity weaker than the lower threshold ( $I < I_L$ ). The halo area ( $A_H$ ) is defined as the total pixel count with the intensity between lower threshold and higher threshold ( $I_L < I < I_H$ ). Total area of the whole out of focus particle is the sum of the particle interior area ( $A_L$ ) and the halo area ( $A_T = A_L + A_H$ ). There are two main dual threshold methods presented here to determine  $I_L$  and  $I_H$  (Yule et al., 1978 and Kashdan et al., 2003):

Method 1 (Kashdan et al., 2003):  $I_L$  and  $I_H$  are the functions of background intensity ( $I_{\text{background}}$ ) of the whole image with a difference of 0.117, calculated from equation (4.1) and (4.2).

$$I_H = 0.85 \times I_{\text{background}} \quad (4.1)$$

$$I_L = I_H - 0.117 \quad (4.2)$$

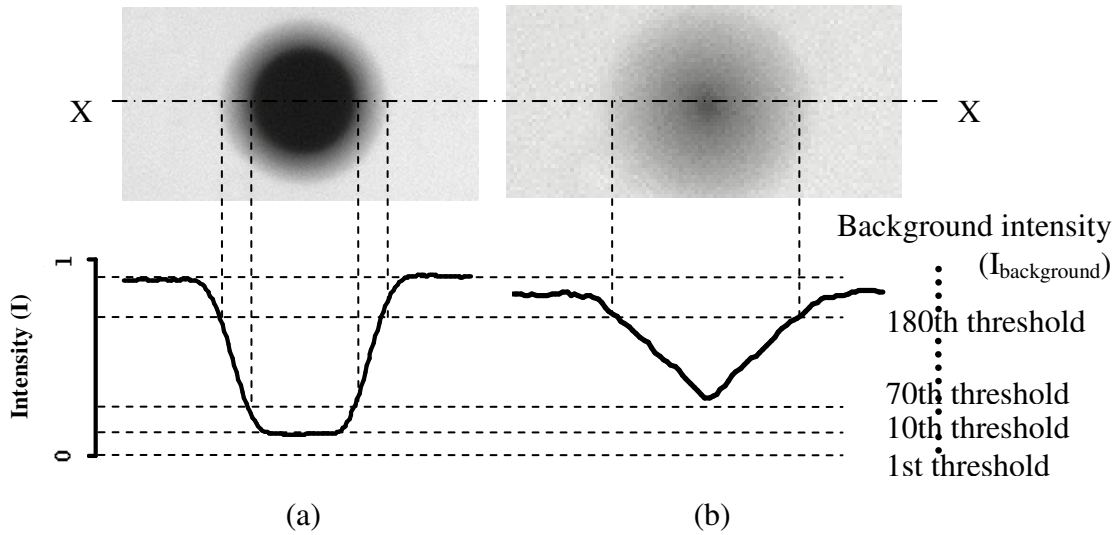
Method 2 (Yule et al., 1978):  $I_L$  and  $I_H$  are the functions of the background intensity ( $I_{\text{background}}$ ) and minimum intensity ( $I_{\text{min}}$ ) of the image, calculated from equation (4.3) and (4.4).

$$I_L = 0.64 \times (I_{\text{background}} - I_{\text{min}}) + I_{\text{min}} \quad (4.3)$$

$$I_H = 0.15 \times (I_{\text{background}} - I_{\text{min}}) + I_L \quad (4.4)$$

Yule et al. (1978) stated that the coefficients (0.64 and 0.15) chosen for equation (4.3) and (4.4) are arbitrary and not critical, provided that the same values are used for both calibration process and the actual particle size measurements. The above equations indicate that both dual threshold methods rely on the background intensity. The following calibration procedure (section 4.4) will detail how background intensities affect PDIA results.

However, neither of the dual threshold methods is capable of analyzing the excessively defocused particles as shown in Figure 4.4(b), since the particle interior can not be detected by the lower threshold. Method 1 (Kashdan et al., 2003) sets the difference between higher and lower thresholds as a constant of 0.117 in equation 4.2, which can only deal with the particles with better focus than that shown in Figure 4.4(b). Although the difference between higher and low thresholds set in Method 2 is the function of background, a similar restriction of detecting far more defocused particle occurs during PDIA process. This limitation is fundamental to dual threshold methods.

**Multi-threshold methods**

*Figure 4.5 Analysis of the defocused particles shown in the Figure 4.4 with multi-threshold method.*

Analysis of the excessively defocused particle as shown in Figure 4.4(b) is the main issue for the dual threshold methods, especially for the small particles which are easily out of focus within a small defocused distance. The maximum defocus distances for small and large particles differ greatly, which causes highly non-uniform control volume weighting factors to be applied to different size classes to reconstruct true particle size distributions. This in turn makes dual threshold methods overly sensitive to the error prone measurements of the smaller objects recorded. The proposed solution is simply to use multiple thresholds, in the aptly named multi-threshold method.

PDIA works best when using the particle local background level to determine the particle information rather than the global image background intensity. It is difficult with dual threshold methods and an additional algorithm is required to find the local background level. However, since the multi-threshold method employs continuous thresholds until the local background level to process each particle in the images, it naturally uses the local background intensity

As shown in Figure 4.5(a), a typical defocused particle can be detected from the 10<sup>th</sup> threshold till the local background intensity of the particle. However, the excessively defocused particle is detectable from the 70<sup>th</sup> threshold till its local background intensity as shown in Figure 4.5(b). It shows the multi-threshold method is capable of analysing

the particles with a wider range of defocused distance than the dual threshold method, which is crucial in small particle analysis. Quantitative comparisons of the dual threshold methods and the multi-threshold method are presented in section 4.4.

### 4.2.3 Calibration procedure

A sample flow chart (Figure 4.6) illustrates how PDIA analyses the calibration circles step by step. With the diameter of  $110\mu\text{m}$  (No.6),  $74\mu\text{m}$  (No.4),  $37\mu\text{m}$  (No.2) and  $18\mu\text{m}$  (No.1), the calibration circles are located at a defocus distance of  $20\mu\text{m}$  from the focal plane. In the end of the process, it produces a detailed report on each particle with the parameters such as area and center of mass into .txt files.

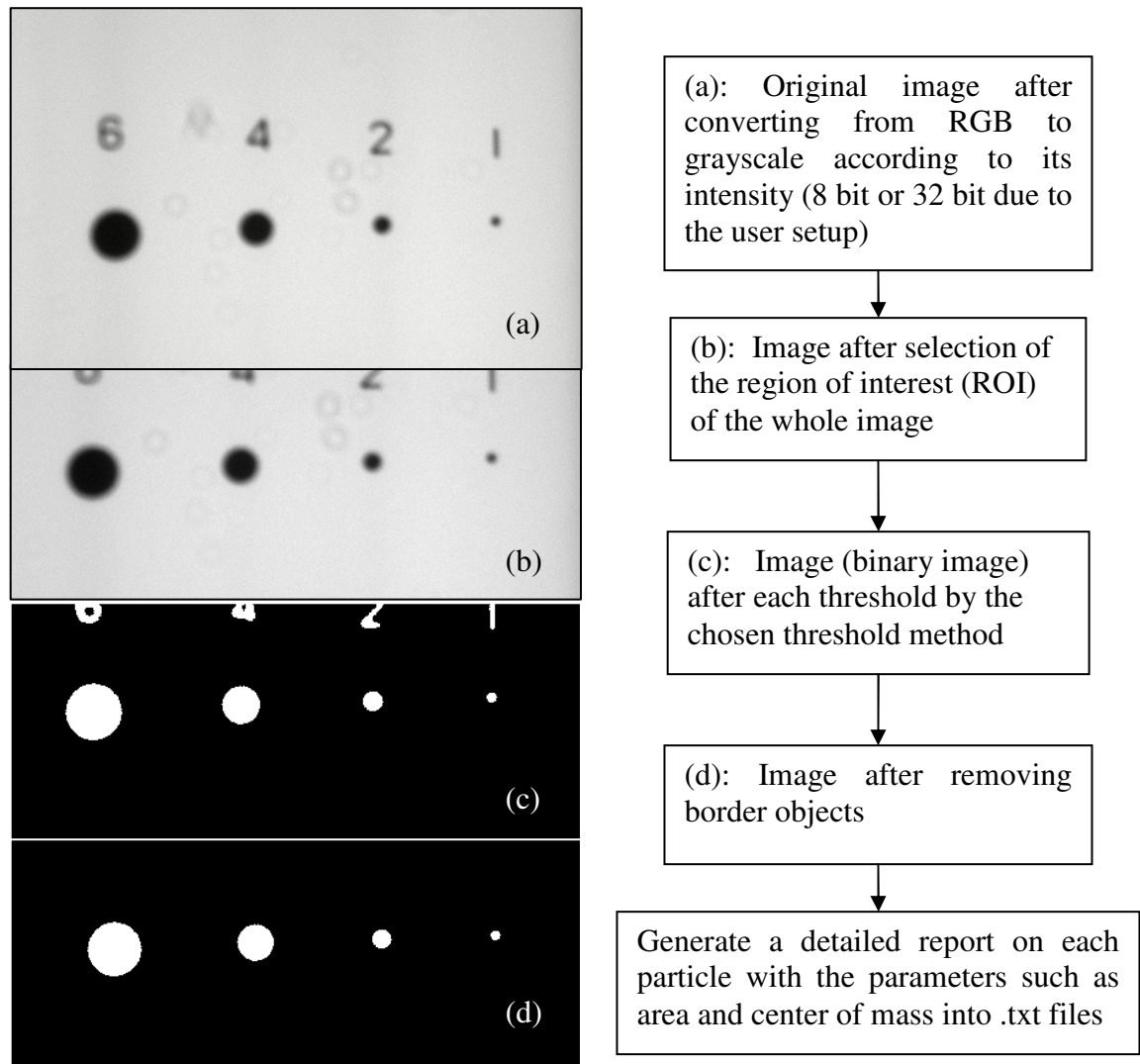


Figure 4.6 Images after each processing step (a): original image; (b): image after ROI selection; (c) image after thresholding; (d): image after removing border objects.



#### 4.2.4 Weighting factor for correction of the particle/droplet size distribution

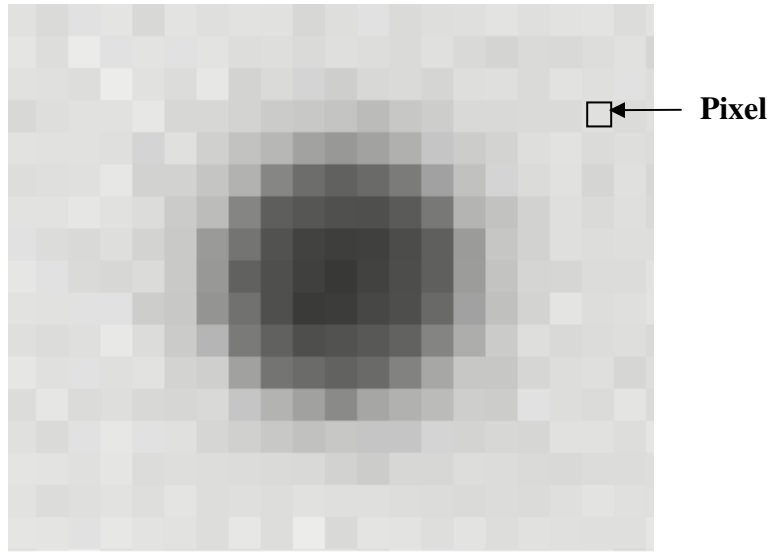
The PDIA algorithm rejects particles touching the edge of the image field-of-view since the amount of particle out of field-of-view cannot be estimated. This results in a statistical correction as the larger particles have more possibilities to touch the boundaries of the images. This weighting factor (Kashdan et al., 2003) is:

$$\frac{1}{1 - n_i} = \frac{WH}{(W - D_i)(H - D_i)} \quad (4.5)$$

Here  $n_i$  is the weighing factor for the particles with a mean diameter of  $D_i$ , and  $W$  and  $H$  are the width and height of the image field of view respectively.

### 4.3 PDIA experiment instrument considerations

#### 4.3.1 Brief introduction to CCD camera



*Figure 4.7 Image of a particle captured by a CCD camera (composed of pixels).*

A charge coupled device (CCD) camera is used to take images in this project, which is an analog device. When light strikes the chip it is held as a small electrical charge in each photo sensor. The charges are converted to voltage one pixel at a time as they are read from the chip. Additional circuitry in the camera converts the voltage into digital information (Janesick, 2001). Figure 4.7 shows a typical photo of particle by a CCD camera. The pixel is the smallest addressable screen element; it is the smallest unit of the picture that can be controlled. Each pixel has its own address. The address of a pixel

corresponds to its coordinates. In this project, pixels are normally arranged in a 2-dimensional grid, and are represented using squares. Each pixel is an integration of the area of the original image; more samples (pixels) typically provide more accurate representations of the original. The intensity of each pixel is variable, therefore the accuracy of indentifying small particles of order 10 pixels in diameter incurs digitization error, which requires a sensitivity test detailed in section 4.4.1. In color image systems, a color is typically represented by three component intensities such as red, green, and blue (RGB) (Graf, 1999). In this project, we convert original RGB into grayscale images before PDIA processing.

### 4.3.2 Conceptual experimental design

Experiment layout of the PDIA system is simple and straightforward compared to the other particle/droplet analysis methods, and is shown in Figure 4.8. Field of view (FoV) of the measurement area is determined by the focal length of the lens, the size of the CCD of the camera and the distance between cameras CCD and lens. Determination of the acceptable depth of field (DoF) of PDIA system is detailed in section 4.4, and the experimental instruments of the PDIA system are listed in Table 4.1.

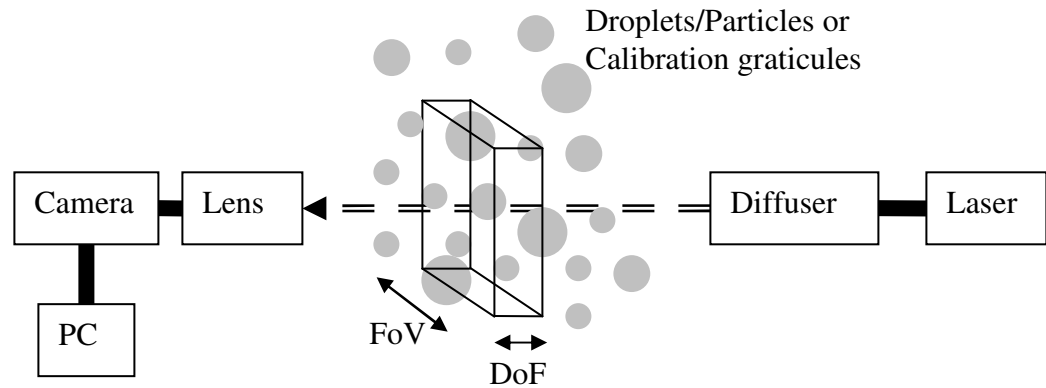
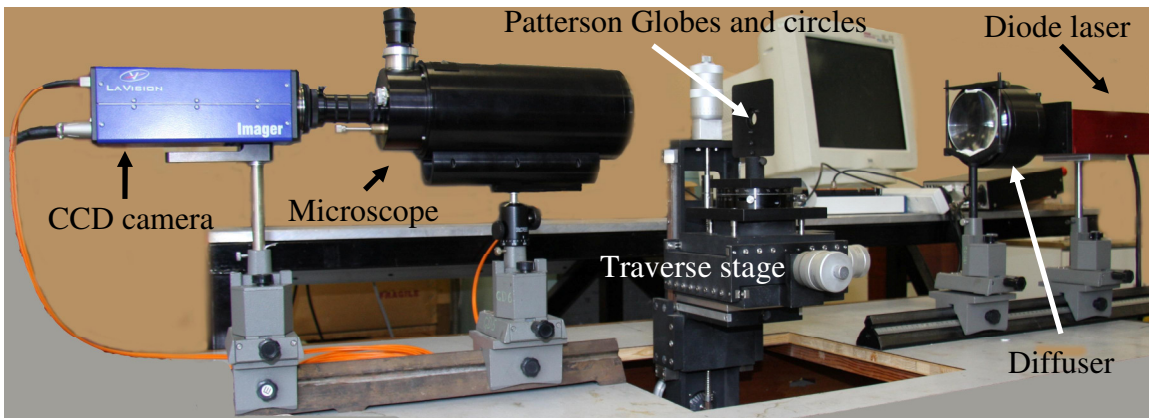


Figure 4.8 PDIA system experiment layout for real spray analysis.

Experiment component	Reference
Camera	LaVision Imager 3S
Calibration circles	Patterson Globes and Circles—NG1 (18 $\mu$ m~450 $\mu$ m) NPL Reference Stage Graticules (3 $\mu$ m~48 $\mu$ m)
Diffuser	LaVision, VZ-illumination high efficiency diffuser
Diode laser	Oxfordlaser Firefly system (model: BS-EN60825-1:2007)
Glass spheres	Diameter Range: 1 $\mu$ m~50 $\mu$ m; 70~110 $\mu$ m; 100~200 $\mu$ m; (Jencons-Plus)
Lens (microscope)	Questar QM100 Model #30003 (working distance: 15cm~35cm)
Neutral density filter	Rosco (transmission 13.7%, 23.5%, 51.2%, 69.3%)
Transparent glass water tank	105mm×65mm×145mm cube

*Table 4.1 PDIA system instruments.*

Before real spray analysis, calibration of the PDIA system is required with the calibration circles of known sizes. In order to calibrate the system at the different defocused distances and with various illumination intensities, an experiment rig for the calibration is built up as shown in Figure 4.9. The graticule of Patterson Globes and Circles is placed at 35cm from the microscope and 40cm from the diffuser (best position stated in the diffuser menu), where the field of view is 2.0mm×1.6mm.



*Figure 4.9 PDIA calibration layout with diode laser system in the lab.*

A schematic diagram is illustrated in Figure 4.10, where the minus sign in defocus distance  $D_F$  indicates the test circles near the diffuser and the laser. As introduced in section 4.2.2, background intensity is important for PDIA. Therefore neutral density (ND)

filters with transmission of 13.7%, 23.5%, 51.2% and 69.3% are implemented to change the illumination intensities and find how the background intensities affect the results.

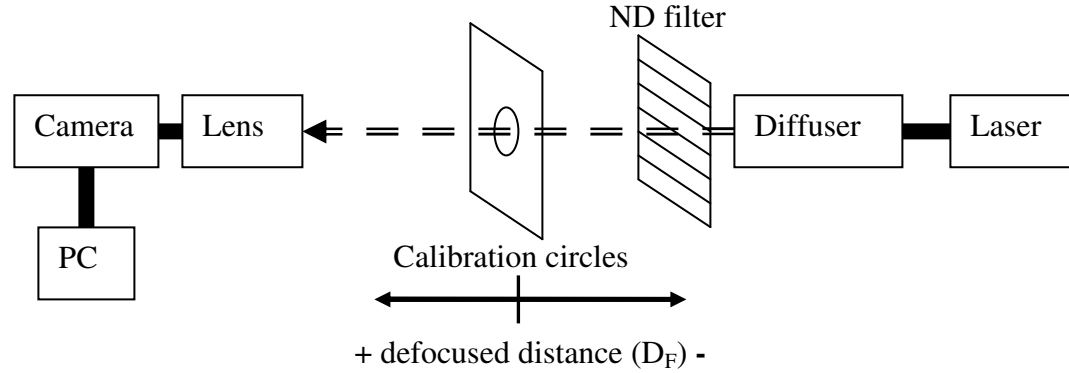


Figure 4.10 Schematic diagram of the PDIA calibration rig.

In order to test the applicability of the PDIA algorithm, the calibrated PDIA system will analyze the glass spheres dispersed in a water tank by the stirrer and the discussions of the results will be presented in section 4.5. The glass spheres are provided by Jencons-Plus with diameter range of 70~110 $\mu\text{m}$  and 100~200 $\mu\text{m}$ . The experiment layout of the glass sphere analysis is similar to the calibration setup as shown in Figure 4.8, where here the glass spheres are dispersed in a transparent glass water tank.

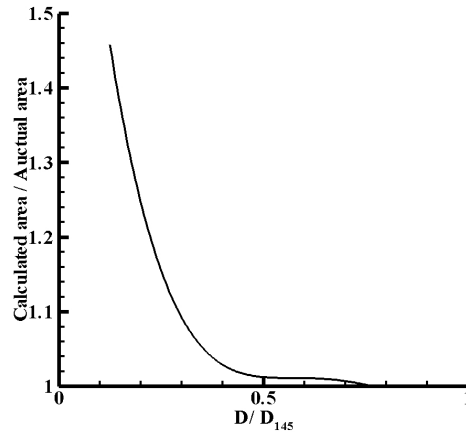
#### 4.4 Calibration with diode laser

The fundamental principles of the technique and a description of the calibration procedure in which the image processing routine was verified with calibration data of known particle sizes were described in Kashdan (2002), Kashdan et al. (2003), Kashdan et al. (2004) and Kashdan et al. (2007). One of the key aims here is to develop the software to process a large amount of images (up to 10,000) with simple user inputs. With the built software, the lens-camera optical behavior is characterized whilst the relative uncertainties of various parameters such as the depth-of-field (DoF) dependence on particle diameter, threshold level sensitivity and illumination intensity issues and their effects on measurement accuracy are discussed in the coming sections. Different threshold methods and functions, especially the dual threshold methods (Yule et al., 1978 and Kashdan et al., 2003) and multi-threshold method are compared. The calibration data will be subsequently incorporated into the PDIA processing algorithm and for defocused droplets or particles, enables their true diameter to be estimated by analyzing the droplet

image properties. A detailed conceptual experimental design was introduced in section 4.3.2.

#### 4.4.1 Pixel sensitivity test at focal plane

As stated in section 4.3.1, the small pixel count adversely affects the accuracy of measured small particles. At this stage, we only comment on the images with the resolution of 1280×1024 (default value of the camera). The ratio of the real area among the calibration circles is  $(145)^2 : (110)^2 : (74)^2 : (37)^2 : (18)^2$ , which should be the same in the images. Since the larger particle is less sensitive to the pixel size, the pixel area of 145μm at focal plane is taken as a reference, the differences between the calculated pixel area and the actual pixel area are shown in Figure 4.11 (D: particle diameter;  $D_{145}$ : diameter of the 145μm calibration circle). The circle with the diameter less than 60μm is more sensitive to the pixel sizes. Especially for the 18μm calibration circle, there is a 1.5 times magnification of its actual area. However, these pixel sensitivity effects will be compensated automatically during the calibration process.



*Figure 4.11 The variations of the ratio of the calculated pixel area and the actual pixel area at focal plane based on the 145μm, 110μm, 74μm, 37μm and 18μm calibration circles at focal plane.*

#### 4.4.2 Determination of acceptable depth of field with the dual threshold method

The literature (Yule et al., 1978, Koh et al., 2001, Kashdan et al., 2003) has revealed that there exist numerous definitions of the depth of field (DoF) with dual threshold methods and it is necessary to clarify how this should be interpreted in the present study.

First the variations of characters for some calibration circles with different diameters ( $D$ ) as a function of defocus distances ( $D_F$ ) are presented.

Obviously from Figure 4.1, the larger particle has wider DoF and more magnification with increasing defocus distances. Figure 4.12 shows, by using dual threshold methods (Yule et al., 1978 and Kashdan et al., 2003) for 145 $\mu\text{m}$ , 110 $\mu\text{m}$ , 74 $\mu\text{m}$ , 37 $\mu\text{m}$  and 18 $\mu\text{m}$  calibration circles, how total area ( $A_T$ ) varies with defocus distances ( $D_F$ ) from their in-focused size ( $A_{\text{infocus}}$ ). For instance for the 145 $\mu\text{m}$  calibration circle, it can be magnified up to 2.5 times of that at the focal plane, while only 1.2 times for the 18 $\mu\text{m}$  circle.

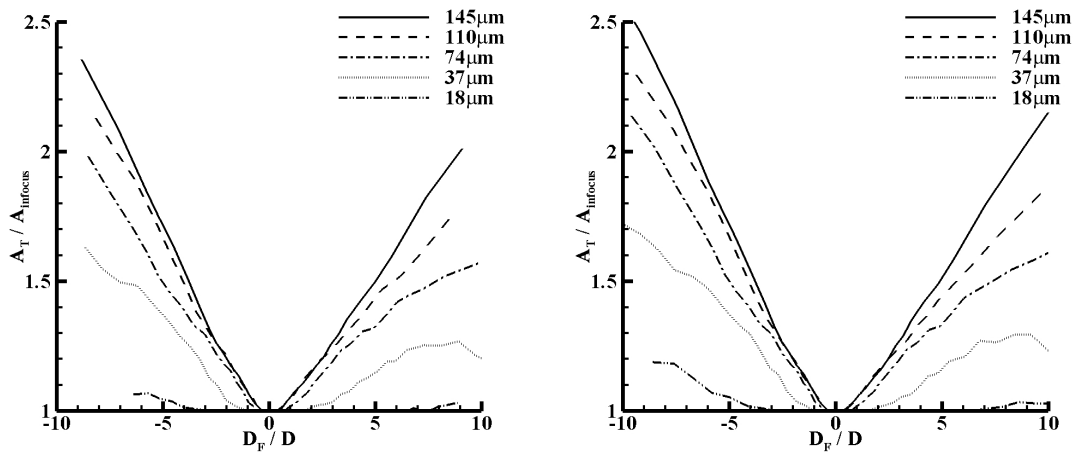


Figure 4.12 Total area variations against the in-focused area at different defocused distances for 145 $\mu\text{m}$ , 110 $\mu\text{m}$ , 74 $\mu\text{m}$ , 37 $\mu\text{m}$  and 18 $\mu\text{m}$  calibration circles by dual threshold methods (left: Yule et al., 1978; right: Kashdan et al., 2003).

In a further study of halo area variation, the ratios between halo area and total area ( $A_H/A_T$ ) at different defocused distances have been plotted in Figure 4.13. At same defocused distance, the ratio generated by the threshold method of Yule (1978) is more than that generated by Kashdan (2003). With the threshold method of Yule (1978) and with increasing the defocus distance,  $A_H/A_T$  increases up to 0.9 for the larger circles ( $D > 18\mu\text{m}$ ) and 0.6 for the one of 18 $\mu\text{m}$ . However, by the method of Kashdan (2003),  $A_H/A_T$  increases only up to 0.8 of the larger circles ( $D > 18\mu\text{m}$ ) and only around 0.4 for the 18 $\mu\text{m}$  one.  $A_H/A_T$  indicates how defocus each particle is from the focal plane and is a significant parameter in real particle sizing. Within the same depth of field, the method of Yule (1978) provides more variations in  $A_H/A_T$  than Kashdan (2003), which generates a

calibration database with a wider dynamic range and hence more accurate subsequent real spray analysis.

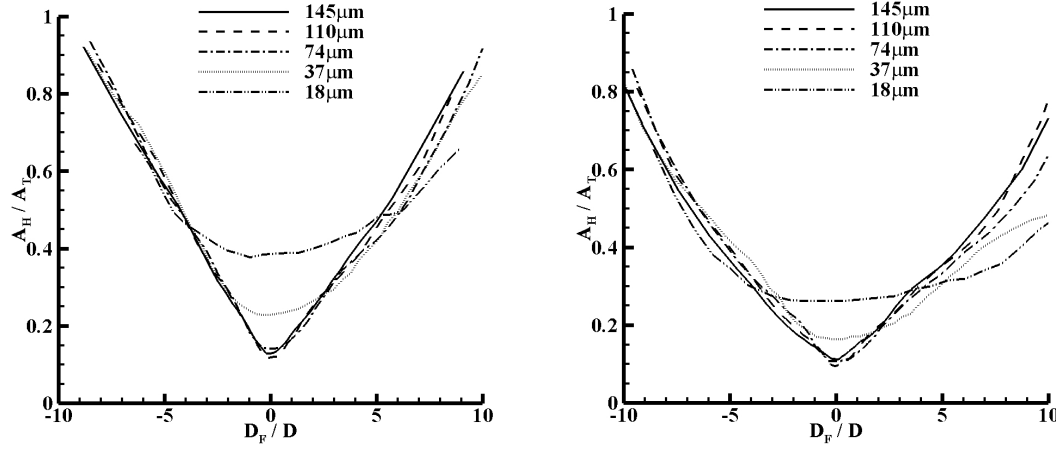


Figure 4.13 Ratio of halo area and total area variations at different defocused distances for 145 $\mu\text{m}$ , 110 $\mu\text{m}$ , 74 $\mu\text{m}$ , 37 $\mu\text{m}$  and 18 $\mu\text{m}$  calibration circles by dual threshold methods (left: Yule et al., 1978; right: Kashdan et al., 2003).

In Kashdan et al. (2003), the acceptable DoF is related to the position where halo area reaches a peak as the function of defocus distances. However, from Figure 4.13, the method of Kashdan (2003) on the determination of the acceptable DoF does not work in this study since there is no peak value in the halo area variation at either side from the focal plane, which is mainly caused by the different set-up of image acquisition system. Therefore, an alternative way is presented here. The particle interior defined in Figure 4.4(a) decreases with increasing defocus distances till it vanishes in the background. The position where the particle interior is minimum is considered as a parameter of acceptable DoF, which is defined as the critical position DoF\*.

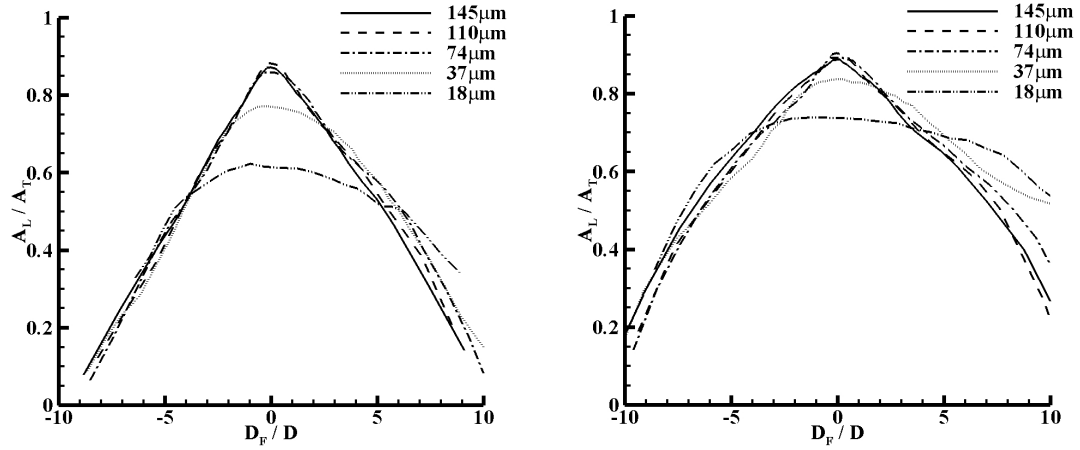


Figure 4.14 Ratio of lower area and total area variation at different defocused distances for 145 $\mu\text{m}$ , 110 $\mu\text{m}$ , 74 $\mu\text{m}$ , 37 $\mu\text{m}$  and 18 $\mu\text{m}$  calibration circles by dual threshold methods (left: Yule et al., 1978; right: Kashdan et al., 2003).

The variations of lower area ( $A_L$ ) as a function of defocus distances for 145 $\mu\text{m}$ , 110 $\mu\text{m}$ , 74 $\mu\text{m}$ , 37 $\mu\text{m}$  and 18 $\mu\text{m}$  calibration circles by dual threshold methods are shown in Figure 4.14.  $A_L/A_T$  decreases continuously with increasing the defocus distance for each calibration circle as expected. The two endpoints of each curve indicate where the particle interior disappears. Therefore, the critical DoF\* should be defined as the position where the lowest  $A_L/A_T$  is. From the figures, DoF\* locates within  $-8 < D_F/D < 8$  with the method of Yule (1978) and  $-10 < D_F/D < 10$  with the method of Kashdan (2003), which indicates DoF\* is a function of diameters ( $D$ ).

It should be noticed that, in Figure 4.12, Figure 4.13 and Figure 4.14, the variations of small particles ( $D=37\mu\text{m}$  and  $18\mu\text{m}$ ) exhibit asymmetry about the focal plane. It is caused by (1) the low resolution for the small particles, which was discussed in section 4.4.1; (2) the reduction of the illumination intensity with increasing the distance between the object and the light source, to which small particles are more sensitive. Changing to a camera with a higher resolution and/or a more powerful light source (so that the light intensity does not decay along the axis) will reduce this measurement error.



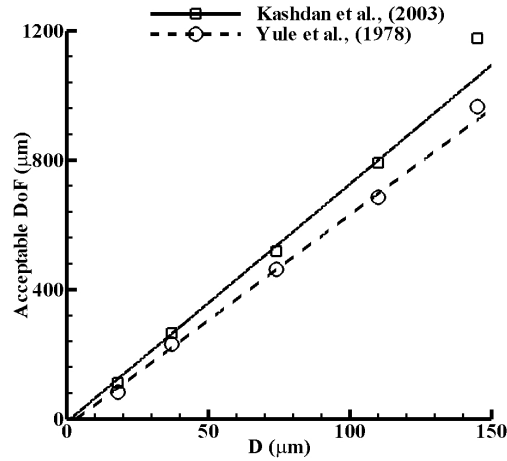


Figure 4.15 Acceptable DoF approximation from  $145\mu\text{m}$ ,  $110\mu\text{m}$ ,  $74\mu\text{m}$ ,  $37\mu\text{m}$  and  $18\mu\text{m}$  calibration circles by dual threshold methods.

Similar to the method of Kashdan (2003), in this study, the acceptable DoF is defined as 70% of the critical position ( $\text{DoF}^*$ ), which is shown in Figure 4.15. It indicates a linear relationship between acceptable DoF and particle sizes for both dual threshold methods. Since the slope of the linear variations of the acceptable DoF determined by the method of Yule (1978) is slightly less than that generated by the method of Kashdan (2003), the method of Yule (1978) requires less weighting of the actual particle diameters measured.

#### 4.4.3 Determination of real particle/droplet characters from the calibration process by dual threshold methods

The aim of the above calibration process is to provide a database in order to analyze the unknown droplet/particle characters from a set of images (e.g. real droplet/particle diameter and its defocus distance from the focal plane). Two main parameters in the determination of real particle/droplet characters are the ratio of halo area and total area ( $A_H/A_T$ ) and the total area ( $A_T$ ) of the particle/droplet.

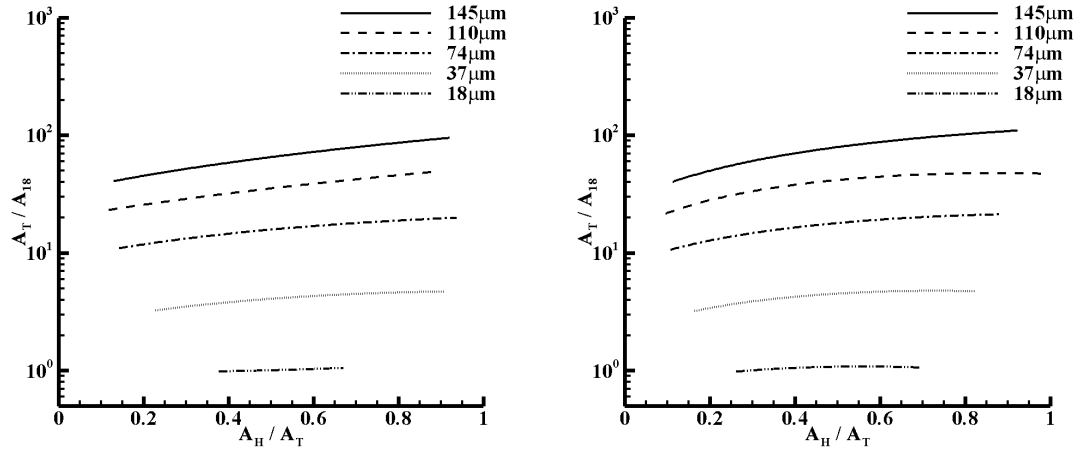


Figure 4.16 Total area variation with the ratio of halo area and total area for 145 $\mu\text{m}$ , 110 $\mu\text{m}$ , 74 $\mu\text{m}$ , 37 $\mu\text{m}$  and 18 $\mu\text{m}$  calibration circles by dual threshold methods (left: Yule *et al.*, 1978; right: Kashdan *et al.*, 2003).

Within the acceptable depth of field as shown in Figure 4.15, the variations of  $A_T$  with  $A_H/A_T$  for 145 $\mu\text{m}$ , 110 $\mu\text{m}$ , 74 $\mu\text{m}$ , 37 $\mu\text{m}$  and 18 $\mu\text{m}$  calibration circles by dual threshold methods are shown in Figure 4.16, where  $A_{18}$  is total pixel area of the 18 $\mu\text{m}$  calibration circle at focal plane. Therefore, for an unknown particle with its  $A_H/A_T$  and  $A_T$  provided, the real diameter (or  $A_{\text{infocus}}$ ) can be easily interpolated from the calibration database. The method of Yule (1978) is better for the larger particles ( $D > 18\mu\text{m}$ ) than the method of Kashdan (2003), as the changes at different defocused positions are more measurable. However, for the small particles ( $D = 18\mu\text{m}$ ), the method of Kashdan (2003) provides wider out of focus degree ( $0.25 < A_H/A_T < 0.7$ ) than the method of Yule (1978) ( $0.35 < A_H/A_T < 0.68$ ), which makes the smaller particles more detectable by the method of Kashdan (2003).

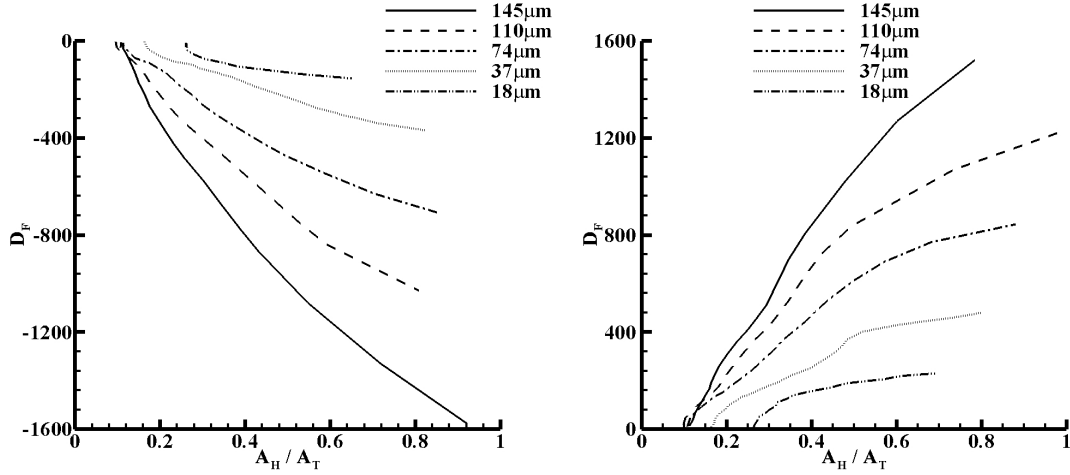


Figure 4.17 Defocus distance variations with the ratio of halo area and total area for 145 $\mu\text{m}$ , 110 $\mu\text{m}$ , 74 $\mu\text{m}$ , 37 $\mu\text{m}$  and 18 $\mu\text{m}$  calibration circles by Kashdan et al. (2003) threshold method.

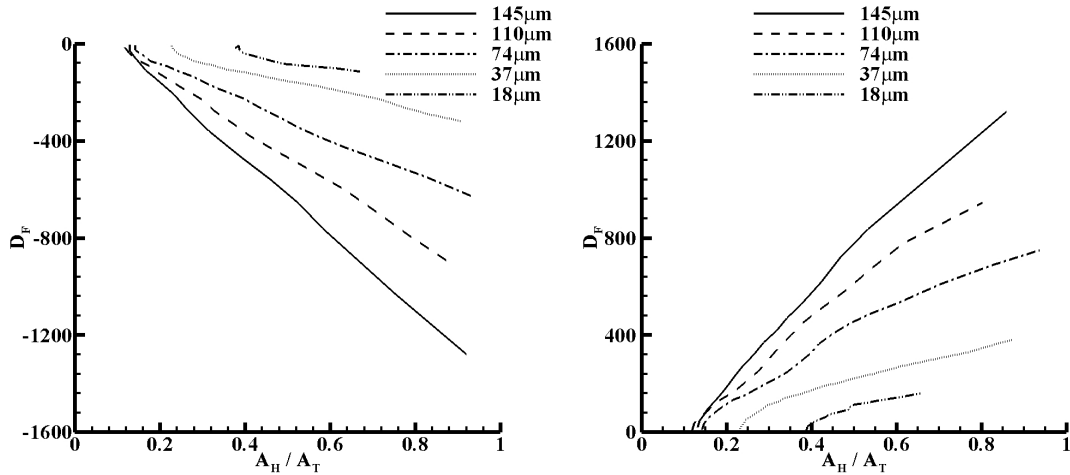


Figure 4.18 Defocus distance variations with the ratio of halo area and total area for 145 $\mu\text{m}$ , 110 $\mu\text{m}$ , 74 $\mu\text{m}$ , 37 $\mu\text{m}$  and 18 $\mu\text{m}$  calibration circles by Yule et al. (1978) threshold method.

Similar to the determination of real diameter for an unknown particle, its defocus distance to the focal plane can be interpolated with its  $A_H/A_T$  provided and real diameter calculated above, by using the defocus distance calibration database shown in Figure 4.17 and 4.18 with dual threshold methods. However, the information is not enough to decide which side of the focal plane the particle locates, since one  $A_H/A_T$  value was found to be

related to only one similar  $A_T$  value at both sides from focal plane, which is not informative to distinguish the side.

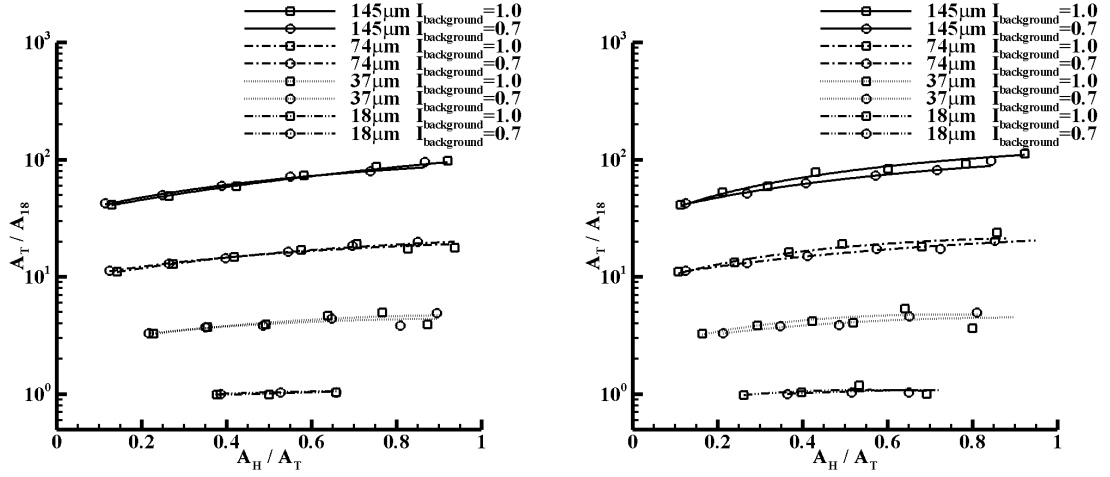


Figure 4.19 Total area variation with the ratio of halo area and total area for 145 $\mu\text{m}$ , 74 $\mu\text{m}$ , 37 $\mu\text{m}$  and 18 $\mu\text{m}$  calibration circles by dual threshold methods at two different illumination intensities (left: Yule et al., 1978; right: Kashdan et al., 2003).

As introduced in section 4.2.2, the background intensity is important for PDIA. Similar to Figure 4.16, Figure 4.19 shows how  $A_T$  varies under two different illumination intensities ( $I_{\text{background}}=0.7$  and 1.0). Background intensities have less influence on  $A_T$  variations by the method of Yule (1987) than the method of Kashdan (2003) for 145 $\mu\text{m}$ , 110 $\mu\text{m}$  and 37 $\mu\text{m}$  calibration circles. However, the method of Kashdan (2003) extended the  $A_H/A_T$  range under higher illumination intensity ( $I_{\text{background}}=1.0$ ). Especially for the 18 $\mu\text{m}$  calibration circle, it increased the range from 0.36~0.68 to 0.25~0.68, which makes the circle more detectable at near focal plane.

#### Discussion: Dual threshold methods

It is difficult to tell from this calibration experiment which dual threshold method is better. The method of Kashdan (2003) has more possibility for detecting wider range ( $0.25 < A_H/A_T < 0.7$ ) of defocused particles. However, the method of Yule (1978) provides less changes of the depth of field for each particle size and less sensitive to the background intensity variations, which gives more similar probability for detecting different size particles within the field of view. No matter which method is used, the real application must employ the calibration function produced from the same threshold method. Although the dual threshold method is robust and simple to be implemented in

commercial software, it still requires correct coefficients chosen in equation (4.1)~(4.4) for each application. It should be noticed that the method of Yule (1978) will be used to compare with the performance of the multi-threshold method in the following content. As stated in section 4.2.2, excessively defocused particles cannot be analyzed by dual threshold methods. Therefore, the multi-threshold method is introduced in section 4.4.4 and section 4.4.5, which is a general threshold methodology and is capable in most particle/droplet analysis application without any requirement to define the coefficients required for dual threshold methods.

#### **4.4.4 Determination of acceptable depth of field with the multi-threshold method**

Different from the dual threshold methods, the multi-threshold method generates an area variation curve against each threshold level for the particle at a certain defocused position from the focal plane. Compared to only two area values provided by the dual threshold methods for detecting one particle, the multi-threshold method generates much more information which gives more possibilities to accurately analyze particle characteristics.

Figure 4.20 shows the variations against each intensity threshold for 225 $\mu\text{m}$ , 180 $\mu\text{m}$ , 110 $\mu\text{m}$ , 74 $\mu\text{m}$ , 37 $\mu\text{m}$  and 18 $\mu\text{m}$  calibration circles from the focal plane to the defocused position of  $D_F/D=1, 2, 3, 4$  and 5 ( $D_F$ : defocused distance;  $D$ : circle diameter). For the large in-focus circles (e.g. the one with diameter of 110 $\mu\text{m}$  or 225 $\mu\text{m}$ ), the variation grows rapidly at the beginning of intensity increase from 0.1 to 0.2 and slows down from 0.4 to the end. However, for the in-focus circle of  $D=18\mu\text{m}$ , it approaches linear variation.

There is a little change in the variation curves at different defocused distance for the small circles ( $D=18\mu\text{m}$  and 37 $\mu\text{m}$ ). Especially for the 18 $\mu\text{m}$  circle, it is very difficult to find  $D_F$  accurately. However, for the  $D=110\mu\text{m}$  and 225 $\mu\text{m}$  circles, it shows that the variation curves change from convex to linear and to concave with increasing the defocused distance. This ‘shape’ information can be exploited to estimated particle size and axial defocused position.

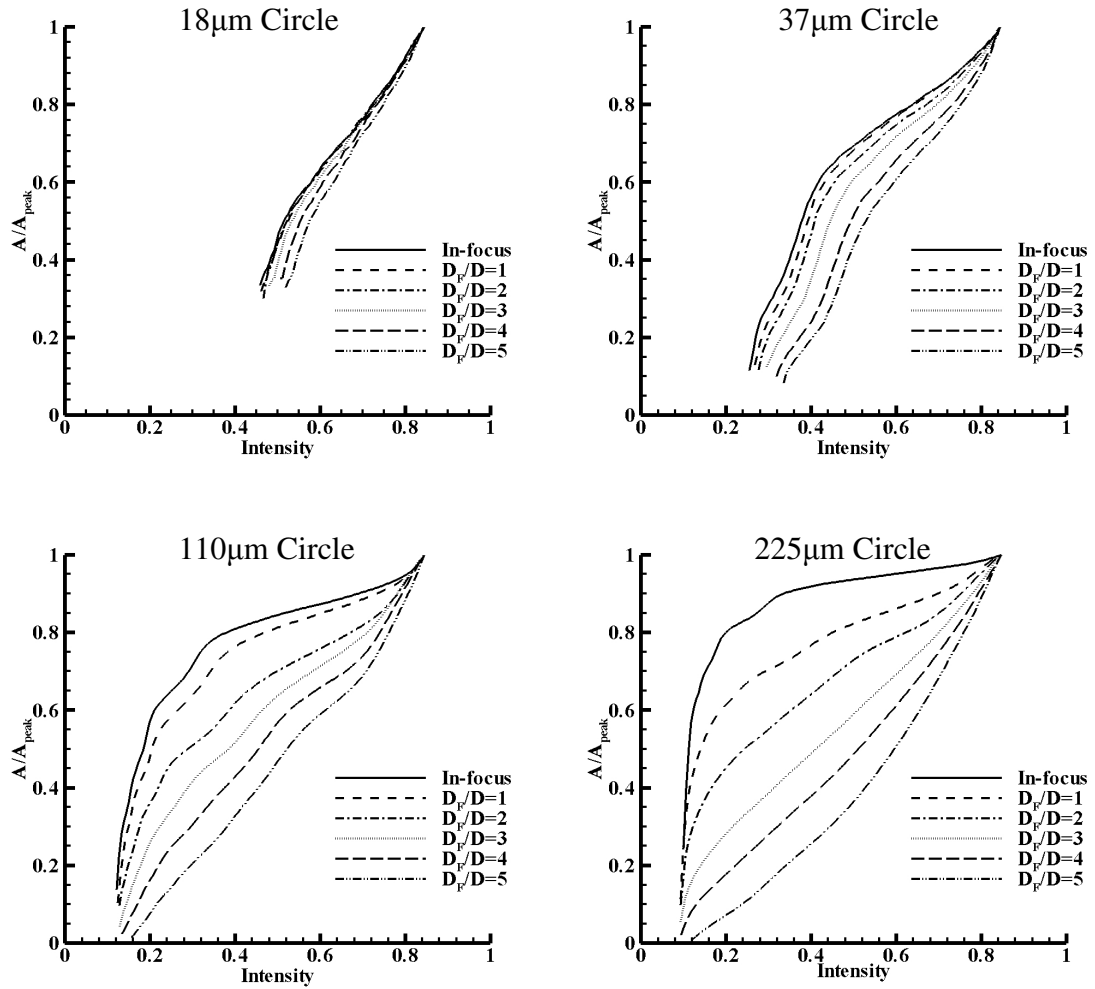


Figure 4.20 Area variations against each intensity threshold for 225 $\mu\text{m}$ , 110 $\mu\text{m}$ , 37 $\mu\text{m}$  and 18 $\mu\text{m}$  calibration circles at different defocused position.

Figure 4.21 shows area variations with increasing intensity thresholds for the 110 $\mu\text{m}$  calibration circle at different defocused position. From the figure, DoF\* locates within  $-15 < D_F/D < 15$  for the 110 $\mu\text{m}$  calibration circle with multi-threshold method. Each calibration circle ( $D=270\mu\text{m}$ , 225 $\mu\text{m}$ , 145 $\mu\text{m}$ , 74 $\mu\text{m}$ , 37 $\mu\text{m}$  and 18 $\mu\text{m}$ ) has similar data points as 110 $\mu\text{m}$  circle, from which it generates the database for measuring real particle/droplet sizes and defocused position from the focal plane.

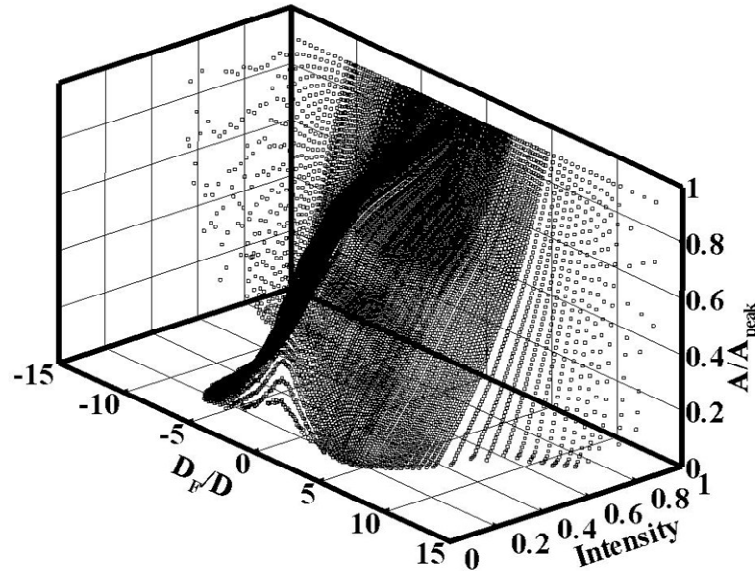


Figure 4.21 Area variations against each intensity threshold for the 110 $\mu$ m calibration circle at different defocused position.

Similar to the dual threshold method, the acceptable DoF is defined as 70% of the critical position ( $DoF^*$ ) in multi-threshold method. It also generates a linear approach to the acceptable depth of field against particle sizes, shown in Figure 4.22. Most importantly it increases the DoF for the small particle size ( $D < 50\mu$ m) up to 1.5 times than that measured by dual threshold methods (Figure 4.15).

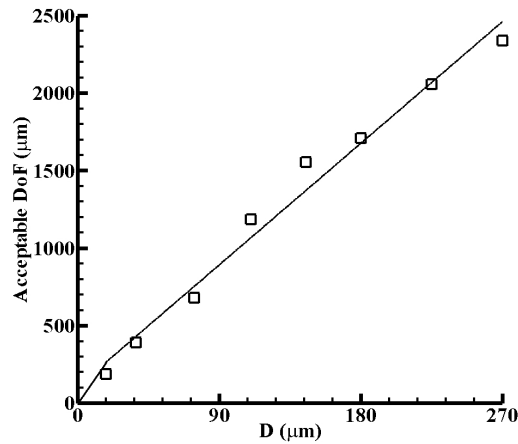


Figure 4.22 Acceptable DoF approximation from 270 $\mu$ m, 225 $\mu$ m, 180 $\mu$ m, 145 $\mu$ m, 110 $\mu$ m, 74 $\mu$ m, 37 $\mu$ m and 18 $\mu$ m calibration circles by multi-threshold methods.

#### 4.4.5 Determination of real particle/droplet characters from the calibration process by multi-threshold methods

The dual threshold methods use  $A_H/A_T$  as a parameter to measure the particle defocused degree. The multi-threshold method takes the curve 'shape' as a defocused degree parameter. Following the PDIA flow chart of Figure 4.6, for a random particle detected from real world like the one shown in Figure 4.4, a curve of  $A/A_{\text{peak}}$  versus intensity (like the one in Figure 4.20) is generated by multi-threshold method and compared to all the curves from the calibration database like the ones shown in Figure 4.21 to find the closest 'shape' in each size group of the calibration circles. (Four different curve matching methods will be compared in section 4.4.6). Of course, both the curve of the interested particle and the curves with the similar shape from the calibration database have the information on variations of area (or pixel) versus intensity (each threshold), where at the same intensity, the larger the particle is, the larger area (or pixel) the particle (or the calibration circle) has corresponding to that threshold. At each intensity, the particle size can be interpolated from calibration circles with known sizes (from the database), which is the same procedure as the dual threshold method. Then the real particle size is determined as an average of the calculated values at all available intensities (thresholds).

#### 4.4.6 Comparisons of curve matching methods

Several curve matching parameters were reviewed by Efrat et al. (2007) and include Fréchet distance, discrete Dynamic Time Warping (DTW) and continuous Dynamic Time Warping. The Fréchet distance is defined as the maximum 'leash length' over the parameter between two curves (Alt et al., 1995; Buchin et al., 2006). The maximum value can usually cause an error, where a small change from the input can misrepresent the parameter. A sum- or average- based process can smooth such distortions, which is named the Dynamic Time Warping method. As cited in Efrat et al. (2007), discrete DTW is widely used in speech signal recognition (Rath and Manmatha, 2002), signature tracking (Munich and Perona, 2003) and for multivariate time series (Rath and Manmatha, 2002). Continuous DTW is introduced by Serra and Berthod (1994) to match sub-pixel contours, and it is explored by Munich and Perona (1999) to measure the similarity of signatures.



Figure 4.23 (Efrat et al., 2007;  $d$  (pixels): the warping distance of the comparison) shows the comparison of the discrete DTW and the continuous DTW methods. Discrete DTW is defined over a sequence of points, while the continuous DTW method samples the input curves before computing the warping distance. Note that the discrete DTW can lead to dramatically different results due to the sampling while the continuous DTW is not significantly affected by the sampling.

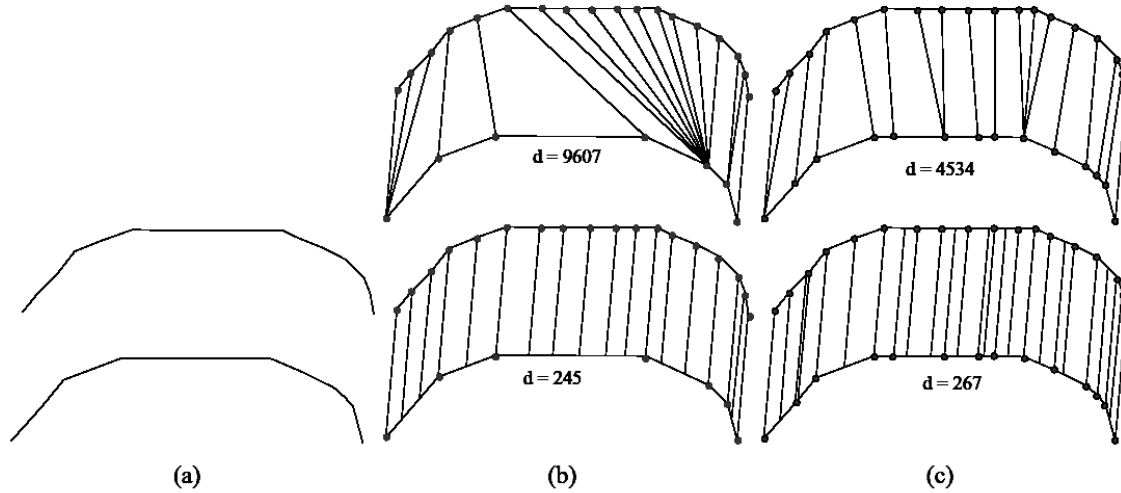


Figure 4.23 Compare two curves by the discrete DTW (top) and compare the same curves by continuous DTW (bottom). (a) shows two curves with a little difference. (b) and (c) illustrate the comparison results with two different samplings of the curves. ( $d$ : the warping distance of the comparison).

Four curve matching methods (Fréchet distance, discrete DTW, continuous DTW and standard deviation method) were tested for two glass spheres of diameter  $4.5\mu\text{m}$  and  $88\mu\text{m}$  at different defocused position, where STD is the standard deviation method. Standard deviation method (STM) finds the curve with the minimum standard deviations (STD) between two curves. The errors generated by each method are based on the differences between the calculated particle diameter by PDIA and the real diameter, which are illustrated in Figure 4.24. Continuous DTW generated the least error especially for the smaller particle ( $D=4.5\mu\text{m}$ ), while the other methods work similarly for the larger particle ( $D=88\mu\text{m}$ ). Therefore an average- based continuous DTW method is implemented in this study, which is to find the curve with the minimum averaged-warping distance ( $d$ ) of the comparison to the target curve.

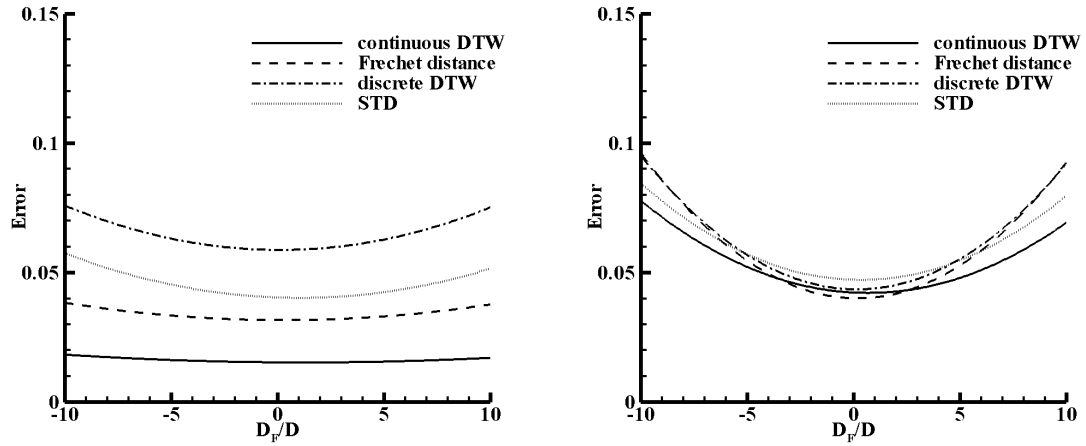


Figure 4.24 Error generated by each curve matching method for the particle diameter of  $4.5\mu\text{m}$  (left) and  $88\mu\text{m}$ (right) at different defocused position.

#### 4.4.7 Analysis on the aspect ratio and sphericity of the calibration circles

The aspect ratio of each particle image profile was defined to be the maximum chord divided by the maximum width normal to the chord. This is consistent with the definitions of aspect ratio for ellipses (maximum diameter divided by minimum diameter). Sphericity ( $S$ ) is defined as the perimeter ( $P$ ) divided by the circumference of a circle with the same area ( $A$ ), calculated by equation (4.6).

$$S = \frac{P}{2\sqrt{\pi A}} \quad (4.6)$$

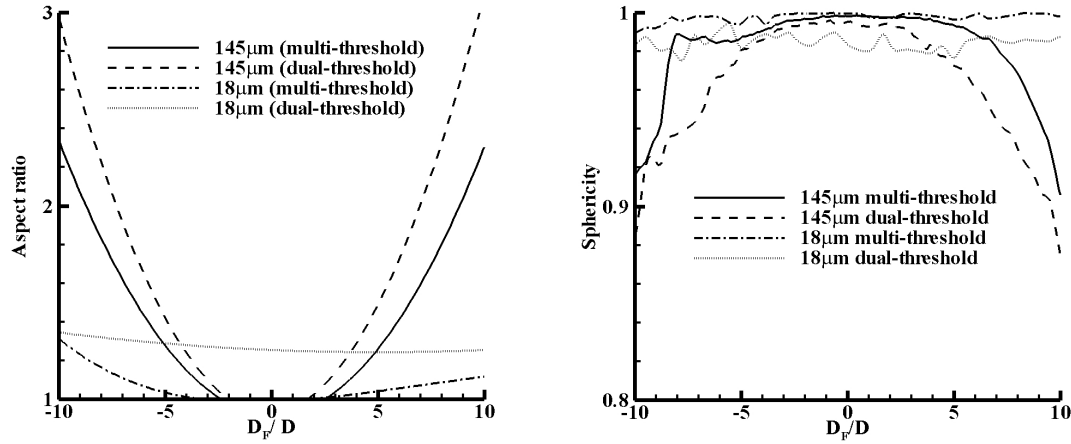


Figure 4.25 Aspect ratio (left) and sphericity (right) variations at different defocused distances for 145μm and 18μm calibration circles by the dual threshold method of Yule (1978) and the multi-threshold method.

The multi-threshold method defines the aspect ratio (or sphericity) of a particle as a mean of the aspect ratios (or sphericities) of the detected shapes at each threshold. Figure 4.25 shows how the aspect ratios and sphericities vary at different defocused distances for the calibration circles by the dual threshold method of Yule (1978) and the multi-threshold method. The calculated aspect ratio of the large circle ( $D=145\mu\text{m}$ ) went up to 2 at  $D_F/D=\pm 8$  by the multi-threshold method, while it reached 2 at closer defocused distance of  $D_F/D=\pm 7$  by the dual threshold method. The dual threshold method over-predicted the aspect ratio of the small circle ( $D=18\mu\text{m}$ ) as a mean of 1.3 even at the focal plane, whereas the multi-threshold method produced a better approach for the small circle. Shape variations of the sphericities of the large circle ( $D=145\mu\text{m}$ ) were detected out of the range of  $-8 < D_F/D < 8$  by the multi-threshold method and out of the range of  $-5 < D_F/D < 5$  by the dual threshold method. The dual threshold method under-predicted the sphericities of the small circle ( $D=18\mu\text{m}$ ) as a mean of 0.98 even at the plane of focus. The deviations of the aspect ratios and sphericity are caused by the blur around the particle edges due to the non-uniformity of the diffused laser light, and with increasing defocused distance the non-uniformity effects enhance the errors due to the wide illumination area of the diffused and slightly non-uniform laser light.

***Discussion: Multi-threshold method***

Compared to the dual threshold methods, the multi-threshold method increases the acceptable DoF from  $-7 < D_F/D < 7$  to  $-10.5 < D_F/D < 10.5$ . It makes the smaller particle ( $D < 18\mu\text{m}$ ) more detectable. However, aspect ratios and sphericities of the particles provide another criterion in the determination of particle sizes accurately. The multi-threshold method allows the reasonable measurement of aspect ratios and sphericities within  $-8 < D_F/D < 8$  for the large circle ( $D = 145\mu\text{m}$ ) and  $-10 < D_F/D < 10$  for the small circle ( $D = 18\mu\text{m}$ ). Whereas the dual threshold method can only process them for the large circle ( $D = 145\mu\text{m}$ ) within a narrower DoF of  $-5 < D_F/D < 5$  accurately and process them with notable errors for the small circle ( $D = 18\mu\text{m}$ ). It provides a possibility to reduce the variations of the DoF due to the particle size groups in the PDIA, which makes the large particles be measured within smaller DoF and vice versa. In general, the circles with diameter of  $18\mu\text{m} \sim 450\mu\text{m}$  has been calibrated from the above procedure using Patterson globes and circles, within the  $2.00\text{mm} \times 1.60\text{mm}$  field of view. In order to test the applicability and the accuracy of the multi-threshold, glass spheres were analyzed with PDIA system and comparisons are made to the results of the dual threshold method of Yule (1978) and PDA in section 4.5.

#### 4.4.8 Overlapping particles

The PDIA system separates overlapping circular particles using the sphericity to reconstitute the form of a particle, provided that the particles are essentially circular.

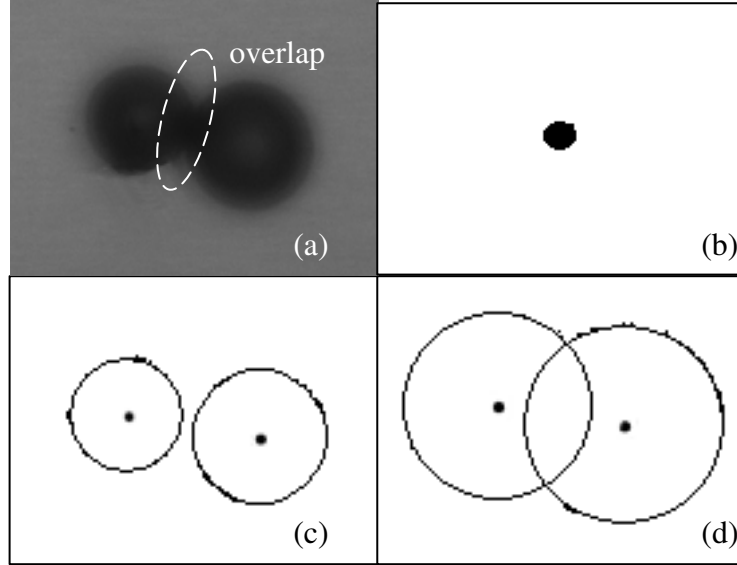


Figure 4.26 Process of the overlapping circular particles by step: (a): original image; (b): image after the 22<sup>nd</sup> threshold; (c): image after the 56<sup>th</sup> threshold; (d): image after the 97<sup>th</sup> threshold).

Figure 4.26 shows the procedure how the multi-threshold method deals with overlapping particles. The background intensity of the image is 0.427, 109 thresholds were used to generate particle information for each threshold. At the lower intensity threshold such as the 22<sup>nd</sup> threshold, only the overlap part of the two particles can be detected as a black spot shown in Figure 4.26(b). This overlapping part will be deleted at a lower intensity threshold and will be compensated in the following threshold procedure. At middle intensity threshold (e.g. 56<sup>th</sup> threshold as shown in Figure 4.26(c)), two individual particles can be detected and their area information is recorded with the corresponding threshold. At higher intensity threshold (e.g. 97<sup>th</sup> threshold as shown in Figure 4.26(d)), two overlapping particles can be separated according to their sphericities and their fully circular areas are recorded. Therefore, the intersecting area will be counted twice at higher intensity threshold for two overlapping particle.

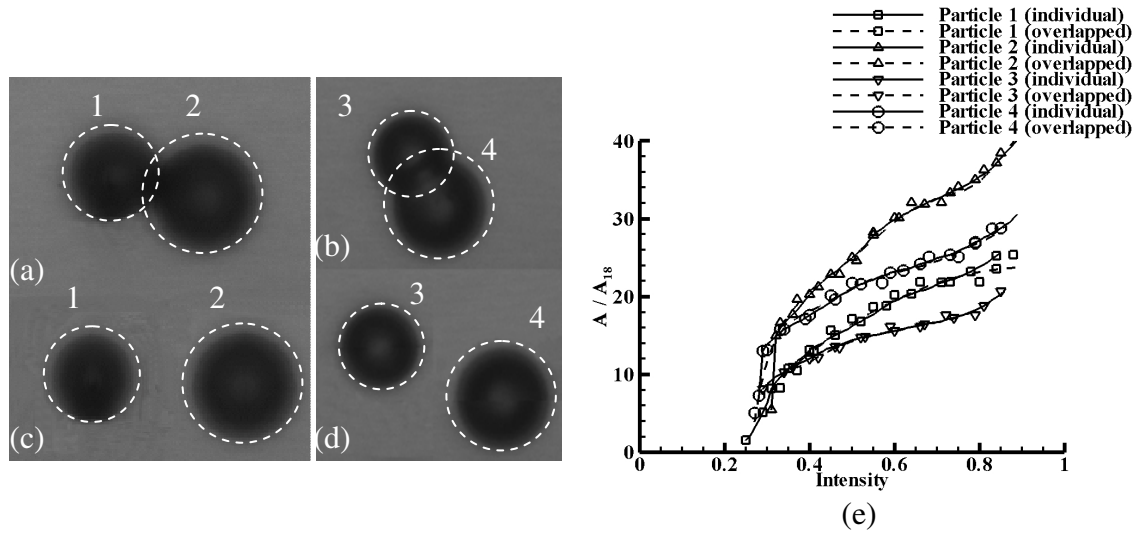


Figure 4.27 (a) shows the particle 1 and 2 with small overlapping fraction; (b) shows the particle 3 and 4 with large overlapping fraction; (c) and (d) show the separated particles from (a) and (b).

Two tests were undertaken to find how accurately the PDIA dealt with overlapping particles: to compare the PDIA results of the overlapping particles and the separated particles. As shown in Figure 4.27, two sets of particles with different overlapping fractions are analyzed. There is less overlapping area fraction of particle 1 and 2 (Figure 4.27(a)) than that of particle 3 and 4 (Figure 4.27(b)). The individual particles (Figure 4.27(c) and Figure 4.27(d)) are created by separating the overlapping particles from Figure 4.27(a) and Figure 4.27(b) and the overlapping parts are compensated by their symmetrically non-overlapping parts.

Figure 4.27(e) shows the PDIA results of the overlapping particles and individual particles by the multi-threshold method. For the particle 1, 2 and 3, the comparison indicates little changes between the results of PDIA in overlapping particles and the original individual particles. There is a mean error of  $1.86\% \pm 0.2\%$  between the calculated diameters of the overlapping particles and the original individual particles. The deviation is due to its non-symmetry and the error due to the compensation procedure of the overlapping part. The comparison indicates that PDIA is capable of analyzing the overlapping particles reasonably.

## 4.5 Glass sphere measurements

### 4.5.1 Measurement

In order to test the applicability and the accuracy of the PDIA system, three sets of glass spheres with different diameter groups (1 $\mu$ m~50 $\mu$ m, 70 $\mu$ m~110 $\mu$ m and 100 $\mu$ m~200 $\mu$ m) were analyzed by the PDIA. The exposure time,  $t_{\text{exp}}$  is usually defined as the time required for a particle to move a small fraction of its own diameter (Chigier, 1991) by equation (4.7),

$$t_{\text{exp}} < \frac{K_E D_{\min}}{u_p} \quad (4.7)$$

where  $K_E$  is a constant with a value of 0.1 (Chigier, 1991),  $D_{\min}$  is the diameter of the smallest particle to be measured, and  $u_p$  is the particle velocity. Thus for 100 $\mu$ m particle travels with a velocity of 10m/s, an exposure time of 1 $\mu$ sec is required, however, for a 5 $\mu$ m particle travels with a velocity of 20m/s, an exposure time of 25ns is required.

Glass spheres were dispersed by the stirrer in the transparent water tank at a mean particle absolute velocity of 0.1m/s, particle images were taken with 2 $\mu$ s of the camera exposure time and 1 $\mu$ s of the laser pulse duration. For the sake of finding what enhancement the multi-threshold method provides, the performance is compared to the dual threshold method in analyzing the glass spheres with diameter of 70 $\mu$ m~110 $\mu$ m and 100 $\mu$ m~200 $\mu$ m. Similarly, in order to find whether the PDIA system is applicable in sizing the pharmaceutical aerosols with mass median diameter (MMD) of 2 $\mu$ m~5 $\mu$ m, the glass spheres with diameter of 1 $\mu$ m~50 $\mu$ m were analyzed based on the calibration with the NPL Reference Stage (3 $\mu$ m~48 $\mu$ m) and Patterson Globes and Circles (18 $\mu$ m~270 $\mu$ m). Furthermore, the effect of motion of the glass spheres in PDIA is also studied.

### 4.5.2 Glass sphere results analysis

#### *Analysis of 70 $\mu$ m~110 $\mu$ m and 100 $\mu$ m~200 $\mu$ m glass spheres*

70 $\mu$ m~110 $\mu$ m and 100 $\mu$ m~200 $\mu$ m moving glass spheres are analyzed by the dual threshold method of Yule (1978) and the multi-threshold method. The number based distribution analyzed from 1000 particle images are compared with the PDA data of Danby (2010) and shown in Figure 4.28. For the 70 $\mu$ m~110 $\mu$ m glass spheres, the plot of the number frequency of the particles with sphericities ( $S$ ) larger than 0.97 have the best

approach to the PDA results. It proves that PDA removes non-spherical particles during the process. However, the peak particle number frequency of the 70 $\mu\text{m}$ ~110 $\mu\text{m}$  glass spheres generated by dual threshold method is 0.24 at the particle diameter of 70 $\mu\text{m}$ , which is clearly different from the results of the other two methods. Similarly, for the 100 $\mu\text{m}$ ~200 $\mu\text{m}$  glass spheres, the outcome of the dual threshold method differs much from the results of the other two methods. Furthermore, as shown in Figure 4.29, the multi-threshold method produced closer results on the volume based distributions to the results of PDA than the dual threshold results method of Yule (1978). The significant deviations of the results of the dual threshold method from those of multi-threshold and PDA are due to the insufficient particles detected by the dual threshold method in 1000 images. The multi-threshold method found 1978 and 890 particles among the 70 $\mu\text{m}$ ~110 $\mu\text{m}$  and 100 $\mu\text{m}$ ~200 $\mu\text{m}$  glass spheres respectively, while the dual threshold method only detected 345 and 99 particle (on average) for each glass sphere group. Compared to the particle numbers found by the multi-threshold method (1045 for the 70 $\mu\text{m}$ ~110 $\mu\text{m}$  glass spheres and 406 for the 100 $\mu\text{m}$ ~200 $\mu\text{m}$  glass spheres) with the sphericities larger than 0.97, the dual threshold method can only detect 71 and 7 among the 70 $\mu\text{m}$ ~110 $\mu\text{m}$  and 100 $\mu\text{m}$ ~200 $\mu\text{m}$  glass spheres respectively, which is not sufficient to generate statistics. As described in section 4.2.2, extremely defocused particles are not detectable by the dual threshold method, and this is fundamental to the method. In addition, dual threshold method will lose particles at darker background due to the coefficients of equation (4.3)~(4.4). For instance, at background intensity of 0.5, the higher and lower thresholds are 0.4 and 0.3 calculated from equation (4.3) and equation (4.4), which barely detects particles with corresponding grayscales.



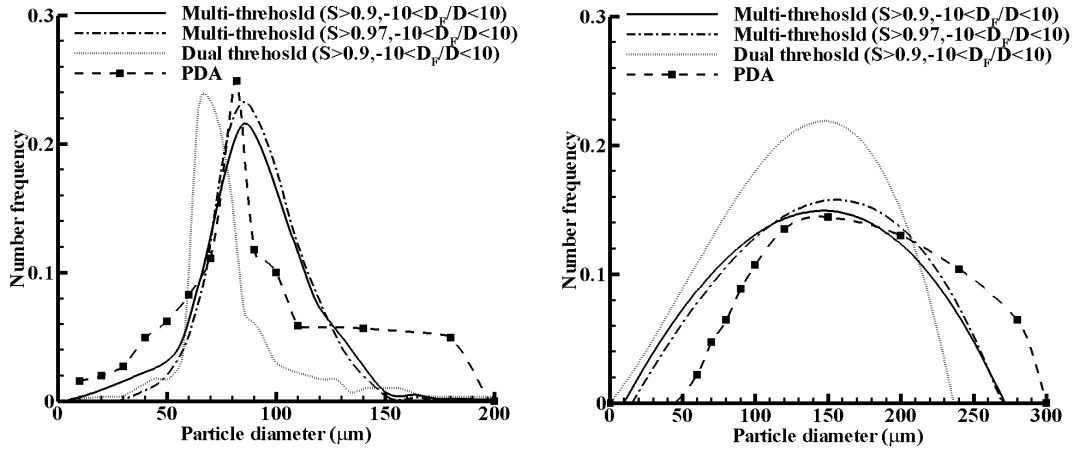


Figure 4.28 Comparison of number-based distributions of 70~110 $\mu\text{m}$  (left) and 100~200 $\mu\text{m}$  (right) glass spheres by PDA (Danby, 2010), dual threshold method (Yule et al., 1978) and multi-threshold method.

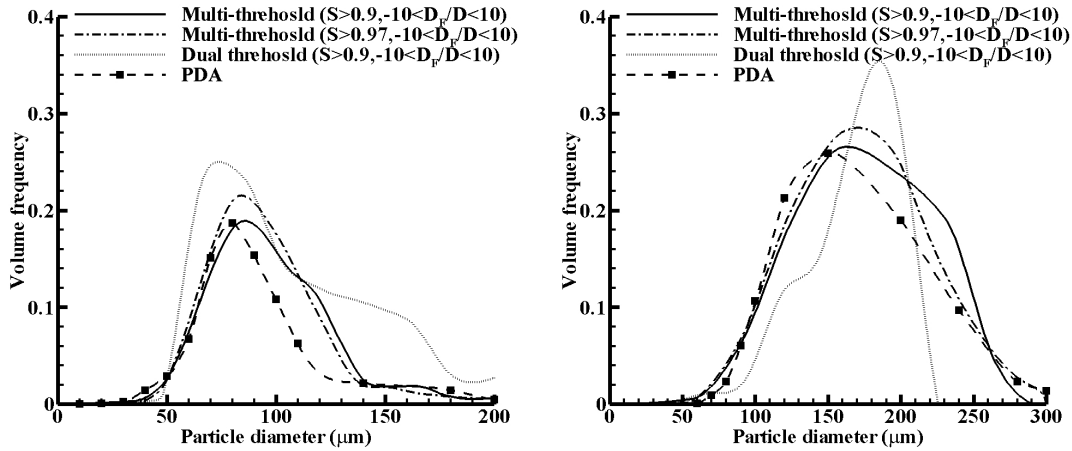


Figure 4.29 Comparison of volume-based distributions of 70~110 $\mu\text{m}$  (left) and 100~200 $\mu\text{m}$  (right) glass spheres by PDA (Danby, 2010), dual threshold method (Yule et al., 1978) and multi-threshold method.

#### Analysis of 1 $\mu\text{m}$ ~50 $\mu\text{m}$ glass spheres

The dual threshold methods (Yule et al., 1978 and Kashdan et al., 2003) cannot detect the 1 $\mu\text{m}$ ~50 $\mu\text{m}$  glass spheres for this experimental setup, because the gap they defined between two thresholds is too large to detect the particle interior, hence we will not comment on the dual threshold methods here. The number-based and volume-based distributions of 1 $\mu\text{m}$ ~50 $\mu\text{m}$  glass spheres acquired by the multi-threshold method are

compared with the data generated by laser diffraction and microscopy (Stevens, 2006) as shown in Figure 4.30, where the results of multi-threshold method are based on 14,150 particles detected. Stevens (2006) took the photos by digital camera fitted with a microscopic lens and around 10,000 in-focused and quiescent particles were measured. With laser diffraction method, glass spheres were poured through the laser beam over 60 repeats and the distribution shown was produced by the RTSizer software (Stevens, 2006). Although it is more sensitive to the smaller particles ( $D=5\sim 10\mu\text{m}$ ) than that from microscopy, the multi-threshold method produces a good approach to the data generated by the laser diffraction (Stevens, 2006) in both of the number-based and volume-based distributions. It proves the multi-threshold method is applicable in sizing small particle with the diameter of  $1\mu\text{m}\sim 50\mu\text{m}$ , although it may be unable to measure the particles of a diameter smaller than  $3\mu\text{m}$  due to the calibration graticule limitations.

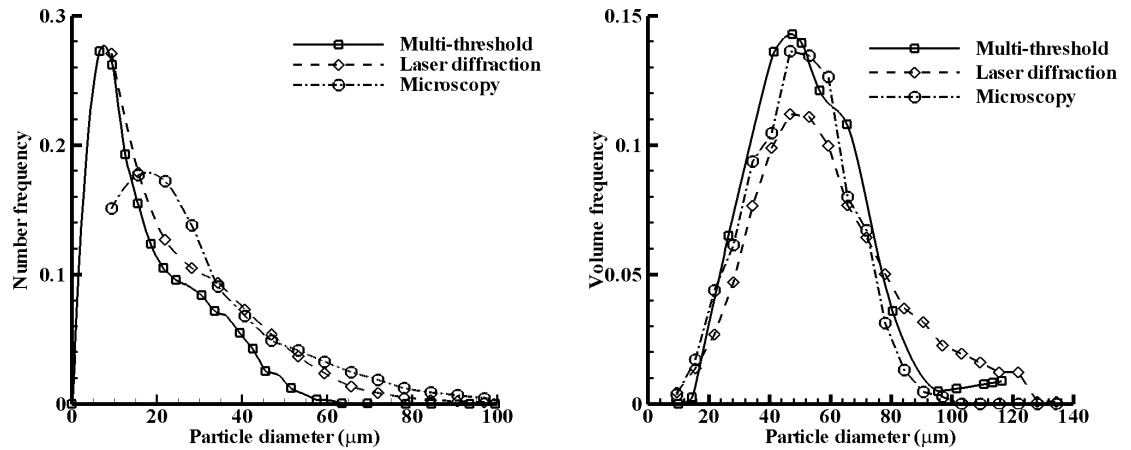


Figure 4.30 Comparison of the number-based (left) and volume based (right) distributions of the  $1\mu\text{m}\sim 50\mu\text{m}$  glass spheres produced by the multi-threshold method with the data generated by laser diffraction and microscopy (Stevens, 2006).

#### ***Effect of motion on glass sphere analysis***

In order to find whether the motion of a particle affects its aspect ratio, two moving glass spheres and two quiescent glass spheres (Figure 4.31(a)) with same diameter ( $D=92\mu\text{m}$ ) were analyzed. The moving defocused glass spheres were obtained from the images of the dispersed  $70\mu\text{m}\sim 110\mu\text{m}$  glass spheres by the stirrer at a mean particle absolute velocity of  $0.1\text{m/s}$ . The moving glass sphere 1 and quiescent glass sphere 3 are at  $D_F/D=4.13$ , while the moving glass sphere 2 and quiescent glass sphere 4 are at

$D_F/D=0.75$ . Figure 4.31(b) and Figure 4.31(c) show the deviations of the aspect ratios and sphericities acquired by the multi-threshold method at each threshold for the glass spheres. The aspect ratios and sphericities of the defocused moving glass spheres vary much more from the mean aspect ratio than those of the near focused and the quiescent glass spheres. The light reflection and refraction from the moving glass spheres caused asymmetry imaging of the defocused particles, and it leads to the differences of the results between the two different states of the glass spheres, which does not greatly influence the results of the near focused or the quiescent particles.

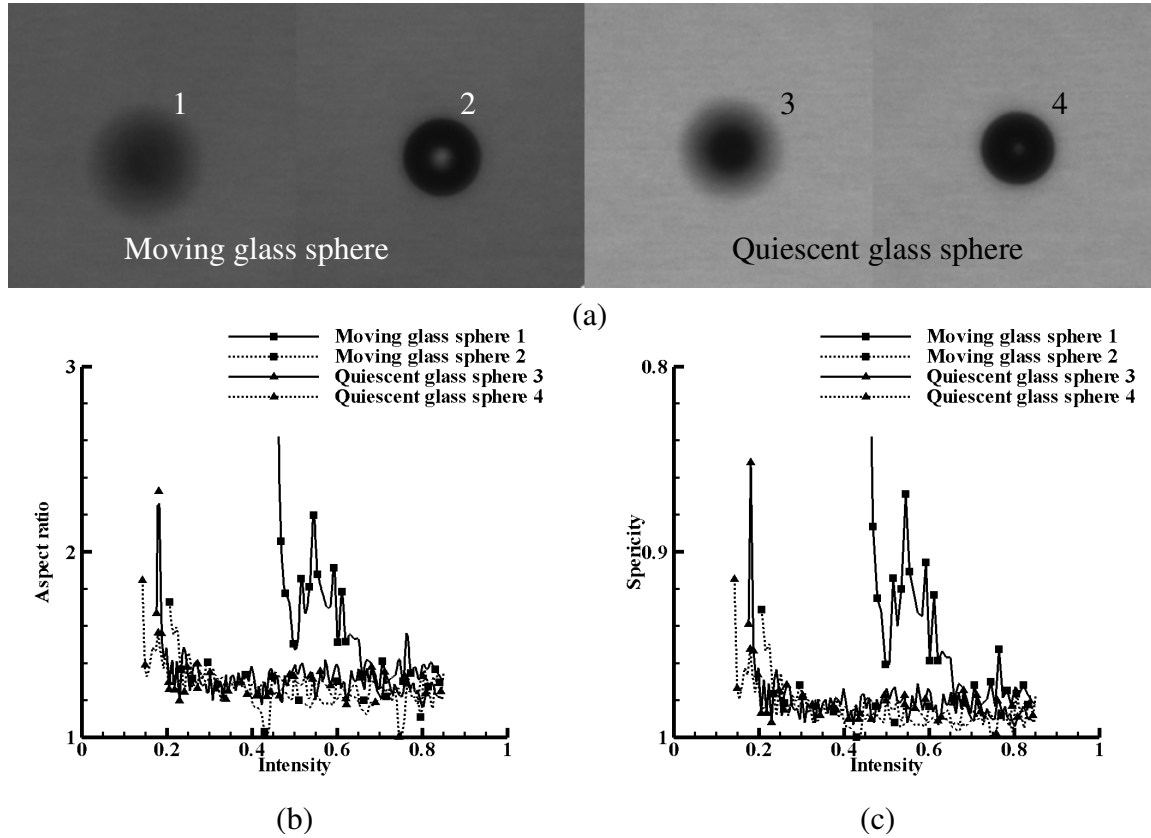


Figure 4.31 (a): images of the moving glass spheres and the quiescent glass spheres at different defocused distancess ( $D_F/D=4.13$  for sphere 1 and 3;  $D_F/D=0.75$  for sphere 2 and 4). (b) and (c): the aspect ratios and the sphericities of the moving glass spheres 1 to 4 of Figure 4.31a at each threshold.

Figure 4.32 shows the comparisons of the aspect ratios and sphericities acquired by the dual threshold method of Yule (1978) and the multi-threshold method for the  $70\mu\text{m}\sim 110\mu\text{m}$  and  $100\mu\text{m}\sim 200\mu\text{m}$  glass spheres. The multi-threshold method produces a more reasonable measurement since the peak of the aspect ratios (and sphericities)

approach 1. The dual threshold method over-predicted the aspect ratios since the peak frequency is generated at the aspect ratio of 2 and it under-predicted the peak sphericity to 0.97 of the 70 $\mu\text{m}$ ~110 $\mu\text{m}$  glass spheres and 0.95 of the 100 $\mu\text{m}$ ~200 $\mu\text{m}$  glass spheres. Because only two thresholds are implemented for the dual threshold method, the aspect ratios of moving particles are susceptible to error.

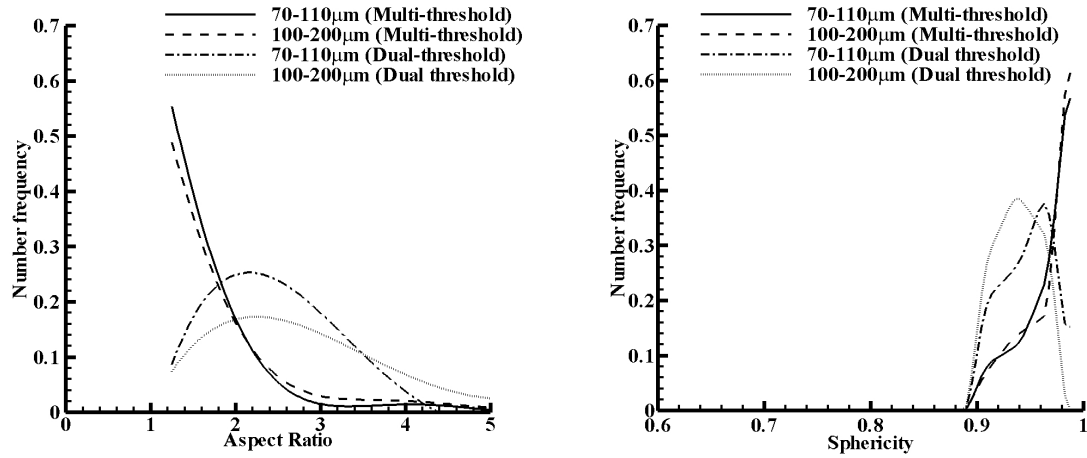


Figure 4.32 Comparisons of the aspect ratios (left) and sphericities (right) acquired by the dual threshold method of Yule (1978) and the multi-threshold method for the 70 $\mu\text{m}$ ~110 $\mu\text{m}$  and 100 $\mu\text{m}$ ~200 $\mu\text{m}$  glass spheres.

## 4.6 Chapter Summary

A newly developed multi-threshold algorithm has been successfully implemented in an automatic particle/droplet image analysis (PDIA) system. It is able to process a large amount of images with simple user inputs, from which the information on particle halo area, total area and distance from plane of focus can be obtained. The variations of halo area and total area for 270 $\mu\text{m}$ , 225 $\mu\text{m}$ , 145 $\mu\text{m}$ , 110 $\mu\text{m}$ , 74 $\mu\text{m}$ , 37 $\mu\text{m}$  and 18 $\mu\text{m}$  calibration circles have been studied with existing dual threshold methods and the new multi-threshold method, from which acceptable depth of field for each particle size has been defined, and acceptable DoF varies linearly with the particle size. The multi-threshold method increases the depth of field (DOF) for small particles ( $D < 50\mu\text{m}$ ). Accurate determination of the aspect ratios and sphericities of the calibration circles provides another criterion in PDIA, which can reduce the DoF variations of different particle size groups. Determination of real particle/droplet characters from the calibration

data has been implemented into PDIA, which has been tested with moving glass spheres. During the analysis of the 70 $\mu\text{m}$ ~110 $\mu\text{m}$  and 100 $\mu\text{m}$ ~200 $\mu\text{m}$  glass spheres, the multi-threshold method performed more efficiently than the dual threshold method of Yule (1978). The dual threshold method can only detect 11%~29% of the particles found by the multi-threshold method, which indicates the results produced by the multi-threshold method for PDIA are more robust and reliable. The multi-threshold method is also capable of generating the aspect ratios and sphericities of the particles more accurately than dual threshold method. Furthermore, the analysis of the glass spheres with diameter of 1 $\mu\text{m}$ ~50 $\mu\text{m}$  proves the PDIA system is applicable in sizing the pharmaceutical aerosols (MMD=5 $\mu\text{m}$ ~10 $\mu\text{m}$ ).

## **Chapter 5**

# **Numerical Modeling for a Multi-component Two Phase Actuation Flow**

---

This chapter develops a numerical multi-component two-phase actuation flow model, in order to test different formulations within various flow domains of the cigarette replacement devices (Oxette®). The simulated results of the numerical model have been compared with the measurements of the dual laser beam method and the results of previous researchers, and it proves the model is applicable to predict the actuation flow characteristics of the Oxette®. In order to acquire an aerosol with relatively low and steady mass flow rate of nicotine with a duration of 2.0s (section 1.1, Chapter 1), some predictions have been made by the numerical model with different nicotine formulations, actuation nozzle diameters and oxygen storage volumes. It is recommended that the mass fraction of HFA 134a should be kept around 75%~90% to avoid the sharp temperature drop causing the sensation of freezing. The actuator nozzle diameter should be 0.2mm~0.3mm to produce a flow with relatively low mass flow rate. If oxygen is required at a constant mass per inhalation, the storage volume of the oxygen is suggested to be the volume of the maximum allowance, which keeps the pressure in the chamber as low as possible to have a slow actuation outlet.

---

## 5.1 Introduction

Pressurized-metered dose inhalers (pMDIs) are widely used pharmaceutical devices designed to deliver an aerosolized medication deep into the lung (Finlay, 2001). To obtain a single dose, a consumer first actuates the device by squeezing the canister into the canister casing, while simultaneously inhaling via the casing mouthpiece. Newman (2005) presents an overview of the pMDI design. When a pMDI is actuated, a pressurized mixture of medication and propellant is forced out of the canister through a metering chamber (MC) and an expansion chamber (EC), specially designed to ensure consistent dosing throughout the life of the device. As the mixture passes through the expansion chamber, the pressure is reduced and the propellant begins to boil. Upon leaving the expansion chamber via the nozzle, the propellant forms droplets together with the drug particles or droplets producing a spray suitable for inhalation by the consumer. This basic design remained unchanged from the introduction of pMDIs in 1956 until a switch from chlorofluorocarbon (CFC) to hydrofluoroalkane-based (HFA) propellants began in the late 1990s (Cripps et al., 2000). The emitted spray is transient, unsteady, turbulent, three-dimensional, and multiphase.

In recent years, several researchers have attempted to use computational fluid dynamics (CFD) to model air flow as well as the transport and deposition of aerosols in the human respiratory system. Farkas et al. (2006), Takano et al. (2006), Jin et al. (2007) and Kleinstreuer et al. (2007) simulated the air flow with particle transport and tracked the releasing particles within the calculated flow domain. Their results indicated the essential role of spray velocity initial conditions on simulating delivery of pharmaceutical aerosols in the respiratory system. For flashing propellant systems, of which pMDIs are an important device class, the specification of these initial conditions is problematic.

Few works have appeared in the published literature in which researchers have attempted to characterize pMDI spray actuations experimentally. Hochrainer et al. (2005) compared the spray duration and velocity of a number of CFC- and HFA-propelled pMDIs delivering different medications. The mean aerosol velocity was reported at a distance of 10cm from the nozzle. Three medical formulations (ipratropium bromide, ipratropium bromide + fenoterol, and fenoterol), were tested in both HFA- and CFC-propelled devices. In these cases, the average velocity of each of the HFA-propelled

pMDIs was always less than half the velocity of the corresponding CFC-propelled pMDI. One detailed study of flash evaporation specifically in pMDIs has been conducted by Clark (1991), who attempted experiments to characterize the spray issued from a pMDI for various formulations in terms of spray mass flow rates, peak velocities, temperature, initial drop sizes and pressure variations in the MC and EC, and also developed a theoretical program for the single component flow to predict the above parameters. A range of peak exit velocities between 35 and 70 m/s were obtained at a distance of 30mm from the actuator orifice, for a propellant of HFA 134a with different orifice diameter ratios. Dunbar (1996) provided a comprehensive theoretical and experimental analysis of the pMDI spray. He simulated the actuation flow with a single component numerical model, which indicates the multi-component actuation flow is required for further study. He made experimental measurements at discrete points in the flow-field using phase-Doppler particle analysis (PDPA), which allowed droplet velocity, droplet size, and spray concentration to be measured. For the spray actuated from an orifice with a diameter of 0.5mm, the axial peak exit velocity of the droplets at a distance of 25mm from the actuator orifice was 60m/s, and it was 15m/s at 100mm from the orifice, with the spray duration of 0.195s.

The direct objective of the current work is to study the process of flashing atomization and dispersion, with a view to supporting the development of devices (Oxettes®) to deliver nicotine based solutions via an aerosol that mimics the action of smoking. Preliminary findings suggest that the nicotine formulations have different volatility characteristics and hence there is a requirement to investigate the multi-component two-phase flow characteristics of the flashing flow typically found in pMDIs with the aim of optimizing the process to provide very fine atomization and to evaluate the effect of different formulations on the spray characteristics for the typical pMDI geometry.

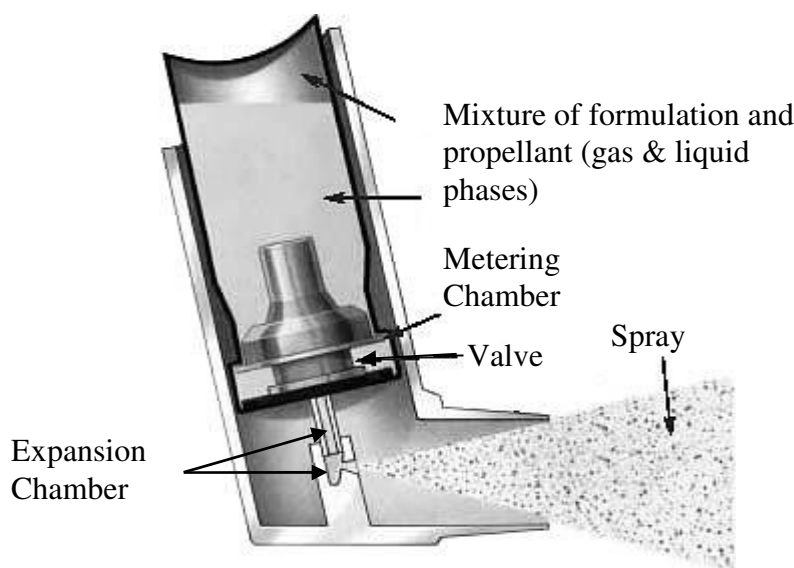
Here, spray velocities and duration were measured using the dual laser method (Dyakowski and Williams, 1993), which utilizes the well known cross-correlation technique (section 3.3, Chapter 3). Measurements were performed using HFA 134a propelled pMDIs, and statistical comparisons were made to study variations in performance with a number of actuations as well as for different formulations (especially



with different propellant mass fraction) actuated using a single pMDI discharging into quiescent air at normal temperature and pressure (NTP: 20°C and 101325Pa).

Numerical multi-component two phase flow has been validated with Dunbar's data (1996) for the single component, and for the multi-component it has been compared with experimental measurements by the dual laser beam method, which will be discussed in section 5.4. With the multi-component numerical model, in order to analyze how different nicotine formulations and pMDI geometries affect the actuation flow performance, a series of predictions are studied in section 5.5. Results of this work will be particularly useful for future researchers seeking to simulate droplet dispersion and deposition in the respiratory system as well as to help validate detailed simulations of the entire pMDI spray process.

## 5.2 Description of the multi-component actuation flow



*Figure 5.1 Pressurised metered-dose inhaler.*

Based upon the work from the previous Ph.D. project of Dunbar (1996), a numerical model for single component flow has been built within the typical pMDI geometry shown in Figure 5.1, where the testing component fluid is  $C_2H_2F_4$  (thermoproperties listed in Appendix II). This model had been programmed in MATLAB and validated with the data provided in the work of Dunbar (1996) with its pMDI geometry and operation conditions, the results will be discussed in *Result A*, section 5.4.2.

The key aim here is to describe what the multi-component actuation flow characteristics are in different flow chambers and to extend the single component model (Dunbar, 1996) to the multi-component flow model in section 5.3.

The nicotine formulation is the main testing fluid in this project (components and mass fractions are listed in Appendix IV). It can be divided into two main parts, one is the bulk concentrate (inerts: a mixture of nicotine free base, absolute ethanol and propylene glycol) and the other is the propellant (HFA 134a). The bulk concentrate does not easily evaporate at the room temperature and atmospheric pressure, as the vapour pressure is far below the atmospheric pressure (Appendix II). Conversely, the propellant is volatile as to provide the propulsion for the bulk concentrate. Since all the liquids are miscible organic compounds, they are considered as ideally mixed. The flow domain is simplified as shown in Figure 5.2, where the dimensions of a typical pMDI are listed in Table 5.1.

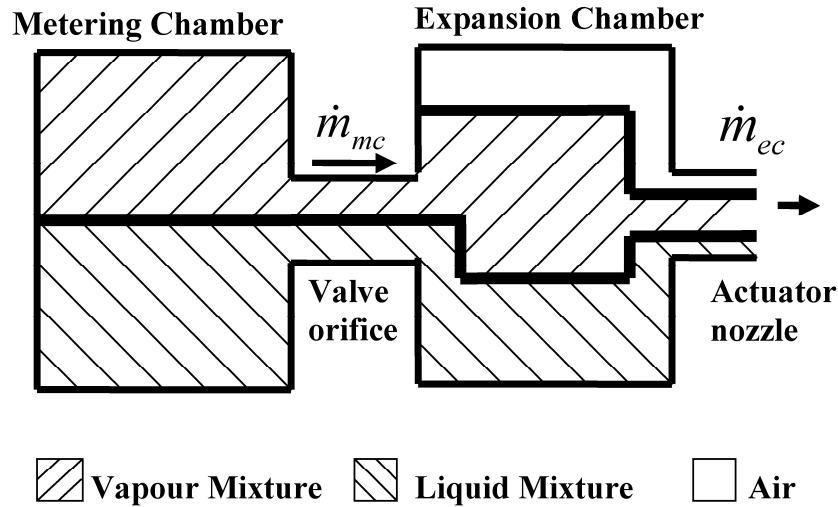


Figure 5.2 Simplified flow model for a typical pMDI.

Volume (mm <sup>3</sup> )	
Metering Chamber	63.0
Expansion Chamber	17.6
Diameter (mm)	
Valve Orifice	0.7
Actuator Nozzle	0.5
Discharge Coefficient	
Valve Orifice	0.61
Actuator Nozzle	0.5

Table 5.1 Dimensions of a typical pMDI (Dunbar, 1996).

***Flow in the metering chamber***

Initially, there are gases (e.g. oxygen and vapour) and liquid mixture remaining saturated in the metering chamber, when the valve orifice is triggered to open, the fluids are released into the expansion chamber. With the vapour generated, a two-phase flow is formed. The flow will be initially choked through the valve orifice as the pressure difference reaches a critical point at sonic conditions. With the loss of mass in the metering chamber, the pressure decreases and the flow become sub-critical till the pressures in the metering and the expansion chambers reach equilibrium.

***Flow in the expansion chamber***

The gas phase coming from the metering chamber is mixed with the air residing in the expansion chamber, and with the liquid phase added in, the pressure in the expansion chamber will increase till the pressures in the metering chamber and the expansion chamber reach equilibrium. At the same time, with the pressure difference increasing between the expansion chamber and atmosphere, initially the two phase flow through the actuator nozzle is sub-critical, and then the pressure difference becomes critical (choked flow forms). Towards the end of actuation, the flow goes back to sub-critical as the pressure in the expansion chamber decreases to atmosphere pressure.

**5.3 Mathematical theory**

As described in section 5.2, the flow of the nicotine formulation is a multi-component two-phase flow. A separated flow model (Wallis, 1969) is used in this study, which means each phase of the fluid is calculated in isolation and modified by the phase quality ( $q$ : gas/mixture mass ratio). In this study, two phases are being considered, one is liquid phase flow, and the other is gas phase flow (including vapours). And the flow characters are mainly calculated from the mean thermophysical properties of the fully mixed gas (Appendix AIII.2) and the liquids (Appendix AIII.3).

Some assumptions are required to be considered:

- (1) The velocity is treated as a constant along the valve orifice or the actuator nozzle during each time step.
- (2) Liquid phase is considered to be incompressible.
- (3) In the expansion chamber, the kinetic energy discharging from the metering chamber will not be taken into account for the energy balance, which means the

releasing fluid to the expansion chamber has the same static temperature as that in the metering chamber.

- (4) The total volume of the liquid mixture is the sum of the volumes of the individual liquid components.
- (5) The flow is adiabatic, which means there is no heat transfer between the fluids and the atmosphere or the device.
- (6) Assume the time for evaporation is negligible, which implies the condition in the metering chamber always remains saturated.
- (7) Assume there are a number of  $N$  different liquid components and  $M$  different gaseous components.
- (8) All the liquid components are miscible organic compounds, they are considered as ideally mixed.

### 5.3.1 Calculation of conditions for the flow in the metering chamber

In the metering chamber, the two phase fluids remain saturated during the actuation, so the thermophysical properties for each component of both phases are the functions of temperature (Appendix II). The properties of multi-liquid component and gas mixture at saturated condition are explained in Appendix AIII.4.

Total mass in the metering chamber is the sum of liquid, vapour and extra gas (e.g. oxygen) mass for each component:

$$m_{T,mc} = \sum_{i=1} m_{l,i,mc} + \sum_{i=1} m_{v,i,mc} + \sum_{j=1} m_{g,j,mc} \quad (5.1)$$

Total enthalpy in the metering chamber is the sum of total liquid mixture enthalpy and total gas, vapour mixture enthalpy:

$$H_{T,mc} = m_{T,l,mc} h_{l,m,mc} + m_{T,v+g,mc} h_{v+g,m,mc} \quad (5.2)$$

where the specific enthalpy of liquid mixture  $h_{l,m,mc}$  is defined in Appendix AIII.3, and that of vapour and gas mixture  $h_{v+g,m,mc}$  is defined in Appendix AIII.2.

The total mass flow rate of the two phase flow through valve orifice  $\dot{m}_{T,mc}$  is explained in Appendix AIII.1, which is the mass flow rate discharging from the metering chamber to the expansion chamber. Respectively, the mass flow rate of the total liquid mixture is named as  $\dot{m}_{l,m,mc}$ , and that of vapour, gas mixture is  $\dot{m}_{v+g,m,mc}$ , where:

$$\dot{m}_{T,mc} = \dot{m}_{l,m,mc} + \dot{m}_{v+g,m,mc} \quad (5.3)$$

At a new time level, the mass of each liquid component in the metering chamber after discharging is defined from the total liquid mixture mass flow rate as:

$$m_{l,i,mc}^n = m_{l,i,mc}^o - \phi_{i,mc} \dot{m}_{l,m,mc} \Delta t \quad (5.4)$$

where  $\phi_{i,mc}$  is the mass fraction of the  $i$ th component in the mixture in the metering chamber, defined in Appendix AIII.3, and  $\phi_{i,mc} \dot{m}_{l,m,mc} \Delta t$  is the discharged amount of the  $i$ th liquid component.

Similarly, mass of each vapour component in the metering chamber at a new time level after discharging is:

$$m_{v,i,mc}^n = m_{v,i,mc}^o - f_{i,mc} \dot{m}_{v+g,m,mc} \Delta t \quad (5.5)$$

and the mass of each gas component is

$$m_{g,j,mc}^n = m_{g,j,mc}^o - f_{j,mc} \dot{m}_{v+g,m,mc} \Delta t \quad (5.6)$$

where  $f_{i,mc}$  is the mass fraction for each vapour of the vapour and gas mixture;  $f_{j,mc}$  is the mass fraction for each extra gas of the vapour and gas mixture, explained in Appendix AIII.2.

At a time point, both liquid and vapour phases reside in the metering chamber. The condition in the metering chamber is assumed to be saturated for every time step, where the mass fraction of the vapour can be calculated by equation AIII.4.7 at a saturated condition. Upon actuation, liquid must evaporate to maintain the pressure as saturated. The evaporation causes the temperature to reduce, as the latent heat energy is expended due to the phase change. Evaporation and latent energy consumption occur simultaneously in reality. For a multi-component liquid, each liquid component evaporates a different amount of vapour according to its partial vapour pressure and latent heat at that temperature. Then, energy balance in the metering chamber can be expressed as:

$$H_{T,mc}^{n'} = H_{T,mc}^o - \Delta H_{T,mc}^o - Latent_{mc} \quad (5.7)$$

$A$ 
 $B$ 
 $C$ 
 $D$

A: Total enthalpy in the metering chamber at current time after discharging and evaporation (5.2).

B: Total enthalpy in the metering chamber at old time before discharging and evaporation (5.2).

C: The enthalpy loss caused by the mass discharged through orifice valve.

$$\Delta H_{T,mc}^o = \dot{m}_{v+g,m,mc} \Delta t \cdot h_{v+g,m,mc}^o + \dot{m}_{l,m,mc} \Delta t \cdot h_{l,m,mc}^o \quad (5.8)$$

D: total latent energy expended by evaporation of liquids in the metering chamber, which is the sum of that for each component.

$$Latent_{mc} = \sum_{i=1} (m_{v,i,mc}^{n'} - m_{v,i,mc}^n) h_{fg,i}^{n'} \quad (5.9)$$

where  $m_{v,i,mc}^{n'}$  is the mass of  $i$ th vapour component after discharging and evaporation;  $m_{v,i,mc}^n$  is the mass of  $i$ th vapour component after discharging but before evaporation, defined in (5.5). Energy balance equation provides the temperature at the new time level in the metering chamber.

### 5.3.2 Calculation of conditions for the flow in the expansion chamber

As the expansion chamber is open to the atmosphere through the actuator nozzle, there is air residing in the expansion chamber before actuation. So the resided air should be taken into account for the thermodynamic conditions in the expansion chamber.

The density of each vapour component in the expansion chamber is calculated from its mass and vapour, gas mixture volume as:

$$\rho_{v,i,ec} = \frac{m_{v,i,ec}}{V_{v+g,ec}} \quad (5.10)$$

Similarly the density of each extra gas is:

$$\rho_{g,j,ec} = \frac{m_{g,j,ec}}{V_{v+g,ec}} \quad (5.11)$$

where  $V_{v+g,ec}$  is the total volume of vapour and gas mixture.

The pressure in the expansion chamber is the sum of total vapour and gas pressures:

$$p_{ec} = p_{T,v,ec} + p_{T,g,ec} \quad (5.12)$$

where the total partial pressure of the vapours is calculated from its density:

$$p_{T,v,ec} = \sum_{i=1} (\rho_{v,i,ec} R_{v,i} T_{ec}) \quad (5.13)$$

and the total partial pressure of extra gases is:

$$p_{T,g,ec} = \sum_{j=1} (\rho_{g,j,ec} R_{g,j} T_{ec}) \quad (5.14)$$

The quality of fluid (gas/mixture mass fraction) in the expansion chamber is:

$$q_{ec} = \left( \frac{m_{T,v} + m_{T,g}}{m_{T,l} + m_{T,v} + m_{T,g}} \right)_{ec} \quad (5.15)$$

Similar to the definition of the mass flow rate of the two phase flow through the valve orifice previously, the mass flow rates of the flow through the actuator nozzle  $\dot{m}_{T,ec}$  is explained in Appendix AIII.1, which is the mass flow rate discharging from the expansion chamber to the ambient condition. The mass flow rate of the liquid mixture is indicated by  $\dot{m}_{l,m,ec}$ , and that of vapour, gas mixture is  $\dot{m}_{v+g,m,ec}$ , then their relations can be expressed as:

$$\dot{m}_{T,ec} = \dot{m}_{l,m,ec} + \dot{m}_{v+g,m,ec} \quad (5.16)$$

The mass of fluid left in the expansion chamber after a time step is calculated as:

$$m_{T,ec}^n = m_{T,ec}^o - \dot{m}_{T,ec} \Delta t + \dot{m}_{T,mc} \Delta t \quad (5.17)$$

A                      B                      C

At a new time level, the total mass of components in the expansion chamber is calculated from three parts at old time level:

A: Total mass already resided in the expansion chamber.

B: The mass discharged through the actuator nozzle out to atmosphere.

C: The mass discharged from the metering chamber, through the valve orifice into the expansion chamber.

From the above expression, the mass of each liquid component in the expansion chamber at a new time level yields:

$$m_{l,i,ec}^n = m_{l,i,ec}^o - \phi_{i,ec} \dot{m}_{l,m,ec} \Delta t + \phi_{i,mc} \dot{m}_{l,m,mc} \Delta t \quad (5.18)$$

Similarly the mass of each vapour component in the expansion chamber at a new time level is:

$$m_{v,i,ec}^n = m_{v,i,ec}^o - f_{i,ec} \dot{m}_{v+g,ec} \Delta t + f_{i,mc} \dot{m}_{v+g,mc} \Delta t \quad (5.19)$$

and the mass of each gas is:

$$m_{g,j,ec}^n = m_{g,j,ec}^o - f_{j,ec} \dot{m}_{v+g,ec} \Delta t + f_{j,mc} \dot{m}_{v+g,mc} \Delta t \quad (5.20)$$

Total mass of fluid in the expansion chamber is the sum of liquid, vapour and extra gas mass:

$$m_{T,ec} = m_{T,l,ec} + m_{T,v,ec} + m_{T,g,ec} \quad (5.21)$$

$A \quad B \quad C$

A: Total mass of liquid (5.18).

B: Total mass of vapour (5.19).

C: The mass of extra gas (5.20).

Similar to the energy balance in the metering chamber (equation 5.7), the condition in the expansion chamber is assumed to be saturated. The enthalpy at a new time level in the expansion chamber is generated from four parts:

$$H_{T,ec}^n = H_{T,ec}^o - \Delta H_{T,ec}^o + \Delta H_{T,mc}^o - Latent_{ec} \quad (5.22)$$

$A \quad B \quad C \quad D$

A: The total enthalpy of the mass resided in the expansion chamber at old time.

B: The total enthalpy discharged through the actuator nozzle.

C: The total enthalpy added from the metering chamber, calculated from (5.8).

D: Total latent energy expended by evaporation of liquids in the expansion chamber, which is similar to (5.9).

$$Latent_{ec} = \sum_{i=1} (m_{v,i,ec}^{n'} - m_{v,i,ec}^n) h_{fg,i}^{n'} \quad (5.23)$$

Similar to (5.2), the total enthalpy in the expansion chamber at old time level is:

$$H_{T,ec}^o = (m_{T,l} h_{l,m} + m_{T,v+g} h_{v+g,m})_{ec}^o \quad (5.24)$$

$A \quad B$

A: total enthalpy of the liquid mixture, which is calculated from the mass of liquids at old time and the specific heat of liquid mixture (Appendix AIII.3).



$B$ : total enthalpy of the vapour and gas mixture, which is calculated from the mass of vapour and gas at old time and the specific heat of vapour, gas mixture (Appendix AIII.2). And similar to equation 5.8, the total enthalpy discharged through the actuator nozzle is

$$\Delta H_{T,ec}^o = \dot{m}_{v+g,m,ec} \Delta t \cdot h_{v+g,m,ec}^o + \dot{m}_{l,m,ec} \Delta t \cdot h_{l,m,ec}^o \quad (5.25)$$

Numerically we solve a two-dimensional fifth order equation set with the time step varying from 0.0001s to 0.00001s. There are several restrictions of the numerical model during each iteration:

(1) For the mass balance calculation at each time step, the discharging mass is always less than the original present mass, which can be expressed as: e.g. for the  $i$ th liquid component:  $\dot{m}_{l,i} \Delta t \leq m_{l,i}^o$

(2) For the enthalpy balance calculation at each time step, the temperature is always higher than the freezing point of each vapour component.

(3) In the expansion chamber, the partial pressure of each vapour component should not exceed the vapour pressure at the corresponding temperature; otherwise the vapour will condense to liquid phase.

Flow charts for the MATLAB programming are shown in Appendix I. Figure A.1 describes the main routine for the whole multi-component two phase actuator flow. Figure A.2 and Figure A.3 are the detailed routines for the conditions in the metering chamber and the expansion chamber, respectively.

## 5.4 Implementation of multi-component actuation flow model

### 5.4.1 Introduction

As described in Chapter 1, the primary objective of Kind Consumer Ltd. is to acquire steady, relatively slow nicotine formulation spray, which should be fine enough to be inhaled deeply into the lung and to have the appearance of cigarette smoke. In the meantime, the mass flow rate of the nicotine is required to be relatively constant. The formulations with different mass fraction of propellant HFA 134a produce the sprays with different quality, exit velocity and duration. Therefore five different nicotine formulations (Table A.6) are tested in a pMDI domain (Figure 5.2) with the dimensions listed in Table 5.1, by the numerical model of the multi-component actuation flow and

the dual laser beam method (section 3.3., Chapter 3). In addition, the pure HFA 134a was used to verify the present model from the data (Dunbar, 1996).

### 5.4.2 Results

There are two parts to the results. First we validate the present model using numerical and experimental data with pure HFA 134a (Dunbar, 1996). Second we use the present model to simulate actuation flow with different multi-component formulations, to focus on the effect of propellant mass fraction, and again, compare the numerical outcomes with the experimental results. It should be noted that the nozzle orifice is 0.5mm for the numerical tests with pure HFA 134a, to match the experimental conditions of Dunbar (1996). For the multi-component formulation numerical work, the nozzle orifice was reduced to 0.3mm, to again match the experimental conditions.

The initial temperatures in the metering chamber and the expansion chamber are the same as the ambient conditions: 293.15K (20°C); the pressure in the metering chamber is the vapour mixture pressure at saturated condition and room temperature. There is air residing in the expansion chamber initially, so the pressure there is atmospheric.

#### *Result part A: comparison of single component pMDI flow model*

Temporal variations of the flow properties within the metering chamber and the expansion chamber are shown in Figure 5.3, with the comparison to the model prediction provided from Dunbar (1996), using simple model assumptions. The actuation duration is the half of that of Dunbar (1996), which is caused by the following reasons: the definitions of the two-phase flow through the nozzle are different. In the present model, the velocities of the liquid phase and the gas phase are defined differently, while they are the same in Dunbar (1996), which leads to the gas flow rate through the nozzle in the present model is greater than Dunbar (1996), and it causes more gas lost so that more latent heat is expended from the liquid for the evaporation to reach the saturated condition. More latent heat lost results in the liquid temperature in the metering chamber decreasing more quickly than Dunbar (1996). This leads to the pressure dropping faster to atmospheric pressure, leading to a shorter actuation time. The quality of fluid in our model is below 0.1 at the end of the actuation, which means there is more fluid left in the metering chamber (roughly  $10^{-6}$  kg left in our model while  $10^{-7}$  kg left in Dunbar (1996)). In practice, if there is extra energy from ambient conditions, actuation time will be longer;

also the evaporation process will not be instantaneous and the saturation may not be achieved at each time step as assumed in the metering chamber. There will be some heat transfer between the fluid and the inhaler case, which would ‘heat up’ the flow slightly and extend the actuation time. Finally the discharge coefficient of the actuator nozzle (which is assumed to be constant in the model, see Table 5.1) will be reduced by the bubble generation, cavitation flow in the expansion chamber. These factors in practice will slow down the actuation flow.

Although the actuation time provided from the experiment of Dunbar (1996) is 0.195 s, the difference between his experimental results and the present numerical results is reasonable considering the complexity of the physics.

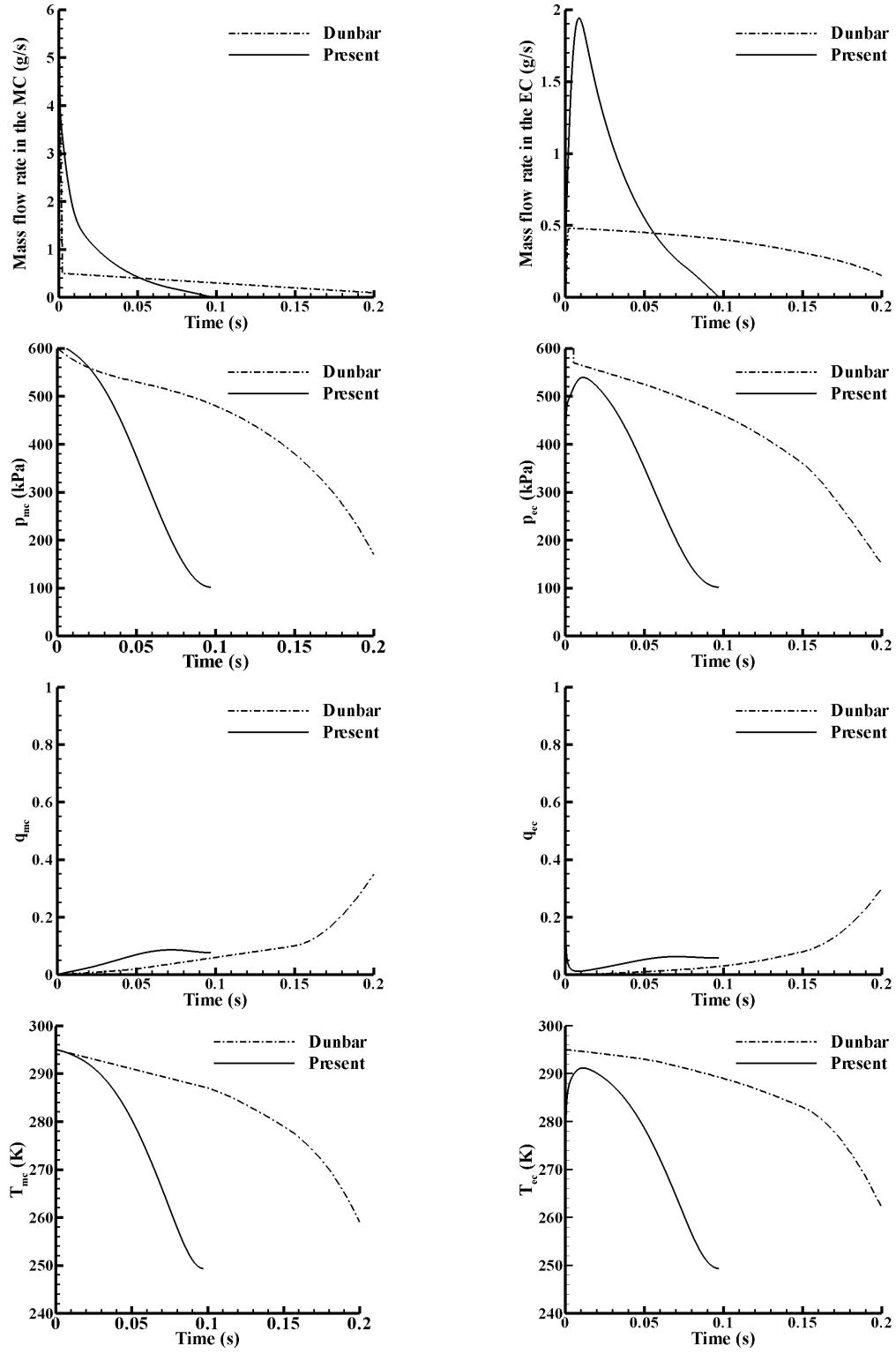


Figure 5.3 Comparison of present model results and the data of Dunbar (1996) (single component actuation flow).

***Result part B: prediction of numerical multi-component pMDI flow model***

The five different formulations (listed in Table A.6, Appendix IV) with different mass fractions of propellant used for single inhalation were tested within the typical pMDI geometry. The expansion chamber volume and the orifice diameter are kept as the same as the values of the pMDI (Dunbar, 1996), with a change of the actuation nozzle diameter to 0.3mm to match the experimental conditions. Numerical model predictions showed that Formula 5 (40% HFA 134a) can not produce a spray due to the low initial pressure in the metering chamber and this was confirmed by the experiment results.

The temporal variations of the actuation flow for the formulations (Table A.6) acquired from the numerical model are shown in Figure 5.4. It shows that the spray durations of different formulations vary slightly from each other, which are approximately 0.28s for the whole actuation and more than twice that of the spray generated by the 0.5mm nozzle (0.1s). Due to the long tail of mass distribution over time this quantity is difficult to verify experimentally. If we defined the “effective” spray duration as the period when the mass flow rate is above 0.1g/s, it would become about 0.19 s, and around 0.12s for the mass flow rate above 0.2g/s. From Figure 5.4, during the first 0.12s actuation, the pressure in the expansion chamber, mass flow rate through actuation nozzle and axial droplet velocity decrease with the reduction of the propellant amount; and it can be calculated that more than 60% of the original formulations were discharged during the first 0.12s.

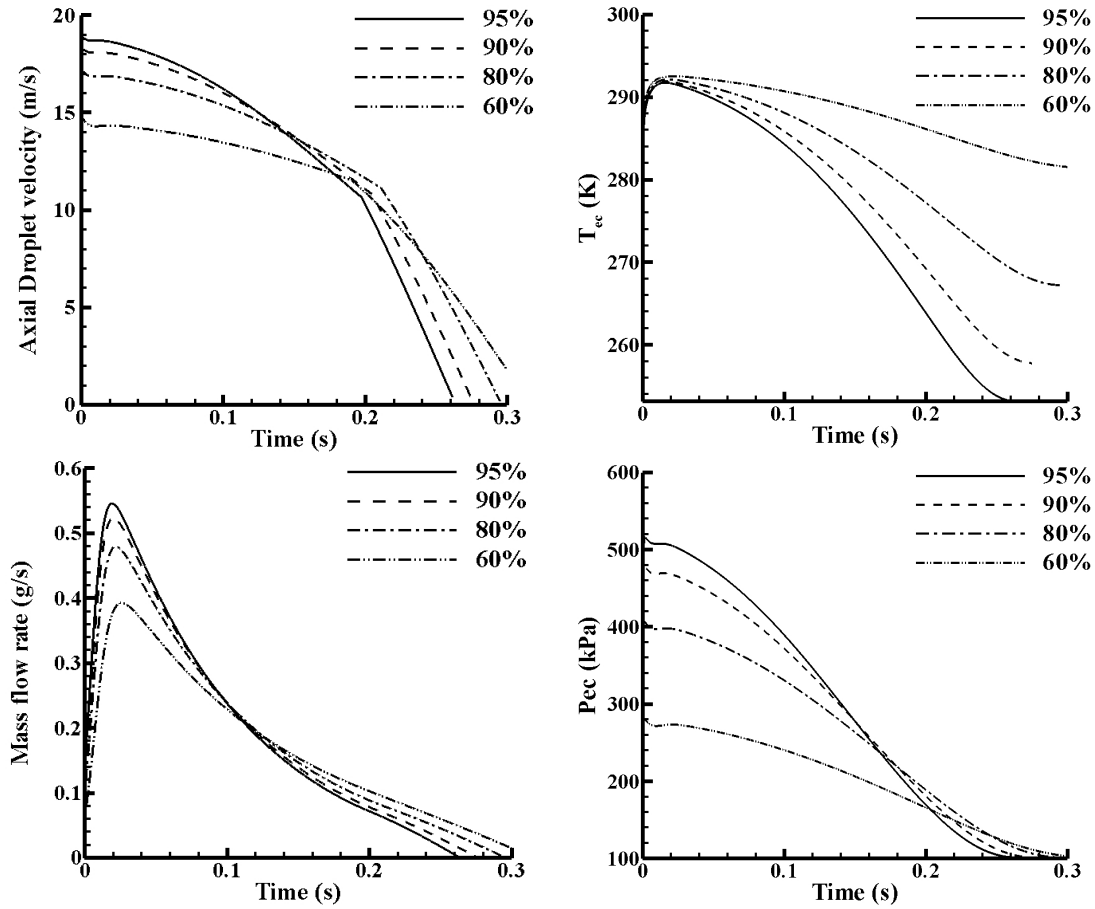


Figure 5.4 Temporal variation of properties within the expansion chamber and actuation flow for the formulations with different mass fraction of propellant HFA 134a.

In order to characterize the spray, two axial positions from the actuation nozzle were defined at  $x=25\text{mm}$  and  $x=100\text{mm}$ . The former station represents the location close to the actuator nozzle and the later one is an approximate distance from the actuator nozzle to the human oropharynx (Swarbrick, 2007). The spray characteristics at  $x=25\text{mm}$  obtained from the dual laser beam method is presented in Figure 5.5, where the markers indicate that the experimental work was carried out in different ambient conditions with variation of humidity (51%~71%) which do not significantly affect experimental results. The peak exit velocity near the orifice decreases with the reduction of the mass fraction of the propellant, and there is a 5.3% deviation between the numerical model and the experimental results. From the experiments, the duration of the spray at  $x=25\text{mm}$  is around 0.1s for the formulations with the propellant above 80% and 0.15s for the one

with 60% propellant; compared with the numerical results (Figure 5.4), it implies that the spray with the predicted mass flow rate below 0.18g/s cannot be detected by the dual laser beam method at  $x=25\text{mm}$ .

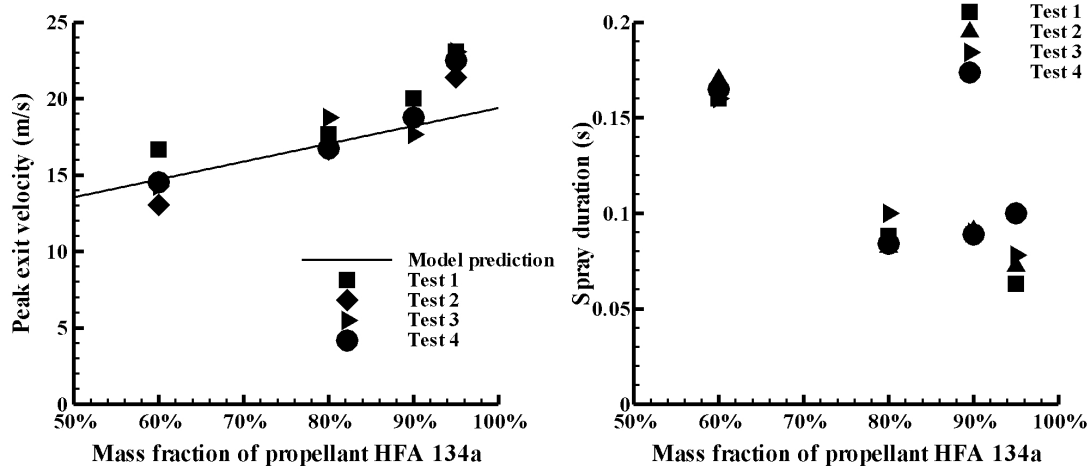


Figure 5.5 Peak exit velocities and spray durations measured by the dual laser method for the formulations with different mass fraction of HFA 134a at  $x=25\text{mm}$ , compared to the numerical predictions.

A further study is on the relative spray characters at  $x=100\text{mm}$  where the human oropharynx locates. The relative light obscuration (Figure 5.6) measured by the dual laser method is proportional to the surface area of the droplets occluding the laser beam. Compared to that at  $x=25\text{mm}$ , especially for the formulation with 60% propellant, the spray duration increases to 0.3s, which is caused by the reduced pressure driving force. However, the spray duration for the formulations with more than 80% of propellant only increases up to 0.14s. As shown in Figure 5.6, the area under the curves is proportional to the total area of the laser beam cross-area occluded by the spray. Since (a) droplet area normal to the laser beam direction is proportional to the second order of the droplet diameter, (b) droplet volume is proportional to the third order and (c) formulation volume per injection is constant, the total area under the curve is inversely proportional to the mean droplet size. As a result, the ratio of the droplet diameters for the spray generated with 90%, 80% and 60% propellant, relative to the mean drop diameter of the spray with 60% propellant, is 0.64:0.73:1. Meanwhile the ratio of the bulk concentrate of the formulations with 90%, 80% and 60% propellant is 0.25:0.5:1, which confirms that the above ratio is the change of the droplet diameters. Furthermore, the deepest points of the

curves in Figure 5.6 indicate how soon the mass of spray reaches the  $x=100\text{mm}$  station (oropharynx). The average time is 0.02s for the spray with 95% propellant arriving at the point and around 0.04s for the others. The main reason for the spray with 95% propellant arriving first is the higher vapour pressure generated in the metering chamber which produces the driving force (5bar shown in Figure 5.4). In summary, the formulations with 80% and 90% propellant seem to produce the most opaque sprays, however, the spray generated by the formulation with 95% propellant probably does not contain enough inert mass to produce a good cigarette ‘smoke’, since it is composed mostly of volatile HFA 134a which easily vapourises.

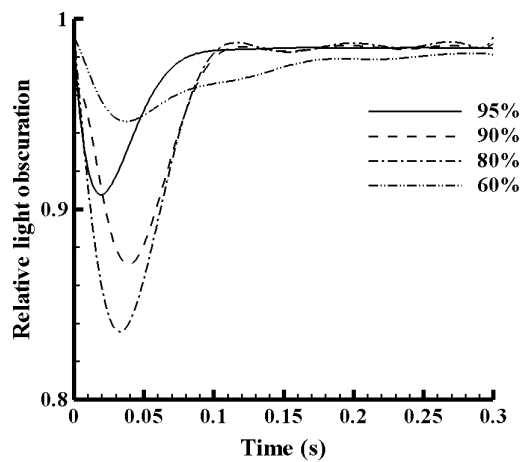


Figure 5.6 Relative light obscuration for the formulations with different mass fraction of HFA 134a at  $x=100\text{mm}$  (pMDI).

### 5.4.3 Summary

A multiphase, multi-component transient model of the key components of a typical metered dose inhaler has been developed and experimentally verified using the dual laser beam method and a range of propellant formulations.

From the numerical and experimental results, it is found that the effective spray duration of the pMDI is around 0.1 s for a formulation with the mass fraction of HFA 134a above 80%. The optimum mass fraction of propellant, to produce a ‘smoke’ like spray occurs in the range 80–90%. Above 90% too little inert mass is present, below 60% and there is not enough flash evaporation to drive the atomization process.



## 5.5 Predictions of the actuation flow characters with different formulations and geometries

### 5.5.1 Introduction

With the aim to predict the mass flow rate of nicotine, the numerical multi-component two-phase actuation flow model has been developed in section 5.4. Two types of actuation flows are compared in this section: one is pure HFA 134a propelled and the other is propelled by a mixture of HFA 134a and oxygen. Four different formulations (Appendix AIV.1 and AIV.2) are studied within the domain of a typical cigarette (Figure 1.1, Chapter 1). Referring back to the early design of the Oxettes® mentioned in section 1.1, chapter 1, one of the key requirements is that 0.012g oxygen (if needed) and 0.1 mg nicotine should be provided per inhalation. Different metering chamber volumes and actuation nozzle diameters are also analyzed to find how the flow characters vary. The expansion chamber volume is kept as the same as that of a typical pMDI (Table 5.1), while the actuation nozzle diameter is tested from 0.2mm to 0.5mm. The formulations used and the geometries of the flow domain for each prediction in the coming sections are listed in Table 5.2.

Formulations (mass fraction of HFA 134a, see Appendix AIV.1 and AIV.2)	Oxygen	Nicotine	Diameter of the actuator nozzle	Oxygen storage volume	Corresponding figures
	required per inhalation				
1. Predictions with the requirement of 0.012g oxygen and 0.1mg nicotine per inhalation					
F1 (90%), F2 (75%), F3 (50%), F4 (95%)	0.012g	0.1mg	0.3mm	½ cigarette volume	Figure 5.7 and Figure 5.8
2. Predictions with different actuator nozzles of various diameters					
F4 (95%)	None	0.1mg	0.2mm, 0.3mm, 0.4mm, 0.5mm	None	Figure 5.9 and Figure 5.10
3. Predictions with different oxygen capacities					
F4 (95%)	0.012g	0.1mg	0.2 mm	1/2, 1/4, 1/8 cigarette volume	Figure 5.11

*Table 5.2 The formulations and the geometries implemented in the numerical predictions by the multi-component two-phase flow model.*

***Initial conditions in the metering chamber***

The temperature in the metering chamber is the ambient temperature of 293.15K (20°C), and the pressure in the metering chamber is the same as the mixture saturated pressure at room temperature.

***Case 1: with additional oxygen in the metering chamber***

If oxygen is needed per inhalation, the mass of the formulation and the volume of the metering chamber are calculated from the requirement of the oxygen and the nicotine for single inhalation, where each inhalation should provide 0.012g oxygen and 0.1mg nicotine (section 1.1, Chapter 1). For different formulations, the masses and the volumes of the other components are calculated referring to mass fractions of the components provided in Appendix AIV.1 and AIV.2. It is assumed that only liquid phase is added in the metering chamber at the beginning, and the maximum available space for oxygen storage is half the size of the standard cigarette with the length of 84mm and the diameter of 7.8mm (Figure 1.1, Chapter 1).

***Case 2: without oxygen in the metering chamber***

Referring to Appendix AIV.1 and AIV.2, the masses and the volumes of the formulations are calculated from the 0.1mg nicotine requirement for single inhalation. The metering chamber volume is the same as the volume of the formulation, assuming only liquid phase exists.

***Initial conditions in the expansion chamber***

There is air residing in the expansion chamber, the temperature and the pressure in the expansion chamber is the same as ambient conditions: 293.15K (20°C) and 101325Pa.

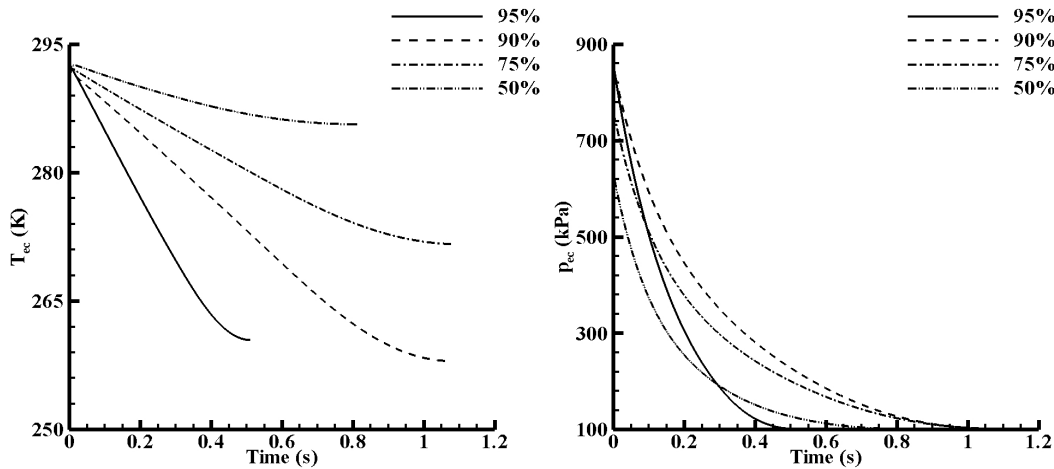
**5.5.2 Results**

There are three parts to the results which are predicted by the developed multi-component two-phase actuation flow model. First we test the performances of the four different formulations (Appendix AIV.1 and AIV.2) with the requirement of 0.012g oxygen and 0.1mg nicotine for one inhalation. Second, with different nozzle diameters and with only propellant of pure HFA 134a, we predict the performances of Formula 4 with 95% HFA 134a (Appendix AIV.2) which is the most concerned by Kind Consumer Ltd.. Last we change the volume of the oxygen storage to find how it affects the actuation

flow characters. It should be noted that the diameter of the nozzle is 0.3mm for the first test and the third test.

***Flow performances with the requirement of 0.012g oxygen and 0.1mg nicotine per inhalation***

Similar to the results in section 5.4, the mass fraction of HFA 134a plays an important role in the flow performances. As shown in Figure 5.7, compared to the other formulations, the temperature of the formulation with 95% HFA 134a drops sharply to 265.15K (-10°C), which can cause the user to feel freezing. Both the formulations with 75% and 90% HFA 134a provide better actuation flow with the duration up to 1.1 seconds.



*Figure 5.7 Temporal variation of the pressure and the temperature in the expansion chamber for four formulations with different mass fractions of HFA 134a (with a requirement of 0.012g oxygen and 0.1mg nicotine for one inhalation, the nozzle diameter is 0.3mm and 1/2 cigarette volume is used for oxygen storage).*

Figure 5.8 shows the variations of the nicotine mass flow rates for the formulations with different mass fractions of HFA 134a. The mass flow rate decreases with the time of actuation. The formulation with 50% HFA 134a generates the flow of lowest mass flow rate, due to the low saturated vapour pressure of the mixture in the metering chamber. For the formulations with 75% and 90% HFA 134a we can calculate that around 0.05mg nicotine is left in the chambers after the actuation. It indicates that nearly half of the original nicotine resides in the device after the actuation, with the requirement of 0.1mg

nicotine per inhalation. Therefore there is a suggestion to double the mass of nicotine in the formulations to meet the requirement.

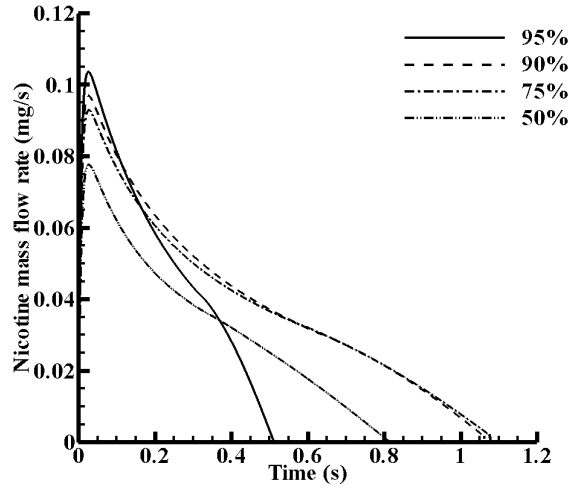


Figure 5.8 Variations of the nicotine mass flow rates for four formulations with different mass fractions of HFA 134a (with a requirement of 0.012g oxygen and 0.1mg nicotine for one inhalation, the nozzle diameter is 0.3mm and  $\frac{1}{2}$  cigarette volume is used for oxygen storage).

#### **Flow performances with different actuator nozzles of various diameters**

The formulation with 95% HFA 134a (without oxygen) is analyzed for the flow characters with different actuator nozzle diameters which vary from 0.2mm to 0.5mm. Figure 5.9 shows the temperature and the pressure variations in the expansion chamber. With the nozzle size of 0.2mm, the flow can stay up to 0.45s with the temperature above 283.15K (10°C). From Figure 5.10, again with the nozzle size of 0.2mm, the duration of the actuation is up to 0.9s with a relative steady nicotine flow rate of 0.2mg/s overall. It indicates that the smaller diameter of the actuator nozzle is, the better the actuation flow performs. Compared to the results when the oxygen is required in Figure 5.8, the nicotine mass flow rate is reduced to half if there is no oxygen requirement (Figure 5.10), which is good to have a relative low mass flow rate of nicotine. It concludes that if the oxygen is not necessary in health treatment for the Oxette®, it can be abandoned, in order to generate a relatively slow and steady aerosol. However there is a problem, especially for the formulation with 95% HFA 134a. A certain amount of nicotine will be left after the actuation, which is due to the reduction of the driven pressure caused by the sharp

decrease of the temperature of the propellant with a higher mass fraction. In reality, there is extra heat available from the ambient environment to extend the actuation duration, which will compensate for this.

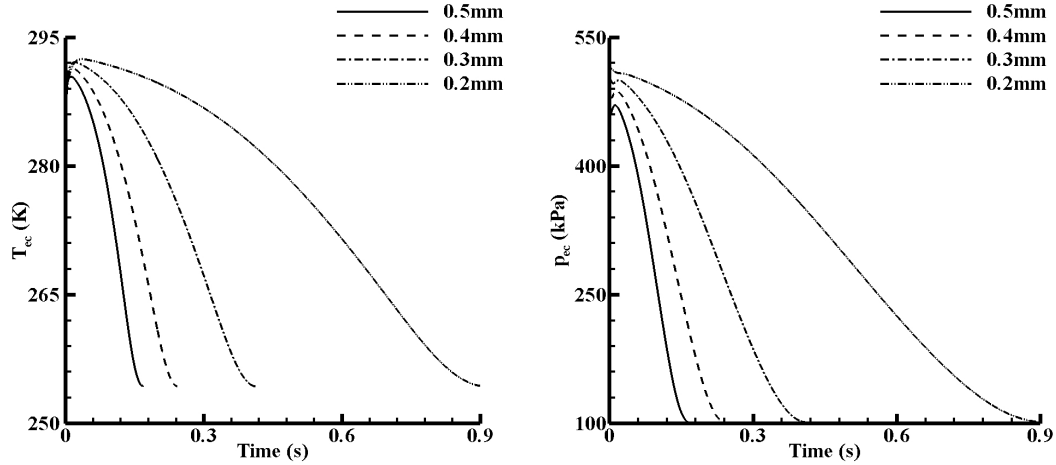


Figure 5.9 Temporal variations of the pressure and the temperature in the expansion chamber with different actuation nozzle diameters (test formulation: Formula 4 (Appendix AIV.4.1); no oxygen in the metering chamber).

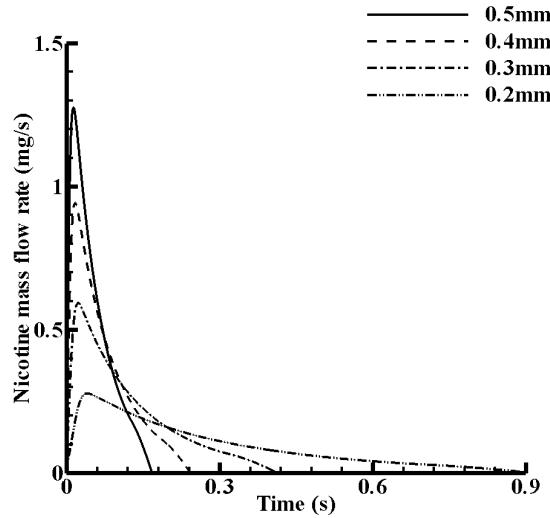


Figure 5.10 Variations of the nicotine mass flow rates with different actuation nozzle diameters (test formulation: Formula 4 (Appendix AIV.4.1); no oxygen in the metering chamber).

### *Flow performances with different oxygen capacities*

In this case, the formulation with 95% HFA 134a is tested with different oxygen storage volumes which are 1/2, 1/4, 1/8 of the total cigarette volume (dimensions shown in Figure 1.1, Chapter 1), where half of the total cigarette volume is assumed to be the maximum allowance for the oxygen storage. As shown in Figure 5.11, when 0.012g oxygen and 0.1mg nicotine are required per inhalation, the actuation duration decreases from 1.2s to 0.8s with the reduction of the oxygen storage volume from 1/2 to 1/8 of the total cigarette volume. Obviously, the one with 1/2 cigarette volume produces more steady nicotine flow rate compared to the others, due to its lower pressure in the metering chamber for the actuation.

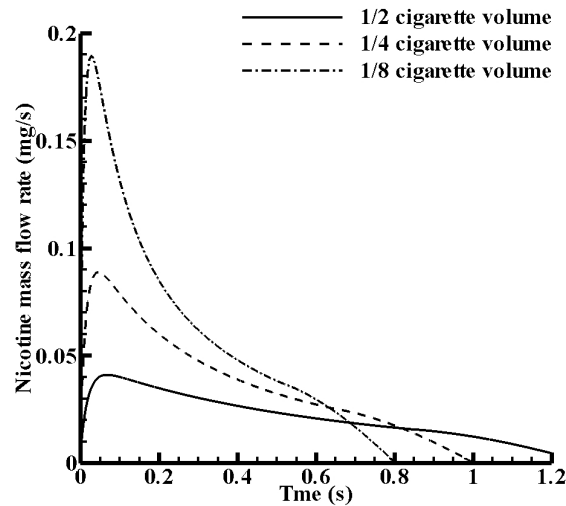


Figure 5.11 Variations of the nicotine mass flow rates with different oxygen storage volumes (test formulation: Formula 4 (Appendix AIV.4.1); with a requirement of 0.012g oxygen and 0.1mg nicotine for one inhalation).

### **5.5.3 Summary**

In order to generate a flow with a relatively steady nicotine mass flow rate and with an actuation duration up to 2 seconds per inhalation (section 1.1, Chapter 1), the formulations with different mass fractions of HFA 134a and the actuator nozzles with different diameters have been analyzed. From the mass fractions of the components point of view, the formulations with 75% and 90% HFA 134a are recommended, since they provide longer actuation duration up to 1.1 seconds. However, the temporal variations of the nicotine mass flow rates are similar among the four formulations. From the geometry

point of view, the nozzle with smaller diameter reduces the nicotine mass flow rate and generates a more steady flow. If a certain amount of oxygen is required per inhalation, the more storage volume is provided for the oxygen, the more steady mass flow rate of nicotine is produced.

## 5.6 Chapter summary

A numerical multi-component two-phase actuation flow model has been developed and validated from the experimental work and the previous literature data, which can be implemented to test different formulations within various flow domains of twin-orifice systems (Figure 5.2).

In order to acquire an aerosol with relatively slow outlet velocity and a steady mass flow rate of nicotine with a duration of 2.0s (section 1.1, Chapter 1), some predictions have been made by the numerical model with different nicotine formulations (mainly with different mass fractions of HFA 134a), different diameters of the actuation nozzle and different volumes of the oxygen storage. It is recommended that the mass fraction of HFA 134a should be kept around 75%~90% to avoid the sharp temperature drop causing the feeling of freezing, and it is suggested that the actuator nozzle diameter should be 0.2mm~0.3mm to produce a flow with low mass flow rate. If an amount of oxygen is required every inhalation, the storage volume of the oxygen is proposed to be the volume of the maximum allowance. From the numerical predictions, there will be a certain amount of nicotine left in the metering chamber after actuations. Of course, in reality, there will be extra heat from the ambient environment to extend the actuation duration so as to compensate for this problem. However, in order to make sure each refill keeps the mass fraction of each component as constant as possible, it is recommended to clear out the formulations in the metering chamber before each refill or to change the mass fraction of the components in the formulation to ensure the overall fractions are constant (probably the first fill is less than the required amount). Please note that the discussion and the recommendations in this chapter were based on the characteristics of the actuation flow (e.g. temperature, velocity, mass flow rate), without the consideration of the real droplet sizes which will be discussed in next chapter.

## Chapter 6

# Local and Global spray analysis of Oxette®

---

The previous chapter has developed a numerical multi-component two-phase actuation flow model, in order to test different formulations within various flow domains of the cigarette replacement devices (Oxette®). With the only consideration in the actuation flow characteristics (e.g. actuation velocity, temperature and mass flow rate), it is recommended that the mass fraction of HFA 134a should be kept around 75%~90% and the actuator nozzle diameter should be 0.2mm~0.3mm to produce a flow with relatively low mass flow rate of nicotine. However, in order to keep the droplet size of aerosols to around 2 $\mu$ m ~5 $\mu$ m, the mass fraction of HFA 134a is required to be above 95% due to the limitation of the atomization device. In this chapter, two different formulations with 95% and 98% mass fraction of HFA 134a, and two prototypes of the cigarette alternatives (Oxettes®) with different expansion chamber volumes, have been analyzed by the numerical model and compared with the dual laser measurements. In addition, it considers the spray characters by high speed imaging, with the special interest in the flashing phenomena and droplet sizes. It concludes that a larger expansion chamber volume enhances the propellant evaporation, recirculation, bubble generation and growth inside the chamber, and it made a significant improvement to produce finer sprays. Although the formulation with 98% of HFA 134a can generate smaller droplets, the formulation with 95% of HFA 134a produces more steady puffs with relatively low mass flow rate.

---



## 6.1 Introduction

As described in the previous chapters, the pressurized Metered Dose Inhaler (pMDI) has become the most prescribed drug delivery system for treating respiratory diseases. The compactness, ease of use, low cost of these devices and reasonable effectiveness in treating lung diseases has ensured strong preference amongst patients as well as clinicians. Hence, Kind Consumer Ltd. intends to use the same concept design of pMDIs to deliver a nicotine based formulation to mimic smoking, and use breath activation to achieve good actuation/inhalation coordination.

However, the pMDI-like devices have some well-known limitations, the most important being their low drug delivery efficiency which is between 5~20% (Versteeg et al., 2006). The conventional pMDIs are known to produce aerosols with excessively high velocities and a substantial fraction of large droplets, which causes high oropharyngeal deposition. Poor coordination between pMDI actuation and inhalation by many patients compounds the problem. Apart from reducing the dose available for delivering to the lungs, this unintended deposition in the oropharynx often causes cough, bronchospasm and oral thrush (Versteeg et al., 2006). Therefore a detailed research on the spray characteristics is required.

Due to the absence of suitable instrumentation, few visualizations of the two-phase flow associated with pre-atomization inside the expansion chamber of the twin-orifice system (Figure 5.2, Chapter 5) and the subsequent external spray formation have been provided. Dunbar (1996) presented small selections of high-speed photographs, but it is difficult to obtain a clear picture of flow conditions. Versteeg et al. (2006) investigated the propellant flow inside the expansion chamber of a pMDI by high speed imaging. They found the existence of an annular flow regime with a vapour core and an unsteady wall film consisting of foamy liquid in the expansion chamber. Vu et al. (2009) studied a flashing jet with superheated water by high speed visualization of the internal nozzle flow. They found the clear bubbles form near the nozzle wall and an annular flow existed in which the bubbles merged into a vapour core surrounded by a liquid sheath.

In spite of its therapeutic significance the spray generation mechanism of the pMDI has not been extensively researched. External spray characteristics in the far-field

( $x=0\sim 100\text{mm}$ ) were documented in two studies by (i) Clark (1991) with an aerodynamic particle sizer and (ii) Dunbar (1996) by means of Phase Doppler Anemometry (PDA).

As reviewed in section 2.3.2, Chapter 2, the expansion chamber geometry affects much on the flashing atomization. Therefore, in this chapter, two prototypes of ‘cigarettes’ (Oxettes®) with different expansion chamber volumes are investigated. The mathematical model (Chapter 5) is implemented to investigate the characteristics of the multi-component two-phase flashing flow, with the aim of optimizing the process to provide very fine atomization, and to evaluate the effect of different formulations on the spray characteristics for different expansion chamber geometry. Spray velocities and durations were measured by dual laser method (section 3.3, Chapter 3). Measurements were performed using different HFA-propelled formulations (especially with different mass fractions of the propellant) within the Oxettes®, and the variations in performance under different smoking profiles were analysed. Furthermore, using high speed imaging, spray characters and drop sizes were studied at sequential puffs under different smoking patterns.

## 6.2 Method

The objective of the design of the Oxette® is to acquire steady, relatively slow spray, which should be fine enough to be inhaled deeply into the lung and to have the appearance of cigarette smoke. During a single inhalation, the mass flow rate of the nicotine is required to be relatively constant. The formulations with different mass fraction of propellant HFA 134a produce the sprays with different quality, exit velocities and durations. Five different nicotine formulations (Appendix AIV.3) have been tested numerically using pMDI in Chapter 5, and the formulation with mass fraction of HFA 134a above 75% was recommended. In order to generate finer spray with the droplet diameter of  $2\mu\text{m} \sim 5\mu\text{m}$ , another two different formulations with high mass fractions of HFA 134a were tested in this chapter, and they are named here as KDCRA103 with 95% mass fraction of propellant and KDCRA122 with 98% mass fraction of propellant. The physical properties of the propellant (HFA 134a) are listed in Appendix II. The remaining components are non-volatile and inert (Appendix AIV.4).

Two prototypes of the cigarette alternatives, named here as Oxette® 1 for the earlier design and Oxette® 2 for the later design, were manufactured at early stage by KIND

CONSUMER LTD., and Figure 6.1 gives a schematic of the geometry of interest here. The same dimensions of the two devices are the metering chamber volume of  $600\text{mm}^3$ , the actuator nozzle diameter of  $0.2\text{mm}$  and the expansion chamber diameter ( $D_{ec}$ ) of  $1.0\text{mm}$ . The valve orifice diameters change between  $0.14\text{mm}$  and  $0.18\text{mm}$  due to the inhaled pressure variation, and a mean value of  $0.17\text{mm}$  is used in the simulation. The expansion chamber lengths ( $L_{ec}$ ) of Oxette® 1 and Oxette® 2 are  $2.0\text{mm}$  and  $6.9\text{mm}$  respectively.

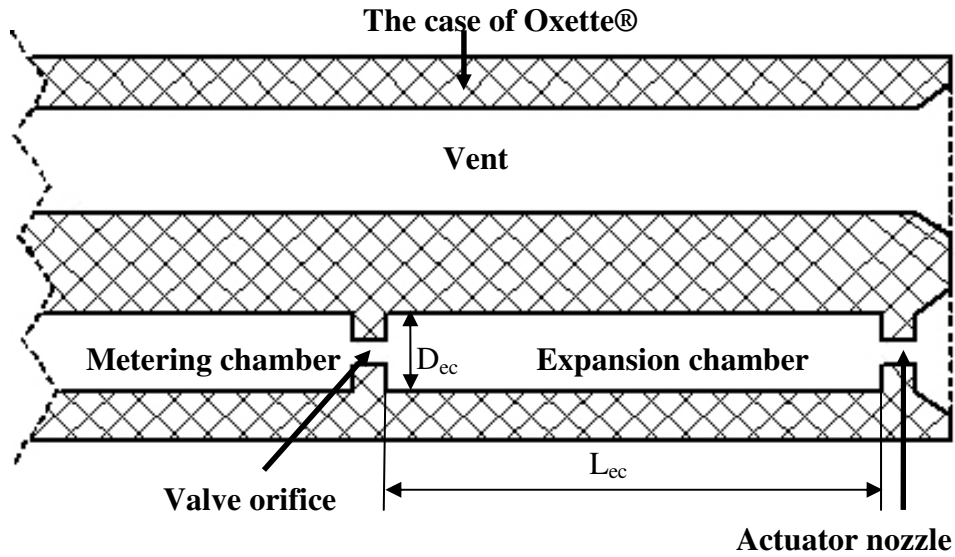


Figure 6.1 Schematic diagram of Oxette® geometry of interest.

The shallow and deep smoking profiles have been programmed for the mechanical lung (section 3.2, Chapter 3) to trigger the prototypes, referring to the lung volume variations of different smokers from the experimental work by Tobin et al., 1982. Pressure variations in the lung under two smoking patterns detected by the pressure sensor installed in the mechanical lung were recorded as shown in Figure 6.2, where  $p_{\text{inhalation}}$  is the inhalation pressure and  $p_{\text{atm}}$  is atmospheric pressure.

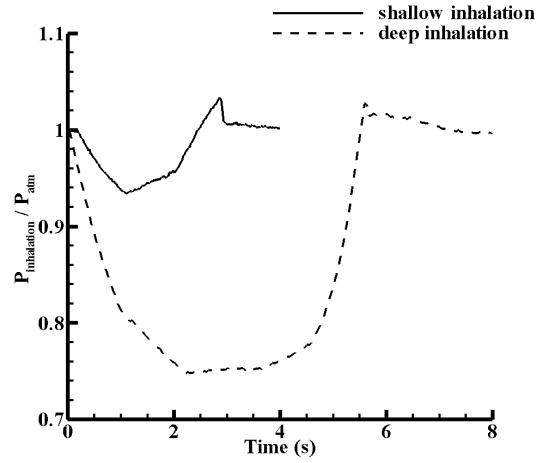


Figure 6.2 Pressure variations in the lung under shallow inhalation and deep inhalation measured by the pressure sensor installed in the mechanical lung.

### 6.2.1 Mathematical modeling

A multiphase, multi-component transient model of the key components of a typical metered dose inhaler has been developed and experimentally verified by using the dual laser beam method and a range of propellant formulations (Chapter 5). This model is implemented to simulate the actuation flow issuing from the two prototypes (Oxette® 1 and Oxette® 2).

From the experiment by Clark (1991), initial mass median diameter (MMD) of the spray generated at the actuator nozzle from a typical pMDI can be estimated from the quality of the fluid ( $q_{ec}$ : gas/total fluid mass ratio) and the pressure ( $P_{ec}$ ) in the expansion chamber by equation 6.1. This has been implemented in the multiphase, multi-component transient model (Chapter 5) to give a further indicator of spray quality.

$$MMD = \frac{8.02}{q_{ec}^{0.56} \left( \frac{P_{ec} - P_{atm}}{P_{atm}} \right)^{0.46}} \quad (6.1)$$

In reality, we are only interested in the droplet sizes at the axial position from the actuator nozzle of  $x=100\text{mm}$  where the human oropharynx locates and it provides important information on the droplet depositions in the human respiratory tract to predict the efficacy of the formulation. Generally it is a combination of evaporation and boiling processes after the liquid discharging from the actuator nozzle (Polanco et al., 2010). Brenn et al. (2007) developed an evaporation model of multi-component liquid droplets,

as detailed in Appendix AV.1. The liquid phase is treated as a thermodynamically real fluid, using the Universal Functional Activity Coefficient (UNIFAC) method for calculating the component activities (equation AV.1.13), and the gas phase as ideal. The properties of structure groups in different molecules of the propellant and inerts can be referred to Reid et al. (1977), Fukuchi et al. (2001), Wittig et al. (2003) and Hou et al. (2008).

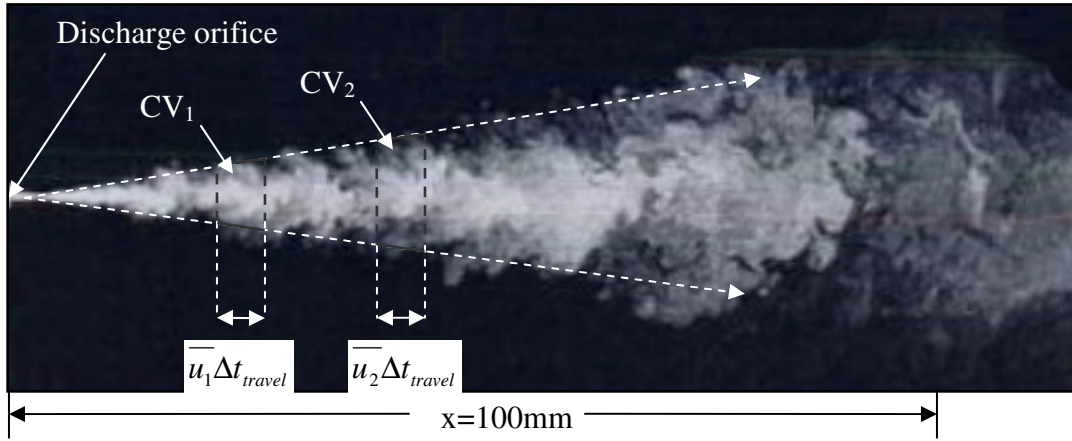


Figure 6.3 Graphic description of droplet evaporation model along a turbulent jet.

Some assumptions to predict the sizes of the residual droplets at  $x=100\text{mm}$ :

1. The flow discharged from the Oxette® is an axisymmetrically turbulent jet with a constant spreading rate (Pope, 2000), and the cone angle of the spray was formed to be,  $21.6^\circ$  which was also measured by Dunbar (1996) for a pMDI device.
2. Figure 6.3 indicates the control volume (CV) is assumed to be a trapezoid and its volume can be calculated by the cone angle and the local mean velocities ( $\bar{u}_1$  in CV1 and  $\bar{u}_2$  in CV2). The condition in each CV is assumed to be saturated, where the relationship between the vapour phase and the liquid phase can be expressed as equation AIII.4.7. At the beginning of the actuation at the orifice exit, it is assumed the control volume is full of liquid.
3. The initial conditions of the droplets at the exit of the discharge nozzle, such as droplet velocity and temperature, are predicted by the multi-component two-phase flow model (Chapter 5).
4. All the droplets are assumed to be spherical with the same size and uniformly distributed in the control volume along the jet, travelling with the same axial velocity.

The initial mass fraction of each component in the droplets at the exit of the actuator nozzle is the same as that of the original formulation.

5. The flow is actuated into atmosphere at normal temperature and pressure (NTP: 20°C and 101325Pa).

***The procedure in determining the sizes of the residual droplets at x=100mm***

In chapter5, it was assumed that the condition in the chambers always remains saturated, where the time for evaporation is neglected. In this chapter, the evaporation rate of the droplet is expressed as equation AV.1.1, and it is required to determine a time scale for the evaporation of the liquid phase to reach a saturated condition in the control volume. In order to calculate the mass fraction of the vapour phase and the liquid phase at saturated condition (equation AIII.4.7), the volume of the control volume should be specified first. Therefore two time steps are implemented here: one is the time step for the droplets travelling along the jet ( $\Delta t_{travel}$ ), which determines the size of control volume (Figure 6.3); the other one is the time step for the evaporation of the droplet ( $\Delta t_{evaporation}$ ). At initial conditions, a reasonable “guess” of the ratio of two time steps ( $\Delta t_{travel} / \Delta t_{evaporation}$ ) is applied here as 0.001. Within the control volume of  $u\Delta t_{travel}$ , the required time of reaching a saturated condition ( $\Delta t_{saturation}$ ) can be calculated by equation AV.1.1 and AIII.4.7. If  $\Delta t_{saturation}$  is less than  $\Delta t_{travel}$ ,  $\Delta t_{travel}$  will be reduced to  $\Delta t_{saturation}$  and another  $\Delta t'_{saturation}$  is computed within the new CV of  $u\Delta t'_{travel}$ . Of course, the reduction of the control volume means a decrease of  $\Delta t_{saturation}$  in a smaller CV, therefore an iteration procedure is carried out until reaching a condition within allowance, vice versa. With the reduction of the droplet size along the jet due to evaporation, the size of the residual droplet will be computed at x=100mm based on the above assumptions and algorithm.

## **6.2.2 Experimental measurement method**

***Dual laser beam method***

In order to verify the numerical model, and acquire the key information on the actuation simply and reliably, the dual laser beam method (section 3.3, Chapter 3) is applied to measure the spray velocity, duration and relative opacity at two positions of

$x=25\text{mm}$  and  $x=100\text{mm}$  from the actuator nozzle. The former station represents the location close to the actuator nozzle and later one is an approximate distance from the actuator nozzle to the human oropharynx (Swarbrick, 2007).

### ***High speed imaging method***

Sprays actuated from the Oxette® were imaged using laser-based high-speed visualization to reveal internal propellant flows and external sprays. The system comprised a Nd-YLF (yttrium lithium fluoride) laser (Darwin-Duo-527-40-M) as the illumination source in conjunction with a Fastcam SA1.1 high-speed digital camera for image recording. The laser provided a pulsed light source with a frequency of 0.1~10kHz. The camera provided 1024×1024 pixel resolution images and was operated with a SIGMA (105mm, F/2.8) lens to image the expansion chamber, near-orifice region and the global spray development. A Questar QM100 lens was used to size the droplets at the axial position of 100mm from the actuator nozzle at much higher magnification.

## **6.3 Results**

There are five parts to the results. Firstly, it measures the actuation flow properties with dual laser beam method (section 3.3, Chapter 3). Secondly, it predicts the actuation flow characteristics using numerical model (Chapter 5) with two different multi-component formulations under deep and shallow smoking inhalation profiles for Oxette® 1 and Oxette® 2, and it compares the actuation flow velocity, duration and relative density to the experiment results. Thirdly, it predicts the residual droplet sizes of the aerosol at  $x=100\text{mm}$  with the inputs from the previous analyzed properties of the actuation flow. Fourthly, it analyzes the internal and external characteristics of the spray issuing from the Oxettes® by high speed imaging method. Finally the residual drop sizes of the aerosol at  $x=100\text{mm}$  are measured by the developed Particle/Droplet Image Analysis (PDIA, Chapter 4) and compared with numerical predictions.

### **6.3.1 Measurements of actuation flow characteristics by the dual laser method**

Similar to the previous work (Chapter 5), the data of actuation flow characteristics was recorded by the dual laser beam method at two axial positions of  $x=25\text{mm}$  and  $x=100\text{mm}$  from the actuator nozzle. Please note the results presented below by the dual laser method

were recorded from the start of the actuation. Two laser beams form two control volumes across which the spray plume passes. The light intensity change of the two laser beams due to beam obscuration by the spray is detected by two photodiodes and recorded by a PC based data acquisition card (AD). When the spray passes through the first laser beam there will be a drop in voltage waveform from the correlative photodiode and similarly this will occur when it traverses the second beam. The distance between the two laser beams is known (3mm in this work), and the time delay can be measured by the delayed signal acquired as a result of the spray taking a finite time to traverse the two beams, therefore the spray velocity could be calculated. Here, this time delay is determined by a cross-correlation procedure (Dyakowski and Williams, 1993), which represents the amount of time it takes a spray element to travel through the two laser beams. Furthermore, assuming the spray is uniform and the droplets are spherical, the depth of the voltage drop is proportional to the surface area (of sum of the droplets) occluding the laser beam, and for a given spray mass it is an indication of the droplet sizes. Therefore a non-dimensional relative light obscuration term is introduced, which is defined by the ratio between the voltage drop when the spray transverse though the laser beams and the peak voltage when there is no spray passing. Although this cannot provide the absolute spray concentration or droplet size, it still can provide some relative measurement of spray opacity due to formulation variations.

Oxette® 1 can hardly generate fine sprays with any formulations, and it can only produce large droplets, bulk liquid jets or sheets, which are difficult to be detected by the dual laser beam method. The relative light obscuration for the spray generated by Oxette® 1 during the 1<sup>st</sup> deep inhalation is shown in Figure 6.4, where it shows the relative opacities of the sprays are not comparable to those produced by Oxette® 2 (Figure 6.5). Similarly, under the shallow inhalations, it can neither generate fine sprays nor can be detected by the dual laser beam method.



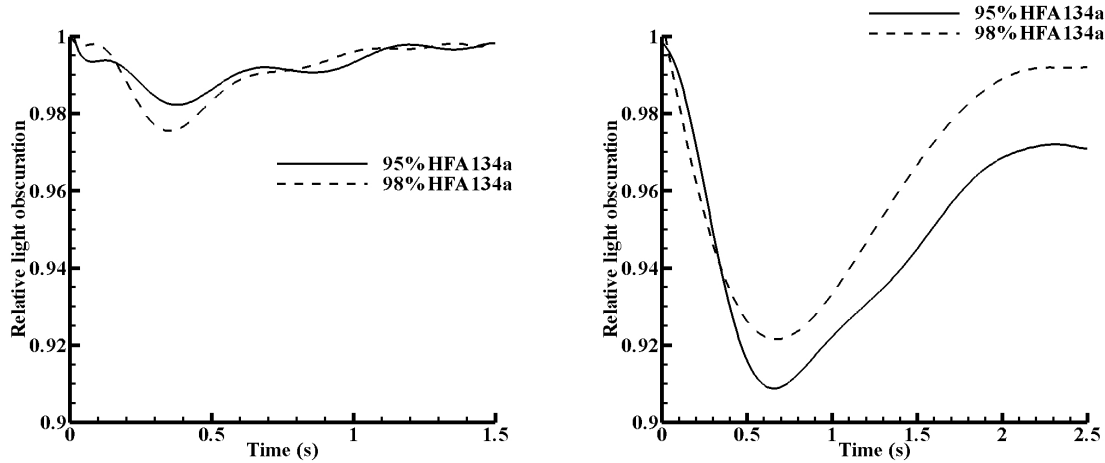


Figure 6.4 Relative light obscuration for the spray generated by Oxette® 1 with KDCRA103 (95% HFA 134a) and KDCRA122 (98% HFA 134a) under the 1<sup>st</sup> deep inhalation (left: at  $x=25\text{mm}$ ; right: at  $x=100\text{mm}$ ).

Figure 6.5 shows the relative light obscuration for the spray generated by Oxette® 2 under the 1<sup>st</sup> deep inhalation. KDCRA103 (95% HFA 134a) generated relatively denser spray than KDCRA122 (98% HFA 134a), which is caused by the lower evaporation rate of KDCRA103 (95% HFA 134a) and more inerts remaining. The light obscuration by the spray after inhalation did not return to the original state before the actuation, which is caused by the droplets filled in the inspiration chamber of the mechanical lung. Without an intermediate refill, the spray generated during 2<sup>nd</sup> deep inhalation was barely detected by the dual laser beam method due to most of the formulation being consumed during the 1<sup>st</sup> deep inhalation.

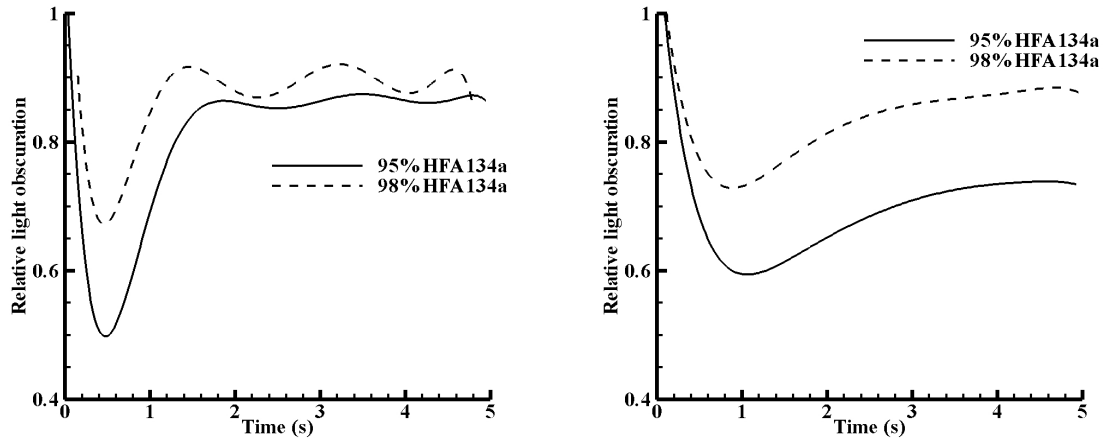


Figure 6.5 Relative light obscuration for the spray generated by Oxette® 2 with KDCRA103 (95% HFA 134a) and KDCRA122 (98% HFA 134a) under the 1<sup>st</sup> deep inhalation (left: at  $x=25\text{mm}$ ; right: at  $x=100\text{mm}$ ).

Figure 6.6 shows relative light obscuration for the spray generated by Oxette® 2 with KDCRA103 (95% HFA 134a) and KDCRA122 (98% HFA 134a) under repeated shallow inhalations without an intermediate refill. The relative density of the sprays decreases at each sequential inhalation and the ratio is 2.8:1.8:1 for KDCRA103 (95% HFA 134a) at  $x=25\text{mm}$ . Compared to KDCRA103 (95% HFA 134a), the mixture vapour pressure of KDCRA122 (98% HFA 134a) is higher due to its higher mass fraction of HFA 134a. It actuated more fluid at the exit of the actuator nozzle ( $x=25\text{mm}$ ) and resulted in denser sprays than KDCRA103 (95% HFA 134a) at  $x=25\text{mm}$  during the first 0.2s. Again the higher mass fraction of HFA 134a caused a faster evaporation rate, and therefore KDCRA122 (98% HFA 134a) produced sparser sprays at  $x=100\text{mm}$  compared to KDCRA103 (95% HFA 134a).

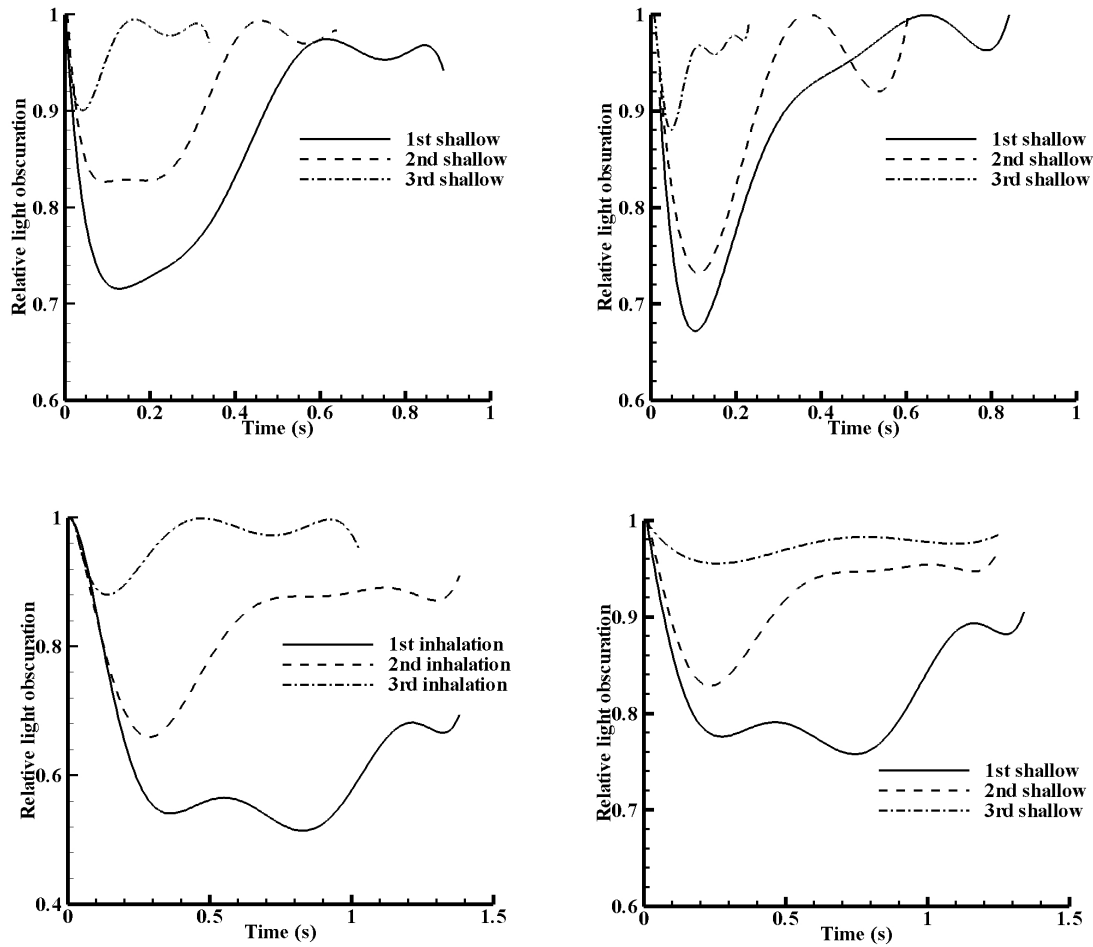


Figure 6.6 Relative light obscuration for the spray generated by Oxette® 2 with KDCRA103 (left column: 95% HFA 134a) and KDCRA122 (right column: 98% HFA 134a) under the 1<sup>st</sup>, the 2<sup>nd</sup> and the 3<sup>rd</sup> shallow inhalation (top row: at  $x=25\text{mm}$ ; bottom row: at  $x=100\text{mm}$ ).

Several researchers (Yildiz et al., 2002; Calay and Holdo, 2008; Polanco et al., 2010) stated the axial velocity increased during the expansion region and started to decrease in the entrainment region due to mixing with ambient air as the jet propagates. The spray expansion region depends upon the geometry of the atomizer, initial conditions of the flow such as superheat level and the liquid properties (Yildiz et al., 2002). More analysis on expansion region characters will be detailed in section 6.3.4 and 6.3.5 where the measurements were taken by high speed imaging. Table 6.1 shows the axial spray velocity calculated by the cross correlation method (section 3.3, Chapter 3) from the dual laser results of Oxette® 2. At  $x=25\text{mm}$ , the jet had higher velocities under the 1<sup>st</sup> and the

2<sup>nd</sup> shallow inhalations than that under the 1<sup>st</sup> deep inhalation. This is because, under the deep inhalation, the jet has shorter expansion region where its velocity starts to decrease earlier than the jet generated under the shallow inhalation. Under sequential shallow inhalations, the axial velocities at  $x=25\text{mm}$  decreased due to the consumption of the formulations, however the axial velocities at  $x=100\text{mm}$  increased due to the less entrainment occurring.

	Axial spray velocity (m/s)			
	KDCRA103		KDCRA122	
	$x=25\text{mm}$	$x=100\text{mm}$	$x=25\text{mm}$	$x=100\text{mm}$
1 <sup>st</sup> deep inhalation	9.38	4.17	10.71	5.36
1 <sup>st</sup> shallow inhalation	14.29	4.54	16.00	4.55
2 <sup>nd</sup> shallow inhalation	13.64	4.55	12.00	4.62
3 <sup>rd</sup> shallow inhalation	13.63	6.12	9.68	6.52

*Table 6.1 Axial spray velocity generated by KDCRA103 (95% HFA 134a) and KDCRA122 (98% HFA 134a) with Oxette® 2 under different inhalation profiles at  $x=25\text{mm}$  and  $x=100\text{mm}$ .*

### 6.3.2 Prediction of flow characteristics by the numerical multi-component actuation flow model

The actuation flows issuing from the Oxette® were simulated by the previous multi-component actuation flow model (Chapter 5). The flow characteristics at the exit of the actuator nozzle, such as axial velocity, gas/liquid mass ratio and liquid temperature, are treated as the initial conditions to predict the initial MMD of the spray at the exit of the actuator nozzle by equation 6.1.

The initial temperatures in the metering chamber and expansion chamber are the same as the conditions for each inhalation: 293K (20°C); the pressure in the metering chamber is the mixture vapour pressure at saturated condition and atmospheric temperature. There is air residing in the expansion chamber initially, so the pressure there is atmospheric before each inhalation. Mass flow in the prototype Oxettes® tested here can only be triggered under the pressure below 96% of the atmospheric pressure. The metering chamber temperature is assumed to stay at the same as the atmospheric temperature at the beginning of each inhalation regardless of how many repeated puffs have been tested.

Temporal variations of the actuation flow properties at the exit of the actuator nozzle for KDCRA103 (95% HFA 134a) and KDCRA122 (98% HFA 134a) under repeated

deep inhalations without an intermediate refill are predicted in Figure 6.7. Different from the dual laser method, the data was recorded from the start of each smoking profile (Figure 6.2). Before the pressure reached below 96% of the atmospheric pressure, the data stayed the same as the initial conditions as shown in Figure 6.7 during the first 0.2s. Oxette® 2 generated the actuation flow with lower mass flow rate but higher axial velocity than Oxette® 1. Oxette® 2 has a larger expansion chamber volume and it provides more room to generate small bubbles in the expansion chamber (Sher et al., 2008) and it increases the vapor/liquid mass ratio in the expansion chamber and results in the reduction of the mass flow rate. There is a sharp temperature drop in the fluid produced by Oxette® 2 at the beginning of the actuation (around 0.2s), because of the rapid latent cooling due to the evaporation of the tiny amount of formulation in the larger expansion chamber compared to Oxette® 1. There are no significant differences between properties of the flows generated by two formulations. Compared to KDCRA103 (95% HFA 134a), higher mass flow rates generated by KDCRA122 (98% HFA 134a) are caused by the higher vapour pressure of the mixture since it contains a higher mass fraction of HFA 134a (98%). For the devices tested, only 13.5%~17.5% of the formulation is left after the first deep inhalation, which only allows the devices to provide one rich puff under deep inhalation, hence the sprays generated under the 1st and 2nd deep inhalation are very different.

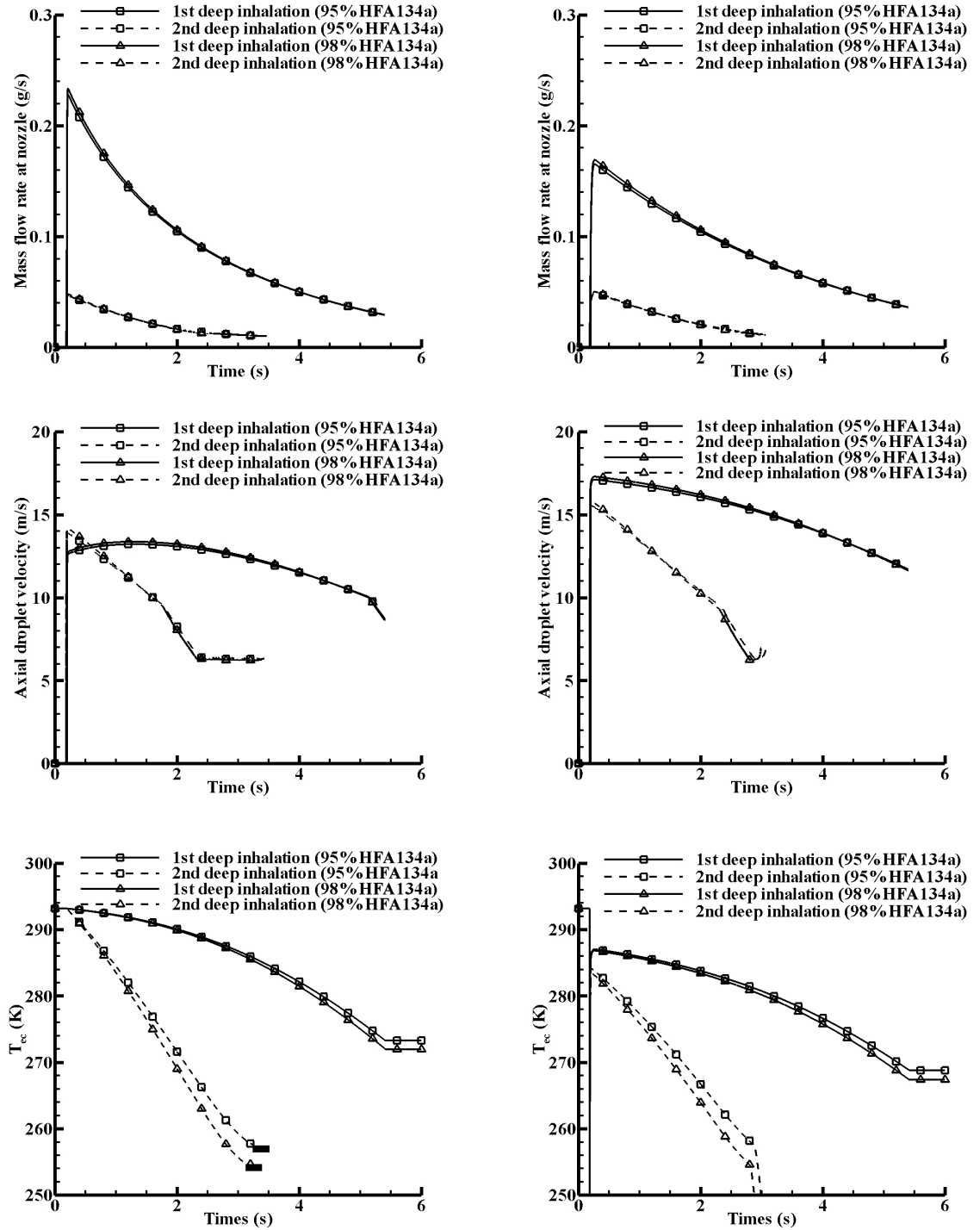


Figure 6.7 Predicted temporal variations of the actuation flow properties at the exit of the actuator nozzle for two formulations (KDCRA103 with 95% HFA 134a and KDCRA122 with 98% HFA 134a) under sequential times of the deep inhalation. (Left column: Oxette® 1; Right column: Oxette® 2).

As there is little difference between the actuation flows of the two formulations under sequential time of the shallow inhalation, only temporal variations of the actuation flow properties at the exit of the actuator nozzle for KDCRA103 (95% HFA 134a) are predicted in Figure 6.8. The pressure reached 96% of the atmospheric pressure after 0.62s from the start of shallow inhalation. Compared to the deep inhalation, a similar conclusion can be made. Oxette® 2 generates the flow with lower mass flow rate but higher axial velocity, which is due to the higher vapour/liquid mass ratio in the expansion chamber, and there is a sharp temperature drop at the beginning of the actuation due to the rapid evaporation. The actuated amount of the formulations decreased after each sequential inhalation, where the spray density ratio at each sequential inhalation is 2.07:1.44:1 according to the predictions of the mass flow rates. This is caused by the increase of vapour/liquid mass ratio in the expansion chamber and results in a reduction of the mass flow rate. The ratio is lower than the measurement by the dual laser beam method (2.8:1.8:1), because the numerical model predicts the flow at actuator nozzle, while the dual laser method measures the spray “accumulated” at  $x=25\text{mm}$  where droplets deposit and are pushed forward by the upstream jet. The axial velocities at  $x=25\text{mm}$  were larger than the measurement by the dual laser method, especially under the 1<sup>st</sup> deep inhalation. There is a 40% deviation from the experimental results. It is thought to be caused by the sharp pressure change at the first 0.2s of the inhalation where turbulent fluctuations influence the velocity measurement by the dual laser method.

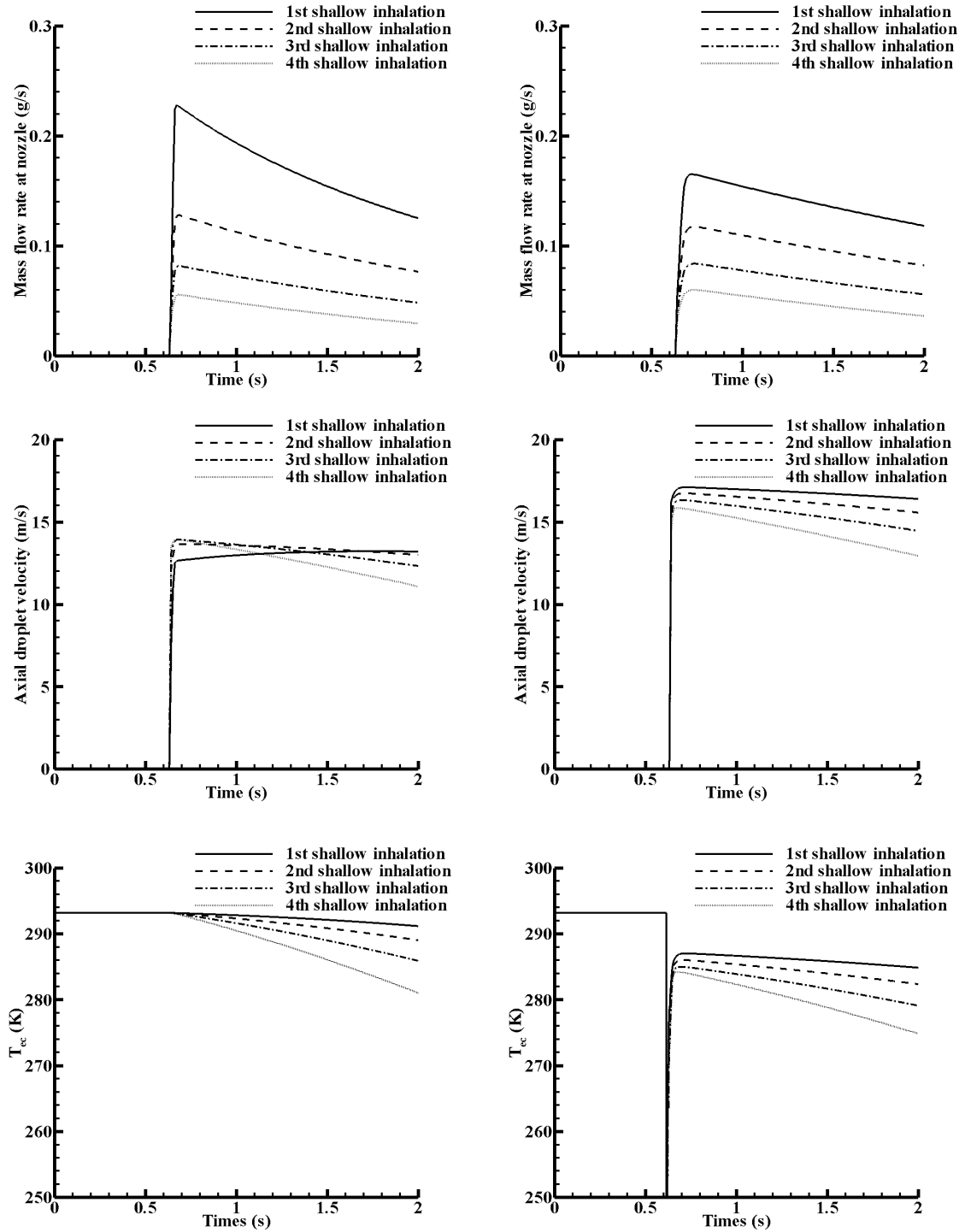


Figure 6.8 Predicted temporal variations of the actuation flow properties at the exit of the actuator nozzle for KDCRA103 (95% HFA 134a) under sequential times of the shallow inhalation (left column: Oxette® 1; right column: Oxette® 2).



	Deep inhalation		Shallow inhalation			
	1st	2nd	1st	2nd	3rd	4th
KDCRA103 (Oxette® 1)	85.88%	11.25%	41.49%	24.09%	15.27%	9.76%
KDCRA122 (Oxette® 1)	86.16%	11.02%	41.90%	24.20%	15.28%	9.72%
KDCRA103 (Oxette® 2)	82.85%	13.18%	34.77%	24.13%	16.80%	11.40%
KDCRA122 (Oxette® 2)	83.25%	12.88%	35.20%	24.30%	16.83%	11.36%

*Table 6.2 Predicted mass fraction of the formulations actuated during each sequentially deep or shallow inhalation for KDCRA103 (95% HFA 134a) and KDCRA122 (98% HFA 134a) with Oxette® 1 and Oxette® 2.*

The flow model predicted the mass fractions of the formulations actuated during each sequential deep or shallow inhalation as listed in Table 6.2. More than twice of the formulation was consumed during the 1<sup>st</sup> deep inhalation (around 86.0%) than that during the 1<sup>st</sup> shallow inhalation (around 41.5%). Although mass flow per inhalation is not particularly constant, the results do highlight how the system can react as would a normal cigarette to a deep or a shallow inhalation. KDCRA103 (95% HFA 134a) generates steadier and relatively slower actuation flow with Oxette® 2 than with Oxette® 1.

Figure 6.9 shows the predictions of initial MMD variations of the sprays at the exit of the actuator nozzle for the two formulations under two smoking profiles and illustrates that KDCRA122 (98% HFA 134a) produces a spray with slightly smaller droplets than KDCRA103 (95% HFA 134a). It indicates that the mass fraction of propellant does not affect the initial MMD very much for these two formulations; hence we will not present the predicted initial MMD variations of KDCRA122 (98% HFA 134a) under the shallow inhalations. Oxette® 1 produces much larger droplet (MMD>50µm) during the actuation and does not meet the design requirement. Oxette® 2 performs better; however, larger droplets are generated at the beginning of 1<sup>st</sup> deep inhalation and 1<sup>st</sup> shallow inhalation. It is caused by the smaller vapor mass fraction in the expansion chamber, which provides less volume for the propellant evaporation, recirculation, bubble generation and growth to produce small droplets. For the spray produced by Oxette® 2, under 1<sup>st</sup> deep inhalation, the predicted initial MMD reaches minimum of 20µm at 3.5s, which is mainly caused by the increasing vapour mass fraction in the expansion chamber. Under 1<sup>st</sup> shallow inhalation, the predicted initial MMD increases at the start of actuation to the maximum of 36µm and then decrease to 30µm at the end of the actuation. The average predicted initial MMD decreases after each shallow inhalation and during the 3<sup>rd</sup> inhalation it

generates the most uniform droplets. Clark (1991) measured the initial MMD of the spray produced by a pMDI as  $12.5\mu\text{m}\sim 22.5\mu\text{m}$  for a formulation with 98% mass fraction of HFA 134a and 2% PEG300 and similarly Dunbar (1996) measured the initial MMD of the spray issued from a pMDI is  $7.3\mu\text{m}$  with pure HFA 134a. Their measured initial MMDs are smaller than our predictions, because the pMDI has a large expansion chamber of  $17.6\text{ mm}^3$ , compared to the  $5.41\text{ mm}^3$  expansion chamber volume of Oxette® 2, and it provides more space for the bubble formation. Encouraging the bubble formation in the expansion chamber results in the increase of  $q_{ec}$  in equation 6.1 and reduces the MMD value.

Large variations of the predicted initial MMD for each sequential inhalation are caused by the increase of the quality of fluid ( $q_{ec}$ ) in equation 6.1. Since the mass fraction of the original fill left at the start of the 2<sup>nd</sup> deep inhalation or the 4<sup>th</sup> shallow inhalation is less than 13%, fine sprays will not be generated and a refill is required. It should be noted that the qualitative predictions of the model for Oxette® 1 and Oxette® 2 are in agreement with the experiment in that the obscuration is much less for Oxette® 2 and that the model predicts far larger primary drops. On the other hand the effect of the formulation is much more sensitive in reality than is predicted in the model. This can be due to the simple equilibrium evaporation assumption that is assumed in the model. The model does however show more variation for Oxette® 1 compared to Oxette® 2.

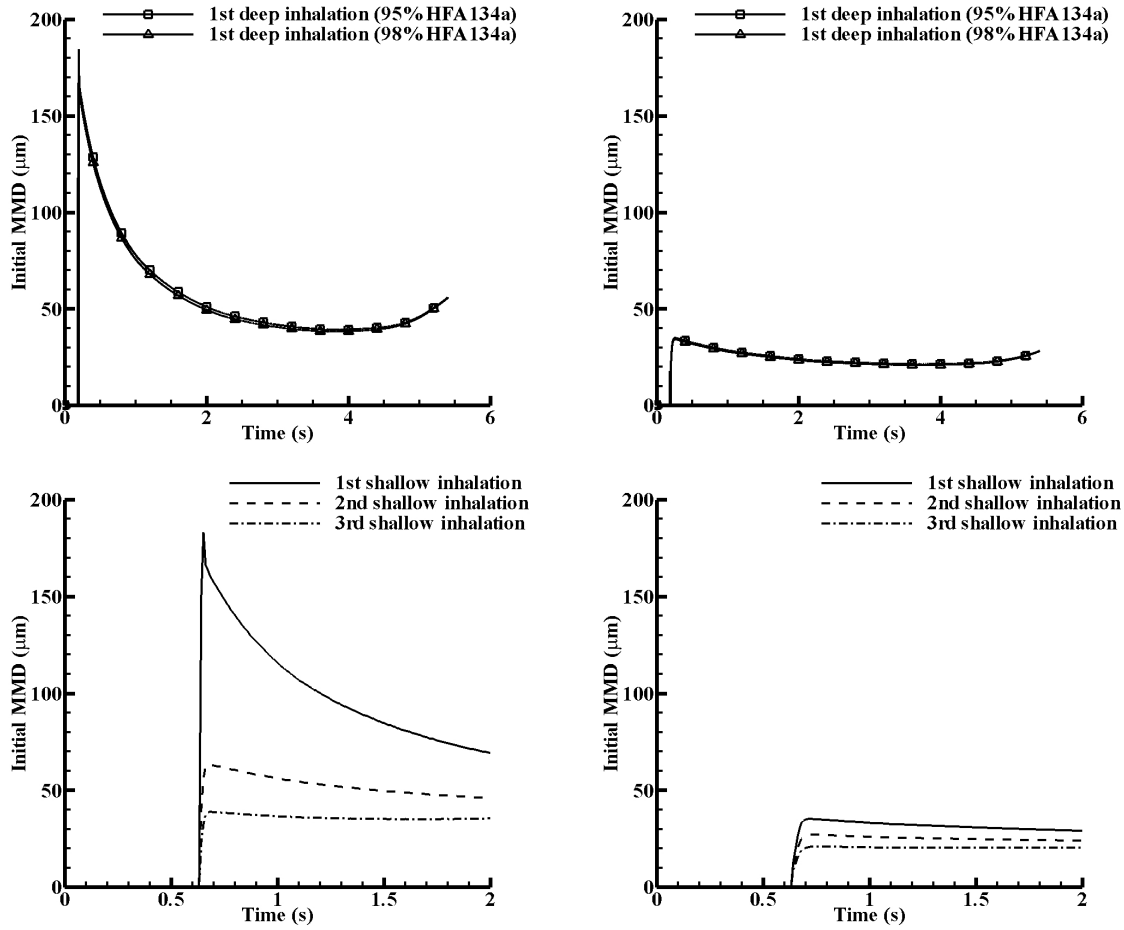


Figure 6.9 Predicted temporal variations of predicted initial MMD at the exit of the actuator nozzle for KDCRA103 (95% HFA 134a) and KDCRA122 (98% HFA 134a) under the 1<sup>st</sup> deep inhalation; and only for KDCRA103 under sequential times of the shallow inhalation (left column: Oxette® 1; right column: Oxette® 2).

### 6.3.3 Prediction of residual droplet sizes of the aerosol at x=100mm from the actuator nozzle

With the known velocities, temperatures and vapour/liquid mass ratios of the actuation flow which were analyzed previously, the residual droplet sizes of the spray at x=100mm from the actuator nozzle can be predicted from the initial droplet sizes at the exit of the actuator nozzle due to the evaporation of the droplet, following the assumptions of the multi-component evaporation model of Brenn et al. (2007) in section 6.2.1. The axial velocities of the droplets are assumed to vary linearly along the jet from the exit of the actuator nozzle to x=100mm (Calay and Holdo, 2008; Polanco et al., 2010), with the

boundary conditions of the flow velocities at  $x=100\text{mm}$  measured by the dual laser method (Table 6.1).

In order to find how the droplets with different initial diameters at the exit of the actuator nozzle affect their residual diameters at  $x=100\text{mm}$  from the actuator nozzle, the droplets with initial diameter of  $1\mu\text{m}\sim 400\mu\text{m}$  at the exit of the actuator nozzle were tested for the two formulations. The ratios between the residual diameter at  $x=100\text{mm}$  from the actuator nozzle and initial diameter at the exit of the actuator nozzle under the 1<sup>st</sup> shallow inhalation are shown in Figure 6.10. KDCRA103 (95% HFA 134a) generates larger droplets than KDCRA122 (98% HFA 134a) due to its higher mass fraction of inerts. For the droplets of KDCRA103 (95% HFA 134a) with initial diameter smaller than  $175\mu\text{m}$ , all the propellant in the droplets evaporated before the droplet reached  $x=100\text{mm}$  and only inerts remained. It indicates that a portion of droplets of KDCRA103 (95% HFA 134a) flow into the human oropharynx with pure inerts but others contain a certain mass fraction of HFA 134a depending on the droplets sizes. It provides the initial conditions on the mass fraction of the components in the droplets when simulating the droplet deposition in the human respiratory tract. Compared to KDCRA103 (95% HFA 134a), similar results were acquired for the droplets of KDCRA122 (98% HFA 134a) (Figure 6.10), with the difference that the droplets with diameters smaller than  $150\mu\text{m}$  fully evaporated without any propellant left in the droplets. Because the propellant with higher mass fraction of HFA 134a in KDCRA122 (98% HFA 134a) takes more time to evaporate than KDCRA103 (95% HFA 134a), it concludes that the residual diameter at  $x=100\text{mm}$  from the actuator nozzle depends on the initial droplet sizes and the mass fraction of the propellant in the formulations.

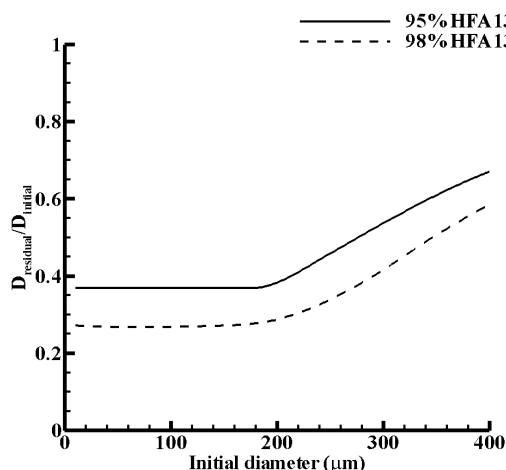


Figure 6.10 The predicted ratios of the residual diameter at  $x=100\text{mm}$  from the actuator nozzle and initial diameter at the exit of the actuator nozzle under the 1<sup>st</sup> shallow inhalation for KDCRA103 (95% HFA 134a) and KDCRA122 (98% HFA 134a).

Following the predicted initial MMDs at the exit of the actuator nozzle acquired previously (Figure 6.9), the residual MMDs at  $x=100\text{mm}$  predicted by the multi-component evaporation model (Brenn et al., 2007) are shown in Figure 6.11. As stated previously, the mass fraction of the propellant does not affect the predicted initial MMD at the exit of the actuator nozzle under the 1<sup>st</sup> deep inhalation (Figure 6.9); it does however influence the predicted residual MMD at  $x=100\text{mm}$  under the 1<sup>st</sup> deep inhalation (Figure 6.11). With higher mass fraction of HFA 134a, KDCRA122 (98% HFA 134a) produced smaller droplets than KDCRA103 (95% HFA 134a). The ratio of the predicted residual MMD of the droplets generated by KDCRA122 (98% HFA 134a) and KDCRA103 (95% HFA 134a) is 0.73, which is the same as the 1/3 order of the ratio of the mass fraction of the inerts between two formulations. At  $x=100\text{mm}$ , the residual MMD of the spray issued from a pMDI measured by Dunbar (1996) is  $6.1\mu\text{m}$  with pure HFA 134a, which is smaller than our predictions. The difference is caused not only by the smaller expansion chamber volume of the Oxette®, but also because the mass fraction of inerts in our formulations is larger than that in the case of Dunbar (1996).

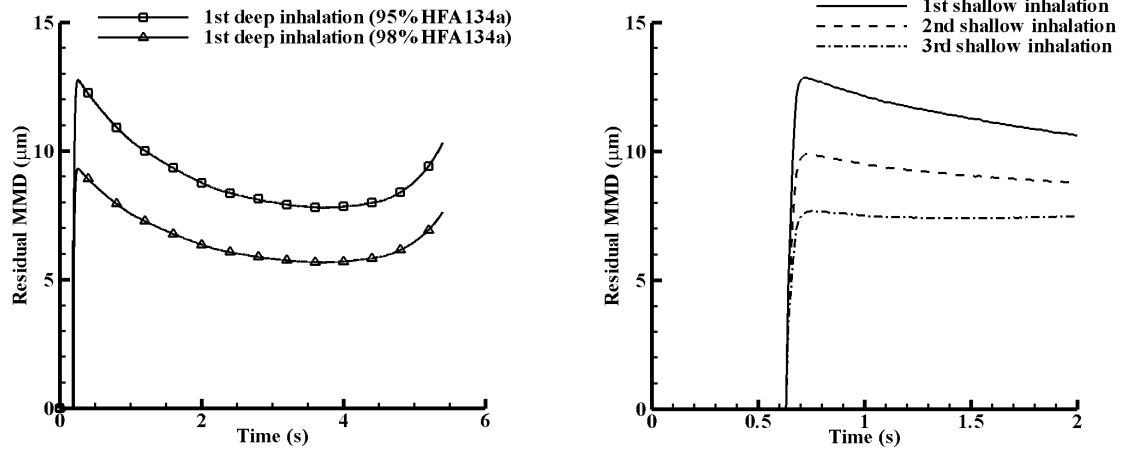
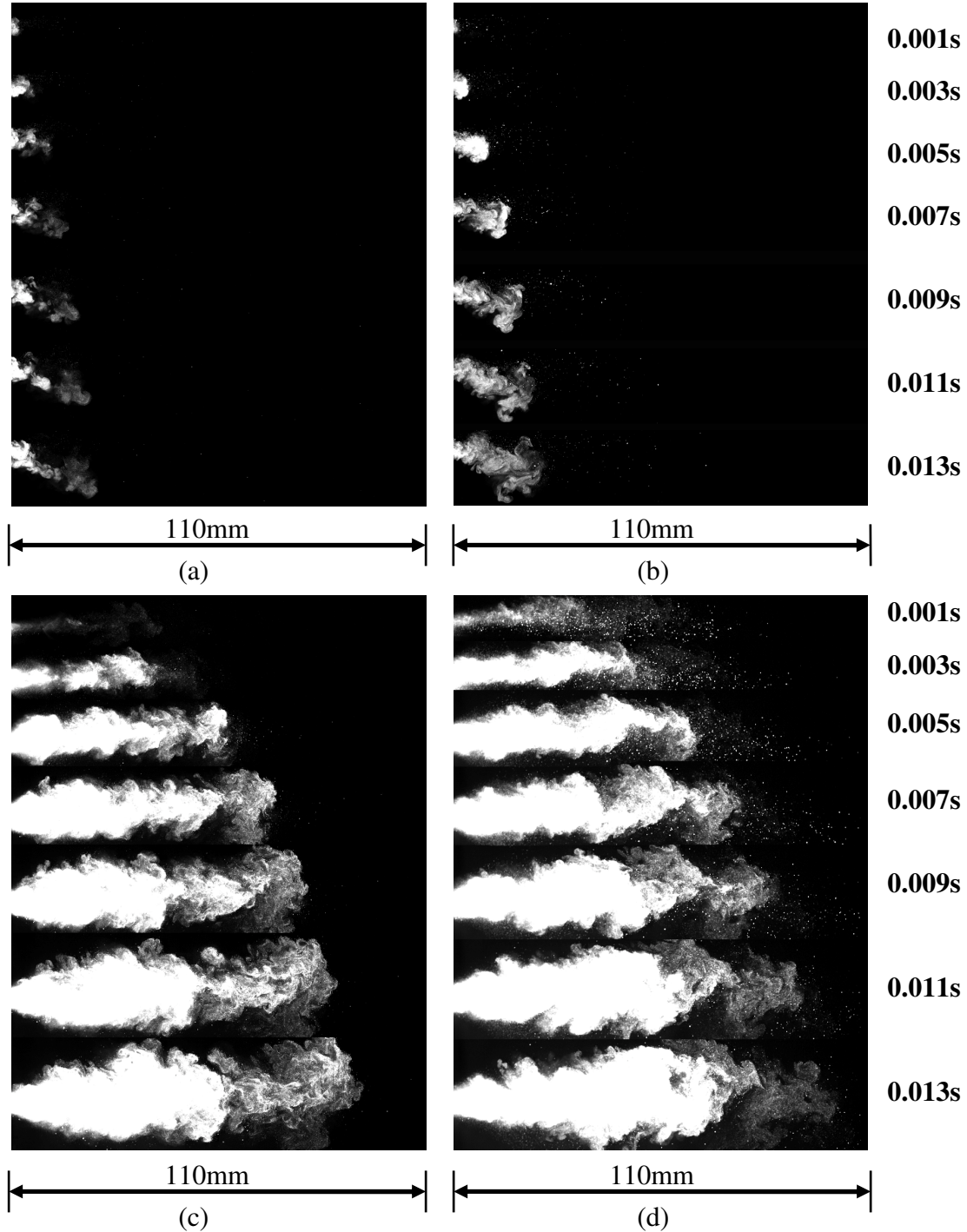


Figure 6.11 Predicted temporal variations of predicted residual MMD of the spray generated by Oxette® 2 at  $x=100\text{mm}$  from the actuator nozzle for KDCRA103 (95% HFA 134a) and KDCRA122 (98% HFA 134a) under the 1<sup>st</sup> deep inhalation (left); and only for KDCRA103 under sequential times of the shallow inhalation (right).

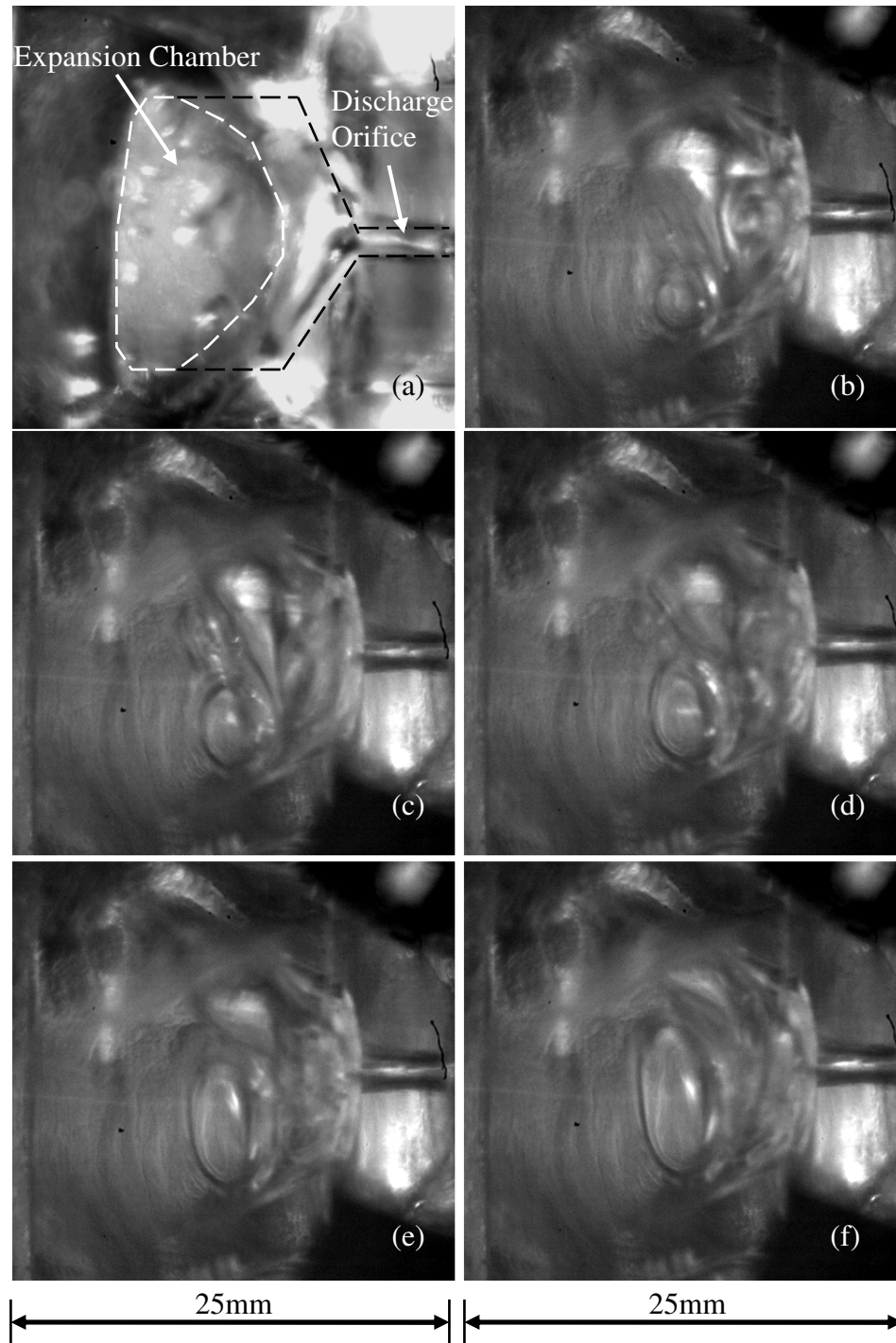
### 6.3.4 Internal and external spray characters

Recorded by high speed imaging, Figure 6.12(a) and Figure 6.12(b) show the spray development at the start (0.001s~0.013s) of the actuation flow under the 1<sup>st</sup> shallow inhalation for KDCRA103 (95% HFA 134a) and KDCRA122 (98% HFA 134a) by Oxette® 1. It shows Oxette® 1 cannot produce fully developed fine sprays, which indicates the small expansion chamber cannot provide enough space and time for the bubble nucleation and formation to generate aerosols. However, KDCRA122 (98% HFA 134a) generated a more “violent” spray (notable boiling phenomena) compared to KDCRA103 (95% HFA 134a), due to its higher mass fraction of volatile propellant (HFA 134a). Figure 6.13 provides sequential visualizations of internal flow regime inside expansion chamber of Oxette® 1 during the actuation at a 500Hz frame rate. Figure 6.13(a) presents the cross section of the expansion chamber and the actuator nozzle without any flow. A bubble formed at the bottom of the expansion chamber and expanded during the sequential 0.008s as shown in Figure 6.13(b)~6.13(f), meanwhile it pushed the liquid out through the actuator nozzle. Oxette® 1 provides only a small expansion chamber volume to form small bubbles but squeezes them into a large single bubble, which causes it to function as a plain-orifice atomizer resulting in poor atomization (reviewed in section 2.2.2, Chapter 2). Since Oxette® 1 produces poor spray, we will not

discuss its spray characteristics in the following sections, and however, the previous sections provide its general spray plume characteristics.



*Figure 6.12 Visualization during 0.001s ~ 0.013s after the start of the 1<sup>st</sup> shallow inhalation: (a) with Oxette® 1 for KDCRA103 (95% HFA 134a); (b) with Oxette® 1 for KDCRA122 (98% HFA 134a); (c) with Oxette® 2 for KDCRA103 (95% HFA 134a); and (d) with Oxette® 2 for KDCRA122 (98% HFA 134a).*



*Figure 6.13 Visualization of internal flow regime inside expansion chamber of Oxette® 1: (a) presents the cross section of the expansion chamber and the actuator nozzle without any flows; (b) ~ (f) sequential images of the internal flow in the expansion chamber recorded at 500Hz.*



Figure 6.12(c) and Figure 6.12(d) show the spray development at the start (0.001s~0.013s) of the actuation flow under the 1<sup>st</sup> shallow inhalation for KDCRA103 (95% HFA 134a) and KDCRA122 (98% HFA 134a) by Oxette® 2. Flashing is shown to be occurring outside the actuator nozzle but it may begin inside the actuator nozzle or expansion chamber. Large droplets were generated by KDCRA122 (98% HFA 134a) during the early atomization phase, and they remained and moved quickly in front of the main spray (Figure 6.12(d)). KDCRA122 (98% HFA 134a) has a higher fraction of propellant HFA 134a and generates a higher pressure, which causes the liquid phase of the formulation to be expelled quickly by high pressure without full evaporation. On the contrary, KDCRA103 (95% HFA 134a) produces better atomization. Different from a typically linearly spreading turbulent round jet (Pope, 2000), Yildiz et al. (2002) divided the flashing liquid jet issuing from a circular nozzle into an expansion region and an entrainment region. They experimentally observed the jet in the expansion region moving with increasing velocity. The velocity starts to decrease in the entrainment region due to mixing with ambient air as the jet propagates until it reaches its minimum as droplets evaporate. Hence, several parameters are required to be defined to characterize the spray as shown in Figure 6.14. Although the cone angle of a spray needs to be measured from the virtual origin of the turbulent jet, the diameter of the actuator nozzle (0.2mm) is small enough to neglect the virtual origin position (Kotsovinos, 1976). All spray angles in this study were measured from the actuator nozzle. An unprocessed sample of jet generated under 1<sup>st</sup> shallow inhalation with KDCRA103 (95% HFA 134a) by Oxette® 2 is shown in Figure 6.14(a), and it was thresholded to pick out the spray outline from the background as shown in Figure 6.14(b). Morgan et al. (2001) concluded that the measured values were insensitive to the threshold level chosen, but the threshold value has to be constant during processing of the images. The spray penetration was measured by finding the spray pixel furthest from the actuator nozzle. This value of penetration was then used to calculate the half spray angle ( $\theta_3$  and  $\theta_4$ ) at half the maximum penetration length. Similarly the half spray angle in the expansion region are defined as  $\theta_1$  and  $\theta_2$  in Figure 6.14(b).

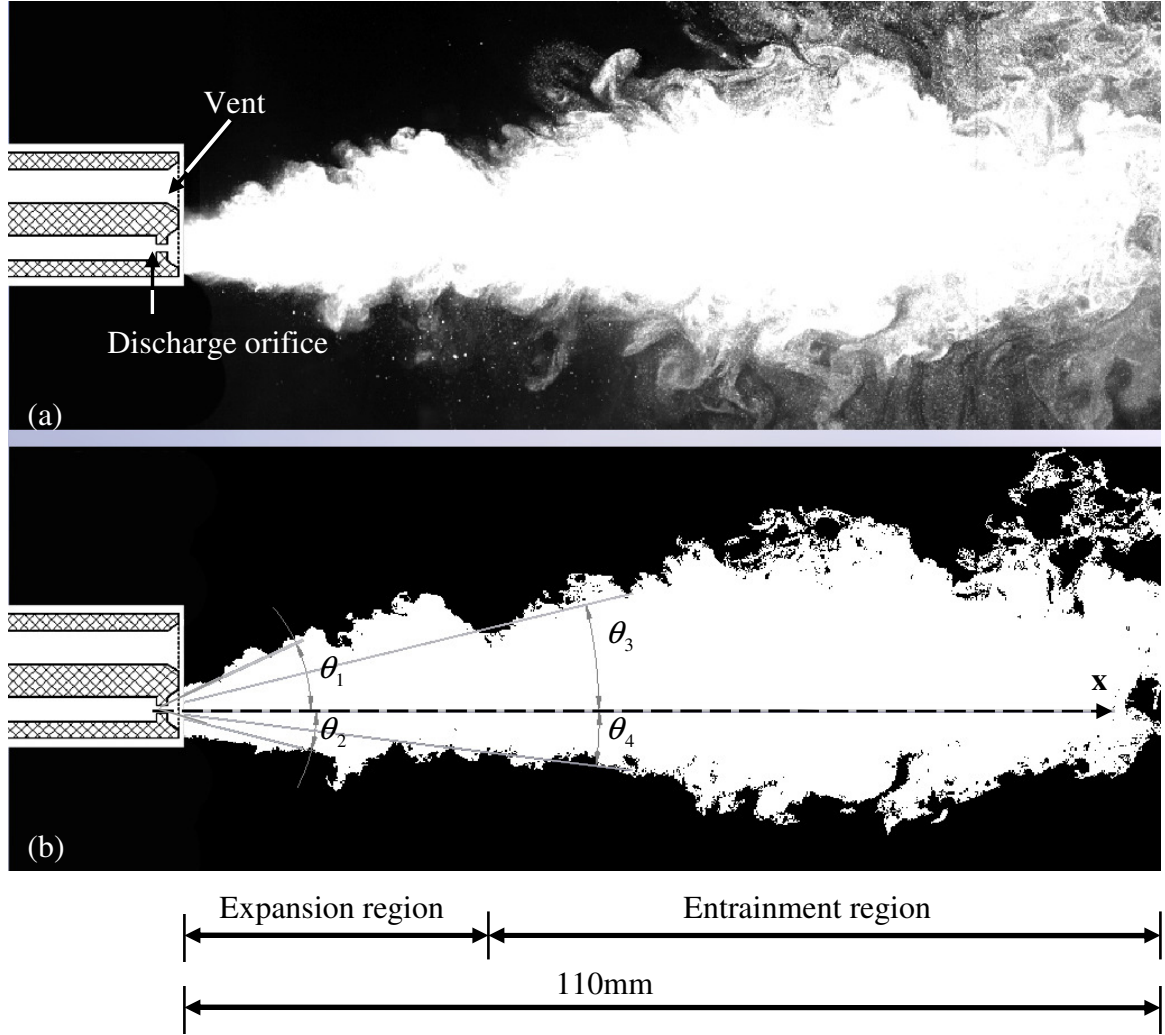


Figure 6.14 A sample of jet generated under 1<sup>st</sup> shallow inhalation with Oxette® 2 for KDCRA103 (95% HFA 134a) (a) unprocessed image and (b) thresholded image.

In our experiment, the corresponding jet tip penetrations and penetration rates under 1<sup>st</sup> shallow inhalation and 1<sup>st</sup> deep inhalation during 0.001s ~ 0.012s from the start of actuation were measured from the raw data (for example, Figure 6.12) and shown in Figure 6.15. Under the 1<sup>st</sup> shallow inhalation, the jet axial velocities followed the trend discovered by the previous researchers (Yildiz et al., 2002; Calay and Holdo, 2008; Polanco et al., 2010), where the peak velocities were detected at 0.002s for both formulations, which indicated the expansion ended at approximately 30mm from the actuator nozzle (spray front tip position at 0.002s); KDCRA122 (98% HFA 134a) generated a faster jet at a mean velocity of 10.1 m/s compared with 9.4m/s generated by KDCRA103 (95% HFA 134a) under the 1<sup>st</sup> shallow inhalation. Under the 1<sup>st</sup> deep

inhalation, the maximum velocities were found at 0.001s around 20mm from the actuator nozzle, which indicates the jet generated by the shallow inhalation has a longer expansion region than that under deep inhalation.

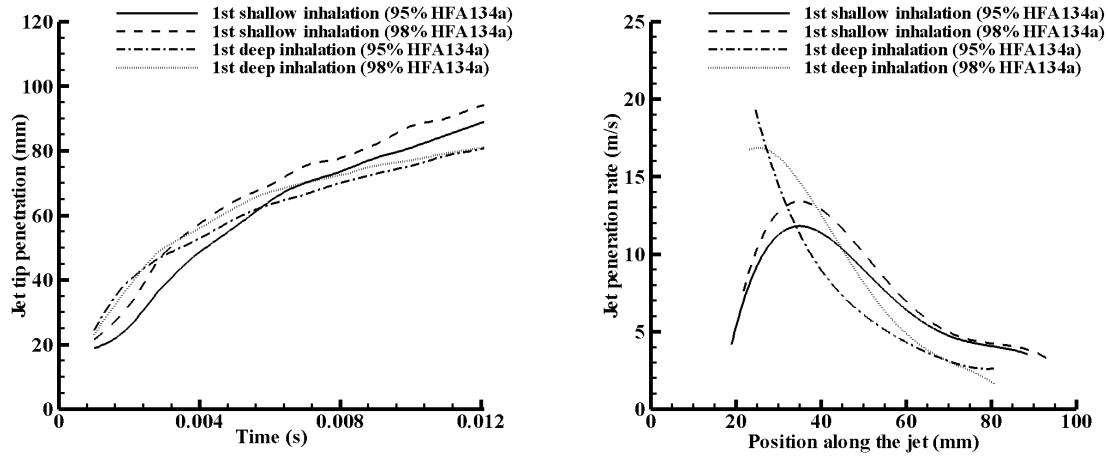


Figure 6.15 Left: The corresponding jet tip penetration and Right: jet penetration rate along the jet during the first 0.001s~0.012s under 1st shallow inhalation profile for KDCRA103 (95% HFA 134a) and KDCRA122 (98% HFA 134a).

The spreading rate of a turbulent round jet can be defined as equation 6.2 from the half spray angle

$$S = \frac{dr_{1/2}(x)}{dx} = \tan(\theta/2) \quad (6.2)$$

where  $r_{1/2}$  is the jets half width,  $\theta$  is the half spray angle ( $\theta_1 \sim \theta_4$  in Figure 6.14(b)) and  $x$  is the axial length of the jet from the actuator nozzle.

Figure 6.16 shows the spray development sequences of the jet flow during 0.1~1.1s under the 1<sup>st</sup> shallow inhalation for KDCRA103 (95% HFA 134a) and KDCRA122 (98% HFA 134a). It is thought the boiling process dominates the spray characters in the expansion region and turbulent mixing dominates during the entrainment region. KDCRA122 (98% HFA 134a) has a higher propellant mass fraction than KDCRA103 (95% HFA 134a), so that KDCRA122 (98% HFA 134a) evaporated more into the ambient environment at 1.1s resulting in a sparser spray than that generated by KDCRA103 (95% HFA 134a). Vu and Aguilar (2009) suggested that a combination of evaporation and boiling processes can describe the external flow of a flashing jet. The boiling process is a volume based phenomenon, which can be observed from the internal

flow (Figure 6.13) and external expansion region. Large drops were produced from upper and lower edges of the actuator nozzle at the expansion region of the spray generated by KDCRA122 (98% HFA 134a), which indicates there is an internal annular flow in the actuator nozzle. At the expansion region, the “explosion” phenomena became weak after 0.8s from the start of the actuation, which is due to the reduction of the formulation actuated and the decrease of the degree of superheat.

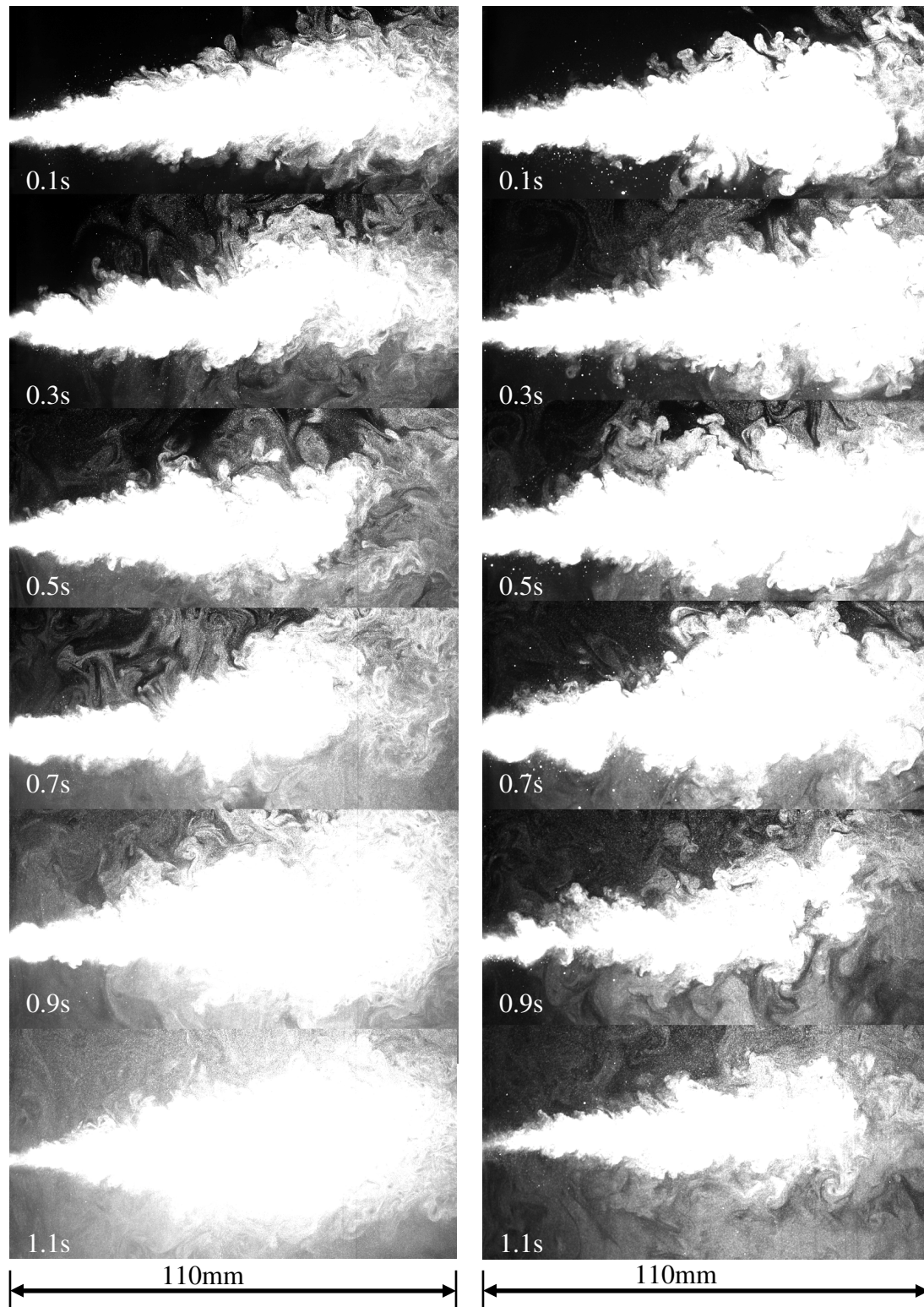


Figure 6.16 Spray visualization from 0.1s to 1.1s under the 1<sup>st</sup> shallow inhalation with Oxette® 2 for KDCRA103 (left: 95% HFA 134a) and KDCRA122 (right: 98% HFA 134a).

The spray cone angles and spreading rates at different time steps were measured under the 1<sup>st</sup> shallow inhalation by Oxette® 2 for both formulations and listed in Table 6.3. Due to the higher vapour pressure of KDCRA122 (98% HFA 134a) caused by the higher mass fraction of propellant, KDCRA122 (98% HFA 134a) was actuated faster and had a shorter flow duration (1.1s) than that of KDCRA103 (95% HFA 134a) (1.4s). For both of the formulations, the averaged upper angles ( $\theta_1$  and  $\theta_3$ ) are larger than the lower angles ( $\theta_2$  and  $\theta_4$ ), which was caused by the entrainment from the vent at the top of the Oxette® (Figure 6.14(a)) and the recirculation in the closed inspiration chamber. Compared to KDCRA103 (95% HFA 134a), the spray generated by KDCRA122 (98% HFA 134a) has higher vapour pressure, which causes the boiling phenomena to be more “violent” and averaged  $\theta_1$  larger than that of KDCRA103 (95% HFA 134a). However, due to a higher mass fraction of HFA 134a, KDCRA122 (98% HFA 134a) evaporated more into the ambient environment resulting in a smaller spray angles ( $\theta_3$  and  $\theta_4$ ) than that generated by KDCRA103 (95% HFA 134a) in the entrainment region.

Different from the turbulent round jet of a single phase spreading linearly at a constant spreading rate of 0.10 (Pope, 2000), the spreading rates of a flashing jet are unsteady with time. Standard deviations (STD) of the spray angle ( $\theta_1$ ) show the pulsations in the spray produced by KDCRA122 (98% HFA 134a) are more notable than those of KDCRA103 (95% HFA 134a) in the expansion region. Dunbar (1996) measured the half spray angles of the jet issuing from a pMDI with pure HFA 134a, the angles are 8.5°~11.3° at 0~50mm from the actuator nozzle and 10.2°~11.9° at 50~125mm from the actuator nozzle. Dunbar (1996) did not observe the boiling phenomena in the expansion region since it was blocked by the mouthpiece. He found the upper and lower region of the spray were approximately symmetric, which is caused by the different vent designs of the pMDI where the ventilation surrounds the whole jet.

Time step	Half spray angle (°)				Spray spreading rate			
	$\theta_1$	$\theta_2$	$\theta_3$	$\theta_4$	$S_1$	$S_2$	$S_3$	$S_4$
<b>KDCRA103</b>								
0.1	16	8	14	6	0.11	0.06	0.10	0.04
0.2	15	13	12	8	0.10	0.09	0.08	0.05
0.3	18	10	12	6	0.12	0.07	0.09	0.04
0.4	14	10	13	9	0.10	0.07	0.09	0.06
0.5	16	10	12	8	0.11	0.07	0.08	0.06
0.6	15	10	13	8	0.10	0.07	0.09	0.06
0.7	14	8	14	7	0.09	0.06	0.10	0.05
0.8	16	10	18	9	0.11	0.07	0.12	0.06
0.9	16	10	18	10	0.11	0.07	0.13	0.07
1.0	22	13	18	11	0.15	0.09	0.12	0.07
1.1	16	12	17	13	0.11	0.08	0.12	0.09
1.2	14	10	16	11	0.09	0.07	0.11	0.07
1.3	12	11	15	12	0.08	0.08	0.10	0.08
1.4	11	10	15	11	0.08	0.07	0.10	0.08
Average	15	10	15	9	0.11	0.07	0.10	0.06
STD	1.4	1.7	0.9	1.0	0.02	0.01	0.02	0.01
<b>KDCRA122</b>								
0.1	16	9	12	7	0.11	0.06	0.08	0.05
0.2	15	12	10	6	0.11	0.08	0.07	0.04
0.3	15	9	13	8	0.10	0.06	0.09	0.05
0.4	17	7	13	7	0.12	0.05	0.09	0.04
0.5	20	7	13	8	0.14	0.05	0.09	0.05
0.6	18	7	17	6	0.12	0.05	0.11	0.04
0.7	20	13	15	7	0.14	0.09	0.10	0.05
0.8	14	6	18	5	0.10	0.04	0.13	0.04
0.9	13	7	14	6	0.09	0.05	0.10	0.04
1.0	13	5	12	5	0.09	0.03	0.08	0.04
1.1	13	5	12	5	0.09	0.03	0.08	0.04
Average	16	8	14	6	0.11	0.06	0.09	0.04
STD	2.0	2.4	2.0	0.7	0.02	0.02	0.02	0.01

Table 6.3 Half spray cone angles and spreading rates under 1<sup>st</sup> shallow inhalation with Oxette® 2 for KDCRA103 (95% HFA 134a) and KDCRA122 (98% HFA 134a) from 0.1s to 1.4s.

Periodic pulsations can be observed near the actuator nozzle and some visualisations of the jet expansion region are shown in Figure 6.17, where the photos were taken between 0.151s~0.158s from the start of actuation at a frame rate of 1000Hz. There are clear gaps



between pulses. Each pulsation causes a large fluctuation of the instantaneous spray cone angle. The time scale between two sequential pulsation is 1ms~2ms.

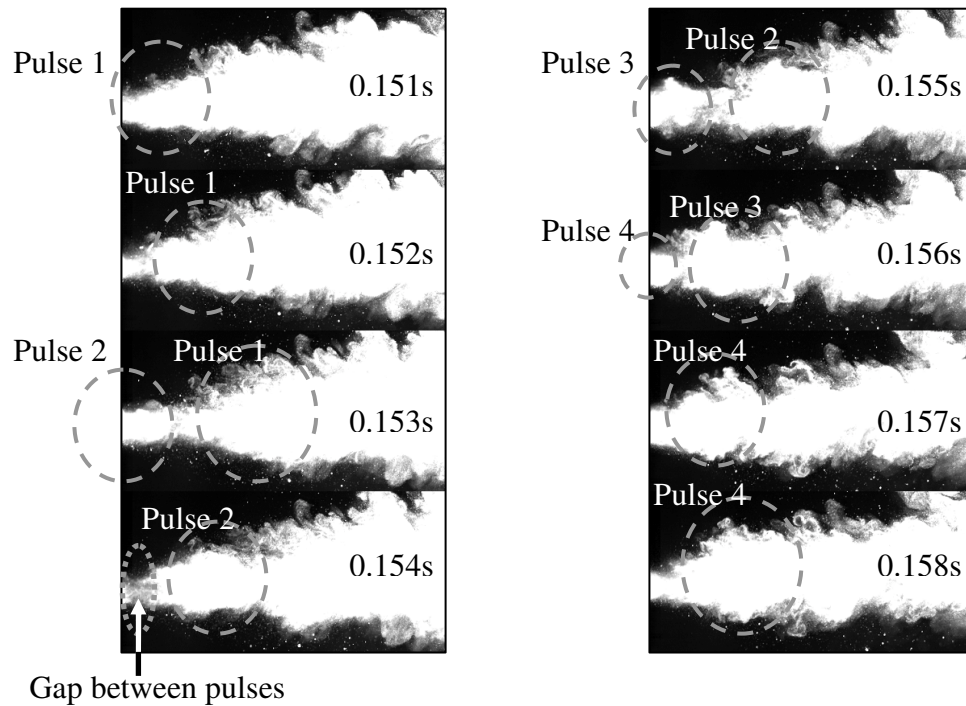


Figure 6.17 Spray visualization at the expansion region from 0.151s to 0.158s under 1<sup>st</sup> shallow inhalation with Oxette® 2 for KDCRA122 (98% HFA 134a).

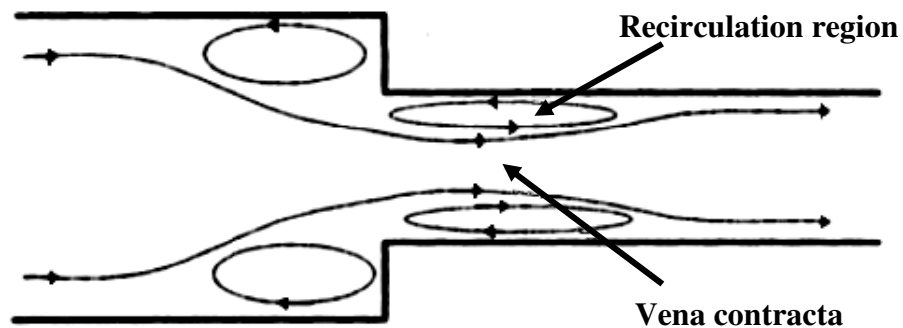


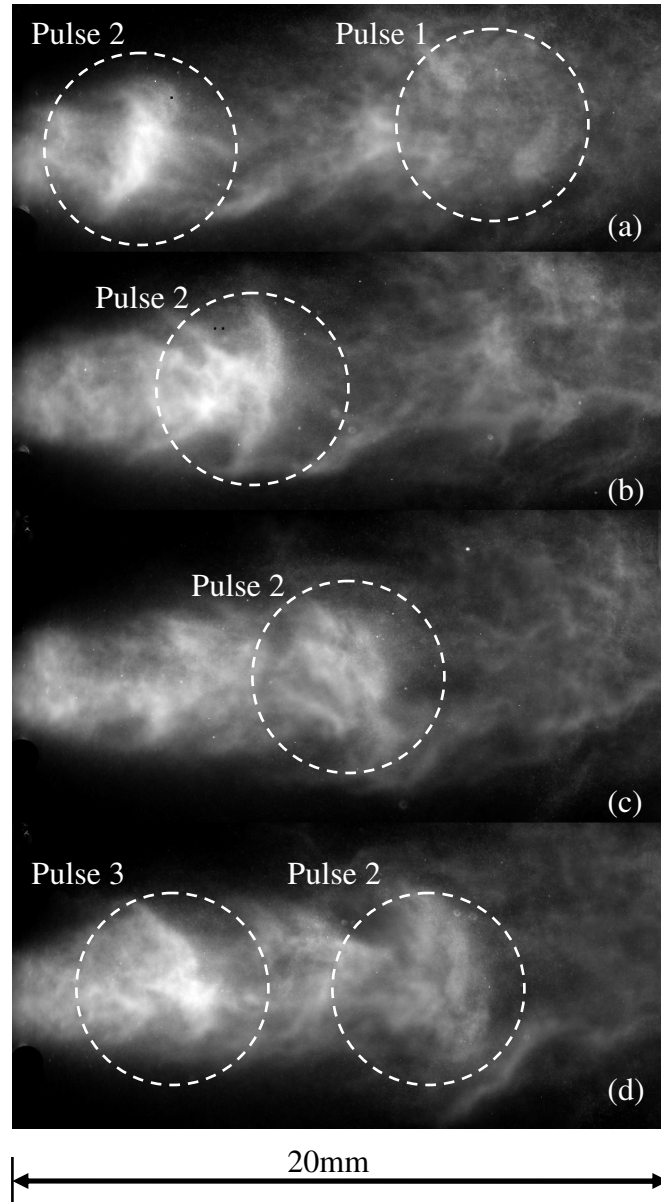
Figure 6.18 Mean streamlines of the flow in a constriction examined by Domnick et al. (1995).

Domnick et al. (1995) concluded that the periodic behaviour is the result of the bubble growth process which depends on the evaporation process and the location of bubble creation. They tested the flow and showed that bubble growth occurs in recirculation



regions inside the constriction (Figure 6.18). The lowest pressure in this flow occurs in the cross-section where the recirculation regions and vena contracta are present. Nucleation bubbles that enter the recirculation region are exposed to this reduced pressure for a longer time than bubbles that stream through and which are not captured by the recirculation region. The increased residence time of bubbles in the recirculation region allows such bubbles to undergo large growth, causing the volume of the recirculation region to grow until it obstructs enough of the channel that the incoming liquid flushes a large portion of the recirculation region downstream. Bubbles in the recirculation region, which are reduced in size after this flushing, then build up the size of the recirculation region, and the cycle occurs again. The result is a rapidly oscillation bubbly flow downstream at a frequency of 500~800Hz (Domnick et al., 1995).

Figure 6.19 provides a closer view on the expansion region of the jet which was recorded at the frame rate of 5kHz. Figure 6.19(a) shows a new pulse (pulse 2) pushed out from the actuator nozzle and pulse 1 dispersed into atmosphere in Figure 6.19(b). Another new pulse (pulse 3) formed in Figure 6.19(d). There is a 0.6ms time interval between pulse 2 and pulse 3, which is smaller than that discovered by Domnick et al. (1995) and Dunbar (1996). It implies the pulsation of the jet is unsteady with time and it remains complex to analyse.



*Figure 6.19 Close visualizations on the pulsations near the exit of the actuator nozzle under 1<sup>st</sup> shallow inhalation with Oxette® 2 for KDCRA103 (95% HFA 134a), sequentially recorded at 5kHz.*

### **6.3.5 Drop sizing at an axial distance of $x=100\text{mm}$ from the actuator nozzle**

Drop sizing work is done at the position of (100mm, 0mm) from the actuator nozzle by the newly developed particle/droplet image analysis (PDIA) method (Chapter 4) using a high speed laser system. The droplet information was recorded during 0~2s of the actuation with 500Hz camera exposure frequency under the 1<sup>st</sup> shallow inhalation. The

number distributions are shown in Figure 6.20 for KDCRA103 (95% HFA 134a) and KDCRA122 (98% HFA 134a). Both formulations generated a peak at  $8\mu\text{m}\sim 10\mu\text{m}$ . Due to the smaller mass fraction of inerts for KDCRA122 (98% HFA 134a), a larger number of droplets with diameter smaller than  $10\mu\text{m}$  were formed by KDCRA122 (98% HFA 134a). The oscillations in the figures are caused by the occasional large droplets generated by the ligaments as show in Figure 6.21.

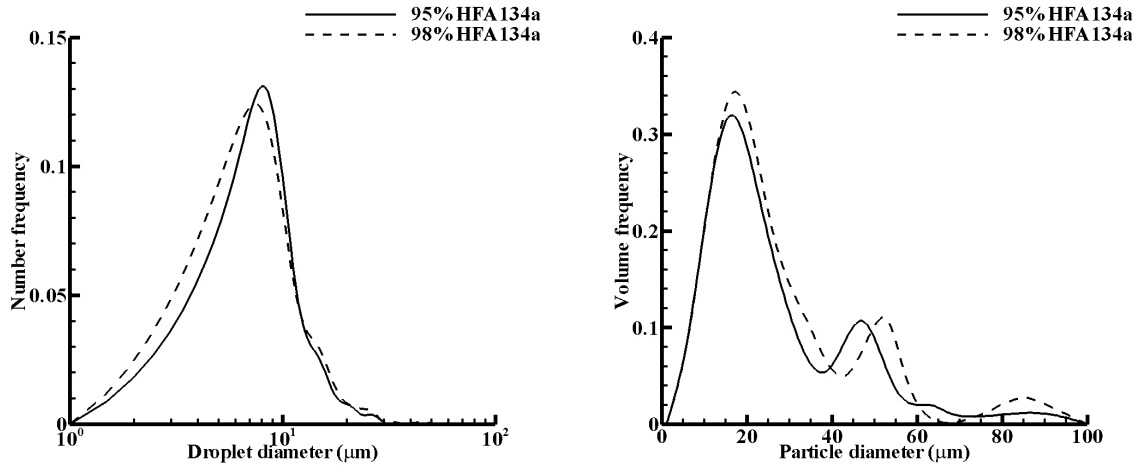


Figure 6.20 Number and volume based size distributions of the droplets for the spray generated by KDCRA103 (95% HFA 134a) and KDCRA122 (98% HFA 134a) under the 1<sup>st</sup> shallow inhalation.

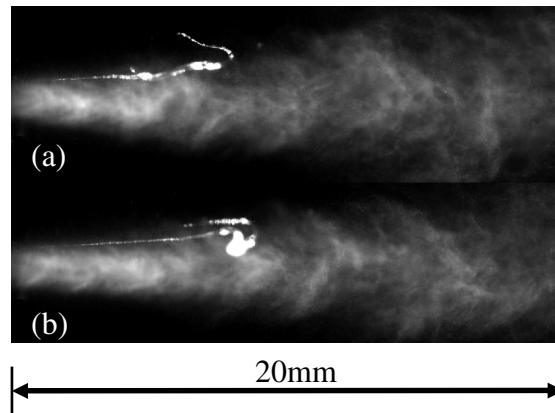


Figure 6.21 Large drop in (b) formed by the ligament from (a) due to the turbulent mixing.

Mean diameters  $D_{10}$ ,  $D_{0.1}$ ,  $D_{0.5}$  and  $D_{0.9}$  (Appendix AIII.5) are used to compare the drop sizes at different time scales and the results are presented in Table 6.4, where the droplet information was acquired from 1000 images every 0.2s time interval. The smallest mean diameters and most dense spray (according to the detected droplet number)

are detected at 0.4~0.6s where the inhalation pressure is minimum and the convection effect is maximum.

Mean diameters ( $\mu\text{m}$ ) for KDCRA103							
Time scale (s)	D <sub>10</sub>	D <sub>32</sub>	D <sub>0.1</sub>	D <sub>0.5</sub>	D <sub>0.9</sub>	D <sub>0.5</sub> /D <sub>32</sub>	Detected droplet number
0~0.2	16.8	24.7	12.8	25.3	44.8	1.02	12
0.2~0.4	9.8	20.1	10.3	25.3	56.3	1.25	3921
0.4~0.6	9.8	17.1	9.3	19.8	46.8	1.15	3527
0.6~0.8	10.3	18.4	10.3	21.3	51.3	1.15	2763
0.8~1.0	10.4	19.2	10.3	24.3	50.3	1.26	2014
1.0~1.2	11.0	21.4	11.8	25.8	66.8	1.21	1787
1.2~1.4	10.8	21.4	12.8	26.3	49.3	1.23	1907
1.4~1.6	10.3	21.0	12.8	25.8	51.3	1.23	1676
1.6~1.8	10.3	20.6	11.8	25.3	55.8	1.23	1513
1.8~2.0	10.1	18.9	10.3	23.3	49.3	1.23	1230
Average	10.9	20.3	11.2	24.2	52.2	1.20	2035
Mean diameters ( $\mu\text{m}$ ) for KDCRA122							
Time scale (s)	D <sub>10</sub>	D <sub>32</sub>	D <sub>0.1</sub>	D <sub>0.5</sub>	D <sub>0.9</sub>	D <sub>0.5</sub> /D <sub>32</sub>	Detected droplet number
0~0.2							0
0.2~0.4	9.3	18.0	9.3	21.3	53.3	1.18	1331
0.4~0.6	9.0	16.0	8.8	17.8	54.3	1.11	1563
0.6~0.8	10.1	18.2	9.3	21.3	61.8	1.17	1326
0.8~1.0	10.1	18.5	9.8	22.3	62.3	1.21	982
1.0~1.2	9.3	16.8	8.8	19.3	54.3	1.14	711
1.2~1.4	9.7	17.0	8.8	19.8	50.8	1.16	577
1.4~1.6	9.9	17.9	9.3	18.3	38.8	1.19	416
1.6~1.8	10.2	16.1	9.3	18.3	38.8	1.14	392
1.8~2.0	10.6	19.2	10.3	22.3	70.8	1.16	362
Average	9.8	17.5	9.3	20.0	53.9	1.16	766

Table 6.4 Mean diameters ( $\mu\text{m}$ ) at different time scales under the 1<sup>st</sup> shallow inhalation with Oxette® 2 for KDCRA103 (95% HFA 134a) and KDCRA122 (98% HFA 134a).

Mean diameters were acquired under the 1<sup>st</sup> shallow inhalation with Oxette® 2 for KDCRA103 (95% HFA 134a) and KDCRA122 (98% HFA 134a). Ten tests were operated under the same conditions for each formulation and results are shown in Table 6.5, where 1000 images were analyzed for each test. According to the droplet number detected, more than twice the droplet number was detected for KDCRA103 (95% HFA 134a) than that for KDCRA122 (98% HFA 134a), which is due to its higher mass fraction of inerts and droplet with diameters smaller than 3 $\mu\text{m}$  may be lost due to the calibration threshold of the system (Chapter 4).

Clark (1991) measured the initial MMD of the spray produced by a pMDI near the exit of the actuator nozzle is  $12.5\mu\text{m}\sim 22.5\mu\text{m}$  for the formulation with 98% mass fraction of HFA 134a and 2% PEG300. Similarly Dunbar (1996) measured residual  $D_{0.1}$  and  $D_{0.3}$  of the spray issued from a pMDI at  $x=100\text{mm}$  are  $2.6\mu\text{m}$  and  $4.5\mu\text{m}$  with pure HFA 134a. Their results are sensibly smaller than our measurement. The difference is caused by the smaller expansion chamber volume of the Oxette® and the in-line geometry of expansion chamber in the Oxette® provides less chance for the recirculation to form bubbles. Our numerical model in section 6.3.3 predicted the residual MMD at  $x=100\text{m}$  is  $8\mu\text{m}\sim 13\mu\text{m}$ , which again under-estimated the droplet sizes compared to our imaging results. The occasional large droplets as shown in Figure 6.2.1 increases the residual MMD in sizing the droplets. Furthermore, the limitations of our imaging system (Chapter 4) will be unable to detect the droplets of a diameter smaller than  $3\mu\text{m}$  due to its calibration threshold.

Test index	Mean diameters ( $\mu\text{m}$ ) for KDCRA103						Detected droplet number
	D <sub>10</sub>	D <sub>32</sub>	D <sub>0.1</sub>	D <sub>0.5</sub>	D <sub>0.9</sub>	D <sub>0.5</sub> /D <sub>32</sub>	
1	9.7	18.1	9.8	21.3	49.3	1.18	2387
2	9.6	19.7	10.3	24.3	62.8	1.23	2284
3	9.7	18.2	9.8	21.3	51.3	1.17	2244
4	9.7	17.8	9.8	21.3	47.3	1.20	2258
5	9.6	18.7	10.3	23.3	53.3	1.24	1856
6	10.5	19.4	10.8	26.8	65.8	1.18	1964
7	10.8	20.1	11.3	24.3	51.3	1.21	2331
8	10.8	22.5	12.8	26.8	65.8	1.19	1891
9	11.0	20.1	11.3	24.3	49.3	1.21	1485
10	10.9	21.5	12.3	26.3	59.8	1.22	1647
average	10.2	19.6	10.8	24.0	55.6	1.20	2035
Test index	Mean diameters ( $\mu\text{m}$ ) for KDCRA122						Detected droplet number
	D <sub>10</sub>	D <sub>32</sub>	D <sub>0.1</sub>	D <sub>0.5</sub>	D <sub>0.9</sub>	D <sub>0.5</sub> /D <sub>32</sub>	
1	9.9	18.8	10.3	22.8	51.3	1.21	1118
2	9.6	16.6	8.8	19.3	55.3	1.16	837
3	9.1	15.3	8.3	17.3	45.3	1.13	907
4	9.5	18.3	9.3	22.8	72.8	1.24	614
5	9.9	16.8	9.3	19.3	52.8	1.14	740
6	9.2	17.0	9.3	19.8	50.8	1.16	607
7	9.9	17.4	9.8	20.3	47.8	1.16	750
8	9.9	18.3	9.8	21.3	61.8	1.16	712
9	9.6	17.8	9.3	20.8	57.8	1.16	783
10	9.5	18.0	9.3	20.8	70.8	1.16	634
average	9.6	17.4	9.3	20.4	56.6	1.17	770

Table 6.5 Mean diameters ( $\mu\text{m}$ ) at each test under 1<sup>st</sup> shallow inhalation with Oxette® 2 for KDCRA103 (95% HFA 134a) and KDCRA122 (98% HFA 134a).

Figure 6.22 shows the background intensity variations of the droplet images, which correlates with the plume opacity of the spray generated by Oxette® 2 at x=100mm from the actuator nozzle with two formulations under sequentially shallow inhalation. The plume opacity of the spray generated by KDCRA103 (95% HFA 134a) is twice of that of KDCRA122 (98% HFA 134a) during the 1<sup>st</sup> and 2<sup>nd</sup> shallow inhalations, because KDCRA122 (98% HFA 134a) has a higher mass fraction of HFA 134a leading to a faster evaporation rate, and it produced sparser sprays at x=100mm compared to KDCRA103 (95% HFA 134a). It agrees with the dual laser measurement in section 6.3.1. The relative densities of the spray are inversely proportional to the background intensities of the droplet images. For KDCRA103 (95% HFA 134a), the ratio of the averaged density of

the spray generated under the 1<sup>st</sup> and 2<sup>nd</sup> shallow inhalation is 0.71, while the ratio is 0.57 for KDCRA122 (98% HFA 134a). It indicates KDCRA103 (95% HFA 134a) produces more steady spray than KDCRA122 (98% HFA 134a). However, it performs differently from a pMDI (Figure 5.6, Chapter 5), since the pMDIs were tested in an open environment while the Oxette® was tested in a closed observation chamber. The spray issued from a pMDI dispersed into atmosphere after the end of the actuation, which is not detectable by the dual laser method. However, the sprays generated by Oxette® were measured in a closed chamber where droplets settled, and recirculated inside the chamber and were detectable by the dual laser method after the inhalation. The pulsations of the curves after 1.0s from the actuation, shown in Figure 6.22, are caused by the recirculation of the flow during the exhalation condition.

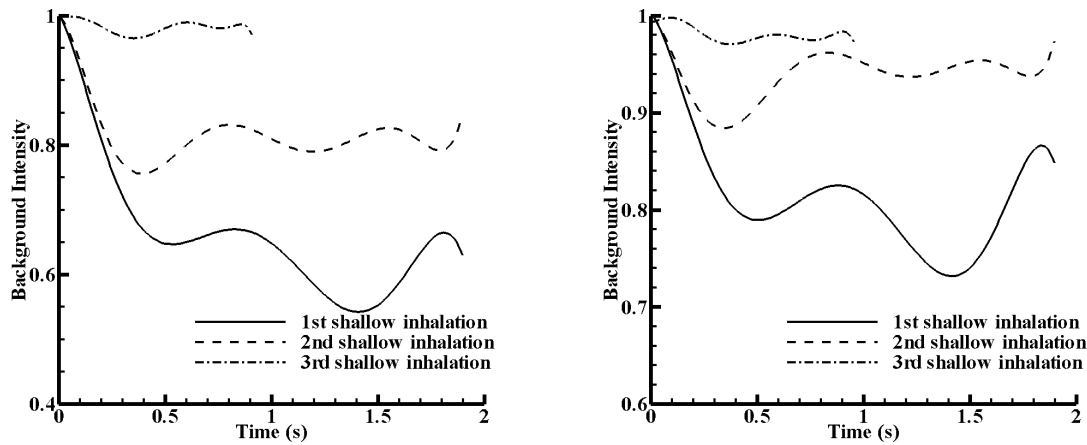


Figure 6.22 The background intensity variations of the droplet images for the spray generated by Oxette® 2 with KDCRA103 (left: 95% HFA 134a) and KDCRA122 (right: 98% HFA 134a) under 1<sup>st</sup>, 2<sup>nd</sup> and 3<sup>rd</sup> shallow inhalation at  $x=100\text{mm}$  from the actuator nozzle.

## 6.4 Chapter summary

A prediction of residual MMD of the spray issuing from twin-orifice devices (Figure 5.2, Chapter 5) has been added to the previous numerical model (Chapter 5) to understand how operational variables affect the sprays quality, using an evaporation model of multi-component liquid droplets. Two different formulations with 95% and 98% mass fraction of HFA 134a and two early stage prototype cigarette designs with different expansion chamber volumes have been analyzed by the numerical model, with comparisons with the dual laser measurements. The internal and external flows issuing from the “Oxette®” devices were visualized by high speed imaging system and discussed along with the boiling and evaporating phenomena. Furthermore, droplet sizes were measured by the newly developed imaging process system (Chapter 4) at the distance from the actuator nozzle where the human oropharynx locates. Although KDCRA122 (98% HFA 134a) can generate smaller droplets, KDCRA103 (95% HFA 134a) produces more steady puffs with relatively low mass flow rate. From the visualization of the internal flow in the earlier design (Oxette® 1), it indicates that small expansion chambers can hardly generate small bubbles with recirculation zones to produce fine sprays. The later design (Oxette® 2) significantly improves the performance and produces finer sprays, due to its larger the expansion chamber volume for the propellant evaporation, recirculation, bubble generation and growth. However, compared to the pMDI, the Oxette® has a smaller expansion chamber and the geometry provides less opportunity for the flow recirculation to form the small bubbles, which causes the residual MMD to be larger than that of a pMDI.





# Chapter 7

## Conclusions and Further Work

---

Due to the health issues regarding to the consumption of tobacco, a cigarette alternative is designed to deliver a dose of safer medicinal nicotine within a timeframe comparable to that of a cigarette, and gives much of what smokers expect from a cigarette without the risks of smoking tobacco. The aim of this Ph.D. project is to study the process of flashing atomization and dispersion, with a view to supporting the development of the cigarette replace device (Oxette®) which is required to produce an aerosol with relatively low and steady mass flow rate of nicotine. In order to test the effectiveness of the nicotine formulations, the analysis is carried on sizing the droplet of the aerosols at the position where human oropharynx locates, to support the further research on the deposition of droplets in the human respiratory tract. This chapter summarizes the work completed and discusses the scope of further research. Some recommendations are made to my sponsor Kind Consumer Ltd.

---

## 7.1 Conclusion

There are two main parts of the conclusion: experimental findings and computational findings.

### 7.1.1 Experimental findings

- A mechanical lung has been assembled and programmed to trigger the ‘cigarette-like’ devices with inputting different inhalation profiles.
- A dual laser system has been designed to measure the global actuation flow characteristics (e.g. spray velocity and opacity).
- In order to efficiently acquire sufficient droplet information (e.g. diameter and aspect ratio) from images of in and out of focus droplets, a multi-threshold algorithm has been developed and successfully implemented in the automatic particle/droplet image analysis (PDIA) system. It increases the depth of field (DoF) of small particles with diameters smaller than 50 $\mu$ m, and it performs more efficiently than the dual threshold methods which are widely used in the commercial software.
- Two different formulations with 95% and 98% mass fraction of HFA 134a, and two prototype cigarette alternatives with different expansion chamber volumes, have been analyzed by high speed imaging, with the special interest in the flashing phenomena and droplet sizes. It concludes that a larger expansion chamber volume enhances the propellant evaporation, recirculation, bubble generation and growth inside the chamber, and it made a significant improvement to produce finer sprays. Although the formulation with 98% of HFA 134a can generate smaller droplets, the formulation with 95% of HFA 134a produces more steady puffs with relatively low mass flow rate of nicotine.

### 7.1.2 Computational findings

- A numerical multi-component two-phase actuation flow model has been developed, in order to test different formulations within various flow domains of the cigarette replacement devices (twin-orifice system). The simulated results of the numerical model have been validated with the experimental measurements and the results of previous researchers. In order to acquire an aerosol with

relatively low and steady mass flow rate of nicotine, it is recommended that the mass fraction of propellant (HFA 134a) should be kept around 75%~90% to avoid the sharp temperature drop causing the feel of freezing. The actuator nozzle diameter should be 0.2mm~0.3mm to produce a flow with relatively low mass flow rate.

- Generally it is a combination of evaporation and boiling processes after the liquid discharging from the actuator nozzle (Polanco et al., 2010). An evaporation model of multi-component liquid droplets (Brenn et al., 2007) has been implemented to predict the residual droplet sizes of the spray at a position where human oropharynx is located, due to the evaporation of the droplets at the exit of the actuator nozzle.

## 7.2 Further research

This work will be useful for future researchers investigating flash atomization systems including the internal and external flows since it informs on the effect of both geometrical and formulation change, including presence of inerts on the final spray quality, and provides verification of a model used to predict such changes. Similarly, there are two main parts for the further work: experimental work and computational work.

### 7.2.1 Experimental work

- For the mechanical lung rig, cumulative error will be generated in the piston zero position. A solution to this problem is to add a zero piston position sensor and a feedback control loop.
- Keith et al. (1960) and Anderson et al. (1989) measured the aerosols generated by the traditional tobaccos with a relatively stable distribution of sizes ranging from 0.1 $\mu$ m to 1.0 $\mu$ m. The particle/droplet image analysis (PDIA) system developed in Chapter 4 is only capable of measuring particles with diameter of 3 $\mu$ m~450 $\mu$ m, hence an additional calibration procedure is required for the particles with diameters smaller than 3 $\mu$ m.
- The flashing atomization is still poorly understood due to its complexity, especially the phase-changing, bubbly flow in the expansion chamber. A transparent twin-orifice device is suggested to be designed, with the allowance of

the high speed imaging access. It is proposed to record the flow in the expansion chamber, the flow in the actuator nozzle and the outlet actuation spray simultaneously, to find how the fluid inside the expansion chamber affects atomization. However, it might need several cameras working at the same time.

### **7.2.2 Computational work**

- Due to its complexity, the computational simulation on the flashing flow inside the expansion chamber with bubble nucleation and growth is barely studied and is required for further study.
- In this project, only evaporation process is considered for the droplets discharging from the actuator nozzle. A combination of the turbulence effect on the drop sizes can be analyzed in the future.
- A contour of the human respiratory tract has been built up by Solidworks, and groups of particles can be injected to find how the shape and size of the particles affect the deposition fractions in different lung sections with immersed boundary method. It is suggested starting from a simple geometry.

## **7.3 Recommendations to Kind Consumer Ltd.**

This work is sponsored by Kind Consumer Ltd., and has reached a number of conclusions that will be of interest in their work to develop the cigarette replace device (Oxette®).

- Model 110 leaked at the mid part after the 3<sup>rd</sup> refill.
- Model 112 leaked at the mid part when it was refilled at the 3<sup>rd</sup> time, and please note that there were two refills 24 hours before the 3<sup>rd</sup> refill.
- Model 88 leaked at the mid part due to the heat from the calibration flood lamp, and it maybe caused that some materials are sensitive to the heat (e.g. glues).
- Model 111 and model 241 work well by now, and model 241 was used in the drop sizing work.
- Each refill generates 3~5 ISO breaths (shallow inhalations), but the spray density decreases after each puff, i.e. a maximum spray density is produced at the first actuation after every refill. Model 110, 170 and 241 can provide up to 5

puffs with decreasing spray densities after each refill, but the others can only produce up to 4.

- Each canister can provide around 20~25 refills.
- Refill process can be optimized to avoid unnecessary loss of the formulations.
- In order to acquire fine atomization, high mass fraction of HFA 134a is required, which causes the feel of freezing. However, it will not be a big issue, since only a small amount is inhaled.
- The expansion chamber geometry is suggested referring to that of a pMDI, which enhances the propellant evaporation, recirculation, bubble generation and growth inside the chamber to produce finer aerosols.



# Appendices

## Appendix I: Flow charts of the numerical multi-component two-phase actuation flow model

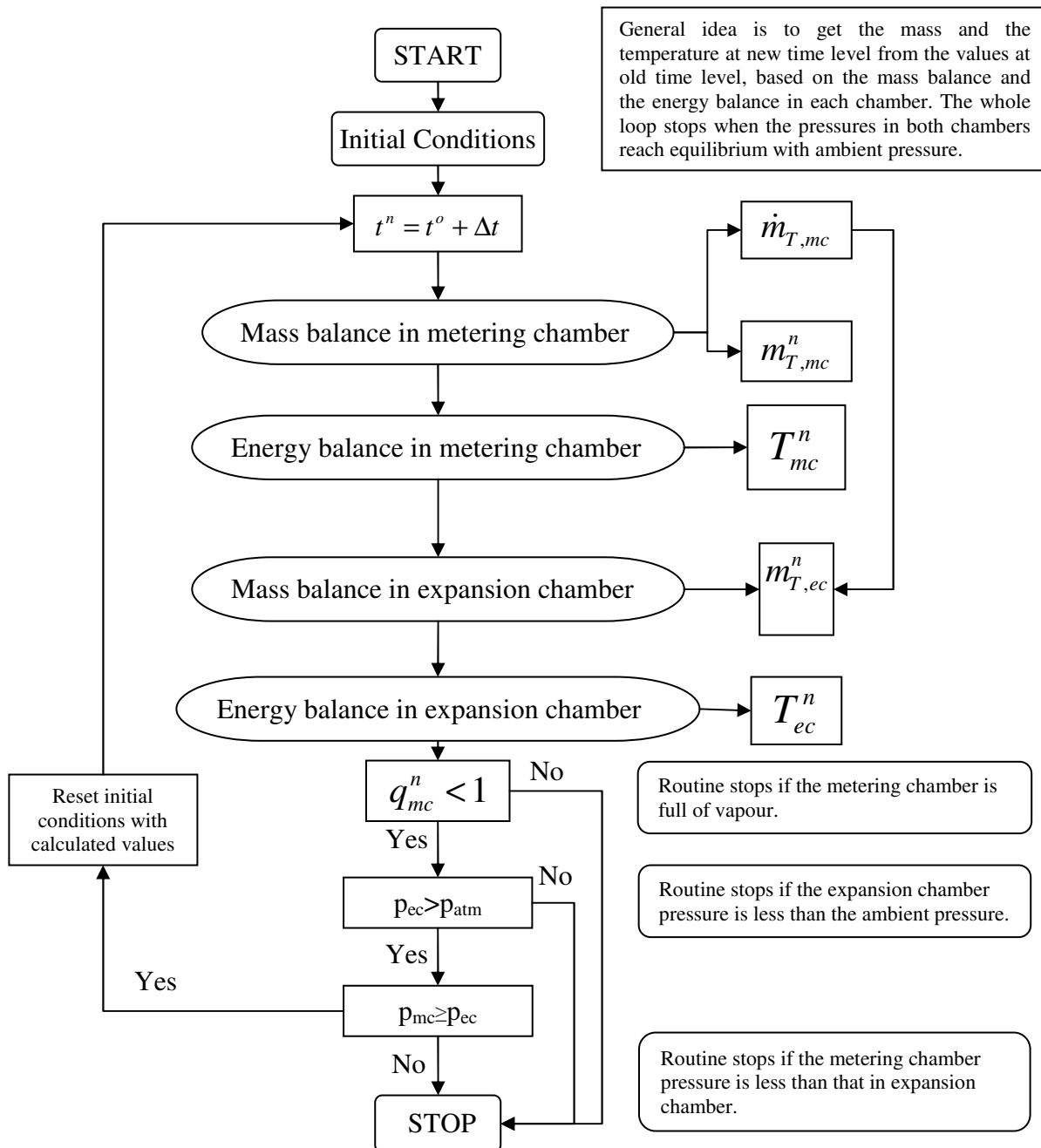


Figure A.1 Flow chart of the numerical multi-component two-phase actuation flow model.



Get the mass and the temperature at new time level from the values at old time level, based on the mass balance and the energy balance in the metering chamber (Corresponding equations are shown).

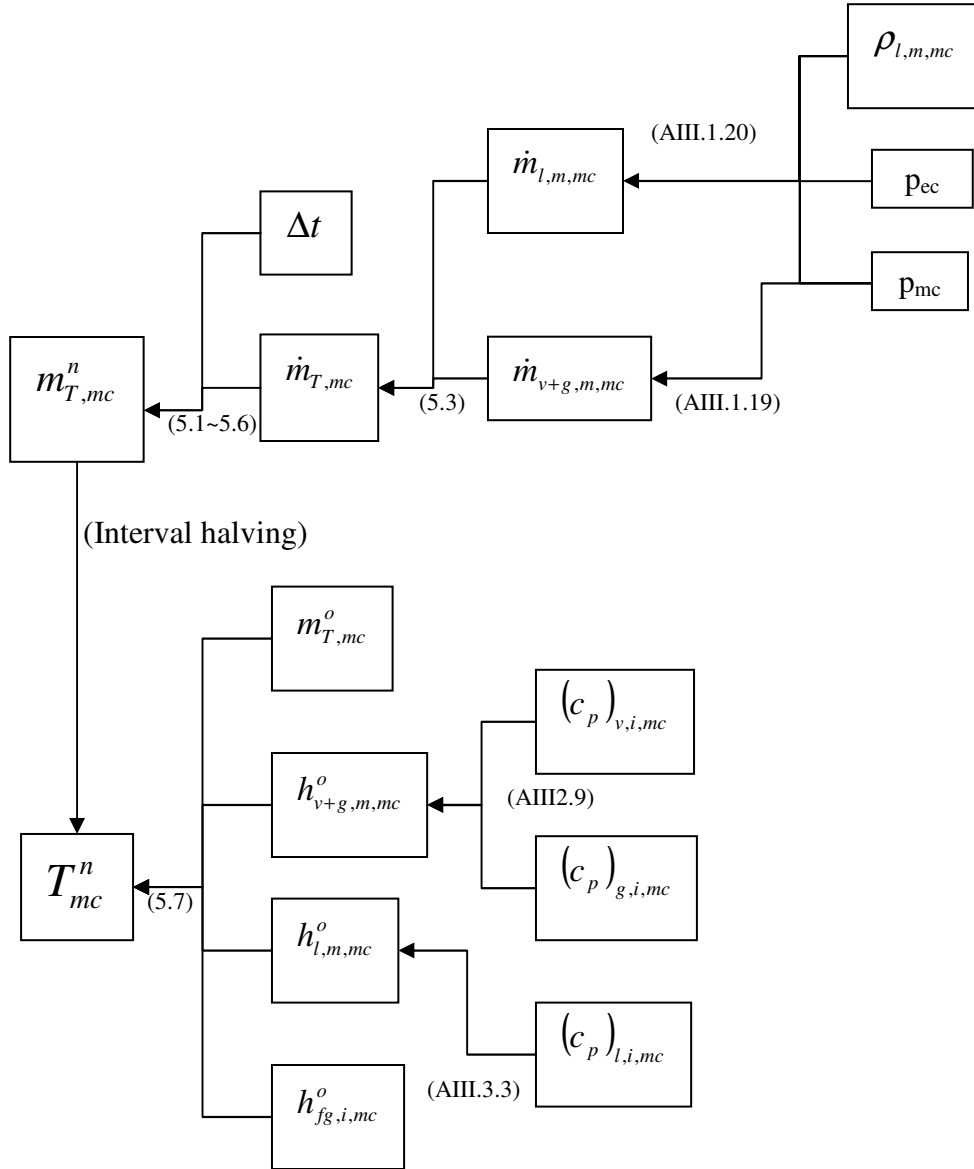


Figure A.2 Flow chart of the mass and the energy balance in the metering chamber of the numerical multi-component two-phase actuation flow model.

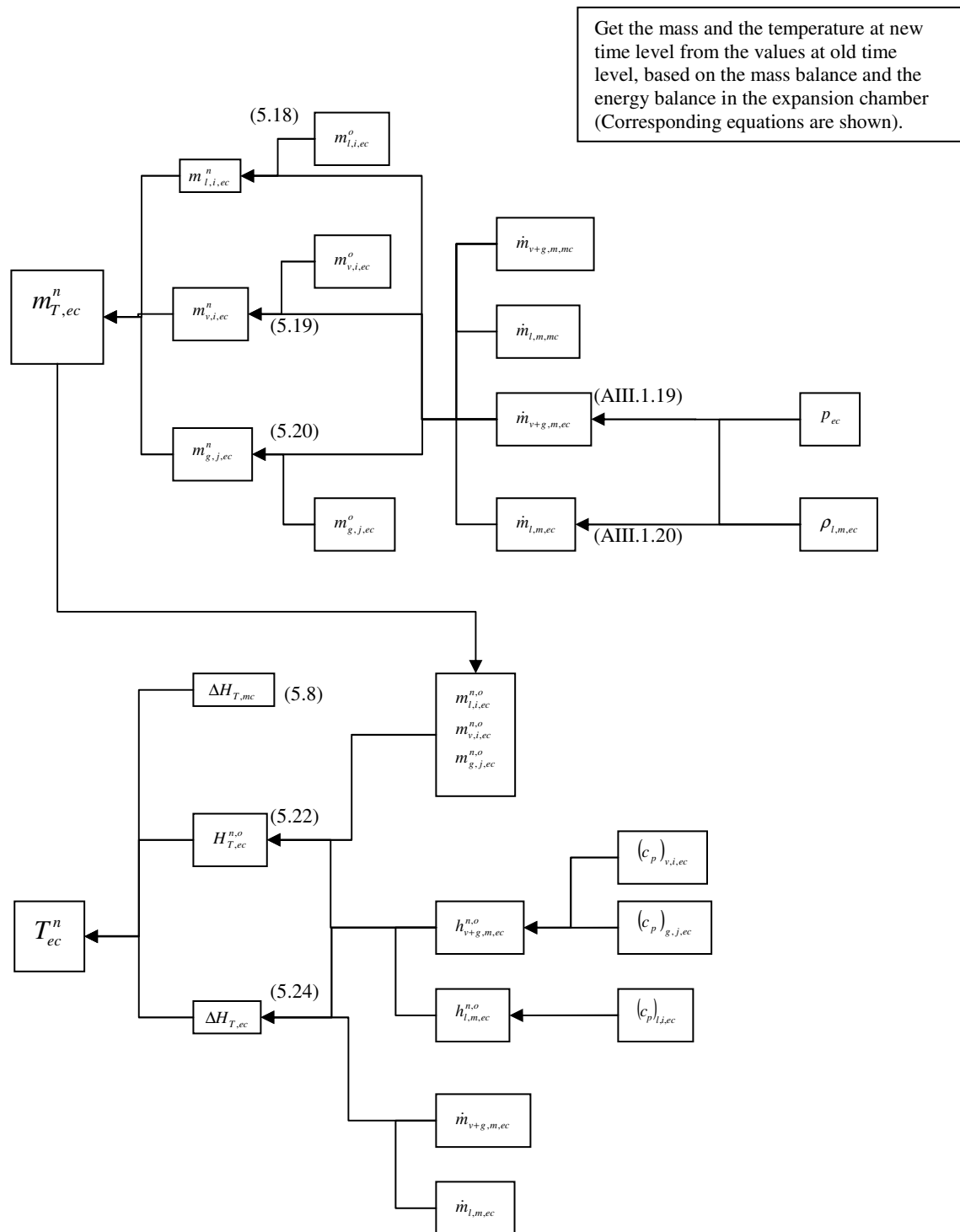


Figure A.3 Flow chart of the mass and the energy balance in the expansion chamber of the numerical multi-component two-phase actuation flow model.

## Appendix II: Thermophysical Properties of different components

### AII.1 HFA 134a (C<sub>2</sub>H<sub>2</sub>F<sub>4</sub>)

- Specific heat capacity at constant pressure of component liquid (J/(kg·K)) (Dunbar, 1996)

$$c_{p,l}=4.137 \times 10^{-3} T^2 - 0.694 T + 1072.3 \quad (\text{AII.1.1})$$

- Specific heat capacity of component vapour (J/(kg·K)) (Dunbar, 1996)

$$c_{p,v} = 1.7812 \times 10^{-6} T^3 - 2.8662 \times 10^{-3} T^2 + 3.005 T + 143.897 \quad (\text{AII.1.2})$$

- Density of the liquid component (kg/m<sup>3</sup>) (Dunbar, 1996)

$$\rho_l = 415.8 T^{*4} - 504.3 T^{*3} + 637.1 T^{*2} + 902.4 T^{*} + 509.15 \quad (\text{AII.1.3})$$

where:

$$T^{*} = \left( 1 - \frac{T}{T_c} \right)^{1/3} \quad (\text{AII.1.4})$$

and critical temperature:  $T_c = 374\text{K}$ ;

- Vapour pressure of component (Pa) (Dunbar, 1996; Fujiwara, 1999; Lide, 2002)

$$p_v = C_1 \cdot T^3 + C_2 \cdot T^2 + C_3 T + C_4 \quad (\text{AII.1.5})$$

where:

$$C_1 = 0.78849489394127359$$

$$C_2 = -490.71249581542827$$

$$C_3 = 102585.30516828218$$

$$C_4 = -7192107.639743919$$

and the melting point/freezing point is  $-102^{\circ}\text{C}$  (171K) (Dunbar, 1996; Lide, 2002)

Latent heat of vaporization (J/kg) (Dunbar, 1996)

$$h_{fg} = 57587.9 T^4 - 142985.0 T^3 + 194560.7 T^2 + 225008.4 T + 509.15 \quad (\text{AII.1.6})$$

- Molecular weight of the component (kg/mol) (Dunbar, 1996)

$$M = 0.102 \quad (\text{AII.1.7})$$

### AII.2 Ethanol (C<sub>2</sub>H<sub>6</sub>O)

- Critical temperature is  $T_c = 513.92\text{K}$ ; (Perry et al., 1997)

- Molecular weight of the component (kg/mol) (Perry et al., 1997)

$$M=0.046069 \quad (\text{AII.2.1})$$

- Specific heat capacity at constant pressure of component liquid (J/kg·K)  
(Touloukian et al., 1970; Ray et al., 1973; Perry et al., 1997; Lide, 2002;)

$$c_{p,l}=2.0386 \times 10^{-3} T^3 - 3.0341 \times 10^{-2} T^2 - 1.3963 \times 10^2 T + 1.0264 \times 10^5 \quad (\text{AII.2.2})$$

- Specific heat capacity of the vapour component (J/(kg·K)) (Touloukian et al., 1970; Perry et al., 1997)

$$c_{p,v} = \left( 4.92 \times 10^4 + 1.4577 \times 10^5 \left[ \frac{1.6628 \times 10^3}{T \cdot \sinh(1.6628 \times 10^3 / T)} \right]^2 + 9.39 \times 10^4 \left[ \frac{744.7}{T \cdot \cosh(744.7 / T)} \right]^2 \right) \quad (\text{AII.2.3})$$

- Density of the liquid component (kg/m<sup>3</sup>) (Perry et al., 1997; Lide, 2002)

$$\rho_l = \frac{1.648}{0.27627^{[1+(1-T/T_c)^{0.2331}]}} \cdot M \quad (\text{AII.2.4})$$

- Vapour pressure of component (Pa) (Perry et al., 1997; Lide, 2002)

$$p_v = \exp[74.475 - (7164.3/T) - 7.327 \cdot \ln(T) + 3.134 \times 10^{-6} \cdot T^2] \quad (\text{AII.2.5})$$

and the melting point/freezing point is -114.14°C (159K) (Ray et al., 1973; Lide, 2002)

- Latent heat of vaporization (J/kg) (Ray et al., 1973; Perry et al., 1997)

$$h_{fg} = 5.69 \times 10^7 (1 - T/T_c)^{0.3359} / M \quad (\text{AII.2.6})$$

### AII.3 1, 2-Propylene Glycol (C<sub>3</sub>H<sub>8</sub>O<sub>2</sub>)

- Critical temperature is T<sub>c</sub>=626K; (Perry et al., 1997)

- Molecular weight of the component (kg/mol) (Perry et al., 1997)

$$M=0.076095 \quad (\text{AII.3.1})$$

- Specific heat capacity at constant pressure of component liquid (J/(kg·K)) (Ray et al., 1973; Perry et al., 1997)

$$c_{p,l}=4.137 \times 10^{-3} T^2 - 0.694 T + 1072.3 \quad (\text{AII.3.2})$$

- Specific heat capacity of component vapour (J/kg·K) (Perry et al., 1997)

$$c_{p,v} = \left( 2.0114 \times 10^5 + 8.8082 \times 10^4 \left[ \frac{1.8656 \times 10^3}{T \cdot \sinh(1.8656 \times 10^3 / T)} \right]^2 - 2.4404 \times 10^5 \left[ \frac{279.98}{T \cdot \cosh(279.98 / T)} \right]^2 \right) \quad (\text{AII.3.3})$$

- Density of the liquid component (kg/m<sup>3</sup>) (Perry et al., 1997; Lide, 2002)

$$\rho_l = \frac{1.0923}{0.26106^{[1+(1-T/T_c)^{0.20459}]}} \cdot M \quad (\text{AII.3.4})$$

- Vapour pressure of component (Pa) (Perry et al., 1997)

$$p_v = \exp[74.475 - (7164.3/T) - 7.327 \cdot \ln(T) + 3.134 \times 10^{-6} \cdot T^2] \quad (\text{AII.3.5})$$

and the melting point/freezing point is  $-60^\circ\text{C}$  (213K) (Ray et al., 1973; Lide, 2002)

- Latent heat of vaporization (J/kg) (Ray et al., 1973; Perry et al., 1997)

$$h_{fg} = 8.07 \times 10^7 (1 - T/T_c)^{0.295} / M \quad (\text{AII.3.6})$$

#### AII.4 Nicotine ( $\text{C}_{10}\text{H}_{14}\text{N}_2$ )

- Molecular weight of the component (jg/mol) (Lide, 2002)

$$M = 0.162231 \quad (\text{AII.4.1})$$

- Density of the liquid component ( $\text{kg/m}^3$ ) (Perry et al., 1997; Lide, 2002)

$$\rho_l = 1.0097 \times 10^3 \quad (\text{AII.4.2})$$

- Vapour pressure of component (Pa) (334.8K-520.8K) (Ray et al., 1973)

$$p_v = C_1 + C_2 \cdot T + C_3 \cdot T^2 + C_4 \cdot T^3 + C_5 \cdot T^4 \quad (\text{AII.4.3})$$

where:

$$C_1 = 1.8535431029411403 \times 10^6$$

$$C_2 = -2.0437225541098782 \times 10^4$$

$$C_3 = 84.881386387309078$$

$$C_4 = -0.15758140743524174$$

$$C_5 = 1.1049142994149309 \times 10^{-4}$$

and the melting point/freezing point is  $-79^\circ\text{C}$  (194K) (Ray et al., 1973)

#### AII.5 Air

- Specific heat capacity at constant pressure ( $\text{J}/(\text{kg} \cdot \text{K})$ ) (Perry et al., 1997; Lide, 2002)

$$c_{p,a} = 1004 \quad (\text{AII.5.1})$$

where air specific heat capacity at constant pressure, approximately constant [variation less than 2% within 240K-300K (Dunbar, 1996)]

- Molecular weight (kg/mol) (Perry et al., 1997; Lide, 2002)

$$M = 0.02897 \quad (\text{AII.5.2})$$

- Heat capacity ratio (Perry et al., 1997; Lide, 2002)

$$\gamma_a = 1.4 \quad (20^\circ\text{C}) \quad (\text{AII.5.3})$$

## AII.6 Oxygen (O<sub>2</sub>)

- Specific heat capacity at constant pressure (J/(kg·K)) (Perry et al., 1997; Lide, 2002)

$$c_{p,O_2} = 918 \quad (\text{AII.6.1})$$

where air specific heat capacity at constant pressure, approximately constant [variation less than 2% within 240K-300K (Dunbar, 1996)]

- Molecular weight (kg/mol) (Perry et al., 1997; Lide, 2002)

$$M = 0.032 \quad (\text{AII.6.2})$$

- Heat capacity ratio (Perry et al., 1997; Lide, 2002)

$$\gamma_{O_2} = 1.4 \quad (20^\circ\text{C}) \quad (\text{AII.6.3})$$

## AII.7 Nicotine Acid (C<sub>5</sub>H<sub>4</sub>NCO<sub>2</sub>H)

Molecular weight of the component (g/mol) (Perry et al., 1997; Lide, 2002)

$$M = 123.11 \quad (\text{AII.7.1})$$

The melting point/freezing point is 235.2 °C (508K) (Perry et al., 1997; Lide, 2002)

## AII.8 Oleic Acid (C<sub>8</sub>H<sub>17</sub>CH:CH(CH<sub>2</sub>)<sub>7</sub>CO<sub>2</sub>H)

- Molecular weight of the component (kg/mol) (Perry et al., 1997; Lide, 2002)

$$M = 0.28345 \quad (\text{AII.8.1})$$

- Specific heat capacity at constant pressure (J/(kg·K)) (Perry et al., 1997; Lide, 2002)

$$c_{p,l} = 2046 \quad (\text{AII.8.2})$$

- Density of the liquid component (kg/m<sup>3</sup>) (Perry et al., 1997; Lide, 2002)

$$\rho_l = 893.5 \quad (20^\circ\text{C}) \quad (\text{AII.8.3})$$

The melting point/freezing point is 14°C (287K) (Perry et al., 1997; Lide, 2002)

## AII.9 Menthol (C<sub>10</sub>H<sub>19</sub>OH)

- Molecular weight of the component (kg/mol) (Perry et al., 1997; Lide, 2002)

$$M = 156.26 \quad (\text{AII.9.1})$$

- Density of component liquid (kg/m<sup>3</sup>) (Perry et al., 1997; Lide, 2002)

$$\rho_l = 890 \quad (\text{AII.9.2})$$

- The melting point/freezing point is 42°C (315K) (Perry et al., 1997; Lide, 2002)

## Appendix III: Fluid characters

### AIII.1 Fluid flow through a nozzle or orifice

#### AIII.1.1 Incompressible flow (liquid phase) through a duct, a converging nozzle or an orifice

Velocity of the incompressible flow is defined as:

$$u_l = \sqrt{\frac{2 \times (p_{us} - p_{ds})}{\rho_l}} \quad (\text{AIII 1.1})$$

where  $p_{us}$  is the upstream pressure and  $p_{ds}$  is the downstream pressure.

Mass flow rate of the incompressible flow is calculated as:

$$\dot{m}_l = \rho_l A_t u_l = A_t \sqrt{2 \rho_l (p_{us} - p_{ds})} \quad (\text{AIII 1.2})$$

In practice, the actual discharge will be  $C_d \cdot \dot{m}$ , where  $C_d$  is the discharge coefficient.

#### AIII.1.2 Compressible flow (gas phase) through a convergent nozzle or an orifice. (Potter et al., 1997)

There are some standard isentropic flow relations for the flow from the stagnation condition to a certain condition:

$$\frac{P}{\rho^\gamma} = \text{const} = \frac{P_o}{\rho_o^\gamma} \quad (\text{AIII.1.3})$$

where  $\gamma$  is the heat capacity ratio.

$$\frac{P}{P_o} = \left( \frac{\rho}{\rho_o} \right)^\gamma = \left( \frac{T}{T_o} \right)^{\frac{\gamma}{\gamma-1}} \quad (\text{AIII.1.4})$$

$$\frac{\rho_o}{\rho} = \left( 1 + \frac{\gamma-1}{2} Ma^2 \right)^{\frac{1}{\gamma-1}} \quad (\text{AIII.1.5})$$

$$\frac{P_o}{P} = \left( 1 + \frac{\gamma-1}{2} Ma^2 \right)^{\frac{\gamma}{\gamma-1}} \quad (\text{AIII.1.6})$$

$$\frac{T_o}{T} = 1 + \frac{\gamma-1}{2} Ma^2 \quad (\text{AIII.1.7})$$

For the critical condition, the sonic flow or the choked flow, where  $Ma=1$ , the above equations are written as:

$$\frac{\rho^*}{\rho_o} = \left( \frac{2}{\gamma+1} \right)^{\frac{1}{\gamma-1}} \quad (\text{AIII.1.8})$$

$$\frac{p^*}{p_o} = \left( \frac{2}{\gamma+1} \right)^{\frac{\gamma}{\gamma-1}} \quad (\text{AIII.1.9})$$

$$\frac{T^*}{T_o} = \frac{2}{\gamma+1} \quad (\text{AIII.1.10})$$

Velocity of the compressible flow is defined as:

$$u_t = Ma_t \sqrt{\gamma R T_t} \quad (\text{AIII.1.11})$$

where the subscript  $t$  stands for the flow properties at the throat of a nozzle.

Mass flow rate of the compressible flow through the throat of a nozzle can be calculated as:

$$\dot{m}_t = \rho_t A_t u_t = \frac{p_t}{R T_t} A_t \cdot Ma_t \sqrt{\gamma R T_t} = p_t \sqrt{\frac{\gamma}{R T_t}} A_t \cdot Ma_t$$

with (AIII.1.6) and (AIII.1.7),

$$\Rightarrow \dot{m}_t = p_o \sqrt{\frac{\gamma}{R T_o}} A_t \cdot Ma_t \left( 1 + \frac{\gamma-1}{2} Ma_t^2 \right)^{\frac{\gamma+1}{2(1-\gamma)}} \quad (\text{AIII.1.12})$$

and for the choked flow ( $Ma=1$ ), the above equation is written as

$$\dot{m}^* = p_o A_t \sqrt{\frac{\gamma}{R T_o}} \left( \frac{\gamma+1}{2} \right)^{\frac{\gamma+1}{2(1-\gamma)}} \quad (\text{AIII.1.13})$$

For the de Laval nozzle, since the mass flow rate is the same at each cross section, the cross section area at any section of the nozzle has the relation with the critical value as:

$$\frac{A}{A^*} = \frac{1}{Ma} \left\{ \frac{1 + [(\gamma-1)/2] Ma^2}{(\gamma+1)/2} \right\}^{\frac{\gamma+1}{2(1-\gamma)}} \quad (\text{AIII.1.14})$$



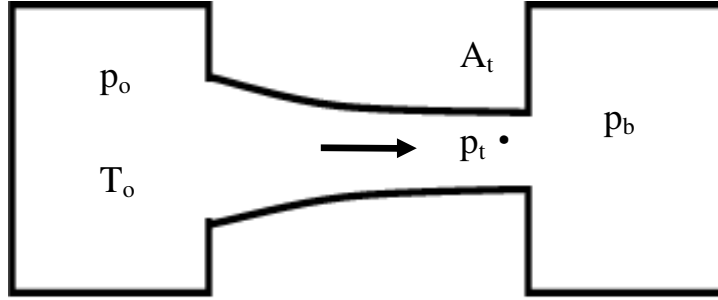


Figure A.4 A schematic diagram of the compressible flow through a convergent nozzle.

Under the three conditions described below, mainly two types of flow regimes are formed in the flow through a convergent nozzle (conditions are shown as the Figure A.4), one is subsonic flow and the other is sonic flow or choked flow.

- i) When  $p_b > p_t^*$ , the flow through the whole nozzle is subsonic,  $\dot{m}/\dot{m}^* < 1$ , and mass flow rate  $\dot{m}$  is expressed as (AIII.1.12).
- ii) When  $p_b \leq p_t^*$ , the flow through throat is sonic,  $\dot{m}/\dot{m}^* = 1$ , choked flow occurs at the throat, and mass flow rate  $\dot{m} = \dot{m}^*$  (AIII.1.13).

In practice, the actual discharge will be  $C_d \cdot \dot{m}$  or  $C_d \cdot \dot{m}^*$ , where  $C_d$  is the discharge coefficient.

### AIII.1.3 Two phase flow (gas and liquid phases) through a convergent nozzle or orifice.

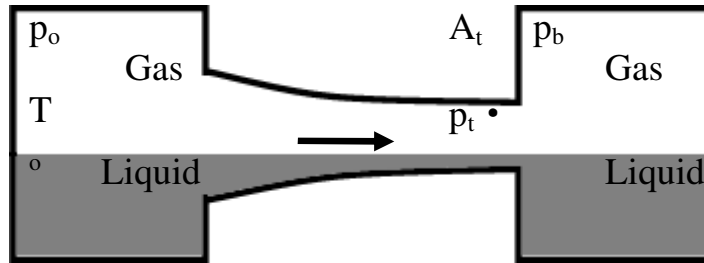


Figure A.5 A schematic diagram of the two phase compressible flow through a convergent nozzle.

As gas mass fraction of the mixture is defined by:

$$q = \frac{m_g}{m_l + m_g} \quad (\text{AIII.1.15})$$

Volume fraction can be calculated from  $q$  as:

$$\phi = \frac{V_g}{V_l + V_g} = \frac{q\rho_l}{(1-q)\rho_g + q\rho_l} \quad (\text{AIII.1.16})$$

and respectively, the area of cross sections of the two streams are:

$$A_g = \phi A_t \quad (\text{AIII.1.17})$$

$$A_l = (1 - \phi) A_t \quad (\text{AIII.1.18})$$

According to the Appendix AIII.1 and AIII.2, for the two phase flow, the mass flow rate of each phase flow is defined as:

$$\dot{m}_g = \phi A_t \cdot p_o \sqrt{\frac{\gamma}{RT_o}} Ma_t \left(1 + \frac{\gamma-1}{2} Ma_t^2\right)^{\frac{\gamma+1}{2(1-\gamma)}} \quad (\text{AIII.1.19})$$

$$\dot{m}_l = (1 - \phi) A_t \sqrt{2\rho_l (p_{us} - p_{ds})} \quad (\text{AIII.1.20})$$

And total mass flow rate is calculated as:

$$\dot{m}_T = \dot{m}_g + \dot{m}_l \quad (\text{AIII.1.21})$$

Assuming the liquid is dispersed as drops in the actuation nozzle, the liquid phase is considered to be ‘choked’ when the pressure reaches critical value at the throat. The pressure  $p_{ds}$  in equation AIII 1.2 is equal to the critical pressure  $p_t^*$  at the throat.

## AIII.2 The functions and definitions of gas mixture properties

### AIII.2.1 Pure gas (vapour) properties calculation

Vapour density can be calculated from a given vapour pressure, e.g. from equation AII.1.5,

$$\rho_v = \frac{p_v}{R_v T} \quad (\text{AIII.2.1})$$

where the gas constant of the vapour is:

$$R_v = R/M_v \quad (\text{AIII.2.2})$$

Heat capacity ratio of the vapour is:

$$\gamma = \frac{c_p}{c_v} \quad (\text{AIII.2.3})$$

where:

$$c_v = c_p - R_v \quad (\text{AIII.2.4})$$

### AIII.2.2 Gas (vapour) mixture properties calculation

The mass fraction of each component is defined as the ratio of its mass and the total mass of the gas mixture:

$$f_{i,g} = \frac{m_{g,i}}{m_{T,g}} \quad (\text{AIII.2.5})$$

where total mass of the gas mixture is ( $M$  components mixture):

$$m_{T,g} = \sum_{i=1}^M m_{g,i} \quad (\text{AIII.2.6})$$

Then, the heat capacity ratio of the gas mixture is:

$$\gamma_{g,m} = \sum_{i=1}^M \gamma_{g,i} \cdot f_{g,i} \quad (\text{AIII.2.7})$$

and the gas constant of the gas mixture is

$$R_{g,m} = \sum_{i=1}^M R_{g,i} \cdot f_{g,i} \quad (\text{AIII.2.8})$$

Similarly, the specific enthalpy at constant pressure of the gas mixture is defined as:

$$h_{g,m} = \sum_{i=1}^M h_{g,i} f_{g,i} = \sum_{i=1}^M (c_p)_{g,i} f_{g,i} \cdot T \quad (\text{AIII.2.9})$$

### AIII.3 The functions and definitions of liquid mixture properties

The mass fraction of each component is defined as the ratio of its mass and the total mass of the liquid mixture:

$$\phi_i = \frac{m_{l,i}}{m_{T,l}} \quad (\text{AIII.3.1})$$

where total mass of liquid is ( $N$  components mixture):

$$m_{T,l} = \sum_{i=1}^N m_{l,i} \quad (\text{AIII.3.2})$$

The specific enthalpy of the liquid mixture is defined from the individual mass fractions as:

$$h_{l,m} = \sum_{i=1}^N h_{l,i} \phi_i = \sum_{i=1}^N (c_p)_{l,i} \phi_i T \quad (\text{AIII.3.3})$$

## AIII.4 Properties of the liquid and gas mixture at saturated condition in a closed container

### AIII.4.1 Single-component liquid at saturated condition in a closed container (Atkins et al., 2006)

The vapour pressure and the density of the liquid are the functions of temperature

$$p_v, \rho_l = f(T) \quad (\text{AIII.4.1})$$

The vapour density can be calculated from vapour pressure as:

$$\rho_v = \frac{p_v}{R_v T} \quad (\text{AIII.4.2})$$

and also the vapour density can be expressed from the mass and volume ratio:

$$\rho_v = \frac{m_v}{V_g} \quad (\text{AIII.4.3})$$

Total volume of the liquid and gas phase is the same as the volume of the container:

$$V = V_g + V_l \quad (\text{AIII.4.4})$$

Where the liquid volume is:

$$V_l = \frac{m_l}{\rho_l} \quad (\text{AIII.4.5})$$

Total mass of the liquid and vapour is known as:

$$m_T = m_v + m_l \quad (\text{AIII.4.6})$$

The known parameters are the total mass of liquid and vapour  $m_T$  (pure liquid at the beginning), the volume of the container  $V$ , the vapour pressure and the liquid density (a function of temperature). With the equation AIII.4.1~AIII.4.6, the mass fraction of the vapour can be calculated out as:

$$q = \frac{m_v}{m_T} = \frac{\frac{\rho_l}{\bar{\rho}} - 1}{\frac{\rho_l}{\rho_v} - 1} \quad (\text{AIII.4.7})$$

where the density of the vapour and liquid mixture  $\bar{\rho}$  is the ratio of total mass and container volume:

$$\bar{\rho} = \frac{m_T}{V} \quad (\text{AIII.4.8})$$

#### AIII.4.2 Multi-component liquid at saturated condition in a closed container

Similar to the single-component liquid, the multi-component liquid in a closed container at saturated condition can be expressed as equation AIII.4.7, where the properties of the pure component should be changed to the properties of the mixture as:

- The liquid density term,  $\rho_l$  in equation AIII.4.7, can be calculated as the ratio of the total mass and the total volume of liquid mixture:

$$\rho_{l,m} = \frac{\sum_{i=1} m_{l,i}}{\sum_{i=1} V_i} \quad (\text{AIII.4.9})$$

where the volume of each liquid component is:

$$V_i = \frac{m_i}{(\rho_l)_i} \quad (\text{AIII.4.10})$$

- The vapour density term  $\rho_v$  can be calculated from the vapour pressure of the liquid mixture which follows Raoult's law (Atkins et al., 2006), assuming the liquid mixture is an ideal solution):

$$p_{v,m} = \sum_{i=1} x_i (p_v^*)_i \quad (\text{AIII.4.11})$$

where  $p_v^*$  is the vapour pressure of the pure liquid component and  $x_i$  is the mole fraction of  $i$ th liquid component in the mixture of liquids, and the partial pressure of  $i$ th component is

$$p_{v,i} = x_i (p_v^*)_i \quad (\text{AIII.4.12})$$

Following Dalton's Law (Atkins et al., 2006), the mole fraction of  $i$ th vapour component in the vapour mixture is the ratio of the partial vapour pressure of each component, and the total vapour pressure of the vapours is

$$y_i = \frac{P_{v,i}}{P_{v,m}} \quad (\text{AIII.4.13})$$

Hence the total mass of the vapour in the closed container can be calculated from equation AIII.4.7, and the mass of liquid and vapour of each component can be derived from  $x_i$  and  $y_i$ .

#### AIII.4.3 A mixture of multi-component liquid and gases at saturated condition in a closed container

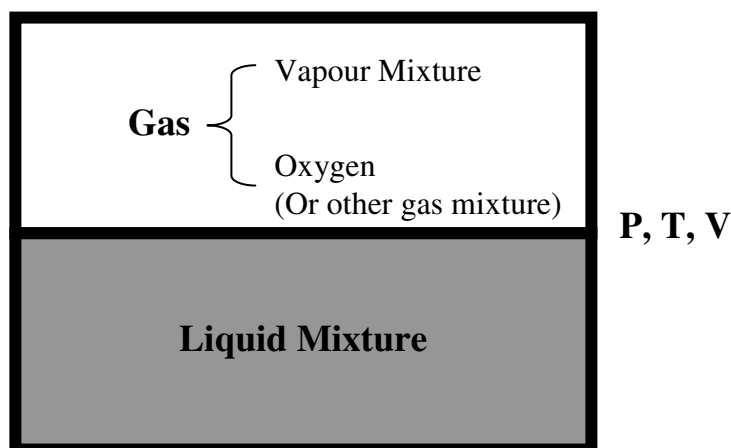


Figure A.6 A schematic diagram of the mixture of multi-component liquid and gases in a closed container.

The extra gas makes little difference to the vapour pressure of the liquid (Atkins et al., 2006). Therefore the only difference is the total pressure in the container, which is the sum of the total vapour pressure generated by the liquid mixture and the partial pressures of the extra gases:

$$P_T = P_{v,m} + P_{g,m} \quad (\text{AIII.4.14})$$

where the total vapour pressure  $p_{v,m}$  is defined by equation AIII.4.11, and the partial pressure of the whole gases is calculated from its mass as:

$$p_{g,m} = \frac{\sum_{j=1} m_{g,j}}{V_{v+g,m}} \quad (\text{AIII.4.15})$$

where  $V_{v+g,m}$  is the total volume of vapour and gas mixture.

### AIII.5 Representative diameters of a spray

In many calculations of mass transfers and flow processes, it is convenient to work only with mean or average diameters instead of the complete drop size distribution. A general expression of the mean diameter is derived by equation AIII.4.16.

$$D_{ab} = \left[ \frac{\sum N_i D_i^a}{\sum N_i D_i^b} \right]^{1/(a-b)} \quad (\text{AIII.4.16})$$

where  $a$  and  $b$  are integers,  $i$  denotes the size range considered,  $N_i$  is the number of drops in size range  $i$ , and  $D_i$  is the middle diameter of size range  $i$ . Thus, for example,  $D_{10}$  is the linear average value of all the drops in the spray;  $D_{30}$  is the diameter of a drop whose volume, if multiplied by the number of drops, equals the total volume of the sample; and  $D_{32}$  (SMD) is the diameter of the drop whose ratio of volume to surface area is the same as that of the entire spray. Some important mean diameters are listed in Table A.1 (Lefevre, 1989).

a	b	a+b (order)	Symbol	Name of mean diameter	Expression	Application
1	0	1	D10	Length	$\frac{\sum N_i D_i}{\sum N_i}$	comparisons
2	0	2	D20	Surface area	$\left( \frac{\sum N_i D_i^2}{\sum N_i} \right)^{1/2}$	Surface area controlling
3	0	3	D30	volume	$\left( \frac{\sum N_i D_i^3}{\sum N_i} \right)^{1/3}$	Volume controlling, e.g., hydrology
2	1	3	D21	Surface area- length	$\frac{\sum N_i D_i^2}{\sum N_i}$	Absorption
3	1	4	D31	Volume-length	$\left( \frac{\sum N_i D_i^3}{\sum N_i} \right)^{1/2}$	Evaporation, molecular diffusion
3	2	5	D32	Sauter (SMD)	$\frac{\sum N_i D_i^3}{\sum N_i D_i^2}$	Mass transfer, reaction
4	3	7	D43	De Brouckere or Herdan	$\frac{\sum N_i D_i^4}{\sum N_i D_i^3}$	Combustion equilibrium

*Table A.1 Mean diameters and their applications (Lefevre, 1989).*

At present the most widely used expression for drop size distribution is one that was originally developed for powders by Rosin and Rammler (1933). It may be expressed in the form as equation AIII.4.17.

$$1 - Q = \exp(-(D / X))^q \quad (\text{AIII.4.17})$$

where Q is the fraction of the total volume contained in drops of diameter less than D, and X and q are constants (Lefevre, 1989).

For most engineering purposes the distribution of drop sizes in a spray may be represented concisely as a function of two parameters (as in the Rosin-Rammler expression, for example), one of which is a representative diameter and the other a measure of the range of drop sizes. In some instances it may be advantageous to introduce another term, such as a parameter to express minimum drop size, but basically there must be at least two parameters to describe the drop size distribution.



There are many possible choices of representative diameter, each of which can play a role in defining the distribution function. The various possibilities include the following:

$D_{0.1}$  = drop diameter such that 10% of total liquid volume is in drops of smaller diameter.

$D_{0.5}$  = drop diameter such that 50% of total liquid volume is in drops of smaller diameter. This is the mass median diameter (MMD).

$D_{0.632}$  = drop diameter such that 63.2% of total liquid volume is in drops of smaller diameter. This is  $X$  in equation AIII.4.16.

$D_{0.9}$  = drop diameter such that 90% of total liquid volume is in drops of smaller diameter.

$D_{0.999}$  = drop diameter such that 99.9% of total liquid volume is in drops of smaller diameter

## Appendix IV Formulation components of the cigarette replacement device (Oxette®)

### AIV.1 Formula 1, 2, 3

The nicotine formulations can be divided into two main parts, one is the bulk concentrate (a mixture of nicotine free base, absolute ethanol and propylene glycol) and the other is the propellant (HFA 134a). The solutions were subsequently mixed to form a bulk composition for Formula 1, 2 and 3 respectively (shown in Table A.2)

	<b>Theoretical Weight</b>	<b>Actual Weight</b>
	<b>Bulk Concentrate (g)</b>	<b>Bulk Concentrate (g)</b>
<b>Formula 1</b>		
Nicotine free base	0.08	0.08
Ethanol	2.88	2.89
Propylene Glycol	91.44	91.45
<b>Formula 2</b>		
Nicotine free base	0.08	0.08
Ethanol	2.88	2.88
Propylene Glycol	43.84	43.84
<b>Formula 3</b>		
Nicotine free base	0.08	0.08
Ethanol	2.88	2.89
Propylene Glycol	15.28	15.28

Table A.2 Mass distributions of Formulas 1, 2, 3.

Formula 1, 2 and 3 contain different amount of propylene glycol and therefore different amounts of HFA 134a were required to fill reservoir units containing different formulation i.e.

Weights for filling 20ml canister (assume 80% fill volume)

<b>Formulation</b>	<b>Quantity (g)</b>	<b>% v/v Composition</b>
<b>Formula 1</b>	Bulk concentrate = 7.55 HFA 134a = 9.02	Bulk concentrate = 50 HFA 134a = 50
<b>Formula 2</b>	Bulk concentrate = 3.74 HFA 134a = 13.54	Bulk concentrate = 25 HFA 134a = 75
<b>Formula 3</b>	Bulk concentrate = 1.46 HFA 134a = 16.24	Bulk concentrate = 10 HFA 134a = 90

*Table A.3 HFA 134a requirement for different formulations (Formula 1, 2 and 3) in 20ml canister.*

Weights for filling 30ml canister (assume 80% fill volume)

<b>Formulation</b>	<b>Quantity (g)</b>	<b>% v/v Composition</b>
<b>Formula 1</b>	Bulk concentrate = 11.33 HFA 134a = 13.54	Bulk concentrate = 50 HFA 134a = 50
<b>Formula 2</b>	Bulk concentrate = 5.62 HFA 134a = 20.30	Bulk concentrate = 25 HFA 134a = 75
<b>Formula 3</b>	Bulk concentrate = 2.19 HFA 134a = 24.36	Bulk concentrate = 10 HFA 134a = 90

*Table A.4 HFA 134a requirement for different formulations (Formula 1, 2 and 3) in 30ml canister.*

## **AIV.2 Formula 4**

Sample name: 09PM020 – 16 (1–12)

Net Weight: 10g

### **Sample composition:**

<b>Ingredient</b>	<b>Amount</b>
Nicotine (API)	10mg
Nicotinic acid	3mg
Oleic acid	43mg
Menthol	5mg
Co-solvent (Ethanol:Propylene glycol – 9:1 ratio)	439mg
Hydrofluoroalkane (HFA 134a)	9.5g

*Table A.5 Mass distribution of Formula 4*

### AIV.3 Formulations tested with dual laser beam method

Net Weight: 10g	Theoretical Weight (g)				
	Formula 1	Formula 2	Formula 3	Formula 4	Formula 5
Nicotine free base	0.01	0.01	0.01	0.01	0.01
Ethanol	0.1	0.2	0.4	0.8	1.5
Propylene Glycol	0.39	0.79	1.59	3.19	5.99
HFA 134a	9.5	9.0	8.0	6.0	4.0

Table A.6 Mass distribution of different formulations analyzed by the dual laser beam method.

### AIV.4 Formulations tested with high speed imaging method

Excipient	Theoretical composition, %, w/w				
	KDCRA103	KDCRA120	KDCRA121	KDCRA125	KDCRA122
Nicotine	0.028	0.028	0.028	0.028	0.028
Ethanol	0.95	0.95	0.95	0.95	0.95
Propylene Glycol	3.8830	2.9123	1.9415	1.4561	0.9708
Saccharin	0.0050	0.0050	0.0050	0.0050	0.0050
Nicotine acid	0.0100	0.0100	0.0100	0.0100	0.0100
Vanillin	0.0500	0.0500	0.0500	0.0500	0.0500
HFA 134a	95.07	96.0448	97.0155	97.5009	97.9863

Table A.7 Mass distribution of different formulations analyzed by the high speed imaging method.

## Appendix V: Programming functions

### AV.1 Multi-component droplet evaporation model

More details should refer to Brenn et al. (2007).

#### *Evaporation rate of a multi-component droplet*

The evaporation rate of the droplet is the sum of all component evaporation rates for an N-component mixture:

$$\dot{m} = \sum_{i=1}^N \dot{m}_i = 2\pi \sum_{i=1}^N r_{v,i} (\overline{\rho D_i})_g Sh_i^* \ln(1 + B_{M,i}) \quad (\text{AV.1.1})$$

where  $\dot{m}_i$  is the evaporation rate of the liquid component  $i$  in the droplet.  $r_{v,i}$  is the volume equivalent partial radius of component  $i$  corresponding to its instantaneous volume fraction  $\varphi_i$  in the liquid mixture, which is defined as  $r_{v,i} = r\varphi_i^{1/3}$  where  $r$  is the radius of the droplet.  $\overline{D_i}$  is the mean diffusion coefficient of the vapour of component  $i$  in

dry air. The modified Sherwood number  $Sh_i^*$  is calculated individually for each component  $i$ , using the component vapour properties and the drop diameter  $d = 2r$  as the length scale of the Re number.

$$Sh_i^* = 2 + \frac{Sh_{0,i} - 2}{F(B_{M,i})} \quad (\text{AV.1.2})$$

with the Sherwood number  $Sh_0$  for the small mass transfer rate given by Frössling correlation (as cited in Brenn, 2007):

$$Sh_{0,i} = 2 + 0.552 \text{Re}_i^{1/2} \text{Sc}_i^{1/3} \quad (\text{AV.1.3})$$

The function  $F(B_M)$ :

$$F(B_{M,i}) = (1 + B_{M,i})^{0.7} \frac{\ln(1 + B_{M,i})}{B_{M,i}} \quad (\text{AV.1.4})$$

The Spalding mass transfer number  $B_{M,i}$  is computed for each component  $i$  according to

$$B_{M,i} = \frac{Y_{i,S} - Y_{i,\infty}}{1 - Y_{i,S}} \quad (\text{AV.1.5})$$

where  $Y_{i,S}$  and  $Y_{i,\infty}$  are the mass fractions of the vapour component  $i$  at the droplet surface and in the undisturbed ambient medium, respectively.

#### ***Heat transfer rate into a multi-component droplet***

The rate of heat transfer into the multi-component droplet is calculated by an equation analogous to equation (AV.1.1) for all components separately:

$$Q_L = \sum_{i=1}^N \dot{m}_i \left[ \frac{\overline{c_{p,i}}(T_\infty - T_S)}{B_{T,i}} - h_{fg,i}(T_S) \right] \quad (\text{AV.1.6})$$

where  $h_{fg,i}(T_S)$  is the latent heat of evaporation of the liquid at the droplet surface temperature  $T_S$ , and  $B_T = (1 + B_M)^\phi - 1$  is the Spalding heat transfer number.

$$B_{T,i} = (1 + B_{M,i})^{\phi_i} - 1 \quad (\text{AV.1.7})$$

The exponent  $\phi$  is:

$$\phi_i = \frac{\overline{c_{p,l}}}{\overline{c_{p,g}}} \frac{Sh_i^*}{Nu_i^*} \frac{1}{Le} \quad (\text{AV.1.8})$$

$\overline{c_{p,l}}$  and  $\overline{c_{p,g}}$  indicate average values between the thermodynamic states at the droplet surface and in the ambient gas.  $\overline{Le}$  is the average Lewis number of the gas mixture. The modified Nusselt number  $Nu^*$  is given by

$$Nu_i^* = 2 + \frac{Nu_{0,i} - 2}{F(B_{T,i})} \quad (\text{AV.1.9})$$

$$Nu_{0,i} = 2 + 0.552 Re_i^{1/2} Pr_i^{1/3} \quad (\text{AV.1.10})$$

$$F(B_{T,i}) = (1 + B_{T,i})^{0.7} \frac{\ln(1 + B_{T,i})}{B_{T,i}} \quad (\text{AV.1.11})$$

***Modeling the component activities in liquid mixtures by UNIFAC approach***

The mass fraction  $Y_i$  of the vapour component  $i$  can be calculated from the mole fraction  $x_i$  :

$$x_i = \frac{P_{vap,i}}{p_m} \gamma_i x_{l,i} \quad (\text{AV.1.12})$$

where  $p_{vap,i}$  is the vapour pressure of the pure component  $i$ ,  $\gamma_i$  is the activity coefficient of the component in the multi-component liquid mixture, and  $x_{l,i}$  the mole fraction of component  $i$  in the liquid phase. The whole mixture equilibrium is established under the total mixture pressure  $p_m$ .

UNIFAC method allows the activity coefficients of components of polynary liquid mixtures to be calculated as functions of mixture composition and temperature. UNIFAC is a combination of the UNIQUAC method with the increment method (as cited in Brenn, 2007). The increment method assumes that  $\gamma_i$  is composed of a combinatoric part (C) and a rest part (R). The combinatoric part stands for a contribution of the excess entropy, and the rest part for the effect of the excess enthalpy:

$$\ln \gamma_i = \ln \gamma_i^C + \ln \gamma_i^R \quad (\text{AV.1.13})$$

The combinatoric part is calculated by the so-called UNIQUAC method as

$$\ln \gamma_i^C = \ln \frac{\psi_i}{x_{l,i}} + 5q_i \ln \frac{v_i}{\psi_i} + l_i - \frac{\psi_i}{x_{l,i}} \sum_{k=1}^N x_{l,j} l_i \quad (\text{AV.1.14})$$

with

$$l_i = 5(r_i - q_i) - (r_i - 1) \quad (\text{AV.1.15})$$

$$v_i = \frac{q_i x_{l,i}}{\sum_{j=1}^N q_j x_{l,j}}, \quad \psi_i = \frac{r_i x_{l,i}}{\sum_{j=1}^N r_j x_{l,j}} \quad (\text{AV.1.16})$$

Here  $x_{l,j}$  is the mole fraction of component  $i$  and  $N$  is the number of components in the liquid mixture.  $q_i$  and  $r_i$  are the relative Van-der-Waals surface and volume, respectively. They are computed as

$$r_i = \sum_{k=1}^M \nu_k^{(i)} R_k, \quad q_i = \sum_{k=1}^M \nu_k^{(i)} Q_k \quad (\text{AV.1.17})$$

where  $\nu_k^{(i)}$  is the number of structure groups of type  $k$  in the molecule  $i$ .  $M$  is the number of different groups in molecule  $i$ , and  $R_k$  and  $Q_k$  are constants specific for group  $k$  given in databases (Reid et al., 1977, Fukuchi et al., 2001, Wittig et al., 2003 and Hou et al., 2008).

The rest part is computed as the sum of the various group contributions:

$$\ln \gamma_i^R = \sum_{k=1}^M \nu_k^{(i)} [\ln \Gamma_k - \ln \Gamma_k^{(i)}] \quad (\text{AV.1.18})$$

$\Gamma_k$  and  $\Gamma_k^{(i)}$  are the group activity coefficients of group  $k$  in the mixture and in the pure liquid  $i$ , respectively. They are computed as

$$\ln \Gamma_k = Q_k \left[ 1 - \ln \left( \sum_{m=1}^M v_m \chi_{mk} \right) - \sum_{m=1}^M \frac{v_m \chi_{km}}{\sum_{n=1}^M v_n \chi_{nm}} \right] \quad (\text{AV.1.19})$$

with

$$v_m = \frac{Q_m X_m}{\sum_{n=1}^M X_n}, \quad X_m = \frac{\sum_{j=1}^N v_m^{(i)} x_j}{\sum_j \sum_{n=1}^N v_n^{(i)} x_j}, \quad \chi_{nm} = e^{-a_{nm}/T} \quad (\text{AV.1.20})$$

Here  $a_{nm}$  is the group interaction parameter between groups  $n$  and  $m$ , which is available for many group combinations (Reid et al., 1977, Fukuchi et al., 2001, Wittig et al., 2003 and Hou et al., 2008).

## AV.2 Approximation of the first derivative by Lagrange interpolating polynomial

As cited in Jeffreys et al., 1988, the Lagrange interpolating polynomial is the polynomial  $P(x)$  of degree  $\leq (n-1)$  that passes through the  $n$  points  $(x_1, y_1=f(x_1))$ ,  $(x_2, y_2=f(x_2))$ , ...,  $(x_n, y_n=f(x_n))$ , and is given by

$$P(x) = \sum_{j=1}^n P_j(x), \quad (\text{AV.2.1})$$

where

$$P_j(x) = y_j \prod_{\substack{k=1 \\ k \neq j}}^n \frac{x - x_k}{x_j - x_k} \quad (\text{AV.2.2})$$

and written explicitly,

$$\begin{aligned} P(x) &= \frac{(x-x_2)(x-x_3)\cdots(x-x_n)}{(x_1-x_2)(x_1-x_3)\cdots(x_1-x_n)} y_1 \\ &+ \frac{(x-x_1)(x-x_3)\cdots(x-x_n)}{(x_2-x_1)(x_2-x_3)\cdots(x_2-x_n)} y_2 \\ &+ \dots + \frac{(x-x_1)(x-x_2)\cdots(x-x_{n-1})}{(x_n-x_1)(x_n-x_2)\cdots(x_n-x_{n-1})} y_n \end{aligned} \quad (\text{AV.2.3})$$

From equation AV.2.1, AV.2.2 and AV.2.3, in order to calculate the first derivative  $P'(x)$  of  $P(x)$ , the first derivative of the term  $\prod_{\substack{k=1 \\ k \neq j}}^n (x - x_k)$  is required to be

calculated as:

$$\left( \prod_{\substack{k=1 \\ k \neq j}}^n (x - x_k) \right)' = \sum_{\substack{i=1 \\ i \neq j}}^n \left( \prod_{\substack{k=1 \\ k \neq i \\ k \neq j}}^n (x - x_k) \right) \quad (\text{AV.2.4})$$

Therefore, with (AV.2.1) and (AV.2.2),  $P'(x)$  can be calculated.



## Appendix VI Parts lists of the experimental rigs

### AVI.1 Parts list of the mechanical lung

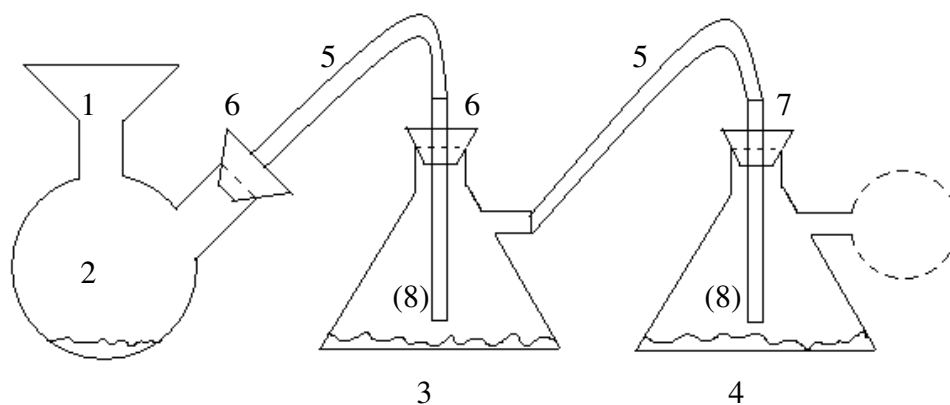
The major parts of the mechanical lung (section 3.2, Chapter 3) are listed below, showing the item codes, and the latest pricing details.

Description	Supplier	Product Code	Unit Pricing	Qty
<b>• Electro-Cylinder Details</b>				
Electro Thrust Cylinder	Parker	ETB32M05LA47FM350A	£849.00	1
Servo Motor	Parker	SMH60301,4892VB640	£286.00	1
Servo Drive	Parker	VIX500IE	£244.00	1
Power Supply	Parker	XLPSU	£236.00	1
Fit Kit	Parker	VIX-KIT	£27.00	1
Motor Power Cable	Parker	VIX-PWR-0500	£77.00	1
Motor Feedback Cable	Parker	VIX-FDB-0500	£77.00	1
RS-232 Lead	Parker	RS232-EASI-0500	£39.00	1
		<b>sub-total:</b>	<b>£1,835.00</b>	
<b>• Pressure Sensor Details</b>				
Pressure Transducer	Strainsense	43A-002G	£89.00	1
7 way cable plug	RS	445-201	£17.53	1
7 way sealed panel	RS	445-346	£21.13	1
		<b>sub-total:</b>	<b>£127.66</b>	
<b>• Rig Components</b>				
Aluminum Frame			£378.00	1
Horizontal Clamps	WDS	WDS4024	£8.61	4
Non return valve	RS	340-3301	£5.45	1
60mm Fan filter	RS	580-635	£4.92	4
Elbow connector	RS	795-326	£1.77	1
Hydraulic blanking plug	RS	283-3420	£0.96	1
		<b>sub-total:</b>	<b>£440.30</b>	
		<b>GRAND TOTAL</b>	<b>£2,402.96</b>	

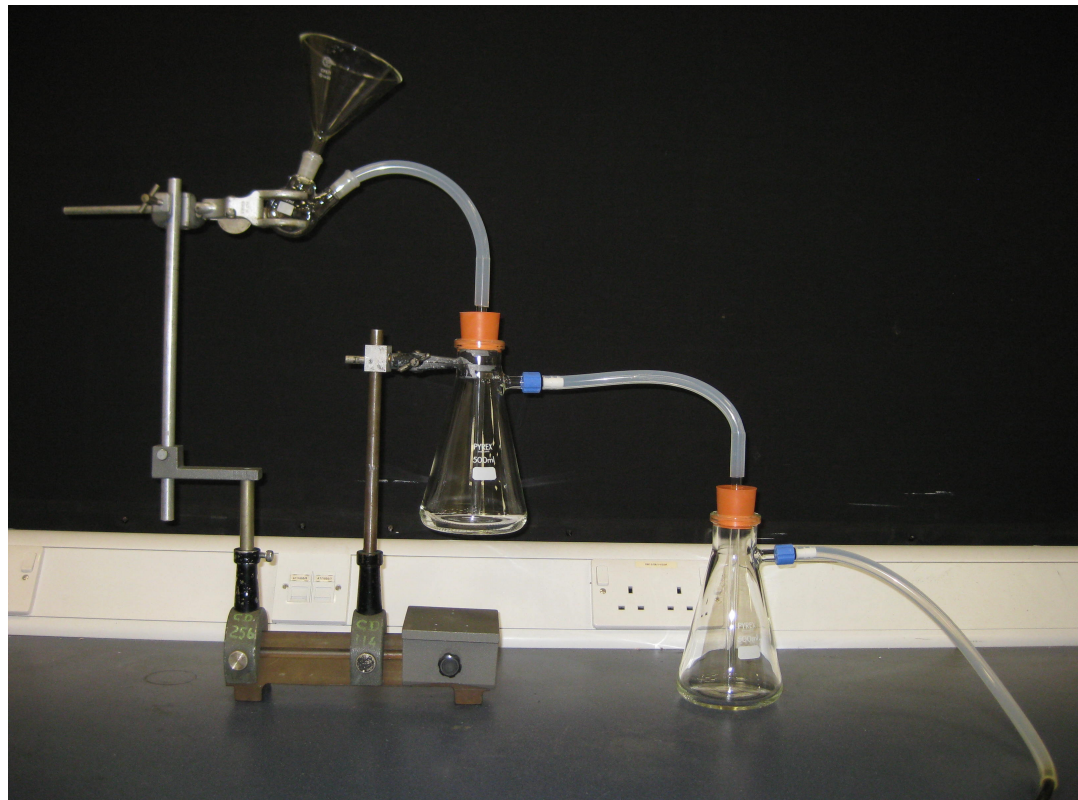
*Table A.8 Parts list of the mechanical lung rig (section 3.2, Chapter 3).*

## AVI.2 Parts list of the mass deposition rig

The mass deposition rig is designed to test how the sizes of the droplets affect the deposition in different regions in different regions of the human respiratory tract. The assembly drawing and a photo are shown in Figure A.7 and A.8, with a parts list in Table A.9.



*Figure A.7 Assembly drawing for the mass deposition rig with the numbered items listed in Table A.9.*



*Figure A.8 Assembly photo of the mass deposition rig.*



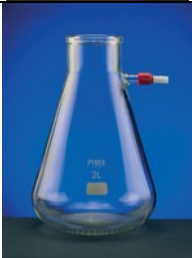

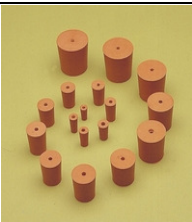
No.	Name	Catalogue no.	Quantity	Price	Image
1	Funnel powder borosilicate glass 105mm diameter 14/23 cone Quickfit	QHL-520-Q	1	£24.42	
2	Flask QQ RB 14/23 round bottom 2 necks borosilicate glass 50mL Quickfit	QFM-015-W	1	£35.04	
3,4	Filter flask Buchner with sidearm and screwthread connector borosilicate glass 500mL Pyrex	FHD-360-075B	1 pack (1 pack of 2)	£40.64	
5	Tubing normal wall BS 2775 silicone translucent 9mm x 2mm (bore x wall) Fisherbrand	FB50873	1	£47.82	
6	Stopper 1 hole BS 2775 rubber red 21mm bottom diameter Fisherbrand	FB53021	1 pack ( 1 pack of 20)	£13.98	
7	Stopper 1 hole BS 2775 rubber red 33mm bottom diameter Fisherbrand	FB53033	1 pack ( 1 pack of 10)	£20.65	
8	Tubing medium wall borosilicate glass 10mm bore Griffin	FB51470	1 pack ( 1 pack of 20)	£26.44	
Total				£146.71	
Available from <a href="http://www.fisher.co.uk/">http://www.fisher.co.uk/</a>					

Table A.9 Parts list of the mass deposition rig (section 3.4, Chapter 3).

## References

- Albrecht, H. E., Borys, I. M., Damaschke, I. N., Tropea, I. C., 2003. *Laser doppler and phase doppler measurement techniques*. Berlin: Springer.
- Alt, H., Godau, M., 1995. Computing the Fréchet Distance between Two Polygonal Curves. *International Journal of Computational Geometry and Applications*, 5(1-2), pp.75-91.
- Anderson, P. J., Wilson J. D., Hiller F. C., 1989. Particle size distribution of mainstream tobacco and marijuana smoke: Analysis using the electrical aerosol analyzer. *American Review of Respiratory Disease*, 140(1), pp.202-205.
- Atkins, P. W., 2006. *Atkins' physical chemistry*. Oxford: Oxford University Press.
- Bar-Kohany, T., Sher, E., 2004. Effervescent atomization under sub-sonic and choked conditions—a theoretical approach. *Chemical Engineering Science*. 59(24), pp.5987-5995.
- Brenn, G., Deviprasath, L. J., Durst, F. and Fink, C., 2007. Evaporation of acoustically levitated multi-component liquid droplets. *International Journal of Heat and Mass Transfer*, 50(25-26), pp.5073-5086.
- Brown, J.H., Cook, K.M., Ney, F.G. and Hatch, T., 1950. Influence of Particle Size upon the Retention of Particulate Matter in the Human Lung. *American Journal of Public Health and the Nation's Health*, 40(4), pp.450-458, 480.
- Buchin, K., Buchin, M., Wenk, C., 2006. Computing the Fréchet distance between simple polygons in polynomial time. In: Proceeding SCG '06, *Proceedings of the twenty-second annual symposium on Computational geometry*. Sedona, Arizona, USA, 05 – 07 June, 2006. New York, USA.

Bucker, H. N., Sojka, P. E., 1993. Effervescent atomization of high viscosity fluid. Part 2: non-Newton liquids. *Atomization and Sprays*, 3(2), pp.157-170.

Calay, R. K., Holdo, A. E., 2008. Modeling the dispersion of flashing jets using CFD. *Journal of Hazardous Materials*, 154(1-3), pp.1198–1209.

Carilli, A. D., Denson, L. J., Rock, F., Malabana, S., 1974. Flow-Volume Loop in Normal Subjects and in Diffuse Lung-Disease. *Chest*, 66(5), pp.472-477.

Centers for Disease Control and Prevention, 2002. *Annual Smoking-Attributable Mortality, Years of Potential Life Lost, and Economic Costs — United States, 1995-1999*. Morbidity and Mortality Weekly Report, 51(14), pp.300-303.

Chan, H. K., & Gonda, I., 1989. Aerodynamic properties of elongated particles of cromoglycic acid. *Journal of Aerosol Science*, 20(2), pp.157–168.

Chavan, V., Dalby, R., 2002. Novel system to investigate the effects of inhaled volume and rates of rise in simulated inspiratory air flow on fine particle output from a dry powder inhaler. *AAPS PharmSci*, 4(2): article 6. DOI: 10.1208/ps040206.

Chigier, N., 1991. Optical imaging of sprays. *Progress in Energy and Combustion Science*, 17(3), pp.11-262.

Clark, A.R., 1991. *Metered atomization for respiratory drug deliver*. Ph.D. Thesis, Loughborough University of Technology, UK.

Cotes, J. E., Chin, D. J., Miller, M. R., 2006. *Lung function: physiology, measurement and application in medicine*, 6<sup>th</sup> ed. Oxford: Wiley-Blackwell.

- Cripps, A., Riebe, M., Schulze, M., Woodhouse, R., 2000. Pharmaceutical transition to non-CFC pressurized metered dose inhalers. *Respiratory Medicine*, 94(2), pp.S3-S9.
- Crowder, T. M., Rosati, J. A., Schroeter, J. D., Hickey, A. J., and Martonen, T. B., 2002. Fundamental effects of particle morphology on lung delivery: Predictions of Stokes' law and the particular relevance to dry powder inhaler formulation and development. *Pharmaceutical Research*, 19(3), pp.239–245.
- Danby, M., 2008. *Mechanical Lung Notes*. [report] (Personal communication, 2008). University of Southampton, UK
- Danby, M., 2010. *Size distribution of the glass spheres*. [email] (Personal communication, 30 September 2010). University of Southampton, UK.
- Darquenne, C., Paiva, M., West, J. B., Prisk, G. K., 1997. Effect of microgravity and hypergravity on deposition of 0.5- to 3- $\mu$ m-diameter aerosol in the human lung. *Journal of Applied Physiology*, 83(6), pp.2029-2036.
- Darquenne, C., West, J. B., Prisk, G. K., 1999. Dispersion of 0.5 to 2 $\mu$ m aerosol in  $\mu$ G and hypergravity as a probe of convective inhomogeneity in the lung. *Journal of Applied Physiology*, 86(4), pp.1402-1409.
- Dunbar, C. A., 1996. *An experimental and the theoretical investigation of the spray issued from a pressurized metered-dose inhaler*. Ph.D. Thesis, Institute of Science and Technology, University of Manchester, UK.
- Dyakowski, T., Williams, R.A., 1993. Measurement of particle velocity distribution in a vertical channel. *Powder Technology*, 77(2), pp.135-142.

- Efrat, A., Fan, Q. F., Venkatasubramanian, S., 2007. Curve matching, time warping, and light fields: New algorithms for computing similarity between curves. *Journal of Mathematical Imaging and Vision*, 27(3), pp.203–216.
- Elkotb, M. M., 1982. Fuel Atomization for Spray Modeling. *Progress in Energy and Combustion Science*, 8(1), pp. 61-91.
- Farkas, A., Balashazy, I., Szocs, K., 2006. Characterization of Regional and Local Deposition of Inhaled Aerosol Drugs in the Respiratory System by Computational Fluid and Particle Dynamics Methods. *Journal of Aerosol Medicine*, 19(3), pp.329-343.
- Finlay, W. H., 2001. *The Mechanics of Inhaled Pharmaceutical Aerosols: An Introduction*. London: Academic Press.
- Frohn, A. and Roth, N., 2000. *Dynamics of droplets*. Berlin: Springer.
- Fujiwara, K., Nakamura S., Noguchi M., 1999. Thermodynamic Properties for R-404A. *International Journal of Thermophysics*, 20(1), pp.129-140.
- Fukuchi, K., Miyoshi K., Watanabe T., Yonezawa, S., Arai, Y., 2001. Measurement and correlation of infinite dilution activity coefficients of bis(2,2,2-trifluoroethyl)ether in dodecane or alkanol. *Fluid Phase Equilibria*, 182(1-2), pp.257–263.
- Goodman, J. E. and O'Rourke, J., 2004. *Handbook of Discrete and Computational Geometry*. 2<sup>nd</sup> ed. Boca Raton, FL.: Chapman & Hall / CRC.
- Granger, R. H., 2005. Oxygen as a therapy for reducing nicotine withdrawal symptoms. *Medical Hypotheses*, 65(6), pp.1161–1164.
- Graf, R.F., 1999. *Modern dictionary of electronics*, 7<sup>th</sup> ed.. Woburn: Newnes.

Grgic, B., Finlay, W. H., Heenan, A. F., 2004. Regional aerosol deposition and flow measurements in an idealized mouth and throat. *Journal of Aerosol Science*, 35(1), pp.21–32.

Hearn, A., alex.hearn@kindconsumer.com, 2010. *Metering chamber volume of Oxette®* [email] Message to Dehao Ju (dj2g08@soton.ac.uk). Sent Wednesday 08 December 2010, 00:15.

Hochrainer, D., Holz, H., Kreher C., Scaffidi, L., Spallek, M., Wachtel, H., 2005. Comparison of the aerosol velocity and spray duration of RespiMat® soft Mist inhaler and pressurized metered dose inhalers. *Journal of Aerosol Medicine*, 18(3), 273-282.

Hou, S., Duan, Y., and Wang, X., 2008. Vapor-Liquid Equilibria Predictions for Alternative Working Fluids at Low and Moderate Pressures. *Industrial & Engineering Chemistry Research*, 47(19), pp.7501–7508.

International Agency for Research on Cancer, World Health Organization, 2002. Tobacco smoke and involuntary smoking. *IARC Monographs on the Evaluation of Carcinogenic Risks to Humans*, Volume 83. Lyon: International Agency for Research on Cancer.

International Organisation for Standardization, 2005. *Routine analytical cigarette-smoking machine -- Definitions and standard conditions*. ISO 3308:2000.

Janesick, J. R., 2001. *Scientific Charge-Couples Devices*. Bellingham: SPIE Press.

Jayaraju, S. T., Brouns, M., Lacor, C., Belkassam, B., Verbanck, S., 2008. Large eddy and detached eddy simulations of fluid flow and particle deposition in a human mouth–throat. *Journal of Aerosol Science*, 39(10), pp.862 – 875.

Jeffreys, H. and Jeffreys, B. S., 1988. *Methods of Mathematical Physics*, 3rd ed. Cambridge: Cambridge University Press, p. 260.



Jin, H. H., Fan, J.R., Zeng, M. J., Cen, K. F., 2007. Large eddy simulation of inhaled particle deposition within the human upper respiratory tract. *Journal of Aerosol Science*, 38(3), pp.257-268.

Johnson, D. L., Martonen, T. B., 1994. Behavior of inhaled fibers: Potential application to medicinal aerosols. *Particulate Science and Technology*, 12(2), pp.161–173.

Kashdan, J. T., 2002. *Experiments in Intermittent Swirl-Generated Sprays*. Ph.D. Thesis. Imperial College, London, UK

Kashdan, J. T., Shrimpton, J. S., Whybrew, A., 2003. Two-Phase Flow Characterisation by Automated Digital Image Analysis, Part 1: Fundamental Principles and Calibration of the Technique. *Particle and Particle Systems Characterization*, 20(6), pp.387-397.

Kashdan, J. T., Shrimpton, J. S., Whybrew, A., 2004. Two-Phase Flow Characterization by Automated Digital Image Analysis. Part 2: Application of PDIA for Sizing Sprays. *Particle and Particle Systems Characterization*, 21(1), pp.15 – 23.

Kashdan, J. T., Shrimpton, J. S., Whybrew, A., 2007. Digital image analysis technique for quantitative characterisation of high-speed sprays. *Optics and Lasers in Engineering*, 45(1), pp.106–115.

Katz-Zeigerson, M., Sher, E., 1998. Spray formation by flashing of a binary mixture: a parametric study. *Atomization and Sprays*, 8(3), pp.255–266.

Keith, C. H., Derrick. J. C., 1960. Measurement of the particle size distribution and concentration of cigarette smoke by the “conifuge”. *Journal of Colloid Science*, 15(4), pp.340-356.

- Kleinstreuer, C., Shi, H. W., Zhang, Z., 2007. Computational analyses of a pressurized metered dose inhaler and a new drug aerosol targeting methodology. *Journal of Aerosol Medicine*, 20(3), pp.294-309.
- Koh, K. U., Kim, J. Y., Lee, S. Y., 2001. Determination of In-Focus Criteria and Depth of Field in Image Processing of Spray Particles. *Atomization and Sprays*, 11(4), pp.317-333.
- Kolonen, S., Tuomisto, J., Puustinen, P., Airaksinen, M. M., 1992. Puffing Behavior during the Smoking of a Single Cigarette in a Naturalistic Environment. *Pharmacology, Biochemistry and Behavior*, 41(4), pp.701-706.
- Kotsovinos, N. E., 1976. A note on the spreading rate and virtual origin of a plane turbulent jet. *Journal of Fluid Mechanics*, 77(2), 305-311
- Lee, K.C., Suen, K.O., Yianneskis, M., Marriott, C., 1996. Investigation of the aerodynamic characteristics of inhaler aerosols with an inhalation simulation machine. *International Journal of Pharmaceutics*, 130(1), pp.103-113.
- Lefevre, A. H., 1989. *Atomisation and Sprays*, CRC Press, Taylor & Francis Group: Boca Raton, FL, USA.
- Lide, D. R., 2002. *CRC Handbook of Chemistry and Physics*, 83rd Edition. Boca Raton : CRC Press.
- Lippmann, M. and Albert, R. E., 1969. The Effect of Particle Size on the Regional Deposition of Inhaled Aerosols in the Human Respiratory Tract. *American Industrial Hygiene Association Journal*, 30(3), pp.257-275.
- Lorenzetto, G. E., and Lefebvre, A. H. 1977, Measurements of drop size on a plain jet airblast atomizer. *AIAA Journal*, 15(7), pp.1006-1010.

Ma, B., Ruwet, V., Corieri, P., Theunissen, R., Riethmuller, M., Darquenne, C., 2009. CFD simulation and experimental validation of fluid flow and particle transport in a model of alveolated airways. *Journal of Aerosol Science*, 40(5), pp.403–414.

Medicines Healthcare products Regulatory Agency, 2010. The regulation of nicotine containing products, consultation letter, MLX 364. London: Medicines Healthcare products Regulatory Agency, 1st February 2010.

Morgan, R., Wray, J., Kennaird, D.A., Crua, C. and Heikal, M.R., 2001. *The Influence of Injector Parameters on the Formation and Break-Up of a Diesel Spray*. Society of Automotive Engineers, Inc., 2001-01-0529

Mugele, R. A., Evans, H. D. 1951. Droplet Size Distribution in Sprays. *Industrial and Engineering Chemistry*, 1951, 43(6), pp.1317–1324. Sanders, P.A., 1970. *Principles of Aerosol Technology*. New York: Van Nostrand Reinhold Co..

Munich, M. E. and Perona, P., 1999. Continuous dynamic time warping for translation-invariant curve alignment with applications to signature verification. In: *IEEE, Seventh international conference on computer vision*. Kerkyra, Greece 20-27 September 1999. pp.108–115.

Munich, M. E. and Perona, P., 2003. Visual identification by signature tracking. *IEEE Transactions on pattern analysis and machine intelligence*, 25(2), pp.200–217.

National Cancer Institute. SEER Training Modules, Bronchi, Bronchial Tree, & Lungs. U. S. National Institutes of Health. [Accessed: 18 April 18, 2012]  
< <http://training.seer.cancer.gov/anatomy/respiratory/passages/bronchi.html> >.

Newman, S. P., 1985. Aerosol Deposition Considerations in Inhalation Therapy. *Chest*, 88, pp.152S-160S

- Newman, S. P., 2005. Principle of metered-dose inhaler design. *Respiratory Care*, 50(9), pp.1177-1190.
- Oldham, M. J., Phalen, R. F., Heistracher, T., 2000. Computational Fluid Dynamic Predictions and Experimental Results for Particle Deposition in an Airway Model. *Aerosol Science and Technology*, 32(1), pp.61-71.
- Parker, 2003. *ViX250IE, ViX500IE Servo Drives User Guide*. Part No: 1600.304.02 July, 2003 (For software revision 2.0 onwards).
- Palsson, B., Hubbell, J. A., Plonsey, R., Bronzino, J. D., 2003. *Tissue Engineering*. Boca Raton: CRC Press.
- Perry, R. H., Green D. W., 1997. *Perry's Chemical Engineers' Handbook*, seventh edition. Sydney: McGraw-Hill.
- Pope, Stephen. B., 2000. *Turbulent flows*. Cambridge University Press: Cambridge, UK.
- Potter, M. C., Wiggert, D. C., 1997. *Mechanics of Fluids*, second edition. Upper Saddle River: Prentice Hall.
- Peto, R., 1994. Smoking and death: the past 40 years and the next 40. *British Medical Journal*, 309(6959), pp.937-939.
- Polanco, G., Holdo, A. E., Munday G., 2010. General review of flashing jet studies. *Journal of Hazardous Materials*, 173(1-3), pp.2-18.
- Rashkovan, A., Sher, E., 2006. Flow pattern observations of gasoline dissolved CO<sub>2</sub> inside an injector. *Atomization and Sprays*, 16(6), pp.615–626.

- Rath, T. M. and Manmatha, R., 2002. *Lower-bounding of dynamic time warping distances for multivariate time series*. Technical report MM-40. Amherst: Center for Intelligent Information Retrieval, University of Massachusetts.
- Ray, E.D., George L. Tuve, 1973. *Handbook of Tables for Applied Engineering Science*. Cleveland: CRC Press.
- Reid, R.C., Prausnitz, J.M., Sherwood, T.K., 1977. *The properties of gases and liquids*, 3rd edition. New York: McGraw-Hill.
- Sanders, P.A., 1970. *Principles of Aerosol Technology*. New York: Van Nostrand Reinhold Co.
- Scollo, M., Lal, A., Hyland, A., Glantz, S., 2003. Review of the quality of studies on the economic effects of smoke-free policies on the hospitality industry. *Tobacco Control*, 12(1), pp.13–20.
- Serra, B. and Berthod, M., 1994. Subpixel contour matching using continuous dynamic programming. In: IEEE, *Computer society conference on computer vision and pattern recognition*. Seattle, WA, USA 21-23 Jun 1994. pp.202–207.
- Sher, E., Bar-Kohany, T., Rashkovan, A., 2008. Flash-boiling atomization, *Progress in Energy and Combustion Science*, 34(4), pp.417–439.
- Shrimpton, J. S., 2008. *Kind group phase I report*. [report] (Personal communication, 2008).
- Solomon, A. S. P., Rupprecht, S. D., Chen L. D., Faeth G. M., 1985. Flow and atomization in flashing injectors. *Atomisation and Spray Technology*, 1, pp.53-76.

- Sovani, S. D., Sojkaa, P. E., Lefebvre, A. H., 2001. Effervescent atomization. *Progress in Energy and Combustion Science*, 27(4), pp.483-521.
- Stahlhofen, W., Rudolf, G., James, A. C., 1989, Intercomparison of Experimental Regional Aerosol Deposition Data. *Journal of Aerosol Medicine*, 2(3), pp.271-284.
- Stevens, N. E., 2006. *Multiphase Modelling Methods for Dry Powder Inhaler Flow*. Ph.D. Thesis, Imperial College London, UK.
- Suyari, M., Lefevre, A. H., 1986. Film Thickness Measurements in a Simplex Swirl Atomizer. *A.I.A.A. Journal of Propulsion and Power*, 2(6), pp.528-533.
- Swarbrick, J., 2007. *Encyclopedia of Pharmaceutical Technology*, 3rd edition. Volume 4, New York: Informa Healthcare USA, Inc..
- Takano, H., Nishida, N., Itoh, M., Hyo, N., Majima, Y., 2006. Inhaled particle deposition in unsteady-state respiratory flow at a numerically constructed model of the human larynx. *Journal of Aerosol Medicine*, 19(3), pp.314-328.
- Tobin, M. J., Jenouri, G. and Sackner, M. A., 1982. Subjective and objective measurement of cigarette smoke inhalation. *Chest*, 82(6), pp.696-700.
- Touloukian, Y. S., Makita, T., 1970. *Specific Heat: nonmetallic liquids and gases*, Thermophysical Properties of Matter, Volume 6. New York : IFI/Plenum.
- UK Department of Health, 2006. *Fact sheet on tobacco*, 277472/1. October, 2006.
- Van Ertbruggen, C., Corieri, P., Theunissen, R., Riethmuller, M.L., Darquenne, C., 2008. Validation of CFD predictions of flow in a 3D alveolated bend with experimental data. *Journal of Biomechanics*, 41(2), pp.399–405.

Versteeg, H. K., Hargrave, G. K. and Kirby, M., 2006. Internal Flow and Near-Orifice Spray Visualisations of a Model Pharmaceutical Pressurised Metered Dose Inhaler. *Journal of Physics: Conference Series*, 45(1), pp 207–213.

Vu, H. and Aguilar, G., 2009. High-Speed Internal Nozzle Flow Visualization of Flashing Jets. ICLASS 2009, *11th Triennial International Annual Conference on Liquid Atomization and Spray Systems*. Vail, Colorado USA, July 2009.

Wallis, G. B., 1969. *One-dimensional two-phase flow*. New York: McGraw-Hill, Inc

Wang, M. R., Lin, T. C., Lai, T. S. and Tseng, I. R., 2005. Atomization Performance of an atomizer with internal impingement. *JSME International Journal*, Series B, 48(4). pp. 858-864.

Wang, X. F., Levebvre, A. H. 1987. Mean Drop Sizes from Pressure-Swirl Nozzles. *A.I.A.A. Journal of Propulsion and Power*, 3(1), pp.11-18.

West, R., 2006. Background smoking cessation rates in England. University College London, STS002, 6<sup>th</sup> December 2006.

Wittig, R., Lohmann, J., and Gmehling, J., 2003. Vapor-Liquid Equilibria by UNIFAC Group Contribution. 6. Revision and Extension. *Industrial & Engineering Chemistry Research*, 42(1), pp.183-188.

World Health Organization, 2008. *The global burden of disease: 2004 update*. Geneva: World Health Organization, ISBN 9789241563710.

Yildiz, D., Rambaud, P., Vanbeeck, J. and Buchlin, J.M., 2002. *A Study on the Dynamics of a Flashing Jet*. Final Contract Research Report EAR0030/2002, von Karman Institute for Fluid Dynamics.

Yule, A. J., Chigier, N. A., Cox, N.W., 1978. Measurement of Particle Sizes in Sprays by the Automated Analysis of Spark Photographs. *Particle Size Analysis*, Heyden Press, pp.61 -73.

Zhang, J., Jiang, D., Huang, Z., Obokata, T., Shiga, S., Araki, M., 2005. Experimental Study on Flashing Atomization of Methane/Liquid Fuel Binary Mixtures. *Energy Fuels*, 19 (5), pp. 2050–2055.